

---

Electronic Thesis and Dissertation Repository

---

5-17-2012 12:00 AM


# Electrohydrodynamic Enhancement of Heat Transfer and Mass Transport in Gaseous Media, Bulk Dielectric Liquids and Dielectric Thin Liquid Films

Seyed Reza Mahmoudi  
*The University of Western Ontario*

Supervisor  
K. Adamiak  
*The University of Western Ontario* Joint Supervisor  
G.S.P Castle  
*The University of Western Ontario*

Graduate Program in Electrical and Computer Engineering

A thesis submitted in partial fulfillment of the requirements for the degree in Doctor of Philosophy and additional works at: <https://ir.lib.uwo.ca/etd>

 Seyed Reza Mahmoudi 2012  
Part of the Condensed Matter Physics Commons, Electromagnetics and Photonics Commons, Electro-Mechanical Systems Commons, Heat Transfer, Combustion Commons, Nanoscience and Nanotechnology Commons, Optics Commons, Other Engineering Commons, Physical Chemistry Commons, and the Tribology Commons

---

## Recommended Citation

Mahmoudi, Seyed Reza, "Electrohydrodynamic Enhancement of Heat Transfer and Mass Transport in Gaseous Media, Bulk Dielectric Liquids and Dielectric Thin Liquid Films" (2012). *Electronic Thesis and Dissertation Repository*. 544.  
<https://ir.lib.uwo.ca/etd/544>

This Dissertation/Thesis is brought to you for free and open access by Scholarship@Western. It has been accepted for inclusion in Electronic Thesis and Dissertation Repository by an authorized administrator of Scholarship@Western. For more information, please contact [wlsadmin@uwo.ca](mailto:wlsadmin@uwo.ca).

Electrohydrodynamic Enhancement of Heat Transfer and Mass Transport in  
Gaseous Media, Bulk Dielectric Liquids and Dielectric Thin Liquid Films

(Thesis format: Integrated Article)

by

Seyed Reza Mahmoudi

Graduate Program in Electrical and Computer Engineering

A thesis submitted in partial fulfillment  
of the requirements for the degree of  
Doctor of Philosophy

The School of Graduate and Postdoctoral Studies  
The University of Western Ontario  
London, Ontario, Canada

© Seyed Reza Mahmoudi, 2012

THE UNIVERSITY OF WESTERN ONTARIO  
School of Graduate and Postdoctoral Studies

**CERTIFICATE OF EXAMINATION**

Supervisors

Examiners

---

Dr. Kazimierz Adamiak  
Dr. G.S Peter Castle

---

Dr. James Cotton

---

Dr. Jun Yang

---

Dr. William D. Greason

---

Dr. Shaun Salisbury

The thesis by

**Seyed Reza Mahmoudi**

entitled:

**Electrohydrodynamic Enhancement of Heat Transfer and Mass  
Transport in Gaseous Media, Bulk Dielectric Liquids and  
Dielectric Thin Liquid Films**

is accepted in partial fulfillment of the  
requirements for the degree of  
Doctor of Philosophy

---

Date

---

Chair of the Thesis Examination Board

## Abstract

Controlling transport phenomena in liquid and gaseous media through electrostatic forces has brought new important scientific and industrial applications. Although numerous EHD applications have been explored and extensively studied so far, the fast-growing technologies, mainly in the semiconductor industry, introduce new challenges and demands. These challenges require enhancement of heat transfer and mass transport in small scales (sometimes in molecular scales) to remove highly concentrated heat fluxes from reduced size devices. Electric field induced flows, or electrohydrodynamics (EHD), have shown promise in both macro and micro-scale devices.

Several existing problems in EHD heat transfer enhancements were investigated in this thesis. Enhancement of natural convection heat transfer through corona discharge from an isothermal horizontal cylindrical tube at low Rayleigh numbers was studied experimentally and numerically. Due to the lack of knowledge about local heat transfer enhancements, Mach-Zehnder Interferometer (MZI) was used for thermal boundary layer visualization. For the first time, local Nusselt numbers were extracted from the interferograms at different applied voltages by mapping the hydrodynamic and thermal field results from numerical analysis into the thermal boundary layer visualizations and local heat transfer results.

A novel EHD conduction micropump with electrode separations less than 300  $\mu\text{m}$  was fabricated and investigated experimentally. By scaling down the pump, the operating voltage was reduced one order of magnitude with respect to macro-scale pumps. The pumping mechanism in small-scales was explored through a numerical analysis. The measured static pressure generations at different applied voltages were predicted numerically.

A new electrostatically-assisted technique for spreading of a dielectric liquid film over a metallic substrate was proposed. The mechanism of the spreading was explained through several systematic experiments and a simplified theoretical model. The theoretical model was based on an analogy between the Stefan's problem and current problem. The

spreading law was predicted by the theoretical approach and compared with the experimental results.

Since the charge transport mechanism across the film depends on the thickness of the film, by continuing the corona discharge exposure, the liquid film becomes thinner and thinner and both hydrodynamic and charge transport mechanisms show a cross-over and causes different regimes of spreading. Four different regimes of spreading were identified. For the first time, an electrostatically accelerated molecular film (precursor film) was reported.

The concept of spreading and interfacial pressure produced by a corona discharge was applied to control an impacting dielectric droplet on non-wetting substrate. For the first time, the retraction phase of the impact process was actively suppressed at moderate corona discharge voltages. At higher corona discharge strengths, not only was the retraction inhibited but also the spreading phase continued as if the surface was a wetting surface.

## Keywords

Electrohydrodynamics, Corona Discharge, Heat Transfer, Natural Convection, EHD Heat Transfer Enhancement, Mach-Zehender Interferometer, Nusselt Number, Critical Heat Transfer, Droplet Cooling, Jet Impingement, Hydraulic Jump, Conduction Pumping, Micropump, Liquid Sheet, Dielectric Liquid Thin Film, Dielectric Droplet, Spreading, Interfacial Electric Pressure, Leaky Dielectric Liquid, Retraction Inhibition.

## Co-Authorship Statement

This thesis has been written by Seyed Reza Mahmoudi under supervision of Dr. Kazimierz Adamiak and Dr. G.S. Peter Castle. Parts of the material presented in this thesis have been published in several peer-reviewed journals and refereed conference proceedings as listed below. The research in each publication has been conducted by the principal author and guided/supported by or in collaboration with the underlined authors, who are the research supervisors or members of the advisory committee.

Chapter 2 presents an interferometric study of natural convection heat transfer from an isothermal horizontal cylinder in the presence of corona discharge. Numerical analysis was conducted to verify the experimental measurements. The interferometric investigation and data reduction procedure were performed by the principal author. The co-authors help to improve the understanding of the heat transfer enhancements, constructing a numerical model to describe the heat transfer mechanisms. The material in Chapter 2 has been published in:

*S. R. Mahmoudi, K. Adamiak, G. S.P. Castle , M. Ashjaee "The Effect of Corona Discharge on Free Convection Heat Transfer from a Horizontal Cylinder" Experimental Thermal and Fluid Science, July 2010, Volume. 34, Issue.5 pp.528-537.*

In Chapter 3 the two-phase cooling characteristics of mono-dispersed droplets impacting on a upward facing disk were investigated. Boiling curves were obtained and the maximum heat transfer removal rate was obtained. Through extensive sets of experiments, two correlations at two different regimes of impact were obtained. The experimental work and data reduction were performed by the principal author. Co-authors helped to understand the observations and proposed several experiments to justify the postulations. The material in Chapter 3 has been published in

*S.R. Mahmoudi, K. Adamiak, G.S. P. Castle "Two-Phase Cooling Characteristics of Mono-Dispersed Droplets Impacted on a Heated Surface" ASME/JSME Thermal Engineering Joint Conference, March 2011, Honolulu, HI, USA*

and reviewed in

*S. R. Mahmoudi, K. Adamiak, G. S.P. Castle "Two-Phase Cooling Characteristics of Mono-Dispersed Droplets Impacted on an Upward-Facing Heated Disk" Experimental Thermal and Fluid Science (under second round of review)*

In Chapter 4 the two-phase cooling characteristics of a saturated free falling jet of HFE7100, dielectric coolant, were investigated. Boiling curves were obtained and the effect of jet length on boiling curves was studied. The effect of electric field on the boiling characteristics was examined for reduced jet lengths. The principal author performed the experiments and data reduction. The co-authors helped to understand the observations and measurements. The material in Chapter 4 is being under-review in:

*S. R. Mahmoudi, K. Adamiak, G. S.P. Castle "Two-phase Cooling Characteristics of a Saturated Free Falling Circular Jet of HFE7100 on a Heated Disk: Effect of Jet Length", International Journal of Heat and Mass Transfer.*

In Chapter 5 a new conduction pump with reduced electrode gap spacing was designed, fabricated and characterized. Different dielectric liquids were used to investigate the static pressure generation of the micropump at different applied voltage. Numerical analysis was performed to understand the pumping mechanism and charge transport across the liquid film layer. The microfabrication, characterization and numerical investigations were performed by the principal author. The co-authors helped in the further understanding of the conduction mechanism involving the pumping effect. The co-authors clarified several difficulties in explaining the observations. The material in Chapter 5 has been published in:

*S. R. Mahmoudi, K. Adamiak, G. S.P. Castle "Study of Electrohydrodynamic Micropumping Through Conduction Phenomenon" IEEE Transactions on Industry Applications, September 2011, Volume. 47, Issue.5, pp. 2224-2234.*

In Chapters 6 and 7 a new technique for spreading of a dielectric droplet over a high energy substrate was proposed. The corona discharge was used to expand the dielectric film over the grounded substrate. A mathematical model was developed to predict the

dynamics of spreading. The principal author observed the spreading phenomenon in 2006 before he joined UWO. At that time, he could not explain the spreading mechanism and due to the lack of understanding the observations could not find a place to publish. After about four years from the first observations, the co-authors proposed a hypothetical explanation for the spreading mechanism and helped in the fundamental understanding of the phenomenon. The principal author performed the experimental work and proposed a mathematical model based on their hypothetical explanations. Both theoretical and experimental work was reviewed by co-authors, who gave several influential comments and suggestions. The principal author reported several new observations. The material in Chapter 6 and part of Chapter 7 has been published in:

*S. R. Mahmoudi, K. Adamiak, G. S.P. Castle " Spreading of a Dielectric Droplet through an Interfacial Electric Pressure" Proceedings of the Royal Society, London Series A, November 2011, Volume. 467, pp. 3257- 3271.*

In Chapter 8 a new technique for controlling of an impacted dielectric droplet over a low energy interface was proposed. The interfacial electric pressure was exploited to suppress the retraction phase of the spreading process. An order of magnitude analysis was applied to demonstrate the importance of interfacial electrostatic forces. The principal author proposed the corona discharge-assisted technique to suppress the retraction phase of the impacting droplets. The co-authors helped to enhance the understanding of the mechanisms involved. They also improved the discussions given by the principal author. The material in Chapter 8 has been published in:

*S.R. Mahmoudi, G.S.P. Castle, K. Adamiak "Retraction Control of an Impacted Dielectric Droplet through Electrical Pressure" Soft Matter, January 2012, Volume. 8, Issue.3, pp. 808-813.*



## Acknowledgments

First of all, I would like to express my sincere respect and deepest gratitude to my principal research advisors, Prof. K. Adamiak and Prof. G.S.P Castle. During the past three years, they were the most influential persons to me. They generously helped me in all the ups and downs I encountered in my research and student life at UWO. They patiently followed every single step of all experimental and theoretical studies and helped me overcome numerous difficulties. I would also like to thank Prof. W.D Greason for all the helpful discussions. In fact, I learned so much from his extensive experience in the field of applied electrostatics. I would like to thank Prof. H.A Stone for discussions on several issues particularly droplet spreading dynamics. Especial thanks to Prof. J. H Leinhard IV and Prof. J. H. Leinhard V for helpful discussions on jet impingement cooling.

The financial support by the NSERC is acknowledged. I had a great opportunity to discuss and get feedback from many professors through annual reviews, local and international conferences.

Moving this project forward was not possible without assistance and guidance of staff members at the electronic shop, machine shop and Nanotechnology lab who helped me bringing new materials and developing several experimental setups and measurements.

I am thoroughly indebted and thankful to my former research supervisor, Prof. Mehdi Ashjaee who motivated me with the world-class research in the field of thermo-fluid sciences, laser diagnostic techniques in fluid flow and heat transfer. I would like to show my gratitude to Prof. Keyvan Sadeghi and Prof. Hossein Shokouhmand for all of their support in mentoring several projects.

I am heartily thankful to my mother and father for all their love and dedication, and my sister, for all the invaluable guidance and instructions, toward this end and through my life. Special thanks to my uncle, Bahman for all the influential mental and spiritual supports through my life. Finally, I would like to thank my wife, for bringing the

meaning of happiness to my life and for all the stolen moments from her during these years.

# Table of Contents

<b>CERTIFICATE OF EXAMINATION .....</b>	<b>ii</b>
Abstract .....	iii
Co-Authorship Statement .....	v
Acknowledgments .....	viii
Table of Contents .....	x
List of Tables .....	xv
List of Figures .....	xvi
List of Appendices .....	xxv
Chapter 1 .....	1
Introduction and general literature review .....	1
1.1 Introduction .....	1
1.2 Outline of the chapter .....	1
1.3 Corona discharge and its applications .....	2
1.4 Electrohydrodynamic pumping .....	3
1.4.1 Direct ion injection pumping .....	4
1.4.2 Conduction pumping .....	5
1.4.3 Induction pumping .....	6
1.5 Micro-scale EHD pumping .....	7
1.6 EHD heat transfer enhancement techniques .....	8
1.6.1 EHD single-phase enhanced heat transfer in gaseous medium .....	9
1.6.2 Single-phase EHD enhanced heat transfer in dielectric liquids .....	9
1.6.3 Two-phase flow EHD enhanced heat transfer .....	10
1.6.4 EHD boiling heat transfer enhancement .....	11
1.7 Wetting and spreading of liquid droplets on solid surfaces .....	12

1.8 Objective .....	14
1.9 Outline of the thesis .....	15
References .....	20
Chapter 2.....	34
The effect of corona discharge on free convection heat transfer from a horizontal cylinder.....	34
2.1 Introduction.....	34
2.2 Experimental setup.....	37
2.3 Experimental procedure and data reduction method.....	40
2.4 Uncertainty analysis .....	43
2.5 Numerical model.....	45
1.5.1 Boundary condition.....	46
2.6 Results and discussion .....	47
Nomenclature .....	57
References .....	59
Chapter 3.....	63
Two-phase cooling characteristics of mono-dispersed droplets impacted on an upward-facing heated disk .....	63
3.1 Introduction.....	63
3.2 Experimental setup and procedure.....	67
3.3 Experimental uncertainty and error analysis.....	74
3.4 Results and discussion .....	75
3.5 Conclusions.....	78
3.1 Nomenclature.....	88
References .....	90
Chapter 4.....	94

Two-phase cooling characteristics of a saturated free falling circular jet of HFE7100 on a heated disk in the presence and absence of electric field .....	94
4.1 Introduction.....	94
4.2 Experimental setup and procedure.....	101
4.3 Experimental uncertainty and error analysis.....	105
4.4 Results and discussion .....	107
4.4.1 In the absence of electric field .....	106
4.4.2 Effect of electric field on CHF for jet impingements .....	114
4.5 Conclusions .....	119
References .....	120
Chapter 5.....	122
5 Study of electrohydrodynamic micropumping through conduction phenomenon.....	123
5.1 Introduction.....	123
5.2 Electrode design for a conduction micropump .....	126
5.3 Experimental apparatus and procedure .....	131
5.4 Numerical Analysis .....	133
5.5 Results and discussion .....	136
5.6 Conclusions .....	146
References .....	147
Chapter 6.....	151
6 Spreading of a dielectric droplet through an interfacial electric pressure.....	151
6.2 Introduction.....	151
1.2 Experimental setup and procedure.....	152
6.3 Results and discussion .....	156
6.3.1 Effect of electric field strength.....	159
6.3.2 Effect of droplet size and electrical conductivity on the spreading process .....	160

6.3.3 Mathematical model.....	164
6.3.4 Analytical results versus experimental measurements.....	168
6.4 Conclusions .....	169
Appendix A .....	171
Appendix B .....	181
References .....	183
Chapter 7 .....	186
Different regimes of corona discharge spreading of dielectric liquid films .....	186
7.1 Introduction.....	186
7.2 Experimental setup.....	190
7.3 Experimental procedure .....	191
7.4 Results and discussion .....	194
7.4.1 Regime I and Regime II: Ohmic conduction across the liquid filml .....	193
7.4.2 Energy balance approach: Verification.....	195
7.4.3 Energy balance approach: Regime I .....	197
7.4.4 Regime III: Field-enhanced dissociation conduction regime.....	202
7.4.5 Regime IV: “Precursor film .....	213
7.5 Conclusions .....	218
Appendix C .....	219
References .....	226
Chapter 8.....	230
Retraction control of an impacted dielectric droplet through electric pressure .....	230
8.1 Introduction.....	230
8.2 Experimental setup.....	234
8.3 Results.....	235

8.4 Discussion.....	240
8.5 Conclusions.....	242
References .....	243
Chapter 9.....	245
9 Summary of the thesis.....	247
9.1 Summary .....	245
9.1.1 Effect of corona discharge on natural convection heat transfer .....	245
9.1.2 Mono-dispersed droplet cooling .....	246
9.1.3 Jet impingement boiling heat transfer .....	247
9.1.4 Conduction micropumping .....	248
9.1.5 Concept of spreading.....	249
9.1.6 Different regimes of spreading.....	249
9.1.7 Droplet retraction inhibition.....	250
9.2 Different regimes of spreading.....	251
9.2.1 Ionic discharge heat exchangers.....	251
9.2.2 Conduction pumping: a candidate for heat removal element.....	251
9.2.3 Thin film evaporator .....	252
9.2.4 Metal coating: monolayer deposition.....	252
Curriculum Vitae .....	253

## List of Tables

### Chapter 2

Table I: Deviation of each quantity for computing local Nusselt number ..... 44

Table II: Bias Errors of Mack-Zehnder interferometer ..... 44

Table III: Grid sensitivity analysis at  $\varphi_o = 17.0 \text{ kV}$  and  $Ra = 5000$  ..... 48

### Chapter 4

Table I: Thermophysical properties of HFE7100 at  $61^\circ\text{C}$  and  $0.1 \text{ MPa}$  ..... 103

Table II: Uncertainty of the measured parameters..... 103

### Chapter 5

Table I: Electrical and thermophysical properties of the working fluids used in this study  
at  $297.7\text{K}$ ..... 131

Table II: Uncertainty of each quantity which was measured in the present work..... 133

Table III: Electrical permittivity of materials ..... 133

Table IV: Summary of boundary conditions ..... 135

Table.I Electrical and thermophysical properties of the working fluids used in this study  
at  $296.7 \text{ K}$ ..... 233



## List of Figures

### Chapter 2

Figure 1-a: Schematic of experimental setup.....	38
Figure 1-b: Details of the cylinder and the blade electrode.....	38
Figure 1-c: Plane view of Mach–Zehnder interferometer.....	40
Figure 2: Examples of interferograms in the absence and presence of corona.....	41
Figure 3: Experimental and numerical local Nusselt number for the free convection heat transfer from the horizontal cylinder compared with other works [15,16,17,18] at $Ra=1000$ .....	49
Figure 4 (a): Numerical results for ion concentration (charge concentration difference between two adjacent lines is $5 \times 10^{-7} \text{ C/m}^3$ ). and (b) electric potential in the blade-cylinder geometry at $V_c = 17.0 \text{ kV}$ , $I = 10 \mu\text{A}$ .....	50
Figure 5: Experimental and numerical local Nusselt number for the horizontal cylinder for various corona voltages at $Ra=1500$ .....	51
Figure 6: Numerical results for isotherms and streamlines for $Ra=1500$ at $V_c = 12.0 \text{ kV}$ and $17.0 \text{ kV}$ .....	53
Figure 7: Experimental and numerical local Nusselt number for the horizontal cylinder for various corona voltages at $Ra=5000$ .....	54
Figure 8: Experimental results for the average Nusselt number enhancement of heat transfer at various applied voltages.....	54
Figure 9: V-I characteristic diagram for blade-cylinder geometry with 40 mm spacing at different $Ra$ numbers.....	55

### Chapter 3

Figure 1-a: Schematics of experimental setup.....	68
Figure 1-b: Details of heater bar and thermocouple locations (dimensions in mm).....	69
Figure 2: Droplet size variation using different hypodermic needle gauges at different volumetric flow rates.....	71
Figure 3: Comparison between the measured impact velocity of the generated droplet and the predicted impact velocity using eq.(2).....	72
Figure 4: Variation of droplet cooling CHF with mass flux of capillary 17g compared with previous studies.....	76
Figure 5: Boiling curves of 17g capillary at various volumetric flow rates.....	77
Figure 6: Boiling curves for 22g capillary at different volumetric flow rates.....	78
Figure 7: Boiling curves for 22g and 17g capillaries at different volumetric flow rates...	78
Figure 8: Boiling curves of droplet cooling of 22g capillary at various impact velocities.....	80
Figure 9: Variation of average CHF for various capillaries at different volumetric flow rates.....	82
Figure 10: Variation of average CHF at different volumetric flow rates.....	83
Figure 11: Comparison between the experimental and the predicted CHF evaluated by Sawyer et al.'s correlation [3].....	84
Figure 12: Comparison between the all experimental and the predicted CHF evaluated by eq.(4) and eq.(5).....	85
Figure 13: Comparison between the experimental CHF and the predicted values using eq.(4) for low Weber numbers ( $We < 10$ ).....	86

Figure 14: Comparison between the experimental and predicted CHF data obtained by the dimensionless groups presented in eq.(5) for $We < 10$ .....	87
--	----

## Chapter 4

Figure 1 (a): Radial spreading of an impingement jet striking on an upward facing disk at (low) volumetric flow rates 20 cc/min and (b)(high) flow rates 60 cc/min. (c) Figurative description of the effect of the jet length at different flow rates.....	99
---	----

Figure 2: Falling jets of HFE7100 at different jet lengths. Hydraulic jump position varies by varying the jet length. Jet lengths are: (a) 5 mm, (b) 10 mm (c) 20 mm at 20 cc/min volumetric flow rate using 15g needle as nozzle.....	99
--	----

Figure 3: Schematic view of experimental setup.....	102
---	-----

Figure 4: Photographs of saturated jet of HFE7100 issued from 15g needle striking a heated disk at different surface temperatures. The volumetric flow rate is 20 cc/min and the jet length is 5 mm. The heat transfer area is 8 mm.....	107
--	-----

Figure 5: Photographs of saturated jet of HFE7100 issued from 15g needle striking a heated disk at different surface temperatures. The volumetric flow rate is 20 cc/min and the separation between the jet and heated disk is 50 mm.....	107
---	-----

Figure 6: HFE7100 Boiling curves obtained by 15g needle for different jet lengths at 20 cc/min.....	109
---	-----

Figure 7: HFE7100 Boiling curves of falling jets issued by 15g needles for different jet lengths at 30 cc/min.....	109
--	-----

Figure 8: HFE7100 Boiling curves of jets issued by 15g needle for different jet lengths at 60 cc/min.....	110
---	-----

Figure 9: HFE7100 Boiling curves of jets issued by 20g needle for different jet lengths at 20 cc/min.....	111
Figure 10: Effect of jet lengths on measured CHF at different volumetric flow rates using 15g needle.....	112
Figure 11: Comparison between all measured CHFs in the present work and the adjusted correlation eq. (6).....	114
Figure 12: Experimental visualization of boiling heat transfer enhancement of HFE-7100 in the presence of strong electric field. The needle was 15g hypodermic needle. The volumetric flow rate was 6 cc/min. Applied voltage is 9 kV DC and separation between electrode was measured to be 4 mm.....	116
Figure 13: Boiling curves of HFE-7100 at different applied voltages. Jets were issued using 15g hypodermic needle. The separation between the target and jet was 4 mm and volumetric flow rate kept constant at 6 cc/min.....	117
Figure 14: Variation of CHF with applied voltage at different volumetric flow rates. Jets were issued using 15g hypodermic needle. The separation between the target and jet was 4 mm.....	117
Chapter 5	
Figure 1: Qualitative description of electrode design.....	127
Figure 2: Top view of (a) high voltage annulus electrodes and (b) grounded electrode patterned on two separate substrates. (Not scaled).....	128
Figure 3: Details of packaged conduction micropump.....	130
Figure 4: Demonstration of the column rise for a conduction micropump in a bath of 10-GBN Nynas transformer oil at V=0 (a) and V=1500 VDC applied voltages (b).....	137

Figure 5: V-I characteristics for conduction micropump measured for two different working fluids.....	137
Figure 6: Distribution of equipotential lines of micro-scale conduction pumping calculated for 10-GBN Nynas at 1500 VDC applied voltage. Potential difference between two adjacent lines is 50V.....	138
Figure 7: Calculated positive and negative charge densities in micro-scale conduction pump with 10GBN-Nynas oil transformer.....	139
Figure 8: Axial electric field in micro-scale conduction pump calculated for different working fluids.....	139
Figure 9: Comparison of calculated and experimental static pressures for conduction micropump using 10GBN-Nynas oil transformer.....	140
Figure 10: Comparison of calculated and experimental static pressures for conduction micropump using Shell Diala AX oil transformer.....	141
Figure 11: Distribution of positive and negative charge densities in micro-scale conduction pump calculated for N-Hexane.....	143
Figure 12: Space charge density and electric field in macro- and micro-gaps and (b)- impact of space averaged conduction parameter on formation of hetero-charge layers in parallel plate geometry filled with a low conductive dielectric liquid, (c) Extension of hetero-charge to the length of gap spacing for micro-scale gap spacing in parallel plate geometry filled with low conductive electrodes at comparatively lower applied voltages, (d) hetero-charge extension for micro-scale gap spacing in parallel plate geometry filled with low conductive electrodes at comparatively higher applied voltages.....	145

## Chapter 6

Figure 1: Schematic view of the experimental setup and a sample of Fizeau fringes observed after 6min (a) and 60min (b) corona discharge exposure.....153

Figure 2: Typical photographic sequence of a silicone oil spreading process on a mirror finished stainless steel grounded substrate in the presence of corona discharge (a). Typical evolution diagram obtained from the above photographic sequential frames (b). The corona discharge emitter electrode was 15g hypodermic needle separated 40 mm from the grounded substrate. The initial diameter of the oil droplet was 3.78 mm. (c) Figurative explanation of the dielectric liquid spreading phenomenon in the presence of corona discharge.....155

Figure 3: V-I characteristics of needle-plate geometry using 15g and 22g hypodermic emitter electrode with  $S=25$  mm gap spacing.....158

Figure 4: Dynamic evolution of medium ( $D_o=2.6$  mm) and large ( $D_o=3.8$  mm) silicone oil droplets in the presence of corona discharge at  $V=15$  kV. The electrode separation in both cases was  $S=62$  mm. The corona currents for 15g and 22g are  $7.5 \mu A$  and  $13 \mu A$ , respectively.....159

Figure 5: Dynamic evolution of large silicone oil droplet ( $D_o=3.8$  mm) in the presence of corona discharge for various gap spacings. The emitter electrode was 22g needle and its voltage was kept constant at 15 kV.....160

Figure 6: Dynamic spreading ratio of silicone oil droplets with different initial sizes in the presence of corona discharge ( $V=15$  kV,  $I=13 \mu A$ ,  $S=62$  mm).....161

Figure 7: Dynamic spreading ratio of silicone oil droplets with different initial sizes in the presence of corona discharge ( $V=15$  kV,  $I=23 \mu A$ ,  $S=40$  mm).....162

Figure 8: Dynamic spreading ratio of silicone oil droplet and drop of silicone oil with surfactant in the presence of corona discharge ( $V=15$  kV,  $I=23 \mu A$ ,  $S=40$  mm). Open circle-symbols represent the dynamic evolution of silicone oil solution with 0.01 mol

surfactant (electrical conductivity  $\sigma \sim 1 \times 10^{-6}$  S/m) and squares are for silicone oil ( $\sigma \sim 5.5 \times 10^{-9}$  S/m).....163

Figure 9: The similarity of the investigated problem to the squeeze flow between two parallel disks (Stefan's classical problem).....165

Figure 10: Evolution of the diameter of a silicone oil droplet exposed to corona discharge. The circles represent the measured expansion of film diameter. The dashed line represents the theoretical predictions of droplet evolution given by Eq. (7). The electrical conductivity of the oil was measured to be  $\sigma \sim 5.5 \times 10^{-9}$  S/m. The kinematic viscosity of the silicone oil was 50 cSt. The calculated field enhancement parameter was calculated to be  $\alpha = 2.25$ . The experimental error bars are smaller than the symbol size.....169

## Chapter 7

Figure 1: Silicone oil film spreading over a conductive substrate through corona discharge exposure. Different regimes of spreading are depicted using different size of droplets. (a) Regime I (transient corona charging): 2ms after corona discharge exposure (b) Regime II (quasi-steady state corona charging): after 300 sec corona discharge exposure. (c) Regime III (hetero-charge interaction): after 1000 sec exposure. (d) Regime IV (corona accelerated precursor film): (d-1) silicone oil film after 2400 sec, (d-2) after 7200 sec (d-3) after  $1.7 \times 10^5$  seconds of corona discharge exposure. The electrode was a modified needle and the separation between the corona needle and substrate for all cases was 25 mm. The corona voltage and total current was measured to be 17 kV and 40  $\mu$ A, respectively.....185

Figure 2: (a-d) Figurative description of charge carrier transport and (e) qualitative demonstration of dielectric film spreading ratio variation,  $\beta(t)$ , versus corona discharge exposure time. Four different regimes of spreading are identified.....186

Figure 3: Schematic view of the experimental setup.....189

Figure 4: Schematics of additional experimental setup for measurement of the surface potential of the oil interface subjected to corona discharge. (a) The schematics of the experimental setup. (b) The laser irradiation is completely reflected from the liquid surface while the liquid film thickness is larger than the height of the probe. (c) The reflected laser irradiation from the surface reduces due to the beam scattering when the thickness of the liquid becomes smaller than the height of the probe.....191

Figure 5: Spreading dynamics of two different silicone oil droplets subjected to the corona discharge. The initial size of the droplet is  $D_o=1.44$  mm (green) and  $D_o=2.64$  mm (red). The applied voltage is 17 kV and total corona current 40  $\mu$ A. The gap spacing was kept constant at  $S=25$  mm.....192

Figure 6: Spreading dynamics of a silicone oil film subjected to corona discharge. The film was produced by expansion of a silicone oil droplet with initial size of  $D_o=1.89$  mm. Second and third regimes of expansion are mapped to the ohmic conduction and enhanced dissociation conduction mechanism, respectively. The applied voltage was 17 kV and the total corona current was 40  $\mu$ A. The gap spacing was kept constant at  $S=25$  mm.....201

Figure 7: Spreading dynamics of a silicone oil film produced by expansion of a small droplet with initial diameter of  $D_o=1.44$  mm. The applied voltage was 17 kV and the total corona current was 40  $\mu$ A. The gap spacing was kept constant at  $S=25$  mm.....202

Figure 8: Spreading dynamics of a silicone oil film produced by expansion of a very small droplet with initial diameter of  $D_o=0.99$  mm. The applied voltage was 17 kV and the total corona current was 40  $\mu$ A. The gap spacing was kept constant at  $S=25$  mm...202

Figure 9: Demonstration of hetero-charge layers formation around the solid/liquid and liquid/air interfaces.....205

Figure 10:  $\log J$ -  $\sqrt{V}$  characteristics obtained for a 2 $\mu$ m-thick silicone oil film.....205



Figure 11: Radial distribution of the relative current density for the hypodermic needle used in this study. The applied voltage was 17 kV and the total corona current was 40  $\mu$ A. The gap spacing was kept constant at  $S=25$  mm.....210

Figure 12: Ellipsometric measurement of silicone oil film thickness after  $1.7 \times 10^5$  seconds of corona discharge exposure. The measurement performed at two different peripheral angles. The applied voltage was 17 kV and the total corona current was 40  $\mu$ A. The gap spacing was kept constant at  $S=25$  mm.....212

Figure 13: Fit line of the experimental data (circles) for the dynamics of the accelerated precursor film. The curve is in the form of  $r(t) - r_o = \delta t^n$ . When  $n$  fixed at 0.5, the fitness parameter and the standard errors are as following:  $\delta = 7.74 \times 10^{-5} m/s^{1/2} \pm 2.06 \times 10^{-6} m/s^{1/2}$  which corresponds to diffusion coefficients of  $D_e = 3.01 \times 10^{-9} m^2/s \pm 1.7 \times 10^{-12} m^2/s$ . The equation is valid for times after 40 min of corona discharge exposure where the accelerated precursor film length was measured to be  $r_0 = -2.556 \times 10^{-3} m \pm 4.32 \times 10^{-5} m$  ...216

## Chapter 8

Figure 1: Stages of droplet evolution in the absence of corona discharge (a) and in the presence of corona discharge (b).....229

Figure 2: Schematics of experimental setup.....230

Figure 3: Comparison of droplet spreading using different fluids at different applied voltages and corona currents. The electrode spacing was 38 mm.....234

Figure 4: Dynamic spreading ratio of an impacted silicone oil droplet in the presence of corona discharge.....235

Fig. 5 Dynamic spreading ratio for ISOPAR-L at different applied voltages. Droplet spreading ratio  $\beta = \frac{D}{D_0}$  versus time in the presence of corona discharge.....235

Fig. 6 Dynamic spreading ratio of ISOPAR-L droplet with  $3.3 \times 10^{-3}$  M AOT additive in the presence and absence of corona discharge. ....236

Figure 7: Retraction speed versus applied voltage.....238

# Chapter 1

## Introduction and general literature review

### 1.1 Introduction

Electrohydrodynamics (EHD) deals with motions in liquid or gaseous media induced by electric fields [1]. Applications of electrohydrodynamics (EHD) are diverse and sometimes striking [2]. One of the most remarkable appearances of the EHD in nature involves the blue haze found above heavily forested areas [3]. B.R Fish, a scientist from Oak Ridge National Laboratory, provided experimental evidence to support his hypothesis that the haze derives from waxy substances sprayed into the atmosphere from the tips of pine needles by high fields accompanying the overhead passage of electrified clouds during thunderstorms. Although Fish proposed the mechanism of haze generation through extensive sets of experiments, several other reasons including the thermal evaporation of the wax is also realized as the haze formation mechanism. As another remarkable example, EHD forces have been used to simulate the earth's gravitational field during convection experiments carried out during a space shuttle flight [4]. In this application, combining a radial electric field with a temperature gradient between concentric spheres produces polarization forces that mimic gravity.

The earliest record of an EHD experiment is in William Gilbert's seventeenth century treatise *De Magnete*, which describes the formation of a conical shape upon bringing a charged rod above a sessile drop [5]. Until the 1960s most studies focused on the behavior of good conductors, (mercury or water) or perfect dielectrics (purified benzene). No significant theoretical work was done during more than three hundred years towards understanding the poorly conductive materials. This began to change following studies on poorly conducting liquids—leaky dielectrics—by Allan & Mason in 1962 [6].

### 1.2 Outline of the chapter

Diverse applications of EHD have introduced different fields of studies in physics and engineering. Corona discharge and its applications, and EHD pumping of dielectric liquids are the main subjects of the EHD studies [2]. In the following sections, corona

discharge and its application will be reviewed briefly. Then, the importance of EHD pumping is described in both macro-scale and micro-scale applications. Different pumping mechanisms are explained and compared. As a particular application, heat transfer enhancement through EHD effects is reviewed. Since the controlling of liquid droplets and liquid films on a solid surface is important in numerous applications, we review the liquid droplet/film spreading over solid surfaces. The new trend of research in controlling the liquid film through electrostatic forces is highlighted.

### 1.3 Corona discharge and its applications

An important part of electrohydrodynamics is concerned with corona discharge in gaseous media [2]. The corona discharge has found broad scientific and industrial applications. In order to establish a corona discharge, at least two separate electrodes, a high voltage sharp emitter and a grounded collector, are needed. By applying a high voltage above the corona discharge threshold to a sharp needle, the electric field ionizes some of the neutral gas molecules in the high field region adjacent to the electrode [7]. The generated ions are accelerated towards the grounded collector. Typically, large and concentrated electric fields are required to generate such ionic discharges [8]. The high momentum accelerated ions drag neutral molecules and a jet-like motion of ambient gas can be developed [9]. The motion is the so-called corona wind or ionic wind [7-9].

As an important application, corona discharge has been used in mass spectrometers to determine the elemental composition and chemical components of a sample by measuring the mass-to-charge ratio [10]. Corona discharge has been also extensively used to produce ozone [11,12]. The ozone production technique through corona discharge found important applications in water treatment industry [13]. As an important application in air pollution control industry, electrostatic precipitators use corona discharge to remove fine particulate matter, such as dust and smoke from the air stream [14,15]. The corona discharge has also found application in electrostatic painting [14], separation [16] and electrospinning of polymers [17].

The corona wind momentum produced by corona discharge has found several applications in heat [18-22] and mass transport enhancement applications [23-29]. The corona wind has demonstrated promising applications in enhancement of convective heat transfer in internal [30-36] and external flows [37-42], evaporation/drying [23-29], and flame control [43-46] in both normal and microgravity conditions.

## 1.4 Electrohydrodynamic pumping

Electrohydrodynamic pumping deals with the interaction between electric fields and fluids [47,48]. This interaction, for instance, may result in electrically induced pumping, fluid mixing [49], or enhancement of heat transfer [50-53]. The application of EHD to heat and mass transport demonstrates promising perspectives in several industrial applications [53-55], where special requirements restricts the device operation condition, but augmented heat transfer and mass transport are of interest. For instance, in microgravity conditions where the gravitational field is absent, a low energy consumption heat transfer enhancement technique with minimum physical maintenance of the cooling circuit elements is required. Circulating pumps typically used in the normal condition consume tens of watts while creating noise and mechanical vibration, which may lower the life of the devices. By eliminating the moving parts, EHD devices offers static operation with significantly lower energy consumption. It is worthy to note that a vibration free cooling system is crucial in several precise optical device applications with high power dissipations, for example, high power laser diodes, optical mirrors, and other optical components where the positioning is important.

The electric body force  $\vec{f}$  in a dielectric liquid, that results from an imposed electric field,  $\vec{E}$ , can be expressed as [56]:

$$\vec{f} = \rho_c \vec{E} - \frac{1}{2} \vec{E}^2 \nabla \epsilon + \frac{1}{2} \nabla \left[ \vec{E}^2 \rho \left( \frac{\partial \epsilon}{\partial \rho} \right)_T \right] \quad (1)$$

where  $\rho_c$  is net volume charge density,  $\epsilon$  is the fluid permittivity,  $\rho$  is the fluid density and  $T$  is the fluid temperature.

The first term on the right hand side of the Eq.(1) is the electrophoretic, or Coulombic, force that results from the net free space charges in the fluid. The second term, known as the dielectrophoretic force, arises from the permittivity gradient. The last term, called the electrostrictive force, is important only for compressible fluids and two phase flows. Free space charges in dielectric liquids can be generated by three different mechanisms. I) Induction [57-59]: occurs in dielectric liquid with variable electrical conductivity, which can be caused due to the presence of a thermal gradient, or in two or multi phase flows, II) Conduction [60-63]: through imbalanced dissociation-recombination reactions in the areas adjacent to the electrodes, III) Injection [64-67]: by direct charge injection from the solid/liquid interface. These three distinctive mechanisms for free space charge generation can be exploited to create induction, conduction and injection EHD pumping [56,60].

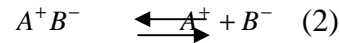
### 1.4.1 Direct ion-injection pumping

One method of generating net free charges in a fluid medium is direct charge injection from electrode/liquid interface [56]. An electric field is imposed between a sharp electrode, called an emitter, and another blunt electrode, called the collector. The free charges are accelerated along the electric field direction dragging the adjacent fluid and induce shear motion. The EHD pumps based on direct ion injection charging are known as ion-drag pumps or direct-ion injection pumps. The ion injection pumping in dielectric liquid by the ion injection mechanism has been known for long time [56]. Early works by Stuetzer [64] and Pickard [65,66] revealed the ion-injection pumping through both a theoretical and experimental approach. In all the initial experimental works, transformer oils were used as the working fluid. Maximum velocities around 10 cm/s were obtained using mesh-type electrodes. More recently, Bryan and Seyed-Yagoobi [68] demonstrated an ion-drag pump with significantly higher pumping velocities around 33 cm/s. Sharbaugh and Walker [67] used their designed pump in a 167 kVA distribution transformer to enhance convective cooling of the transformer. However, before 500 h of operation, its operation declined in pumping efficiency due to the fact that the collector electrode behaved as a filter. The filtering behavior resulted in the accumulation of the contaminations around the collector electrode. The ion-injection pump showed significant

pressure drops in the cooling circuit caused by this contamination accumulation. As a main disadvantage, recent studies revealed that these pumps may cause degeneration of the thermophysical and electrical properties of the working fluid, thus, they are not reliable for long term operation [69]. For instance, the typical electrode life time in an ion injection small scale pumps was reported to be less than an hour [70]. The electrochemical effects cause irreversible electrode damages which affect the desired sharp profile of the emitter electrode and therefore the static head generation produced by the device.

### 1.4.2 Conduction pumping

Unlike the ion-injection pumping, the concept of conduction pumping in dielectric liquids has been proposed very recently [71]. This is probably due to the fact that the conduction mechanism of creating space charge is a rather complicated phenomenon. When a relatively small electric field (below  $0.1 \text{ V}/\mu\text{m}$ ) is established between a low potential and a high potential electrode immersed in a dielectric liquid, the ion injection is negligible, but the liquid impurities adjacent to the electrodes may begin to dissociate. The process of dissociation of the neutral species and recombination of the created ion pairs can be schematically written as follows [63]:



By increasing the applied voltage, but before reaching some threshold value of electric field (approximately  $0.1 \text{ V}/\mu\text{m}$ ), the existing ions due to the dissociation of neutral species experience strong enough electrical Coulomb force, which concentrates the positive and negative ions around counter-polarized electrodes. The concentrated ions around each electrode form charge layers around them. The ion density distributions in the dielectric liquid bulk can be determined on the basis of the conservation law of neutral species. The attraction between the electrodes and the charges results in a net fluid flow from the blunt electrode towards the electrode having smaller radii of curvature. The conduction mechanism in this regime is mainly due to the ionic dissociation and is referred to as EHD conduction pumping and the charge layer around

the electrodes is known as hetero-charge layers. Further increasing of the electric field (in the order of  $10\text{V}/\mu\text{m}$ , depending on the liquid characteristics and impurity concentration), results in ion injection from the liquid/metal interface and produces a reverse pressure. Beyond this threshold, the ion-injection pumping mechanism will be dominant [63] and the pumping direction is reversed.

Several theoretical [6,17], numerical [12,15,18,19] and experimental works [5,13,21,16] were carried out to determine the feasibility of EHD pumping through the conduction phenomenon. In all of the previous studies, commercial refrigerants R-123, R-134a and N-Hexane were introduced as working fluids to a single or multi-stage pump with the electrode spacing in the order of millimeters and the steady-state static pressure generation of the pump was determined. Furthermore, several geometries for high voltage electrodes were investigated to increase pressure generation [21]. Typical static pressure generation for macro-scale conduction pumps is in the order of 10-1000 Pa at 15 kV applied voltage with few millimeters gap spacing between electrodes.

### 1.4.3 Induction pumping

Induction pumping can be achieved by inducing space charge in a liquid due to a gradient or discontinuity of the electric conductivity [56]. An AC traveling electric wave attracts or repels these induced charges, leading to fluid motion. The concept of EHD induction pumping was introduced by Melcher in 1966 [57]. Extensive theoretical and experimental studies were performed by Melcher and Firebaugh [58], Wong and Melcher [59], Kervin et al. [72], and Seyed-Yagoobi et al. [73,74]. More recently, Wawzyniak and Seyed-Yagoobi [75,76] conducted a theoretical and experimental study on EHD induction pumping of a stratified liquid/vapor medium in a rectangular channel configuration. They extended Melcher's work by taking into account the induction of charges in the bulk of the liquid (due to Joule heating) along with those induced at the interface. This augmentation is largest for the highest heat flux and applied voltage.

Brand and Seyed-Yagoobi [77] demonstrated EHD induction pumping of liquid films and showed its potential for heat transfer augmentation purposes in heat exchangers through



flow control. Utilizing the EHD induction mechanism to pump liquid films makes this technology attractive for several industrial applications.

## 1.5 Micro-scale EHD pumping

In recent micro-scale applications, the importance of EHD-based devices has been highlighted [78]. It might be attributed to the fact that the EHD forces can be significant in a small-scale process, even though in large-scales they might have smaller contribution [79].

A strong motivation for decreasing the size of EHD ion-drag pumps has been known since their inception: a decrease in the electrode gap produces better performance and requires lower operating voltage. However, producing electrode geometries and spacing in the sub-millimeter range was not possible until the development of micro-fabrication technologies in the mid-eighties.

Credit for the first micro-scale EHD pump is owed to Richter and Sandmaier [80] who fabricated electrode grids on a silicon substrate. A maximum static pressure of 1200 Pa with ethanol as the working fluid was achieved with an input voltage of 300 V. Such a small input voltage was due to the reduced electrode spacing. Static pressure was comparable to the pressure obtained with the large -scale pumps. They proposed using this pump as a flow meter by recording the time of flight method for injected charges. Sandia National Laboratory researchers used laser micromachining to develop a micro-EHD pump [81]. They produced two designs. The first one had two silicon substrates with gold layers stacked on top of each other and fluid channels were drilled with a laser. The second design had silicon grids manufactured and attached back-to-back, which reduced the electrode distances to about 100  $\mu\text{m}$ . A static pressure head of 290 Pa was obtained with an input voltage of 120 V. To date it was the lowest input voltage used for an EHD pump and is the power required is within an order of magnitude of that provided by a typical battery. Several different ion drag EHD micropumps were reported [82-86].

## 1.6 EHD heat transfer enhancement techniques

The EHD enhancement of heat transfer refers to the coupling of an electric field with the fluid field in a dielectric fluid medium. In this technique, either a DC or an AC high-voltage low-current electric field is applied in the dielectric medium between a charged and a receiving (grounded) electrode. The heat transfer medium can be gaseous, single-phase or two-phase flows. The EHD heat transfer enhancement method is particularly important in microgravity applications, where the gravitational field is absent and minimization of energy consumption in active cooling elements is of great concern. Typically, significant heat transfer improvements with small energy consumption can be obtained in the presence of electric field. Moreover, minor maintenance for EHD devices is required since the mechanical moving parts and the associated vibrations are eliminated. Therefore, EHD enhancement techniques can be an excellent candidate for special application including the devices operating in space.

### 1.6.1 Single-phase EHD enhanced heat transfer in gaseous medium

Convective heat transfer can be enhanced in the presence of strong electric fields [19-22]. As mentioned earlier, most of the previous works in air used corona discharge to develop corona wind over a heat transfer target. The EHD enhancement technique can be applied for both external [37-42] and internal [30-36] fluid flows. In both applications, the corona discharge can be generated by establishing a strong field between a corona discharge emitter electrode and an electrically grounded heated object. The momentum of the corona wind resulting from a corona discharge may disturb the thermal and hydrodynamic boundary layer. Moreover, the corona wind resulting from a highly non-uniform electric field is accompanied with strong vorticities [87-89] and local increase in coolant velocity. These electrostatic interactions in a flow field may promote significant local or average heat transfer enhancements.

The corona discharge was extensively used in natural convection heat transfer enhancement from an external object such as cylindrical single tube [42], bunch of

tubes [41, 89, 92-96], vertical [90] and horizontal heated plates [40, 91]. Different types of electrodes, such as wires, blades and razors, have been used to generate corona discharge. Typical EHD heat transfer enhancements compared with natural convection have been more than 100% for all of those studies with energy consumption in the order of less than a watt. Most of the previous studies have been limited to measuring the average enhanced heat transfer coefficients. Several authors used interferometers to visualize the thermal boundary layer affected by corona discharge [42,90]. Even more significant corona wind enhancements have been reported locally just around the corona sharp electrode [30,42,90]. The natural convection heat transfer enhancement showed promise for microgravity conditions.

### 1.6.2 Single-phase EHD enhanced heat transfer in dielectric liquids

As described earlier, EHD pumps can be used as an active element to control the heat removal from a heated surface. Since the pumps are operated with dielectric liquids, the direct cooling method can be applied, which is particularly important in hot spot management in electronic cooling [84, 85]. Direct cooling reduces the heat resistance across the heat sink by eliminating the need for soldering or bonding of the heat sink to the hot spot. Therefore, EHD pumps with dielectric liquids can be exploited for high performance direct cooling.

In single-phase flows, the Coulombic force is responsible for inducing liquid motion in the fluid and enhancement of the local or average heat transfer from a surface. The electrostatic forces may increase the momentum of the liquid around the heated target. The hydrodynamic and thermal boundary layer thinning leads to typically high heat transfer coefficients. Several electronic cooling applications have benefited from EHD pumping [83-85] to enhance heat removal capacity.

### 1.6.3 Two-phase flow EHD enhanced heat transfer

The phase change phenomenon occurring during the boiling and condensation processes is an important mode of heat transfer. Boiling and condensation heat transfer enhancement can be particularly important to design more efficient evaporators and condensers. Several passive and active techniques have been used to improve the heat removal capacity in the presence of phase change heat transfer. The study of EHD effects as an active technique on phase change heat transfer enhancements began about 40 years ago [97]. Although several theoretical and experimental works have been conducted to explore the enhancement mechanisms involving the phase change heat transfer, a complete theory does not exist to describe the enhancement mechanisms in the presence of an electric field. This is attributed to the fact that the enhancement mechanisms are complicated and the understanding depends on the detailed macroscopic and microscopic knowledge of heated surface wettability, roughness, microscopic surface forces, and so on. Phase change phenomena during heat transfer can be directly or indirectly affected by the electrostatic forces [98]. Some of the above parameters such as wettability and microscopic balance in surface forces can be affected by electrostatic forces. EHD effects may improve the heat transfer through enhancement of wettability over the heat transfer surface [97-99].

Boiling heat transfer enhancement has been a subject of more intensive studies compared with the condensation heat transfer. This is because of the fact that the condensation enhancement through electrostatic effects includes many unknown interrelated microscopic parameters, which might be essential but may complicate the processes. The more extensive interest in boiling heat transfer enhancement through EHD might be attributed to the fact that the boiling heat transfer enhancement experiments are more repeatable since they rely on better-defined physical parameters. In both cases, the microscopic surface forces may cause macroscopic effects, which drastically change the thin liquid film wetting dynamics and control the heat transfer from the surface. In the following section, a review on boiling heat transfer enhancement through EHD effect is given.

### 1.6.4 EHD boiling heat transfer enhancement

Although EHD boiling heat transfer has been subject of many studies [100-108], only a few limited works have focused on exploring the EHD enhancement of this process [100]. Most of the previous studies have concentrated on heat transfer enhancement at nucleation boiling [102-106] and critical heat flux regimes (CHF) [101]. Only limited literature exists on the effect of electric field at the beginning of the phase change and last regimes of boiling (post-CHF) [109-111]. The mechanisms by which EHD techniques enhance the boiling process are summarized as follow:

- 1) movement of vapor bubbles on the heated surface due to Maxwell stress,
- 2) spreading of the vapour bubble base over the heat transfer surface due to electrostatic forces,
- 3) increasing the number of bubbles by breaking up large bubbles by decreasing the bubble detachment diameter and creating more turbulence,
- 4) elimination of boiling hysteresis, by decreasing the degree of the superheat required to start nucleate boiling,
- 5) improving the transitional and minimum film boiling conditions by destabilizing the blanketing vapor film,
- 6) improving the wetting of the heating surface due to the interfacial normal and shear stresses arising from surface charge accumulation in the presence of a strong electric field,
- 7) introducing the EHD waves and perturbations at the surface of a boiling liquid, causing an increase in re-wetting of the heated surface due to the EHD interfacial instability of the vapor/liquid interface.

In most of previous studies, improvement of the wettability of the heated surface through EHD effect was the main enhancement mechanism [100, 112]. The two-phase heat transfer results as well as many other practical applications may stimulate research on the EHD-enhanced wetting and spreading of liquid films. This investigation can be beneficial

in understanding of the electro-spreading/wetting mechanisms that promotes two-phase heat transfer enhancements through EHD effects.

## 1.7 Wetting and spreading of liquid droplets on solid surfaces

The spreading of liquids on solids is of significant importance in everyday life, for instance, while painting, writing with ink on a sheet of paper and spreading of the oil film over the pan. Wetting and spreading also play basic role in many industrial applications [113-120], wetting of porous rocks in oil/water reservoirs [121], in agriculture [117,119], phase-change heat transfer [115, 116] as well as numerous other fields such as coating, deposition, soldering, and lubrication.

In all the above applications, detailed knowledge of the spreading dynamics is needed. In general, spreading is a complicated problem since many known or unknown parameters are involved. This is a common problem in the field of surface science. Even a small amount of impurity in the liquid phase or solid surface may significantly affect the macroscopic observed phenomena. The topography of the solid surface and even its crystallographic structure may affect the spreading dynamics [122].

Spreading of fluids belongs to the broad field of wetting phenomena. There is a macroscopic difference between the case where liquid completely spreads over substrate (oil over stainless steel) and partial wetting (water over stainless steel) [122]. Complete wetting corresponds to the situation, where the macroscopic contact angle tends to zero when the time goes to infinity [123]. Partial wetting corresponds to an equilibrium condition with a non-zero finite contact angle [124].

The key to the analysis of spreading can be found in the experimental studies presented by Hardy [125], who recognized that an ultra thin film always precedes a spreading droplet. The thickness of the film is normally below micron range. This ultra thin film has been called the precursor film. At the early stages of precursor film spreading, the molecular thickness (below 1 nm) develops progressively during the spreading process of a droplet as a tongue-like structure ahead of the nominal contact line of the main spreading film. From the experimental observations through detailed optical techniques at

the Naval Research Laboratory, Bascom realized that the long-range forces should be considered to explain the behavior and dynamics of the ultra thin film precursors [126]. He noticed that in the case of non-ionic precursor films, the dynamics of the film is governed by a dispersive van der Waals forces, while for the charged films the dynamics of the thin film is governed by both van der Waals forces and charged layer interactions. This was only the beginning and led to more than a century of struggles to better understand different aspects of this complicated problem [125-134]. In spite of such extensive efforts, the mechanisms of the precursor film formation still remained one of the most challenging issues in the field of condensed matter. Moreover, some fundamental paradoxes, most famously, the Huh-Scriven paradox [135] regarding the no-slip boundary condition at the solid substrate that the precursor film spreads, remained unanswered. As Huh and Scriven wrote [135]: “Not even Hercules could sink a solid if the physical model (no-slip boundary condition) were entirely valid.” This has opened more than 40 years ongoing effort of physicists to understand seemingly one of the easiest fluid mechanics problems, coating flow, appearing in every undergraduate fluid mechanics textbooks.

Electrocapillarity, the basis of modern electrowetting, was first explained in detail in 1875 by an ingenious physicist Gabriel Lippmann, who won the Nobel prize in 1908 [136,137]. Lippmann found that the capillary depression of mercury in contact with electrolyte solutions could be varied by applying a voltage between the mercury and electrolyte. The original Lippmann paper has only been available in French, but the interested reader may find a translation of his work in [136]. The work of Lippmann and of those who followed him in the subsequent more than a hundred years was devoted to aqueous electrolytes in direct contact with mercury surfaces or mercury droplets in contact with insulators. A major obstacle to broader applications was electrolytic decomposition of water upon applying voltages beyond a few hundred millivolts. The recent developments were initiated in the early 1990s by Berge [138], who introduced the idea of using a thin insulating layer to separate the conductive liquid from the metallic electrode in order to eliminate the electrolysis phenomenon at the metallic interface. This is the concept that has also become known as electrowetting on dielectric (EWOD).

Electrowetting on dielectric layer techniques are only limited to the case of controlling a droplet on a low energy surface. Gently deposited droplets over partial wetting substrates reach an equilibrium thermodynamic state with an equilibrium contact angle. The method is difficult or technically impossible to apply for manipulating droplets over a high energy surface since the droplet will completely wet the substrate. Therefore, an alternative method should be used to control the liquid film/droplet on high energy substrates.

The literature dealing with spreading of dielectric liquids over a solid surface is very sparse. Although several investigations were performed to investigate the EHD instabilities induced by corona discharge over a dielectric interface, no net spreading effect has been reported [139,140]. In a recent attempt, the alternative technique for droplet/film spreading over high energy substrates, such as a metallic substrate, was introduced by a joint research group at Harvard and Princeton [141] who demonstrated a selective spreading of a silicone oil film on a relatively high energy substrate. In their technique, the surface charge is accumulated over the dielectric interface and the tangential component of electric forces was created by an inclined planar electrode. A strong shear stress is developed over the interface, which expands the liquid from the low field region to the high field region. The spreading was accompanied by formation of Taylor cones at the liquid interface with several periodic jets ensuing during the film expansion process.

## 1.8 Objectives

The overall objective of the thesis is to increase the understanding of the effect of electrostatic forces to control or enhance fluid flow and heat transfer in gaseous media, bulk liquids, dielectric droplets and thin films. The main subject of the Chapters 2-4 is to investigate single-phase and two-phase cooling and the potential application of the EHD effect for heat transfer enhancement purposes. It was found that the EHD enhanced rewetting process plays a pivotal role in boiling heat transfer enhancement. In order to further understand the EHD wetting enhancement mechanisms, one may understand the spreading mechanisms of charged liquid/vapor interfaces and charge transport



mechanisms across the thin films. Investigation of the conduction pumping with reduced gap spacing presented in Chapter 5 provides an intuitive understanding about charge transport mechanism and the electrostatic pressure generation across dielectric liquid films.

Chapters 6-8 comprise the main part of the thesis where the main subject of the investigations was electrostatic-assisted spreading and in particular the wetting and spreading process of charged interfaces. A new concept of spreading based on the ionic bombardment of the dielectric liquid interface through corona discharge was proposed. When exposed to a corona discharge, the thickness of the dielectric liquid becomes monotonically thinner and liquid films with even nanometer size can be obtained, if the exposure time is long enough. Since the spreading dynamics and charge transport across the thin film are strongly coupled, it is crucial to understand the charge transport mechanism across the film. This understanding originated from our studies in the conduction pumping effect presented in Chapter 4, where the liquid film was confined between two electrodes. This new concept of corona discharge-assisted spreading was also applied to suppress or inhibit the retraction phase of an impacting droplet.

The spreading dynamics of the charged interface may be encountered in numerous applications including EHD boiling heat transfer enhancement. As mentioned earlier, the charge transport mechanism across the thin film may govern the hydrodynamics of spreading. Since the spreading of thin films is one dimensional in nature, the study of the thin film dynamics may give intuitive understanding about the charge transport mechanism across the thin film. Since the charge transport across the thin films occurs in several recent applications, such as thin film transistors and other molecular electronic devices, the study of one dimensional film spreading may help the understanding of the charge carrier transport phenomena across thin films.

## 1.9 Outline of thesis

The thesis objective described above has been presented in seven chapters followed by a closing chapter, where the thesis summary and new applications are discussed. The material presented in each chapter is outlined below.

### Chapter 2

Chapter 2 presents experimental and numerical results for natural convection heat transfer enhancement from an iso-thermal horizontal cylinder in the presence of corona discharge. A Mach-Zehnder interferometer was used to visualize the thermal boundary layer around the cylinder in air. Local Nusselt numbers were extracted from the interferograms. A numerical study was performed to predict the measured local Nusselt numbers around the cylinder at different surface temperatures and corona discharge voltages.

### Chapter 3

In Chapter 3, two-phase cooling of free-falling mono-dispersed water droplets impacting on a smooth upward-facing horizontal heated disk at pre-CHF regimes was revisited. The goals of this investigation were to show that (i) the existing correlations are not applicable for very low impacting velocities and (ii) several complications associated with the experimental setups and procedure made their results unreliable. The effect of droplet size and impacting frequency on the boiling curves and CHF was investigated in the absence of electric field. With more than 150 experimental data, two different hydrodynamic regimes of impact were characterized and different correlations for each regime were proposed to predict the CHF results in the absence of electric field. For the experiments in the presence of electric field it was found that the imposed electric field significantly changed the path of the falling droplets. Moreover, sporadic jetting and random Taylor cone formation re-directed the main volume of the coolant off the heated surface. Although the droplet cooling in the presence of electric field results were not encouraging, the authors included this chapter in this thesis. Two new correlations in this

chapter applicable at very low Weber numbers might be of interest for further studies. Moreover, one may find an appropriate technique to control impacting droplets through electrostatic forces and compare those results with the current study in the absence of electric field.

## Chapter 4

Direct jet impingement boiling heat transfer operating at low flow rates is of great interest for the localized moderate heat fluxes found with delicate mechanical structures, where the aggressive techniques such as high-speed jets are not suitable. Boiling heat transfer from an upward facing disk targeted by a falling jet was studied experimentally at different volumetric flow rates and various jet lengths. Using previous CHF correlations in their original form, valid at very low volumetric flow rates, result in large disagreements since it was found that variation in the jet length changes the boiling characteristics. Since the conventional correlations for impinging jets are not valid for low flow rates, the problem of the impinging jet in the absence of electric field was revisited. The working fluid chosen was the dielectric liquid HFE7100.

In the absence of an electric field, the simplest way to increase the momentum of the liquid sheet around the rim is by increasing the flow rate. However it is shown that an alternative way to enhance the momentum of the liquid sheet around the edge is to introduce EHD forces. The last part of this chapter investigates boiling heat transfer enhancement of falling jet in the presence of electric field.

## Chapter 5

In Chapter 5, an EHD conduction micropump was designed, fabricated and characterized for the first time. Comparing with previous macro-scale conduction micropumps, the gap spacing between the electrodes was reduced by one order of magnitude. The static pressure generation was determined at different applied voltages. A numerical solution was used to predict the static pressure generation at different electric field strengths. The hetero-charge layer interactions, static pressure generation mechanism in such a confined structure provide a deeper understanding of the charge transport mechanism across the

thin liquid layers. This was the foundation for understanding of the charge transport mechanism across the dielectric liquid films encountered in following three chapters.

## Chapter 6

Chapter 6 focuses on understanding the enhancement of the liquid film contact with a substrate through the use of electrostatic forces over an isothermal substrate. Here, a corona discharge-assisted technique for spreading a gently deposited dielectric droplet into a uniform thin film over a dry isothermal conductive substrate is proposed. The surface charge was built up over the droplet interface through ion bombardment using a sharp emitter electrode. Interaction of the surface charge density and the intense electric field generates an interfacial electrical pressure and leads to a uniform axisymmetric spreading of the droplet in the radial direction. The dynamics of the film spreading due to the corona discharge was confirmed through a simplified analytical model.

## Chapter 7

As it was demonstrated in Chapter 6, a dielectric liquid interface exposed to the corona discharge spreads over the grounded substrate. In Chapter 7, the spreading of a dielectric liquid film subjected to a long-term corona discharge was investigated. It has been demonstrated that the charge transport mechanism across the film determines the regime of spreading. Four different regimes of spreading were identified and each regime was discussed in detail. By further increasing the corona discharge exposure time, in the fourth regime the thickness of the dielectric film decreases, and an electrostatically-accelerated precursor film with nanometric thickness is developed and diffuses ahead of the apparent contact line. The thickness and spreading dynamics of the precursor film were measured by an ellipsometer. Deposition of such nanometric thin films through the corona discharge forced-spreading may create a platform for further fundamental studies such dielectric phenomena in thin films, hydrodynamics of the thin films, accelerated

wetting process, coating and deposition. As a result several industrial applications may benefit from such investigations.

## Chapter 8

Controlling the deposition of impacted droplets on a non-wetting solid substrate is important for numerous industrial and scientific applications including droplet impact cooling. In Chapter 8, a new active method based on the corona discharge-assisted spreading concept is proposed to control the deposition of an impacted dielectric droplet. An electric pressure resulting from the electric surface charge produced by the corona discharge squeezes the droplet interface towards the grounded substrate and generates a resistance against the droplet retraction. It is demonstrated that the electrical pressure effectively suppresses the droplet retraction at voltages above the corona discharge threshold.

## Chapter 9

This chapter summarizes the material presented in Chapters 2 through 8. It also suggests possible applications for the proposed concepts described in the thesis.

## References

- [1] J.R. Melcher, G.I. Taylor, Electrohydrodynamics: a review of the role of interfacial shear stresses, *Annual Review of Fluid Mechanics* 1969, 1, pp.111-146.
- [2] D.A. Saville, Electrohydrodynamics: the Taylor-Melcher leaky dielectric model, *Annual Review of Fluid Mechanics* 1997, 29, pp.27-64.
- [3] B.R. Fish, Electrical generation of natural aerosols from vegetation, *Science* 1972, 175, pp.1239-1240.
- [4] J.E. Hart, G.A. Glatzmaier, J. Toomre, Space-laboratory and numerical simulations of thermal convection in a rotating hemispherical shell with radial gravity. *Journal of Fluid Mechanics* 1986, 173, pp.519–544.
- [5] G.I. Taylor, Electrically driven jets, *Proceedings of the Royal Society A* 1969, 313, pp.453–475.
- [6] R.S. Allan, S.G. Mason, Particle behavior in shear and electric fields. I. Deformation and burst of fluid drops, *Proceedings of the Royal Society A* 1962, 267, pp.45–61.
- [7] R.S. Sigmond, The unipolar corona space charge flow problem, *Journal of Electrostatics* 1986, 18(3), pp. 249-272.
- [8] K. Adamiak, I.I. Inculet, G.S.P. Castle, The control of corona current distribution using shaped electrodes, *Journal of Electrostatics* 1993 30, pp.381-392.
- [9] K.T. Hyun, C.H. Chun, The wake flow control behind a circular cylinder using ion wind, *Experiments in Fluids* 2003, 35(6), pp.541-552.
- [10] J.R. Chapman, *Practical organic mass spectrometry*, New York, Wiley & Sons, 1993.

- [11] J. Zhang, K. Adamiak, G.S.P. Castle, Numerical modeling of negative-corona discharge in oxygen under different pressures, *Journal of Electrostatics* 2007, 65(3), pp.74-181.
- [12] P. Pignolet, S. Hadj-Ziane, B. Held, R. Peyrous, J.M. Benas, C. Coste, Ozone generation by point to plane corona discharge, *Journal of Physics D: Applied Physics* 1990, 23(6), pp.1069-1072.
- [13] B.R. Locke, M. Sato, P. Sunka, M.R Hoffmann, J.S Chang, Electrohydraulic discharge and nonthermal plasma for water treatment, , *Industrial & Engineering Chemistry Research* 2006, 45 (3), pp.882-905.
- [14] J.S. Chang, A.J. Kelly, J. M. Crowley, *Handbook of Electrostatic Processes*, Marcel Dekker Inc., NewYork, 1995.
- [15] K.P. Parker, *Applied Electrostatic Precipitation*, Chapman & Hall, West Midland, UK, 1997.
- [16] I.I. Inculet, Y. Murata, G.S.P. Castle, A new electrostatic separator and sizer for small particles, *IEEE Transactions on Industry Applications* 1983, 19, pp.318-323.
- [17] J. Doshi, D.H. Reneker, Electrospinning process and applications of electrospun fibers, *Journal of Electrostatics*, 1995, 35, pp.151-160.
- [18] A. Yabe, Y. Mori, K. Hijitata, EHD study of the corona wind between wire and plate electrodes, *AIAA Journal*, 1978, 16(4), pp.340–345.
- [19] T.B. Jones, Electrohydrodynamically enhanced heat transfer in liquids - a review, *Advances in Heat Transfer*, 1978, 14, pp.107-148.
- [20] M. Robinson, Convective heat transfer at the surface of a corona electrode, *International Journal of Heat and Mass Transfer*, 1970, 13, pp.263-274.
- [21] J. Yamaga and M. Jido, Corona discharge cooling technique, U.S. Patent No. 3,938,345, 1976.

- [22] J.H. Davidson, F.A. Kulacki, P.F. Dunn, Convective Heat Transfer with Electric and Magnetic Fields. In Handbook of Single-Phase Convective Heat Transfer; Kakac, S., et al., Eds.; Wiley, New York, 1987.
- [23] F.A. Kulacki, J.A. Daubenmier, A preliminary study of electrohydrodynamic augmented baking, Journal of Electrostatics, 1978 5, pp.325–336.
- [24] H.R. Carlon, J. Latham, Enhanced drying rates of wetted materials in electric fields, Journal of Atmospheric and Terrestrial Physics, 1992 54, pp.117–118.
- [25] A. Wolny, Intensification of the evaporation process by electric field, Chemical Engineering Science 1992 47(3), pp.551–554.
- [26] A. Wolny, P. Kaniuk, The effect of electric field on heat and mass transfer. Drying Technology 1996 14(2), pp.195–216.
- [27] N.N. Barthakur, N.P. Arnold, Evaporation rate enhancement of water with air ions from a corona discharge, International Journal of Biometeorology 1995 39, pp.29–33.
- [28] K.W. Lai, EHD-enhanced drying with a single wire electrode, M.S. Thesis; University of Oklahoma, U.S.A., 2000.
- [29] S.E. Sadek, R.G. Fax, M. Hurwitz, The influence of electric fields on convective heat and mass transfer from a horizontal surface under forced convection, Journal of Heat Transfer 1972 94(2), pp.144–148.
- [30] D.B. Go, S.V. Garimella, T.S. Fisher, R.K. Mongia, Ionic winds for locally enhanced cooling, Journal of Applied Physics, 2007 102, pp.053302.
- [31] M. Molki, K.L. Bhamidipati, Enhancement of convective heat transfer in the developing region of circular tubes using corona wind, International Journal of Heat and Mass Transfer, 2004 47, pp.4301–4314.
- [32] D.A. Nelson, S. Zia, R.L. Whipple, M.M. Ohadi, Corona discharge effects on heat transfer and pressure drop in tube flows, Enhanced Heat Transfer, 1998 7, pp.81–95.



- [33] M. Molki, M.M. Ohadi, B. Baumgarten, M. Hasegawa, A. Yabe, Heat transfer enhancement of airflow in a channel using corona discharge Enhanced Heat Transfer, 2000 7 , pp.411–425.
- [34] M.M. Ohadi, N. Sharaf, D.A. Nelson, Electrohydrodynamic enhancement of heat transfer in a shell-and-tube heat exchanger, Experiments in Heat Transfer, 1991 4 (1), pp.19–39.
- [35] F.C. Lai, Effects of buoyancy on electrohydrodynamic-enhanced forced convection in a horizontal channel, Journal of Thermophysics and Heat Transfer, 1998 12 (3), pp.431–436.
- [36] M. Molki, P. Damronglerd, Electrohydrodynamic enhancement of heat transfer for developing air flow in square ducts, Heat Transfer Engineering, 2006 27(1), pp.35-45.
- [37] B.L. Owsenek, J. Seyed-Yagoobi, Theoretical and experimental study of electrohydrodynamic heat transfer enhancement through wire-plate corona discharge, Journal of Heat Transfer, 1997 119, pp.604–610.
- [38] B.L. Owsenek, J. Seyed-Yagoobi, R.H. Page, Experimental investigation of corona wind heat transfer enhancement with a heated horizontal flat plate, Journal of Heat Transfer, 1995 117, pp.309–315.
- [39] H. Kalman, E. Sher, Enhancement of heat transfer by means of a corona wind created by a wire electrode and confined wings assembly, Applied Thermal Engineering, 2001 21, pp.265–282.
- [40] H.R. Velkoff, R. Godfrey, Low-velocity heat transfer to a flat plate in the presence of a corona discharge in air, Journal of Heat Transfer, 1979 101, pp.157–163.
- [41] S. Wangnipparnto, J. Tiansuwan, S. Jiracheewanun, T. Kiatsiriroat, C.C. Wang, Air side performance of thermosyphon heat exchanger in low Reynolds number region: with and without electric field, Energy Conversion and Management, 2002 43 , pp.1791–1800.

- [42] M.E. Franke, Effect of vortices induced by corona discharge on free-convection heat transfer from a vertical plate, *Journal of Heat Transfer*, 1969 91, 427-433.
- [43] S.M. Lee, C.S. Park, M.S. Cha, S.H. Chung, Effect of electric fields on the liftoff of nonpremixed turbulent jet flames, *IEEE Transactions of Plasma Science*, 2005 33(5),1 pp.703-1709.
- [44] H. Ohisa, I. Kimura, H. Horisawa, Control of soot emission of a turbulent diffusion flame by dc or ac corona discharges, *Combustion and Flame*, 1999 116, pp.653–661.
- [45] M. Saito, T. Arai, M. Arai, Control of soot emitted from acetylene diffusion flames by applying an electric field, *Combustion and Flame*, 1999 119, pp.356–366.
- [46] J. Vinogradov, E. Sher, I. Rutkevich, M. Mond, Voltage-current characteristics of a flame-assisted unipolar corona, *Combustion and Flame*, 2001 127, pp.2041–2050.
- [47] P. Atten, J. Seyed-Yagoobi, Electrohydrodynamically induced dielectric liquid flow through pure conduction in point/plane geometry, *IEEE Transactions on Dielectrics and Electrical Insulation*, 2003 10(1), pp.27-36.
- [48] J. Seyed-Yagoobi, Electrohydrodynamic pumping of dielectric liquids, *Journal of Electrostatics*, 2005 63, pp.861-869.
- [49] C. Tsouris, W. Shin, S. Yiacoumi, Pumping, spraying, and mixing of fluids by electric fields, *The Canadian Journal of Chemical Engineering*, 1998 76(3), pp.589-599.
- [50] J. Darabi, M.M. Ohadi, D. Devoe, An electrohydrodynamic polarization micropump for electronic cooling, *Journal of Microelectromechanical Systems*, 2001 10(1), pp.98-106.
- [51] C. Lin, J. Jang, 3D numerical micro-cooling analysis for an electrohydrodynamic micro-pump, *Sensors and Actuators A: Physical*, 2005 122(1), pp.167-176.

- [52] V. Singhal, S.V. Garimella, A novel valueless micropump with electrohydrodynamic enhancement for high heat flux cooling, *IEEE Transactions on Advanced Packaging*, 2005 28(2), pp.216-230.
- [53] C.K. Lee, A.J. Robinson, C.Y. Ching, Development of EHD ion-drag micropump for microscale electronics cooling, 13th International Workshop on Thermal Investigation of ICs and Systems, 2007, Budapest, pp.17-19.
- [54] V. Singhal, S.V. Garimella, A. Raman, Microscale pumping technologies for microchannel cooling systems, *Applied Mechanics Reviews*, 2004 57(3), pp.191-222.
- [55] J. Darabi, M.M. Ohadi, Electrohydrodynamically enhanced microcooling system for integrated circuits, US Patent 6,443,704.
- [56] J.R. Melcher, *Continuum Electromechanics*, MIT Press, Cambridge, MA, 1981.
- [57] J.R. Melcher, Traveling-wave induced electro-convection, *Physics of Fluids*, 1966 9, pp.1548-1555.
- [58] J.R. Melcher, M.S. Firebaugh, Traveling-wave bulk electroconvection induced across a temperature gradient, *Physics of Fluids*, 1967 10, pp.1178-1185.
- [59] J. Wong, J.R. Melcher, Thermally induced electroconvection, *Physics Fluids*, 1969 12, pp.2264-2269.
- [60] S.I. Jeong, J. Seyed-Yagoobi, P. Atten, Theoretical/numerical study of electrohydrodynamic pumping through pure conduction phenomenon, *IEEE Transactions on Industry Applications*, 2003 39, pp.355-361.
- [61] S.I. Jeong, J. Seyed-Yagoobi, Fluid circulation in an enclosure generated by electrohydrodynamic conduction phenomenon, *IEEE Transactions on Dielectrics and Electrical Insulation*, 2004 11, pp.899-910.
- [62] S.I. Jeong, J. Seyed-Yagoobi, Innovative electrode design for electrohydrodynamic conduction pumping, *IEEE Transactions on Industry Applications*, 2004 40, pp.900-904.

- [63] Y. Feng, J. Seyed-Yagoobi, Understanding of electrohydrodynamics conduction pumping phenomenon, *Physics of Fluids*, 2004 16, pp.2432-2441.
- [64] O.M. Stuetzer, Ion-drag pressure generation, *Journal of Applied Physics*, 1959 30, pp.984-994.
- [65] W.F. Pickard, Ion-drag pumping I-theory, *Journal of Applied Physics*, 1963 34, pp.246-250.
- [66] W.F. Pickard, Ion-drag pumping II—experiments, *Journal of Applied Physics*, 1963 34, pp.251–258.
- [67] A.H. Sharbaugh, G.W. Walker, The design and evaluation of an ion-drag dielectric pump to enhance cooling in a small oil-filled transformer, *IEEE Transactions on Industry Applications*, 1985 pp.950-955.
- [68] J.E. Bryan, J. Seyed-Yagoobi, An experimental investigation of ion-drag pump in a vertical and axisymmetric configuration, *IEEE Transactions on Industry Applications*, 1992 28, pp.310-316.
- [69] V. Betis, Experimental and computational investigation of planar ion drag micropump geometrical design parameters, Ph.D. thesis, University of Maryland, College Park, MD, 2005.
- [70] L.J. Yang, J.M. Wang, Y.L. Huang, The micro ion drag pump using indium-tin-oxide (ITO) electrodes to resist aging, *Sensors and Actuators A: Physical*, 2003 111(1), pp.118-122.
- [71] J. Seyed-Yagoobi, J.E. Bryan, Electrohydrodynamic conduction pump, U.S Patent 6,932,580, 2005.
- [72] D.J. Kervin, J.M. Crowley, P. Krein, J.C. Chato, Parametric studies of a large thermal EHD induction pump, *IEEE-Industry Applications Society Annual Meeting*, New York City, New York, 1981, pp.1015-1020.

- [73] J. Seyed-Yagoobi, J.C. Chato, J.M. Crowley, P.T. Krein, Induction electrohydrodynamic pump in a vertical configuration part 1-Theory, *Journal of Heat Transfer*, 1989 111, pp.664-669.
- [74] J. Seyed-Yagoobi, J.C. Chato, J.M. Crowley, P. Krein, Induction electrohydrodynamic pump in a vertical configuration part 2-experimental study, *Journal of Heat Transfer*, 1989 111, pp.670-674.
- [75] M. Wawzyniak, J. Seyed-Yagoobi, G.L. Morrison, An experimental study of electrohydrodynamic induction pumping of a stratified liquid/vapor medium, *Journal of Heat Transfer*, 2000 122, pp.200-203.
- [76] M. Wawzyniak, J. Seyed-Yagoobi, Electrohydrodynamic induction pumping of a stratified liquid/vapor medium in the presence of volumetric and interface electric charges, *IEEE Transactions on Industry Applications*, 37 (2001), pp.950-958.
- [77] K. Brand, J. Seyed-Yagoobi, Experimental study of electrohydrodynamic induction pumping of a dielectric micro liquid film in external horizontal condensation process, *Journal Heat Transfer*, 2003 125, pp. 1096-1105.
- [78] N. Nguyen, X. Huang, T. Chuan, MEMS-micropumps: A review, *Journal of Fluid Engineering*, 2002 124(2), pp.234-293.
- [79] S. Hardt, F. Schönfeld, *Microfluidic technologies for miniaturized analysis systems*, Boston, MA, 2007.
- [80] A. Richter, H. Sandmaier, *An electrohydrodynamic micropump*, *IEEE Micro Electro Mechanical Systems. An Investigation of Micro Structures, Sensors, Actuators, Machines and Robots*, New York, NY, 1990.
- [81] C.C. Wong, D. Chu, S.L. Liu, M.R. Tuck, Z. Mahmud, V. Amatucci, Rapid prototyping of a micro pump with laser micromachining, *Proceedings of SPIE: Micromachined Devices and Components*, Austin, TX, 1995.

- [82] S.H. Ahn, Y.K. Kim, Fabrication and experiment of a planar micro ion drag pump, *Sensors and Actuators, A: Physical*, 1995 70(1-2), pp.1-5.
- [83] J. Darabi, H. Wang, Development of an electrohydrodynamic injection micropump and its potential application in pumping fluids in cryogenic cooling systems, *Journal of Microelectromechanical Systems*, 2005 14(4), pp.747-755.
- [84] J. Darabi, M. Rada, M. Ohadi, J. Lawler, Design, fabrication, and testing of an electrohydrodynamic ion-drag micropump, *Journal of Microelectromechanical Systems*, 2002 11(6), pp.684-690.
- [85] M. Rada, *Electrohydrodynamics (EHD) Pumping of Liquid Nitrogen Application to Spot Cryogenic Cooling of Sensors and Detectors,*” Ph.D Dissertation, University of Maryland, College Park, USA, 2004.
- [86] L.J. Yang, J.M. Wang, K.C. Ko, W.P Shih, C.L Dai, A circular microchannel integrated with embedded spiral electrodes used for fluid transportation, *Sensors and Actuators A*, 2007 139, pp.172–177.
- [87] A.M. Jacobi, R.K. Shah, Heat transfer surface enhancement through the use of longitudinal vortices: A review of recent progress, *Experimental Thermal and Fluid Sciences*, 1995 11(3), pp.295-309.
- [88] M.E. Franke, L.E. Hogue, Electrostatic cooling of a horizontal cylinder, *Transaction of ASME*, 1991 113, pp.544-548.
- [89] M.E. Franke, Effect of Vortices Induced by Corona Wind Discharge on Free Convection Heat Transfer From Vertical Plate, *Journal of Heat Transfer*, 1969 No.68-WA/HT-9.
- [90] J. O'Brien, A.J. Shine, Some effects of an electric field on heat transfer from a vertical plate in free convection, *Journal of Heat Transfer*, 1967, pp.114-116.
- [91] A.S. Mitchell, L.E. Williams, Heat transfer by the corona wind impinging on a flat surface, *Journal of Electrostatics*, 1978 5, pp.309-324.

- [92] T. Kohya, M. Kuriyama, M. Toda, E. Harada, H. Konno, Heat transfer from horizontal, parallel tube banks under a corona discharge, *International Chemical Engineering*, 1989 27 (2), pp.319-325.
- [93] T. Kuriyama, E. Harada, H. Konno, Application of corona wind to practical tubular heat exchangers, *Heat Transfer—Japanese Research*, 1989 18 (4), pp.1-8.
- [94] T. Kuriyama, E. Harada, H. Konno, Enhancement of heat transfer from horizontal tube-banks by the use of a corona wind, *International Chemical Engineering*, 1989 29 (4), pp.715-721.
- [95] S. Vithayasai, T. Kiatsiriroat, A. Nuntaphan, Effect of electric field on heat transfer performance of automobile radiator at low frontal air velocity, *Applied Thermal Engineering*, 2006 26, pp.2073–2078.
- [96] N. Kasayapanand, Numerical study of electrode bank enhanced heat transfer, *Applied Thermal Engineering*, 2006 26 pp.1471-1480.
- [97] P. Carrica, P. Marco, W. Grassi, Nucleate pool boiling in the presence of an electric field: Effect of subcooling and heat-up rate, *Experimental Thermal and Fluid Science*, 1997 15(3), pp.213-220.
- [98] X. Quan, G. Chen, P. Cheng, Effect of electric field on microbubble growth in a microchannel under pulse heating, *International Journal of Heat and Mass Transfer*, 2011 54, pp.210-215.
- [99] M.C. Zaghdoudi, M. Lallemand, Electric field effects of pool boiling, *Journal of Enhanced Heat Transfer*, 2002 9, pp.187-208.
- [100] W. Eames, H.M. Sabir, Potential benefits of electrohydrodynamic enhancement of two-phase heat transfer in the design of refrigeration systems, *Journal of Applied Thermal Engineering*, 1997 17, pp.79–92.
- [101] J. Berghmans, Electrostatic fields and the maximum heat flux, *International Journal of Heat and Mass Transfer*, 1975 21, pp.791-799.

- [102] J. Ogata, A. Yabe, Augmentation of boiling heat transfer by utilizing the EHD effect-EHD behaviour of boiling bubbles and heat transfer characteristics, *International Journal of Heat and Mass Transfer*, 1993 36, pp.783–91.
- [103] J. Ogata, A. Yabe, Basic study on the enhancement of nucleate boiling heat transfer by applying electric fields, *International Journal of Heat and Mass Transfer*, 1993 36, pp.742–75.
- [104] J. Ogata, A. Yabe, Augmentation of nucleate boiling heat transfer by applying electric fields: EHD behaviour of boiling bubble, *ASME/JSME Thermal Engineering*, 1991 3, pp.41-46.
- [105] H.J. Cho, I.S. Kang, Y.C. Kweon, M.H. Kim, Study of the behaviour of a bubble attached to a wall in a uniform electric fields, *International Journal of Multiphase Flow*, 1996 22, pp.909-922.
- [106] H.J. Cho, I.S. Kang, Y.C. Kweon, M.H. Kim, Numerical study of the behavior of a bubble attached to a nonuniform electric field, *International Journal of Multiphase Flow*, 1998 24, pp.479-498.
- [107] K. Cheung, M.M. Ohadi, S.V. Dessiatoun, A. Singh, EHD-enhanced boiling coefficients and visualization of R-134a over enhanced tubes, *Transactions of ASME*, 1997 119, pp.332-338.
- [108] P. Cooper, EHD enhancement of nucleate boiling, *Journal of Heat Transfer*, 1990 112, pp.446–58.
- [109] F. Verplaetsen, J.A. Berghmans, The influence of an electric field on the heat transfer rate during film boiling of stagnant fluids, *Revue Générale de Thermique*, 1997 37(2), pp.83-88.
- [110] G. Tomar, G. Biswas, A.Sharma, S.W.J Welch, Influence of electric field on saturated film boiling, *Physics of Fluids*, 2009 21, 032107.



- [111] S.W. J Welch, G. Biswas, Direct simulation of film boiling including electrohydrodynamic forces, *Physics of Fluids*, 2007 19, pp.012106.
- [112] S.M. Ghiaasiaan, *Two-Phase Flow, Boiling, and Condensation in Conventional and Miniature Systems*, Cambridge University Press, New York, 2008.
- [113] V. Bergeron, D. Bonn, J. Yves Martin, L. Vovelle, Controlling droplet deposition with polymer additives, *Nature* 2000 405, pp.772-774.
- [114] A. Carré, J. Gastel, M. Shanahan, Viscoelastic effects in the spreading of liquids, *Nature*, 1996 379, pp.432-434.
- [115] S. Schiaffino, A. Sonin, Molten droplet deposition and solidification at low Weber numbers, *Physics of Fluids*, 1997 11, pp.3172-3187.
- [116] J.D. Bernardin, C.J. Stebbins, I. Mudawar, Mapping of impact and heat transfer regimes of water drops impinging on a polished surface, *International Journal of Heat and Mass Transfer*, 1997 40(2), pp.247-267.
- [117] A. Frohn, R. Roth, *Dynamics of Droplets* Springer, Berlin, 2000.
- [118] T. Mang, W. Dresel, *Lubricants and Lubrication* Wiley, Weinheim, 2007.
- [119] M. Bussmann, S. Chandra, J. Mostaghimi, Modeling the splash of a droplet impacting a solid surface, *Physics of Fluids*, 2000 12, pp.3121-3132.
- [120] N.Z. Mehdizadeh, S. Chandra, J. Mostaghimi, Formation of fingers around the edges of a drop hitting a metal plate with high velocity, *Journal of Fluid Mechanics*, 2004 510, pp.353-373.
- [121] M.J. Blunt, Flow in porous media-pore-network models and multiphase flow, *Current Opinion in Colloid & Interface Science*, 2001 6(3), pp.197-207.
- [122] A.M. Cazabat, How does a droplet spread?, *Contemporary Physics*, 1987 28(4), pp.347-364.

- [123] P. Ball, Spreading it about, *Nature*, 1989 338, pp.624-625.
- [124] L. Leger, J.F. Joanny, Liquid spreading, *Reports on Progress in Physics*, 1992 55, pp.431-486.
- [125] H.W. Hardy, The spreading of fluids on glass, *Philosophical Magazine*, 1919 38, pp.49-55.
- [126] W.D. Bascom, R. Cottington, C. Singleterry, *Wetting, Spreading, and Adhesion*, Academic press, London, 1978.
- [127] A. Hoang, H. P. Kavehpour, Dynamics of nanoscale precursor film near a moving contact line of spreading drops, *Physical Review Letters*, 2011 106, 254501-1-4.
- [128] P.G. de Gennes, Wetting: statics and dynamics, *Review of Modern Physics*, 1985 57, pp.827-863.
- [129] D. Ausserre, A.M Picard, L. Leger, Existence and role of the precursor film in the spreading of polymer liquids, *Physical Review Letters*, 1986 57, pp.2671-2674.
- [130] L. Leger, M. Erman, A.M. Picard, D. Ausserre, C. Strazielle, Precursor film profiles of spreading liquid drops, *Physical Review Letters*, 1988 60, pp.2390-2393.
- [131] H. Xu, D. Shirvanyants, K. Beers, K. Matyjaszewski, M. Rubinstein, S.S. Sheiko, Molecular motion in a spreading precursor film, *Physical Review Letters*, 2004 93, pp.206103.
- [132] H. P. Kavehpour, B. Ovryn, G.H. McKinley, Microscopic and macroscopic structure of the precursor layer in spreading viscous drops, *Physical Review Letters*, 2003 91, pp.196104.
- [133] J. Yang, J. Koplik, Molecular dynamics of drop spreading on a solid surface, *Physical Review Letters*, 1991 67, pp.3539-3542.
- [134] Q. Yuan, Y. Zhao, Precursor film in dynamic wetting, electrowetting, and electro-elasto-capillarity, *Physical Review Letters*, 2010 104, pp.246101.

- [135] C. Huh, L.E. Scriven, Hydrodynamic model of steady movement of a solid/liquid/fluid contact line, *Journal of Colloid and Interface Science*, 1971 35(1), pp.85-101.
- [136] F. Mugele, J. Baret, Electrowetting: from basics to applications, *Journal of Physics: Condensed Matter*, 2005 17(28), R.705
- [137] G. Lippmann, Relations entre les ph'énomènes électriques et capillaries, *Annales des Chimie et des Physique*, 1875 5pp.494-549.
- [138] B. Berge, Electrocapillarite et mouillage de films isolants par l'eau, *Académie Royale des Sciences II*, 1993 317, pp.157-163.
- [139] F. Vega, A.T. Pérez, Corona-induced electrohydrodynamic instabilities in low conducting liquids, *Experiments in Fluids*, 2003 34, pp.726-735.
- [140] F. Vega, F. García, Pattern imaging of primary and secondary electrohydrodynamic instabilities, *Journal of Fluid Mechanics*, 2006 549, pp.61-69.
- [141] P. Kim, C. Duprat, S.S.H. Tsain, H.A. Stone, Selective spreading and jetting of electrically driven dielectric films, *Physical Review Letters*, 2011 107, pp.034502-1-4.

## Chapter 2

# The Effect of Corona Discharge on Free Convection Heat Transfer from a Horizontal Cylinder

### 2.1 Introduction

Establishment of corona discharge between a sharp electrode and a grounded heated surface usually induces an ionic wind whose momentum can be used for enhancement of heat transfer from the heated surface. The corona discharge and ionic wind are caused by the ionization of air molecules in the intense electric field region around the sharp electrode that accelerates ions and drags the air molecules toward the grounded surface. Electrostatic cooling devices operate without any moving parts, which reduces the mechanical vibration, energy losses and associated noises. Therefore, the electrostatic cooling is potentially attractive.

Corona enhancement of heat transfer from various objects has been the subject of many investigations because of a comparatively significant local enhancement of heat transfer coefficient with small corona discharge power consumption. For the first time, Marco and Velkoff [1] reported a 500% enhancement of average heat transfer coefficient and even higher local enhancements from a vertical heated plate in the presence of corona wind. The momentum integral analysis was carried out to further verify the experimental results. The theoretical results were in good agreement with experimental studies.

Yabe et al. [2] investigated the enhancement of heat transfer from a horizontal downward-facing plate using 40 $\mu$ m wire electrode in a Plexiglass chamber connected to a high voltage source. A Langmuir probe was used to measure the space charge density distribution and to verify the numerical results. They were able to model the recirculation flow inside the chamber and achieved a good agreement with their experimental results.

O'Brien and Shine used an interferometer to measure the ElectroHydroDynamic (EHD) enhancement of local heat transfer from a vertical isothermal flat plate for various air

pressures [3]. They concluded that the boundary layer was distorted in the vicinity of the plate surface and the heat transfer coefficient increased with corona current.

Franke and Hogue [4] studied the corona wind effect on a heated horizontal cylinder using both a multi-emitter electrode and a wire electrode. The average heat transfer enhancement was quantitatively calculated by a heat-balance method and qualitatively measured with a Mach-Zehnder interferometer. Enhancement of heat transfer from the cylinder due to the corona discharge was reported to be as much as six times the free convection heat transfer. The authors found that the multi emitter electrode was more effective compared with the stretched wire electrode. However, they did not report the local heat transfer coefficient around the cylinder.

The literature review shows that finding the average heat transfer rate for external free convection flows in the presence of corona discharge has been the subject of several investigations. Various heated test sections, such as horizontal plate [22, 23], vertical plate [24] and horizontal tube bank [25,26,27,20], were investigated. Owsenek and Seyed-Yagoobi [5] experimentally investigated the corona wind heat transfer enhancement from a horizontal flat plate. Needle electrodes with different heights were used as the corona electrode. An enhancement of more than 25:1 over free convection was reported. More recently [6], the same authors continued their theoretical and experimental studies and focused on a comparison between single and multiple wire electrodes. They concluded that for a given applied voltage, multiple wire electrodes yield smaller heat transfer enhancement per wire electrode than that of a single wire electrode. It was also found that dual recirculation may be formed between wire electrodes. Numerical simulations of novel electrode geometries revealed that this inefficiency may be eliminated through the use of blade geometry.

Franke [7] investigated heat transfer from a vertical plate in the presence of corona-generated vortices. The vortices were generated by the corona discharge from parallel Multi-wire electrpoles. He also visualized the thermal boundary layer using a Mach-Zehnder interferometer and measured the resulting heat transfer through both an energy

balance and interferograms. A doubling of the convective component of total heat transfer was reported when the applied corona voltage was above the corona onset value.

Although enhancement of free convection heat transfer through corona discharge has been widely studied, few experimental studies have been performed to find the local heat transfer rate for external free convection flows in the presence of corona discharge. Moreover, previous studies on ionic wind-enhanced heat transfer show that the corona discharge has comparatively smaller effect on high-Reynolds force convection [21]. Likewise, investigation of the interaction between the corona discharge and buoyancy-driven flow has been investigated.

In most of the previous interferometric studies, the EHD enhancements in heat transfer investigations have been limited to a qualitative visualization of the thermal boundary layer. In those studies, the average Nusselt number was determined using the energy balance method. The investigation reported here involves a quantitative interferometric study of the positive corona discharge on the local heat transfer enhancement from an isothermal horizontal cylinder for different Rayleigh numbers. A circular cylinder was selected as the test section, because the circular tube is widely used in typical heat exchangers. Considering the limitations of the interferometer plates, the diameter of the cylinder and the surface temperature were selected to obtain an appropriate range of Rayleigh number ( $1500 < Ra < 5000$ ) which is frequently encountered in conventional HVAC systems. In order to generate a uniform distribution of discharge effects along the laser beam, which is needed for the two dimensional interferometric studies, a sharp tip blade was used as a high voltage corona electrode. Moreover, compared with other electrode geometries, alignment of the blade electrode can be achieved more precisely along the laser beam. In order to find the details of the flow patterns and to further verify the experimental results, a numerical simulation was also performed.

## 2.2 Experimental Setup

The apparatus used in this experiment consisted of three major components: (i) an isothermally heated surface, heating facilities, instrumentation, and control (ii) high

voltage apparatus and measurement devices (iii) temperature field visualization system. The schematic view of the experimental setup and apparatus is presented in Fig.1-a.

The test section was an extruded aluminum hollow cylinder with a highly polished outer surface. The details of the test section are shown in Fig.1-b. The length of the cylinder was chosen as 160 mm (16 times of diameter) which causes the induced flow to be two-dimensional. In order to minimize the thermal end effects, two wooden fiber end caps with  $k = 0.05 W/m^2K$  were installed at both ends of the test section. In order to position the cylinder in the horizontal direction, two plastic rods were connected to these end caps and installed on the XYZ holders. The cylinder had an axial cavity to facilitate installation of a coiled nickel-chromium wire heater element at the center of the cavity. The space between the heater coil and inner wall of the hollow cylinder was filled with magnesium oxide powder. Four holes with 0.55 mm diameter were drilled into the base surface of the cylinder at 30, 50, 60 and 80 mm from the base ends in different peripheral angles. Four calibrated K type thermocouples were inserted and fixed in these holes. All the temperatures were monitored continuously by a TESTO 177 data logger which was connected to a PC. The maximum difference in surface temperature readings at the four thermocouple junctions were about 0.2 degree before tests. Furthermore, the outer surface temperature of the cylinder was measured at 20 different locations both in the peripheral and longitudinal directions with a calibrated hand held digital thermometer. The difference between the readings did not exceed 0.2 degree. The combination of the relatively thick-walled aluminum cylinder and the high thermal conductivity of magnesium oxide powder helped achieve the desired uniformity of the surface temperature both peripherally and longitudinally. The electrical power supplied to the heater was controlled by a variable transformer, therefore, it was possible to achieve different surface temperatures and different Rayleigh numbers.

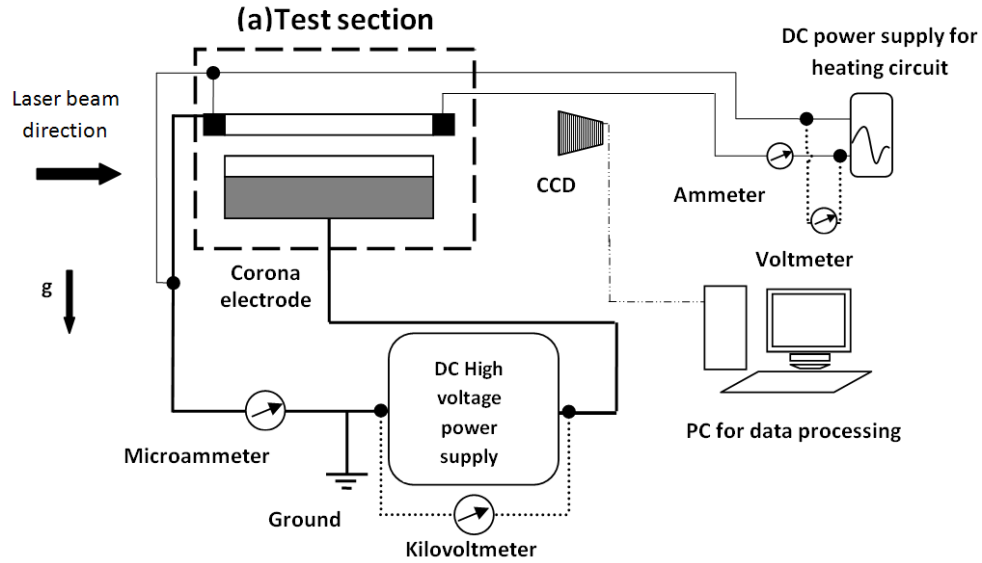


Figure 1-a: Schematic of experimental setup

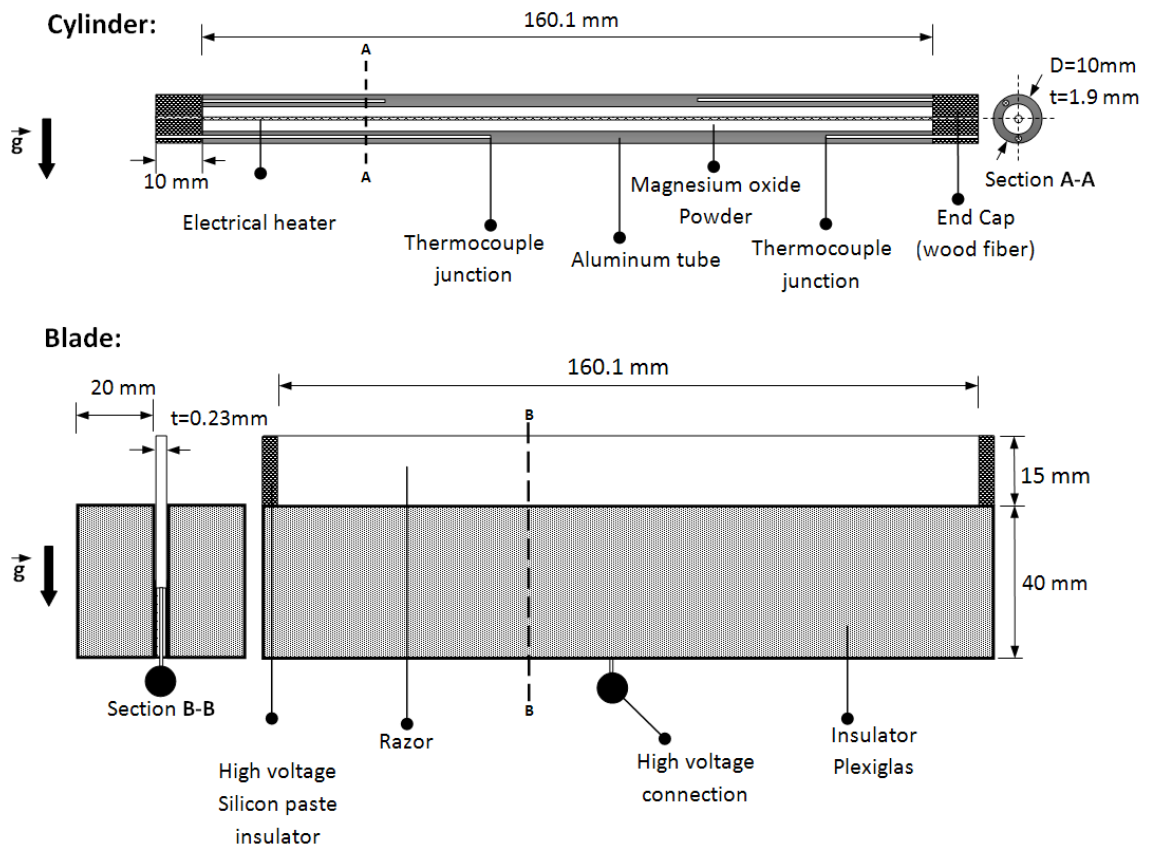
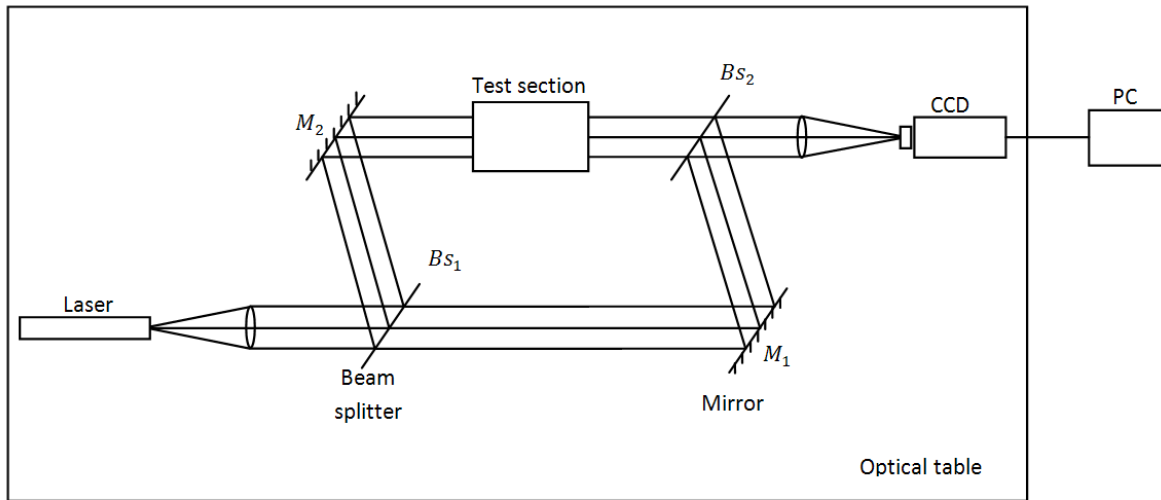


Figure 1-b: Details of the cylinder and the blade electrode.



The electrical input power was varied to keep the surface temperature constant in the presence and the absence of corona discharge. After changing the power level, it took about one hour to obtain steady state condition with quasi-constant surface temperature in the absence of corona discharge. For the corona discharge experiments it took about 20 minutes to obtain quasi-constant surface temperature. At the steady state condition and before initiating the tests, the maximum differences in surface temperature readings of four thermocouple junctions were about 0.2 degree. A high voltage DC power supply (0-30kV Spellman supply SL-600) was used to generate the positive DC corona discharge. The blade electrode was fixed 40 mm below the cylinder and connected to the positive terminal of the high voltage DC power supply. This comparatively large spacing provided larger voltage range between corona onset and breakdown allowing larger number of different voltages to be tested. Parallelism and adjustments of the blade with respect to the cylinder were done using optical positioners.

A Mach-Zehnder interferometer with 100 mm diameter optical plates and 100 mW He-Ne laser light source was used to visualize the temperature field around the cylinder. A schematic of the interferometer is shown in Fig.1-c. Infinite fringe interferograms were digitized by a Panasonic WV-CP410- 1/3 CCD camera which was connected to a PC. In this set up, the laser beam splits into two beams of approximately equal intensity. A reference beam passes through the thermally undisturbed ambient air, and the test beam passes through the thermally disturbed air adjacent to the heated cylinder. Because the refractive index varies with temperature, the two laser beams are no longer in the same phase when they are recombined. This phase shift produces an interference pattern in the optical output of the Mach-Zehnder interferometer, which can be recorded with a CCD camera. When these two beams are parallel upon recombination, the constructive and destructive interference fringes correspond directly to the isotherms in the flow field. Further adjustments of the test section and its parallelism along the laser beam were examined by the laser beam, CCD camera, and a simple image processing procedure.



**Figure 1-c: Plane view of Mach–Zehnder interferometer.**

## 2.3 Experimental procedure and data reduction method

The test procedure was initiated by testing the free convection heat transfer from the horizontal cylinder in the absence of corona discharge. After reaching the steady state condition, interferograms were taken. The corona discharge was generated near the cylinder by applying the high voltage to the blade, with magnitude in the range between onset of corona discharge and breakdown voltage. At each voltage, five interferograms were recorded for assurance of the experiment repeatability and data reduction. Fig.2 represents examples of the infinite fringe interferograms for two extreme cases, at lowest and highest Rayleigh numbers, for different applied voltages. The atmospheric pressure and the relative humidity of the laboratory were recorded during all the experiments. The infinite temperature  $T_{\infty}$  was monitored at two different vertical locations about 500 mm away from the test section and they both indicated the same value. A code was developed to calculate the local Nusselt number around the cylinder using infinite fringe interferograms. The data reduction procedure was similar to the work done by Ashjaee et al. [28].

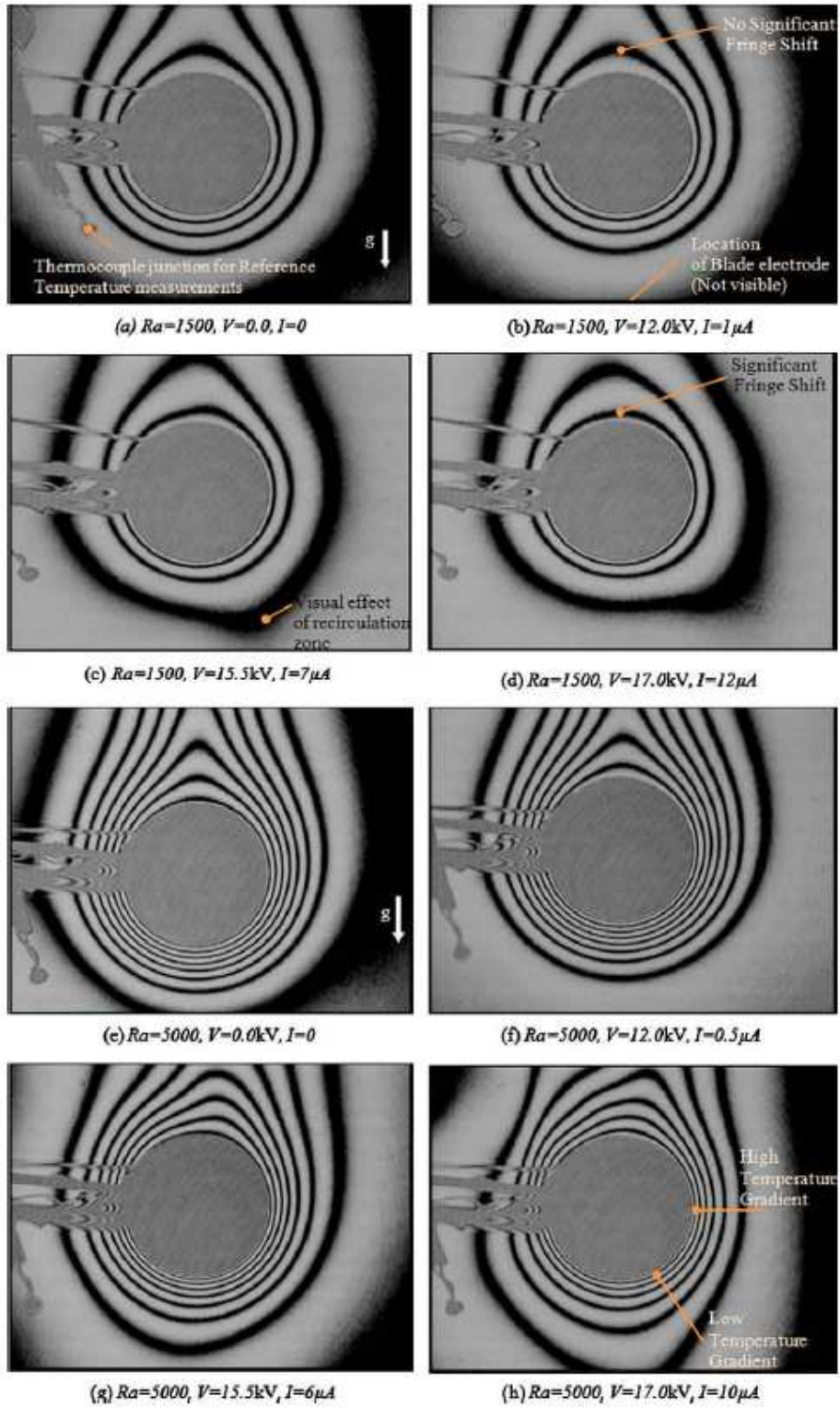


Figure 2: Examples of interferograms in the absence and presence of corona.

The local Nusselt number is defined as follows:

$$Nu_\theta = \frac{h_\theta D}{k_f} \quad (1)$$

The local heat transfer coefficient can be obtained as:

$$h_\theta = -k_f \left( \frac{dT}{dr} \right)_{r=D/2, \theta} \cdot \frac{1}{T_s - T_\infty} \quad (2)$$

The local temperature gradient can be calculated from infinite fringe interferograms as:

$$\left. \frac{dT}{dr} \right|_{r=D/2, \theta} = \left. \frac{dT}{d\varepsilon} \right|_{r=D/2, \theta} \cdot \left. \frac{d\varepsilon}{dr} \right|_{r=D/2, \theta} \quad (3)$$

The fringe shift due to the spatial temperature difference in the interferometer test arm can be obtained as [8,9]:

$$\left. \frac{dT}{d\varepsilon} \right|_{r=D/2, \theta} = \frac{6ClP_\infty \lambda R_o T_{ref}^2}{(3ClP_\infty - 2\lambda R_o T_{ref} \varepsilon)^2} \quad (4)$$

$\left. \frac{d\varepsilon}{dr} \right|_{r=D/2, \theta}$  can be calculated by the measuring the distance between the fringes from the cylinder surface. The temperature of the farthest fringe from the cylinder surface was logged by a K-type thermocouple. The order number of this fringe is set to zero ( $\varepsilon = 0$ ) and is considered as the reference fringe. The reference temperature readings,  $T_{ref}$ , near the heated surface are slightly higher than the infinite temperature readings, which were located sufficiently far from the test section.

The local Nusselt number can be written as:

$$Nu_\theta = -\frac{D}{T_s - T_\infty} \cdot \frac{6ClP_\infty \lambda R_\circ T_{ref}^2}{(3ClP_\infty - 2\lambda R_\circ T_{ref} \varepsilon)^2} \cdot \frac{d\varepsilon}{dr} \Big|_{r=D/2, \theta} \quad (5)$$

The average Nusselt number can be calculated as:

$$\overline{Nu} = \frac{1}{\pi} \int_0^\pi Nu_\theta d\theta \quad (6)$$

The average Nusselt number was obtained by integrating the local Nusselt number over the left hand side and right hand side of the cylinder for each interferogram. Comparing the average Nusselt number calculated for the both sides shows maximum 4.5% discrepancy at ( $Ra = 5000$  and  $\varphi_o = 17.0kV$ ) which is within the uncertainty band. In some cases, the experimental asymmetry observed in the interferograms may be greater than the thickness of the fringe. However, in order to get more accurate local Nusselt number, the middle of the fringes was recorded instead of their edges.

## 2.4 Uncertainty Analysis

The experimental uncertainty of the local Nusselt number was performed using the ASME guidelines on reporting the uncertainties in experimental measurements and results [10]. The propagation equation of Kline and McClintock for local Nusselt number calculation from Eq.(5) can be written as:

$$P_{Nu_\theta}^2 = \left(\frac{\partial Nu_\theta}{\partial T_\infty}\right)^2 P_{T_\infty}^2 + \left(\frac{\partial Nu_\theta}{\partial T_s}\right)^2 P_{T_s}^2 + \left(\frac{\partial Nu_\theta}{\partial T_{ref}}\right)^2 P_{T_{ref}}^2 + \left(\frac{\partial Nu_\theta}{\partial P_\infty}\right)^2 P_{P_\infty}^2 + \left(\frac{\partial Nu_\theta}{\partial l}\right)^2 P_l^2 + \left(\frac{\partial Nu_\theta}{\partial D}\right)^2 P_D^2 + \left(\frac{\partial Nu_\theta}{\partial (\Delta r)}\right)^2 P_{\Delta r}^2$$

The precision limit of the experimental values and associated uncertainties for  $Ra = 1500$  is listed in Table I. The precision limit of  $\Delta r$  is related to the digitized interferogram readings of the radial fringes distance from the cylinder surface. The precision limits for universal gas constant, the Gladstone–Dale constant, the laser wave

length, and the fringe shifts have been neglected. The bias error for the thermocouples, pressure gage, voltmeter (80K-40 Fluke high voltage probe), microammeter, and micrometer was negligible because they had been calibrated. A Mach-Zehnder interferometer encounters various sources of bias errors including refraction errors in thermal boundary layer, misalignment of test section, and light distortion errors due to the test section end effects. The systematic errors,  $B_{Nu_\theta}$ , associated with the temperature gradient measurement using Mach-Zehnder interferometer are summarized in Table II.

Table. I Deviation of each quantity for computing local Nusselt number Eq. (5)

Measurement Parameter( $x_i$ )	$x_i$	$P_{x_i}$	$\frac{\partial Nu_\theta}{\partial x_i} \cdot \frac{P_{x_i}}{Nu_\theta}$
$T_\infty$	296.7 K	$\pm 0.1$ K	0.89%
$T_s$	318-367.8 K	$\pm 0.1$ K	0.89
$T_{ref}$	297.1 K	$\pm 0.1$ K	0.52%
$P_\infty$	87200 Pa	$\pm 100$ Pa	0.11%
$\phi_o$	12kV-17kV	$\pm 100$ V	-
$I_C$	0.5-12 $\mu$ A	$\pm 0.5 \mu$ A	-
$l$	160.1mm	$\pm 2 \times 10^{-5}$ m	0.01%
$D$	10mm	$\pm 2 \times 10^{-5}$ m	0.12%
$\Delta r$	0.24mm	$\pm 6.3 \times 10^{-5}$ m	4.8%*

\* maximum precision error at  $\theta = 0^\circ$  at  $\phi_o = 17.0$  kV

Table.II Bias Errors of Mach-Zehnder interferometer

Type of Bias Error	$B_{Nu}(\%)$
Refraction (Ref.[11])	0.07*
End effect [7]	1.67*
Misalignment [12]	0.4

\* Maximum errors at  $Ra = 5000$

The theory of the propagation of uncertainty ( $U_{Nu} = \sqrt{(P_{Nu}^2 + B_{Nu}^2)}$ ) was applied to evaluate the 95% confidence uncertainty of the local Nusselt numbers. The maximum uncertainty associated with the Rayleigh number, local Nusselt numbers, and average Nusselt numbers were estimated to be 3.73, 6.28, and 4.85% respectively.

## 2.5 Numerical Model

The free convection heat transfer in the presence of corona discharge is a multiphysics problem. The combination of buoyancy body force and corona-driven flow can potentially induce various flow patterns. Because the interferometric study only provides an interstitial temperature gradient, the numerical study was performed to find the flow pattern and further verify the experimental results. Commercial software COMSOL was used to solve the governing equations. The electric body force can be expressed as [13]:

$$\mathbf{f} = \rho_c \mathbf{E} - \frac{1}{2} |\mathbf{E}|^2 \nabla \epsilon_o + \frac{1}{2} \nabla \left[ |\mathbf{E}|^2 \rho \left( \frac{\partial \epsilon_o}{\partial \rho} \right)_T \right] \quad (7)$$

The first term on the right side of Eq.(7) is the electrophoretic, or Coulombic, force that results from the net free charges in gas. The second term, known as the dielectrophoretic force, arises from permittivity gradients. The last term is called the electrostrictive force and is important only for compressible fluids and two phase flows. The corona wind arises completely from the electrophoretic force term. The bulk flow is laminar and two dimensional. The buoyancy effect is estimated using the Boussinesq approximation. The governing equations are as follows [14]:

$$\nabla \cdot (\rho \mathbf{u}) = 0 \quad (8)$$

$$\nabla \cdot (\rho \mathbf{u} \mathbf{u}) = -\nabla p + \nu \nabla^2 \mathbf{u} + \mathbf{g} \beta (T - T_\infty) + \rho_c \mathbf{E} \quad (9)$$

$$\mathbf{u} \cdot \nabla T = \alpha \nabla^2 T + \frac{\rho_c b |\mathbf{E}|^2}{\rho C_p} \quad (10)$$

The second term on the right hand side is Joule heating heat source caused by ionic current.

The electric field around the sharp tip, which is responsible for the free ion generation, is distorted by the free charges in the ionized medium and is governed by Poisson's equation as:

$$\nabla \cdot \mathbf{E} = \nabla \cdot (-\nabla\phi) = \frac{\rho_c}{\varepsilon_0} \quad (11)$$

The generated ions are moved from the high voltage electrode toward the grounded surface through the electric force. The transport equation for conservation of ions is governed by:

$$\nabla \cdot \mathbf{J} = 0 \quad (12)$$

where current density is defined as:

$$\mathbf{J} = \rho_c b \mathbf{E} - D_i \nabla \rho_c \quad (13)$$

In the present work, the ion mobility and ion diffusion coefficient are assumed as  $b = 1.88 \times 10^{-4} \text{ m}^2 \text{V}^{-1} \text{s}^{-1}$  and  $D_i = 3.50 \times 10^{-5} \text{ m}^2 \text{s}^{-1}$ , respectively [14].

### 2.5.1 Boundary conditions

The 2D fluid flow was simulated using the steady Navier–Stokes equation in which the source terms are electric body force and buoyancy force and the cylinder was modeled as a no-slip and isothermal surface. A symmetry condition (zero normal gradient) was implemented along the vertical line of symmetry and the equations were solved for half of the domain. The far field was also modeled as a symmetry boundary condition and set at a height ten times the expected boundary layer thickness at the domain exit. Two common boundary conditions exist for the Poisson equation. A specified potential value (Dirichlet boundary condition) was used at the grounded electrode and the emitter



electrode. The cylinder electrode was grounded and modeled with a zero value, whereas the 15mm of the blade electrode, which was exposed to the air, was given the applied potential. The blade support was assumed to be insulating (Neumann boundary condition) due to the dielectric plexiglass used in the experiment. Although the real computational domain for electric field extends to infinity, truncating boundaries were considered in order to limit the computational domain. These artificial boundary conditions were set as zero normal electric field (Neumann boundary condition).

The charge transport equation was also simulated with two types of boundary conditions. Along the symmetry line, dielectric surface and truncating boundaries, normal current density was assumed to be zero and known space charge density for the blade electrode was assumed to be emitted from the tip of the electrode. The diffusive flux of the charge carrier assumed to be zero over the cylinder surface [29]. The microammeter readings were used to determine the total current flow across the cylinder surface for different applied voltages. The space charge assumption on the blade electrode updated and numerical total current flow integrated over the cylinder surface. The numerical total current compared with the microammeter readings and solution procedure continued until reaching the same numerical value.

Equations (8) to (12) were solved in a two-dimensional domain using the commercial finite element-based software COMSOL. The charge transport and Poisson's equations were solved using the general form PDE solver. The momentum and energy equations were solved with PDE general form solvers as well. The solution procedure was initiated by solving Poisson's equation for the electric field and the charge transport equation in order to determine the electric body force. Next, the momentum equation was solved considering the electric body force. The solution procedure was continued by the solution of the energy equation. The momentum equation was solved by considering the electric body force and buoyancy body force. An unstructured mesh was used with increased mesh densities in the area of the intense electric field around the blade tip and in the boundary layer region around the cylinder. In order to ensure that the numerical results are independent of the computational grid, a grid sensitivity analysis was performed. The

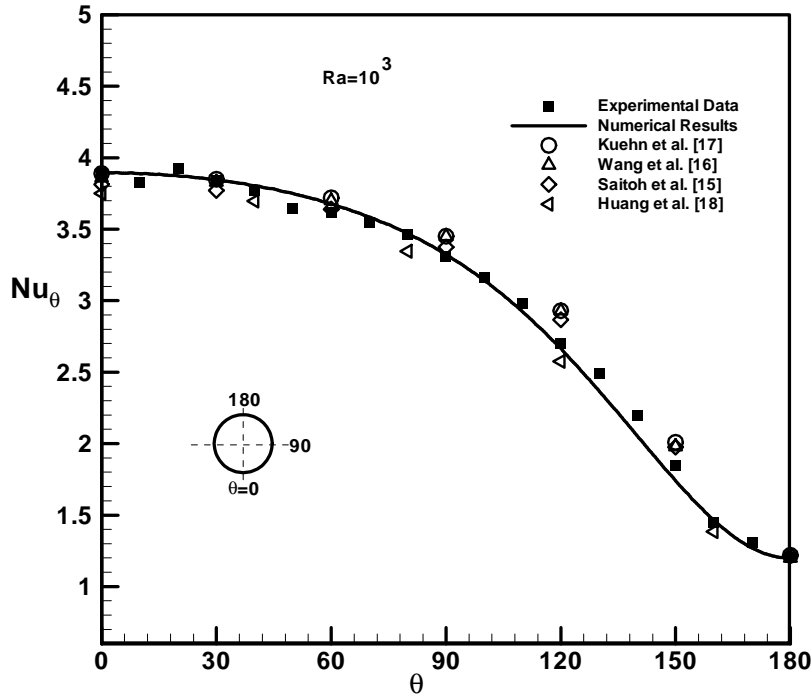
details of the grid sensitivity analysis in the extreme case ( $\phi_o = 17.0\text{kV}$ ,  $I = 10\mu\text{A}$  and  $Ra = 5000$ ) are given in the Table III.

Table.III Grid sensitivity analysis at  $\phi_o = 17.0\text{kV}$  and  $Ra = 5000$

Number of elements	$\overline{Nu}$	Percentage of change(abs)
4700	5.9522	2.4
10900	5.8118	0.02
14500	5.8109	0.0017
17320	5.8108	-

## 2.6 Results and discussion

In order to test the accuracy of the experimental results and the data reduction procedure, the local Nusselt numbers were obtained for an isothermal horizontal cylinder in absence of corona wind at  $Ra = 10^3$ . Furthermore, the computational results were reproduced for the same conditions. Fig.3 shows the comparison of the experimental and numerical local Nusselt numbers for the horizontal isothermal cylinder with previous works [15-18] at  $Ra = 10^3$ . Our experimental and computational results are in good agreement with previous studies showing a maximum difference of 5.6% and 5.3%, respectively. The numerical deviations fall well within the experimental uncertainty bands.



**Figure 3: Experimental and numerical local Nusselt number for the free convection heat transfer from the horizontal cylinder compared with other works [15,16,17,18] at  $Ra=1000$ .**

The numerical solution for the electric potential and the distribution of charges at  $\varphi_o = 17.0\text{kV}$ ,  $I = 10\mu\text{A}$  are shown in Fig. 4. The concentration of ions around the blade tip is highest, where the electric field is strongest.

Fig.5 represents the experimental results for the variation of the local Nusselt number around the cylinder in the absence and presence of the corona discharge at  $Ra = 1500$ . For further verification, the numerical results are also compared with the experimental data. The numerical local Nusselt numbers are in good agreement with experimental data at various applied voltages and show a maximum difference of 2.1%. By increasing the blade voltage from 0.0kV to 11.0 kV, no charge was injected to the air, the electrical current is negligible and no change in local Nusselt number occurs.

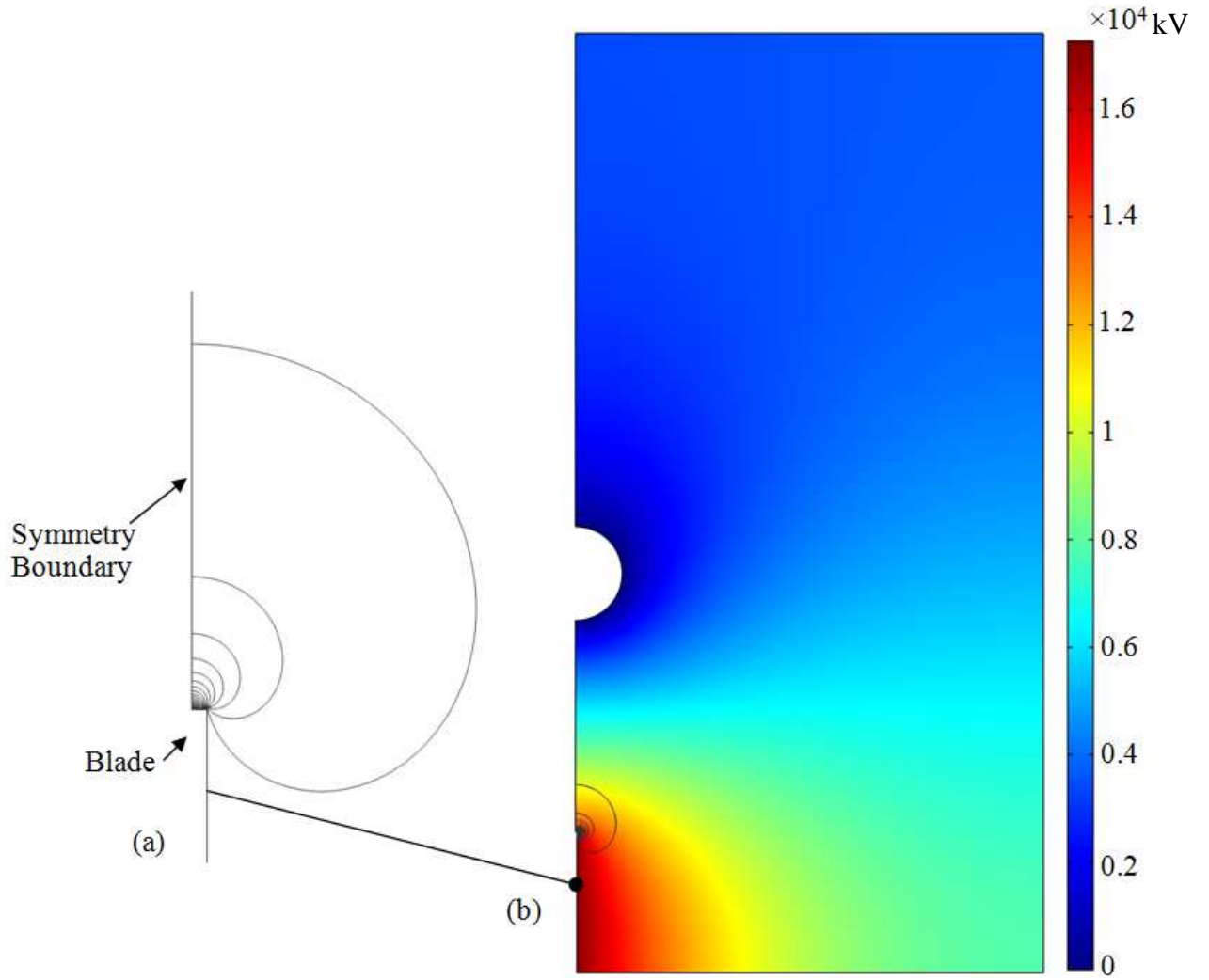


**Figure 4 (a): Numerical results for ion concentration (charge concentration difference between two adjacent lines is  $5 \times 10^{-7} \text{ C/m}^3$ ). and (b) electric potential in the blade-cylinder geometry at  $V_c = 17.0 \text{ kV}$ ,  $I = 10 \mu\text{A}$ .**

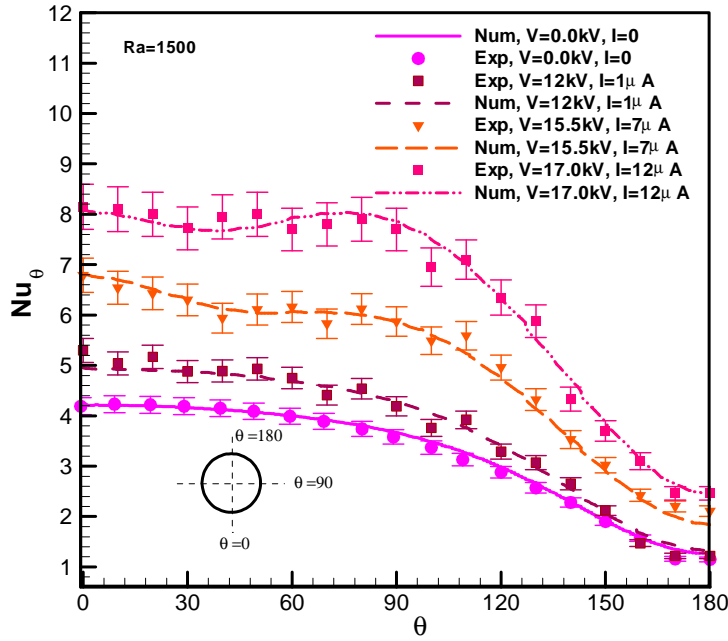


**Figure 5: Experimental and numerical local Nusselt number for the horizontal cylinder for various corona voltages at  $Ra=1500$ .**

When the blade electrode is supplied with 12.0kV, the corona discharge is initiated, which was confirmed by audible acoustic noise, and the measured current at this voltage was  $I_c = 1 \mu A$ . At the onset of corona discharge, corona-driven flow is established around the cylinder and caused the abrupt increment of local Nusselt number especially around the lower stagnation point ( $\theta = 0^\circ$ ). The enhancement of local Nusselt number at the onset of corona discharge is 23% for the lower stagnation point. Because the corona current is comparatively small at the onset of corona, the ionic wind does not have enough momentum to enhance the local Nusselt number around the upper stagnation point. As shown in Fig.2-b, it can be found qualitatively that there is no significant displacement of fringe toward the cylinder surface at  $\theta = 180$ . As depicted in Fig.5, the corona wind has a weak effect on temperature gradient at  $\theta > 150^\circ$ .

By increasing the voltage, the corona current increases. The increment of corona current results in stronger ionic wind and higher heat transfer rate; this enhancement can be seen

in all peripheral positions around the cylinder. For example, for  $Ra = 1500$  and  $\phi_o = 17.0\text{kV}$ , the enhancement of local Nusselt number at  $\theta = 180^\circ$  is 78% as compared with the free convection.

In the high electric field region, the space charge concentration can generate intense electric body force. However, at voltages around  $\phi = 15.5\text{kV}$  and  $I = 7\mu\text{A}$ , a small local decrease in local Nusselt number occurs around  $\theta = 30^\circ$ , near the lower stagnation point. By increasing the voltage to  $\phi_o = 17.0\text{kV}$  and current to  $I = 12\mu\text{A}$ , this reduction in local cooling becomes greater. The numerical results predict the same local decrease in local Nusselt number around  $\theta = 30^\circ$ . In order to understand this local reduction of the Nusselt number around the lower stagnation point, detailed information of the flow pattern is useful.

Fig.6 shows the numerical results for the streamline patterns and isotherms around the cylinder for  $Ra = 1500$  at  $\phi_o = 12.0\text{kV}$  and  $17.0\text{kV}$ . As seen in this figure, at  $\phi_o = 12.0\text{kV}$  and  $I = 1\mu\text{A}$  the flow pattern around the cylinder remains streamwise. However, for voltages above the  $\phi_o = 15.5\text{kV}$  and  $I = 6\mu\text{A}$ , the electric body force becomes strong enough to produce high velocity gradients near the blade. This strong velocity gradient results in a recirculation zone establishing below the cylinder. The recirculation zone causes an insufficient entrainment of the cool fresh air into the thermal boundary layer at  $0^\circ < \theta < 80^\circ$  and results a decrease in local Nusselt number at the same location. Stronger recirculation is produced by higher corona current. Therefore, a greater local decrease in Nusselt number near the lower stagnation point is expected at higher corona currents. As shown in Fig.2-c, the visual effect of recirculation zone and its impact on the last fringe can be qualitatively recognized for  $\phi = 15.5\text{kV}$  and  $17.0\text{kV}$  at  $Ra = 1500$ .

In order to investigate the corona wind effects at higher  $Ra$  numbers, the results of experimental and numerical investigations for  $Ra = 5000$  are presented in Fig. 7. A similar trend in the variation of local Nusselt numbers can be seen as in Fig.6. For  $Ra = 5000$ , the enhancement of heat transfer at lower stagnation point for  $\phi_o = 17.0\text{kV}$ ,  $I = 10\mu\text{A}$  is only 10% less than the enhancement of heat transfer at  $Ra = 1500$ . In

contrast, the local Nusselt number at the upper stagnation point at  $Ra = 5000$  and  $\varphi_o = 17.0\text{kV}$  shows the enhancement 200% less than that of  $Ra = 1500$ .

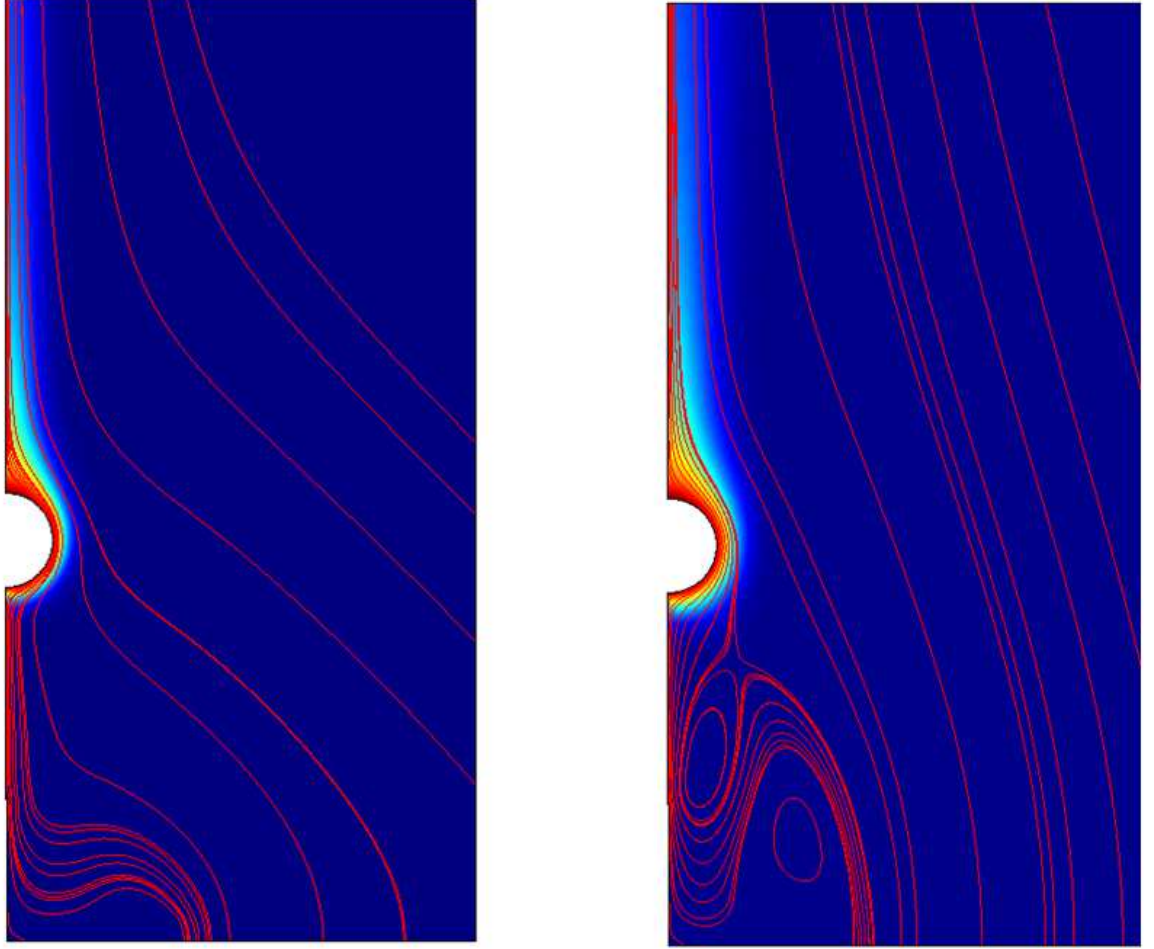


**Figure 6: Numerical results for isotherms and streamlines for  $Ra=1500$  at  $V_c = 12.0\text{kV}$  and  $17.0\text{kV}$ .**

The comparatively small enhancement of the local Nusselt number at  $Ra = 5000$  with respect to the  $Ra = 1500$  is mainly due to the dominance of buoyancy-driven flow regime around the cylinder over the corona wind driven flow at higher  $Ra$  numbers.

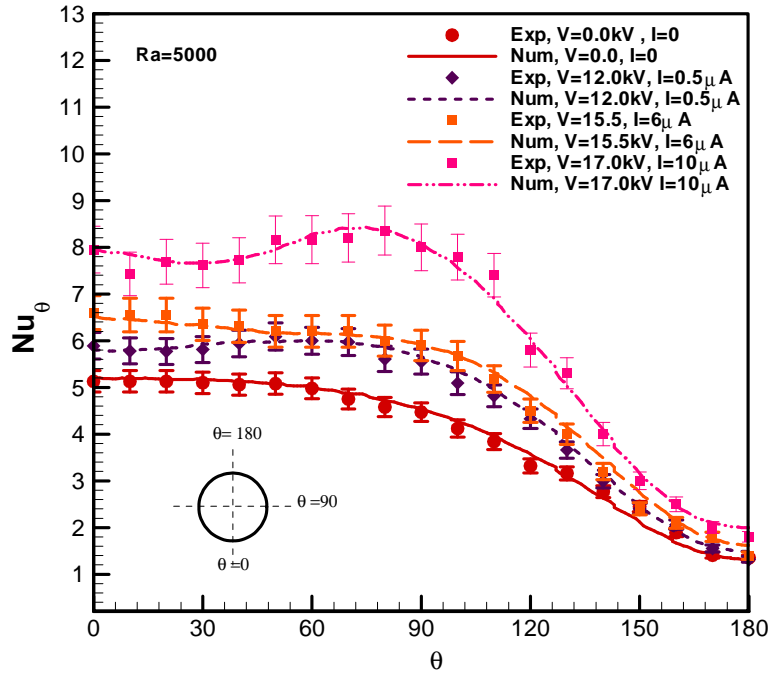


**Figure 7: Experimental and numerical local Nusselt number for the horizontal cylinder for various corona voltages at  $Ra=5000$ .**

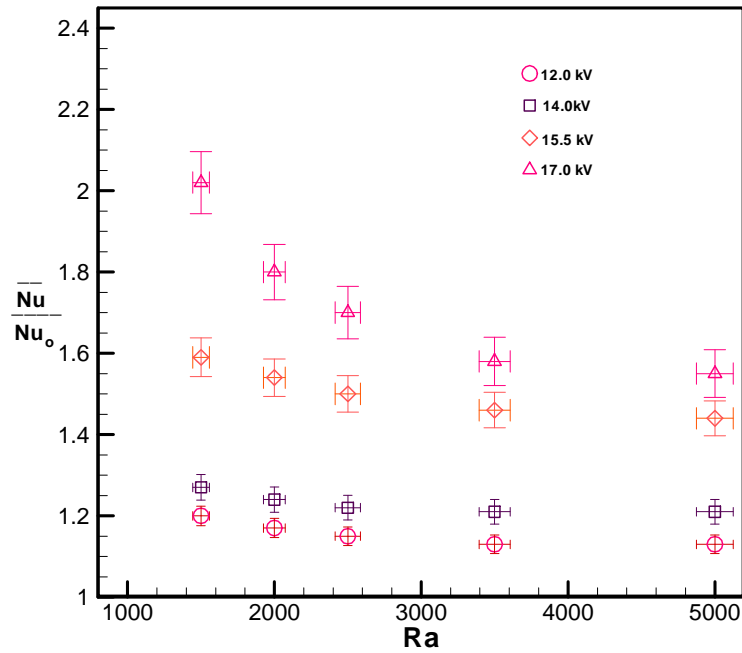


**Figure 8: Experimental results for the average Nusselt number enhancement of heat transfer at various applied voltages**



Fig. 8 shows the variation of average Nusselt numbers versus  $Ra$  for different corona discharge voltages. It should be noted that for higher  $Ra$  numbers, the EHD effect on the average Nusselt number decreases at the same corona voltage and spacing. At higher  $Ra$  numbers, buoyancy-driven flow becomes stronger compared to corona-driven flow. Therefore, the trend of average Nusselt number enhancement versus  $Ra$  for a specific applied voltage is a decreasing function. The maximum enhancement of the average Nusselt number around the cylinder occurs at the lowest  $Ra$  number ( $Ra = 1500$ ) and 17kV applied voltage. As expected, at a specific voltage the average Nusselt number is a decreasing function of the  $Ra$ . By increasing the applied voltage, the slope of average Nusselt function becomes steeper because the electric body force decreases for higher  $Ra$  numbers. The observations showed that the electric body force is affected by the temperature field around the heated cylinder. The  $V$ - $I$  characteristics for  $Ra = 0$ ,  $Ra = 1500$ , and  $Ra = 5000$  are shown in Fig.9.

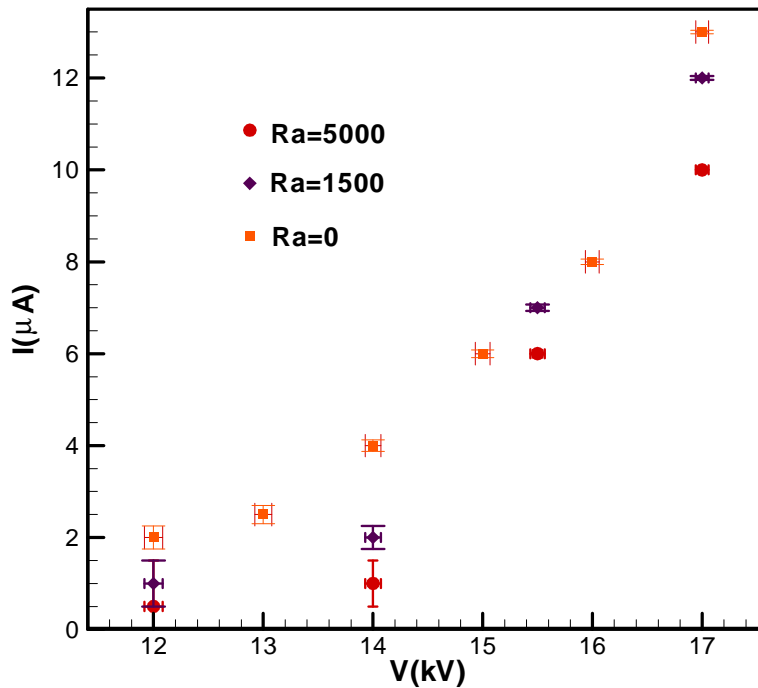


**Figure 9:  $V$ - $I$  characteristic diagram for blade-cylinder geometry with 40 mm spacing at different  $Ra$  numbers.**

The thermal effect causes the change in the trend of the  $V-I$  characteristics at different Rayleigh numbers. For example, at  $Ra = 5000$  and  $\phi_o = 15.5\text{kV}$ , the discharge current is 15% less than that of  $Ra = 1500$ . This may be attributed to the ion mobility temperature dependence. Ion mobility and current density decrease with increasing the surface temperature of the ground electrode [19]. In other words, the thermal effect reduces the current density, the corona power consumption, the electric body force, and local Nusselt number enhancements for a specific corona voltage.

The effect of Joule heating is numerically investigated through considering the source term in the energy equation. The numerical results show that the effect of Joule heating does not cause temperature increments of air temperature around the intense electric field zone. It is mainly because of the relatively low level of current density, which is unable to produce significant thermal effects in surrounding air. At higher  $Ra$  numbers, the effect of Joule heating inside the thermal boundary layer becomes even less important because the electrical conductivity of air is inversely proportional to the temperature.

According to the results presented in this paper, the enhancement of heat transfer through the corona discharge is stronger for lower  $Ra$  numbers and a decreasing function of  $Ra$  number. At a specific voltage with a fixed spacing between electrodes, a recirculation zone, which is created by the electric body force, causes the local decrease in heat transfer from the cylinder. By increasing the corona voltage, the stronger recirculation zone is generated and causes a larger local decrease in heat transfer rate. Systematic study is needed to find the optimum electrode spacing and the applied voltage in the various ranges of  $Ra$  numbers for single or array of cylinder. This knowledge can be implemented for high performance ionic heat exchanger design.

## Nomenclature

$b$	Ion mobility ( $\text{m}^2\text{V}^{-1}\text{s}^{-1}$ )
$C$	Gladstone–Dale coefficient ( $\text{m}^{-3}\text{Kg}^{-1}$ )
$C_p$	Specific heat ( $\text{J Kg}^{-1}\text{K}^{-1}$ )
$D$	Diameter of cylinder (m)
$D_i$	Ion diffusion coefficient ( $\text{m}^2\text{s}^{-1}$ )
$E$	Electric field ( $\text{V m}^{-1}$ )
$f$	Electric body force ( $\text{N m}^{-3}$ )
$g$	Gravitational acceleration ( $\text{m s}^{-2}$ )
$h$	Heat transfer coefficient ( $\text{W m}^{-2}\text{K}^{-1}$ )
$I_c$	Corona current (A)
$J$	Current density ( $\text{A m}^{-2}$ )
$k_f$	Thermal conductivity ( $\text{W m}^{-1}\text{K}^{-1}$ )
$l$	Length of cylinder (m)
$Nu$	Nusselt Number
$P$	Pressure (Pa)
$r$	Radial distance from the cylinder surface (m)
$R_o$	Gas constant ( $\text{J Kg}^{-1}\text{K}^{-1}$ )

$Ra$	Conventional Rayleigh number based on temperature, $g\beta(T_s - T_\infty)D^3/\nu\alpha$
$T$	Temperature (K)
$\mathbf{u}$	Velocity field vector ( $\text{m s}^{-1}$ )

### **Greek symbols**

$\alpha$	Thermal diffusivity ( $\text{m}^2\text{s}^{-1}$ )
$\beta$	Volumetric thermal expansion coefficient ( $\text{K}^{-1}$ )
$\varepsilon$	Shift fringe
$\varepsilon_o$	Vacuum permittivity $\approx$ air permittivity ( $\text{A s V}^{-1}\text{m}^{-1}$ )
$\varphi$	Electric potential (V)
$\varphi_o$	Voltage applied to corona electrode (V)
$\lambda$	Laser wave length (m)
$\rho$	Air density ( $\text{Kg m}^{-3}$ )
$\rho_c$	Charge density ( $\text{C m}^{-3}$ )
$\sigma$	Electrical conductivity ( $\Omega^{-1}\text{m}^{-1}$ )
$\nu$	Kinematic viscosity ( $\text{m}^2\text{s}^{-1}$ )

### **Subscripts**

$S$	Referred to surface
$\theta$	Referred to periphery angle
$\infty$	Referred to infinite medium

## References

- [1] S.M. Marco, H.R. Velkoff, Effect of electrostatic field on free convection heat transfer from flat plates, ASME Paper (1963) No.63-HT-9.
- [2] A. Yabe, Y. Mori, K. Hijitata, EHD study of the corona wind between wire and plate electrodes, AIAA Journal 16-4 (1978) 340-345.
- [3] J. O'Brien, A.J.Shine, Some effects of an electric field on heat transfer from a vertical plate in free convection, Journal of Heat Transfer February (1967) pp.114-116.
- [4] M.E Franke, L.E Hogue, Electrostatic cooling of a horizontal cylinder, Transaction of ASME 113 (1991) 544-548.
- [5] B.L. Owsenek, J. Seyed-Yagoobi, and R.H. Page, Experimental investigation of corona wind heat transfer enhancement with a heated horizontal flat plate, Journal of Heat Transfer 177 (1995) 309-315.
- [6] B.L. Owsenek, J. Seyed-Yagoobi, Theoretical and experimental study of electrohydrodynamic heat transfer enhancement through wire-plate corona discharge, Transaction of the ASME 119 (1997) 604-610.
- [7] M.E. Franke, Effect of vortices induced by corona wind discharge on free-convection heat transfer from vertical plate, Journal of Heat Transfer (1969) No.68-WA/HT-9.
- [8] E.R.G. Eckert, R.J. Goldstein, Measurements in Heat Transfer, McGraw-Hill, New York, 1972.
- [9] W. Hauf, U. Grigull, Optical methods in heat transfer, Advances in Heat Transfer, vol. 6, Academic Press, New York, 1970, p.133–366.
- [10] R.J.Moffat, Using uncertainty analysis in the planning of an experiment, ASME Journal of Fluids Engineering 107 (1985) 173-178.

- [11] J. M. Mehta and W. Z. Black, Errors associated with interferometric measurement of convective heat transfer coefficients, 16-6 (1977) 1720-1726.
- [12] R. D. Flack, Mach-Zehnder interferometer errors resulting from test section misalignment, Applied Optics, 17 (1978) 985-987.
- [13] W.K.H Panofsky, M. Phillips, Classical Electricity and Magnetism, Addison-Wesley, 1962, p.1-119.
- [14] J.R. Melcher, Continuum Electromechanics, Cambridge, MIT press, 1981, chap.3 and 10.
- [15] T. Saitoh, T. Sajiki, K. Maruhara, Bench mark solution to natural convection heat transfer problem around the horizontal circular cylinder, Int. J. of Heat and Mass Transfer 36 (1993) 1251–1259.
- [16] P. Wang, R. Kahawita, T.H. Nguyen, Numerical computation of the natural convection flow about a horizontal cylinder using splines, Numerical Heat Transfer 17 (1990) 191–215.
- [17] T.H. Kuehn, R.J. Goldstein, Numerical solution to the Navier-Stokes equation for laminar natural convection about a horizontal isothermal circular cylinder, International Journal of Heat and Mass Transfer 23 (1980) 971-979.
- [18] S.Y. Huang, F. Mayinger, Heat transfer with natural convection elliptic tubes, Wärme-und Stoffubertagung 18 (1984) 175-183.
- [19] J-S. Chang, F. Pontiga, P. Atten and A. Castellanos, Hysteresis effect of corona discharge in a narrow coaxial wire-pipe discharge tube with gas flow, IEEE Transactions on Industry Applications (1996) 1250-1256.
- [20] S. Wangnipparnto , J. Tiansuwan, S. Jiracheewanun, T. Kiatsiriroat, C. Wang, Air side performance of thermosyphon heat exchanger in low Reynolds number region: with and without electric field, Energy Conversion and Management 43 (2002) 1791–1800.

- [21] S. Vithayasai, T. Kiatsiriroat, A. Nuntaphan, Effect of electric field on heat transfer performance of automobile radiator at low frontal air velocity, *Applied Thermal Engineering* 26 (2006) 2073–2078.
- [22] H. Kalman, E. Sher, Enhancement of heat transfer by means of a corona wind created by a wire electrode and confined wings assembly, *Applied Thermal Engineering* 21 (2001) 265-282.
- [23] A. Rashkovan, E. Sher, H. Kalman, Experimental optimization of an electric blower by corona wind, *Applied Thermal Engineering* 22 (2002) 1587–1599.
- [24] Y. Yonggang, H. Junping, AI. Zhongliang, Y. Lanjun, A. Qiaogen, Experimental Studies of the Enhanced Heat Transfer from a Heating Vertical Flat Plate by Ionic Wind, *Plasma Science & Technology* 8-6 (2006) 697-700.
- [25] T. Kohya, M. Kuriyama, M. Toda, E. Harada, H. Konno, Heat transfer from horizontal, parallel tube banks under a corona discharge, *International Chemical Engineering* 27 (2) (1989) 319–325.
- [26] T. Kuriyama, E. Harada, H. Konno, Application of corona wind to practical tubular heat exchangers, *Heat Transfer—Japanese Research* 18 (4) (1989) 1–8.
- [27] T. Kuriyama, E. Harada, H. Konno, Enhancement of heat transfer from horizontal tube-banks by the use of a corona wind, *International Chemical Engineering* 29 (4) (1989) 715–721.
- [28] M. Ashjaee, A.H. Eshtiaghi, M. Yaghoubi, T. Yousefi, Experimental investigation on free convection from a horizontal cylinder beneath an adiabatic ceiling, *Experimental Thermal and Fluid Science* 32 (2007) 614–623.
- [29] J. Q. Feng, Application of Galerkin finite-element method with Newton iterations in computing steady-state solutions of unipolar charge currents in corona devices, *Journal of Computational Physics* 151(1999) pp.969–989.

- [30] J.H. Davidson, E.J. Shaughnessy, Turbulence generation by electric body forces, *Experiments in Fluids*, 4(1) (1986), pp.17-26.
- [31] L. Leger, E. Moreau, G.G. Touchard, Effect of a DC corona electrical discharge on the airflow along a flat plate, *IEEE Transactions on Industry Applications*, 38(6) (2002), pp.1478-1485.
- [32] P. Atten, F.M.J. Mccluskey, A. Lahjomri, The electrohydrodynamic origin of turbulence in electrostatic precipitators, *IEEE Transactions on Industry Application*, 23(4) (1987), pp.705-711.
- [33] J.H. Davidson, P.J. McKinney, Turbulent mixing in a barbed plate-to-plate electrostatic precipitators, *Atmospheric Environment*, 23(10) pp.2093-2107.
- [34] A. Soldati, S. Banerjee, Turbulence modification by large-scale organized electrohydrodynamic flows, *Physics of Fluids* 10(7) (1998), pp.1742-1756.
- [35] M.M. Ohadi, D.A. Nelson, S. Zia, Heat transfer enhancement of laminar and turbulent pipe flow via corona discharge, *International Journal of Heat and Mass Transfer*, 34(4-5) (1991), pp.1175-1187.
- [36] A.S. Mitchell, L.E. Williams, Heat transfer by the corona wind impinging on a flat surface, *Journal of Electrostatics*, 5 (1978), pp.309-324.



## Chapter 3

# Two-phase cooling characteristics of mono-dispersed droplets impacted on an upward-facing heated disk

### 3.1 Introduction

Dramatic shrinking in the dimensions of electronic devices results in high speed operation but is accompanied by higher density heat generation. Thermal management of these devices is an important limiting design factor for further size reduction. High density heat generation at relatively low temperatures (for silicon carbide devices typically  $150 \text{ W/cm}^2$  at reliable operation temperature of about  $150^\circ\text{C}$ ) can be dissipated by applying high performance phase-change based techniques. Recently, spray cooling and mono-dispersed droplet cooling have been proven to be efficient methods for high heat dissipation at low surface temperature superheats using only a few hundred *cc/min* of the coolant. As an important advantage, using a small volume of the coolant reduces considerably the size of cooling circuit elements, such as the circulation pump and condenser.

Two-phase droplet cooling uses latent heat to dissipate extremely high heat fluxes at relatively low temperature differences. Since the vapor is not trapped by the pool of liquid and can be easily released, the amount of heat transferred by the stream of atomized or mono-dispersed droplets (MDSD) impacted on a heated surface is higher than the pool boiling. The droplets are evaporated and replaced by fresh droplets, so that the heated surface remains at relatively uniform low superheat temperatures. Heat fluxes as much as  $1000 \text{ W/cm}^2$  and  $300 \text{ W/cm}^2$  at low superheats (typical superheat at CHF for water is about  $30^\circ\text{C}$ ) can be removed by atomized droplets (sprays) and MDSD, respectively. Spray cooling techniques dissipate higher heat transfer rates, but typically operate at higher pressures ( $1.5\text{-}4 \text{ atm}$ ) and higher mass flow rates ( $100 \text{ cc/min}$ ).

Eliminating the need for bulky pumps makes the MDSD suitable for a number of applications with moderate thermal loads between the pool boiling and spray cooling heat removal range. However, MDSD cooling introduces additional complexities such as droplet generation reproducibility, complex droplet impact dynamics, and stabilization of liquid film over the heated surface.

Due to the high heat flux removal at relatively uniform low superheats droplet cooling has been a subject of many investigations and has been found suitable for a number of applications [1-10]. However, comparing the MDSD cooling and spray cooling method through the literature, spray cooling has been studied more extensively [20-24]. A comprehensive review of the spray cooling technique can be found in several publications [5, 25]. In the MDSD cooling technique, a free falling stream of droplets can be produced by forcing the coolant through a capillary tube. The droplets are generated by gravity-surface tension interaction or other external actuators, such as ultrasonic devices, and deposited on the heated surface. The axial momentum of the falling droplets converts to the radial momentum due to the initial kinetic energy; the droplets spread over the heated surface and create a film of coolant. At a low range of impact Weber numbers ( $We < 20$ ), the deformation of impacted droplets results in a continuum film of liquid, while at higher range of Weber numbers the impacted droplets break up to tiny fragments [14,15]. The thin film of coolant heats up quickly during the early stages of the spreading process, dominantly due to the conduction mechanism, and the heat transfer rapidly enters to nucleation boiling. High amounts of heat flux are removed due to the phase change process. The rate of heat transfer is determined by the film spreading characteristics, which depend on several parameters related to the droplet/target interactions such as: impact velocity [31], initial size of the droplet, frequency of impact, surface temperature, surface wettability [30] and roughness [15], heated surface material properties and the operating pressure.

High speed photographic analysis of impact droplet boiling provides better understanding of the relationship between the spreading dynamics, phase change phenomenon and dry-out initiation at CHF Regime. A good historical review for high speed photographic studies of pool boiling, flow boiling, and droplet impact boiling can be found in the work

of Kandlikar and Steinke [26]. Early photographic investigations by Chandra and Avedisian [27, 28] reveal that droplet dynamic contact angle determines the initiation of critical heat flux regime. When the surface temperature increases, the dynamic contact angle increases significantly during the spreading process due to the rapid evaporation of the liquid around the solid-liquid and vapor interface around the droplet edge. The study of the dynamic contact angle variation during the spreading process and its effect on the maximum spreading ratio and critical heat flux initiation was continued by Kandlikar and Steinke [29]. It was found that the curl back phenomenon, which was reported previously by Chandra and Avedisian [27, 28], profoundly affects the maximum spreading ratio and it is responsible for critical heat flux initiation. Bernardin et al. [14] used high speed photographic techniques to investigate the pattern showing the impact behavior of water droplets on a hot aluminum plate with surface temperature ranging from 100 to 280 °C. Droplet impact velocity and surface temperature were found to be important parameters governing both impact behavior and the heat transfer process. These authors identified four different boiling regimes: film boiling, transition boiling, nucleate boiling, and film evaporation through matching the sequential photographs corresponding to the heat transfer measurements. As an important result, the temperature corresponding to the critical heat flux and Leidenfrost point showed little sensitivity to both droplet impact velocity and frequency in the range of their experimental parameter.

Several early experimental investigations were performed to characterize the maximum heat flux dissipated by the MDSD technique as a function of relevant parameters and various non-dimensional numbers. Watchters and Westerling [9] suggested that the Weber number, a measure to compare the strength of the inertia force and surface tension, has significant importance in characterizing the droplet impact heat transfer process. McGinnis and Holman [8] developed a correlation for normalized CHF based on the modified Weber number. They introduced the ratio of liquid and vapor density in the standard Weber number definition at the film temperature. Their correlation could predict normalized CHF based on the modified Weber number. Sawyer et al. [3, 10] reviewed the experimental study on liquid jets conducted by Monde and Inoue [4] and hypothesized that, due to the analogy between impingement jet and droplet cooling, the CHF can be determined by referring to the standard definition of Weber number and

Strouhal number. In order to examine their hypothesis, a complex fluid delivery system was developed and the dripping parameters such as droplet size, impact velocity and frequency were varied independently. After many sets of experiments, they concluded that although the Weber number is the primary parameter which affects CHF, the droplet impact frequency might be taken into account as a secondary relevant parameter. The Strouhal number,  $(f d_p / V)$ , along with a standard form of Weber number,  $(\rho_L V^2 d_p / \sigma)$ , were found to be essential parameters for determining the CHF. The experimental CHFs for various cases were modified based on the total area initially wetted. The Kurabayashi–Yang correlation [32] was used to predict the maximum spreading ratio of the impacted droplet,  $\beta$ . A correlation for the modified CHF was proposed for the range of Weber number ( $175 < We < 730$ ) and Strouhal number ( $7 \times 10^{-3} < St < 3 \times 10^{-2}$ ). They also continued the study and proposed an empirical correlation of adjusted CHF (based on the K-Y spreading ratio correlation) [1] for MDSD cooling using the same dimensionless numbers as in Halvorson’s experimental data [6, 7]. The range of experimental Weber and Strouhal numbers in [6,7] ( $55 < We < 109$  and  $1.9 \times 10^{-3} < St < 3.7 \times 10^{-2}$ ) was well below the range of Sawyer’s correlation applicability. They concluded that the Sawyer’s correlation is not applicable for low Weber number droplet cooling. Ignoring the uncertainty of K-Y correlation in modified CHF calculation at low Weber numbers, the difference between two correlations was reported due to the different spreading mechanism (droplet fragmentation) at higher impact velocity and high Weber number regime. It should be highlighted here that the K-Y correlation provides the best agreement among several other similar analytical expressions, which were derived from energy balance equation [11], however, it overestimates the maximum spreading ratio, especially at lower Weber numbers [2] (for instance,  $\sim +70\%$  at  $We=10$  and  $\sim +40\%$  at  $We=58$ ). Since the wetted area is proportional to  $\beta^2$ , the  $\beta$ -calculation using the K-Y correlation leads to significant errors (by the factor of  $\sim 1.5$ -2) in the modified CHF calculation.

Although several empirical CHF correlations have been proposed in the literature for mono-dispersed droplet cooling, they are not applicable for low Weber numbers ( $< 50$ ) [3,7,10]. The various authors frequently used complicated external sources to control the

droplet parameters, which make their result reproducibility difficult or even impossible. Moreover, two complications regarding the previous experimental setup design [6], which will be discussed in results and discussion section, motivated the authors to revise the previous experimental setup and revisit the mono-dispersed droplet cooling problem experimentally. This paper aims to investigate the two-phase characteristics of free-falling MDSD impact on smooth upward-facing horizontal heated surface at the range of low Weber numbers  $3 < We < 100$  and Strouhal numbers  $1.81 \times 10^{-3} < St < 3.86 \times 10^{-2}$ . The droplets were generated by a natural formation-breakup mechanism due to the gravity and surface tension interaction. The impact velocity of the droplets, their size and frequency were varied by changing the capillary size, the spacing between the capillary and heated surface, and varying the volumetric flux, respectively. Deionised water was chosen as the working fluid and the experiments were conducted at atmospheric pressure. The time-averaged boiling curves were obtained up to the CHF-regime for various droplet parameters. In order to predict the experimental results for average CHF, two separate correlations based on the relevant dimensionless numbers were developed.

### 3.2 Experimental setup and procedure

The experimental setup was designed to investigate the heat transfer from a horizontal, upward-facing, heated surface impacted by a stream of mono-dispersed water droplets of different sizes, impact velocities and impact frequencies. The experimental apparatus consisted of three major components, (I) heat surface, (II) measurement system and instrumentation (III) for fluid delivery system. The schematic diagram of the experimental circuit is presented in Fig.1-a. The circular heat transfer surface is a tapered base of nickel-plated heated cylinder. The heated cylinder was made of copper, coated with a protective layer of 30 micron nickel. The heat transfer surface was fully polished and coated with an additional layer of 25 micron nickel. Surface measurement after the coating process showed its arithmetic average roughness was less than 200 nm. Four identical cavities were drilled in the cylinder and four identical 300 W-cartridge WATLOW heaters were inserted axially into the cavities, connected in parallel and supplied with a programmable power supply (QuadTech Model: 42000). The upper end of the heated cylinder was tapered to a smaller diameter (8 mm) to increase surface heat

flux and instrumented with 12 calibrated K-type thermocouples with a 0.25 mm bead (Omega K-type thermocouples 0.25 mm- 5SRTC series Kapton®). The thermocouples were embedded in the neck of the heat transfer surface and fixed using a mixture of ultrafine copper powder and high thermal conductive adhesive epoxy (OMEGABOND 200®). The thermal conductivity of copper at saturation temperature was used in the present work (395 W/m.K). A linear function for variation of thermal conductivity of copper was used to estimate the thermal conductivity of copper at higher temperatures. The decrease in thermal conductivity is  $\sim 3$  W/m.K at  $T_s=130$  °C. The heated cylinder was inserted into a Teflon block to minimize the heat losses. Extra slag wool with thermal conductivity  $\sim 0.04$  W/m.K was used in the neck region to reduce the radial heat transfer.

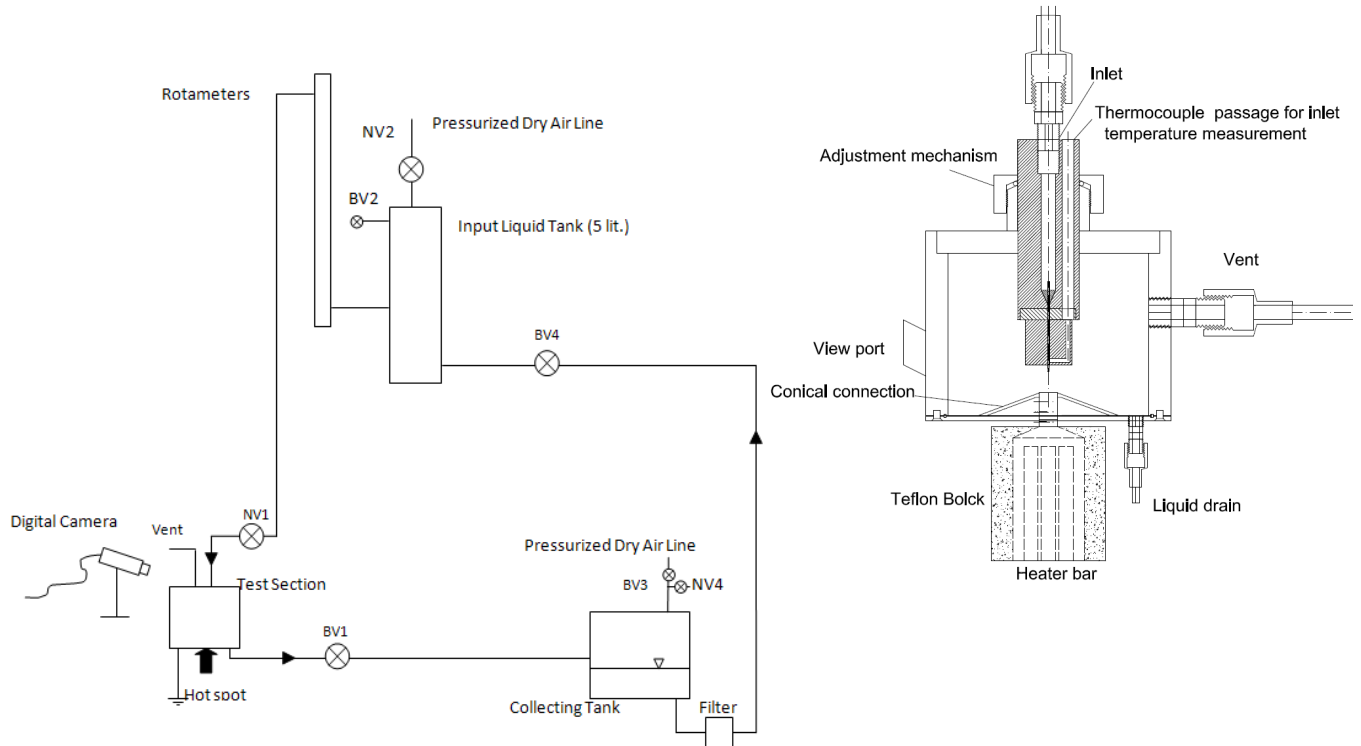


**Figure 1-a: Schematics of experimental setup**

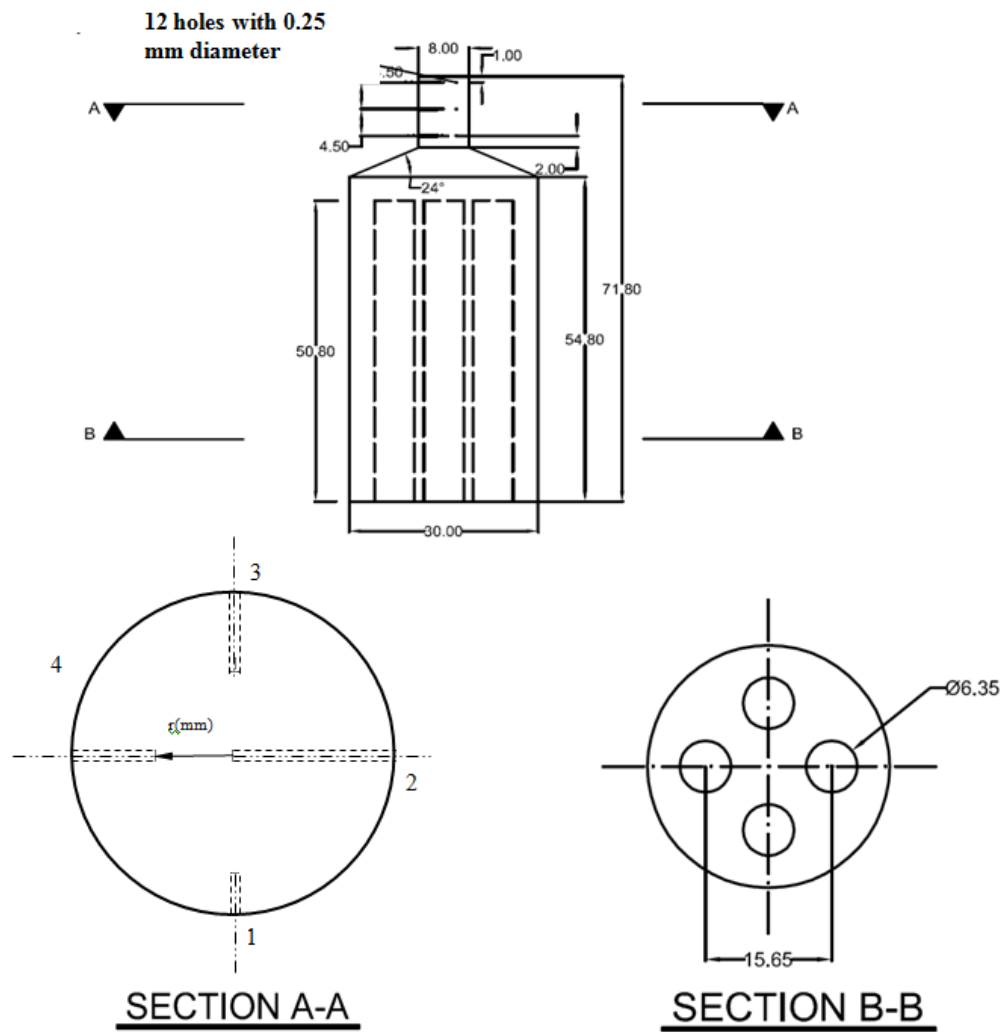


**Figure 1-b: Details of heater bar and thermocouple locations (dimensions in mm)**

The heated surface was fitted to a truncated Teflon ring to seal the neck of the heat transfer surface and to direct the excess liquid to the drain. The rim of the impacted surface was insulated using a conical ceramic connection and sealed with a thin strip of a high temperature resistant silicone rubber. An adjustable holder was used to precisely align the heated surface in  $x$ - $y$ - $z$  direction. The details of heater bar and thermocouple location are presented in Fig.1-b.

In order to examine the uniformity of temperature over the heated surface at different levels and to allow accurate heat flux calculation, the 12 calibrated thermocouples (Omega K-type thermocouples 0.25 mm- 5SRTC series Kapton®) were placed at three different levels and in four different radial depths and peripheral angles using a 16-channel data acquisition system NI-DAQ 9213. A LABVIEW code was developed to calculate the heat flux and surface temperature measurements from the thermocouple readings. The local heat flux was calculated from 1-D steady state Fourier's law of conduction for the cylinder neck at four different peripheral angles at different radial distances. The detailed locations of thermocouple junctions are presented in Fig.1-b. The local heat flux variations measured at four different locations never exceeded 2% of measured value. The surface temperature was obtained by real time linear extrapolation of thermocouple readings. The surface temperature variation calculated at different peripheral angles showed typically less than 0.5% variation. At high superheats and pre-CHF, the boiling curve fluctuates due to the transient boiling regime and it depends on the mass flow rate and the impact velocity. Polynomial curves were fitted to this portion to interpolate the maximum heat transfer and its corresponding superheat. The liquid volumetric flux was measured using calibrated rotameters. The frequency and size of droplets were obtained using high-speed video recording along with time-dependent frame-shot capturing software.

Figure 2 shows the variation of the generated droplet as a function of capillary size at different volumetric flow rates. Decreasing capillary diameters at a given volumetric flow rate resulted in decreasing droplet diameters. Reduced initial droplet diameter, impacting a heated surface at a given velocity, creates a thinner liquid film with reduced maximum spreading ratios. Since the area of the surface wetted by the stream of droplets can be controlled by volumetric flow rate, initial size of the droplets and capillary size, the range of these experimental parameters was chosen to maximize the wetted area for all test cases. Selecting the range between 1 and 4.8 cc/min and choosing capillaries ranged between 17 and 21g, the smallest measured wetted area for stream of droplets generated by a 17g needle was 96% of the heated surface area. For the narrowest capillaries (21g) and at the lowest impact velocities, 0.28 m/s, the dry area of the disk was measured to be less than 17% at the lowest volumetric flow rate 1 cc/min. It was



observed that the average surface temperature variation for all thermocouple readings adjacent to the surface was below 1%. Therefore, the average heat flux is presented based on the entire heated surface area.

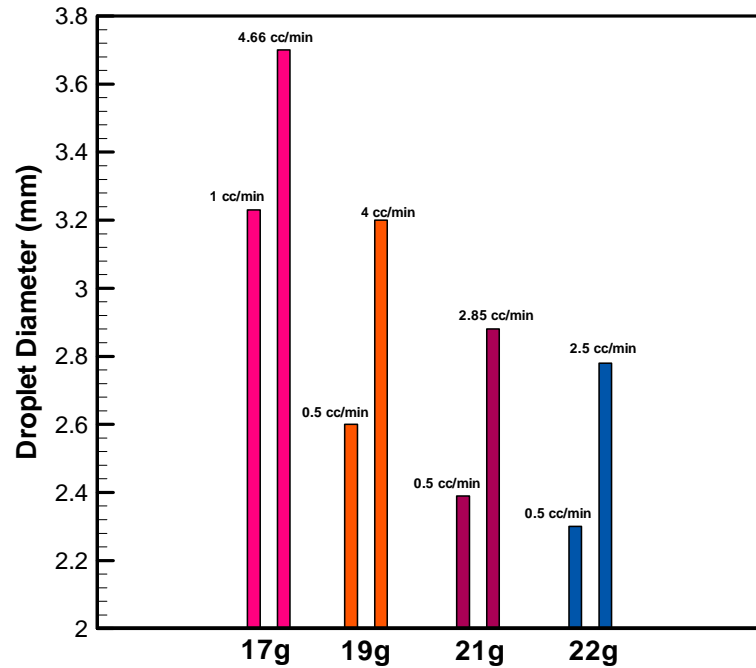


**Figure 2: Droplet size variation using different hypodermic needle gauges at different volumetric flow rates.**

The fluid delivery system consisted of a recycling circuit with the following components: hydrostatic pressurized acrylic reservoir, acrylic vessel, nozzle cartridge, standard hypodermic needles ranged from 17g to 22g and fine thread needle valves. The liquid was forced by pressurizing the reservoir and directed to the nozzle cartridge, and the hypodermic needle was positioned above the heated surface. The needles were insulated with a 10-*mm* in diameter Teflon cylinder to minimize the heat transfer due to the condensation of the hot vapor generated in the test section. A thermocouple was inserted into the Teflon block and fixed at the needle wall 2-*mm* away from its tip to measure the inlet coolant temperature. The nozzle cartridge was equipped with a universal fitting to readily mount various capillaries centered above the heat transfer surface. Various droplet sizes were obtained through variation of volumetric flux using different capillaries. In

order to obtain various impact velocities ranged between  $\sim 0.28$  to  $1.3 \text{ m/s}$ , the spacing between the heated surface and capillaries was varied between  $\sim 3$  and  $90 \text{ mm}$  through a vertical adjustment mechanism. Two OMEGA needle valves (NV1 and NV2) were used to precisely control the flow rate passing through the capillary. Applying different hypodermic needles along with varying the gap between the capillary and heated surface provides a reasonably wide range of droplet size, impact velocity and frequency. The nozzle cartridge, needle, and heated surface were placed in an acrylic vessel with a small vent on its top. The free convection heat transfer from the acrylic box walls is enough to condense the saturated vapor. The excess coolant and the vapor were recycled and directed to a tank through a drain connection at the bottom of the acrylic vessel. A removable view port was mounted for imaging purposes.

Before starting the heat transfer experiments, the fluid delivery system was tested to examine the reproducibility of the droplets. The reservoir was filled out with DI water, pressurized to maximum  $300 \text{ kPa}$  and the stream of droplets was generated by forcing the coolant to the various capillaries. The impact velocity of droplets was estimated by taking into account the effect of drag and buoyancy forces. The details of the impact velocity calculation can be found in [13].

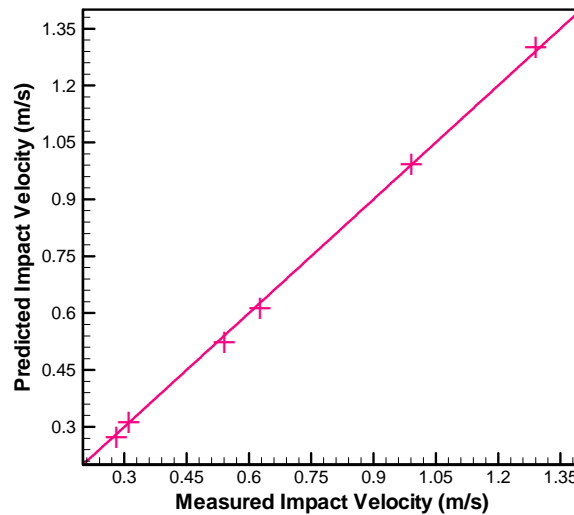


**Figure 3: Comparison between the measured impact velocity of the generated droplet and the predicted impact velocity using Eq.(2)**

Assuming that the terminal velocity has not been reached and the droplet initial velocity is zero [13] (i.e, the droplets are still accelerating with the gravitational acceleration), the momentum balance equation in the vertical direction gives the net force

$$\sum F = F_g + F_b + F_d = ma = m \frac{dV}{dt} \quad (1)$$

where  $F_g$ ,  $F_b$ , and  $F_d$  refer to the gravitational, buoyancy, and drag force, respectively. They are given by  $F_g = mg$ ,  $F_b = m\rho_a / \rho_L g$  ( $\rho_a$  is the mass density of the air), and  $F_d = bV$  where  $b$  is a drag coefficient defined by  $b = 6\pi\mu d_p / 2$ ;  $m$  is mass of the droplet. The solution of the above differential equation gives the impact velocity as

$$V = \frac{mg}{b} \left( 1 - \frac{\rho_a}{\rho_L} \right) \left( 1 - e^{-\frac{bt}{m}} \right) \quad (2)$$

In the above derivation, the internal circulation of the fluid in the droplet, the effect of interfacial condensation and the variation of mass density of air due to the presence of vapor are assumed to be small. The calculation of velocity based on this method and measurement of instantaneous velocity of the impacted droplet are consistent (See Fig.3).

The size and frequency of generated droplets were obtained using a digital camera and an image processing MATLAB code for each individual capillary at different volumetric fluxes. The measured diameter sizes were consistent with volume-weight conversion calculation. The standard deviation of the size and frequency of the droplets generated by the hypodermic needle 17g for  $d_p = 3.71 \text{ mm}$  at  $f = 5.5 \text{ Hz}$  was below  $\pm 1\%$ . The size and frequency of the generated droplet were found to be constant in all the experiment since the variation of pressure in pressurized reservoir showed variations of  $300 \text{ kPa} \pm 0.5 \text{ kPa}$ . It should be noted that the size of the generated droplets and the temperature of the droplet might be affected by the generated vapor cloud in the experimental test section due to the condensation of the vapor on the droplet surface during its flight. In the present study, we measured the size of droplets at room temperature. Monitoring the falling droplets during its impact to the heated surface showed that the droplet diameter change due to the condensation is small and it is below the certainty of the droplet size

measurements. The frequency of the droplet generation at a specific mass flow rate does not show measurable change in the heat transfer experiments.

The heating power was set to 20 W, while the thermocouple readings were recorded in 1 to 3-second intervals. The desired stream of droplets was generated and directed to the heated surface and the time-space averaged thermocouple readings were monitored to determine the steady-state condition. It was assumed that the steady-state was reached at the heated surface, when the calculated time-spaced averaged surface temperature changed by  $< 0.1^\circ \text{C}$  over a 30 s period. It took generally less than 15 s per 1 W input power increment to reach the steady-state condition. After reaching steady-state condition, the space-time averaged heat flux and surface temperature were recorded for a 30-second period. The data acquisition process was initiated when the surface temperature reached the steady-state saturation temperature. By increasing the electrical power, surface temperature rises and heat transfer shows sharp increase due to the evaporation and boiling process. By further increasing the input power, the heat transfer approaches to maximum value and is followed by a steep decrease and rapid temperature rises. This maximum value of the heat flux is defined as CHF. After reaching the post-CHF boiling regime, the electrical power was switched off and the heated surface and insulation were allowed to cool down. The procedure was repeated for the next run. The coolant flow rate and impact frequency were monitored periodically during the test. All of the experiments were repeated three times to verify the reproducibility of results.

### 3.3 Experimental uncertainty and error analysis

Three sources of error contribute to the heat flux calculation: errors in thermocouple readings, uncertainty in thermal conductivity of copper, and uncertainty in thermocouple locations. The propagation equation of Kline McClintock for heat flux calculation can be expressed as:

$$\delta q'' = \left( \left( \frac{\partial q''}{\partial (dT/dx)} \delta \left( \frac{dT}{dx} \right) \right)^2 + \left( \frac{\partial q''}{\partial k} \delta k \right)^2 \right)^{\frac{1}{2}} \quad (3)$$

The precision errors,  $U_{x_i}$ , associated with the various measured quantities,  $x_i$  were summarized in Tab. 1. The bias error for the thermocouples, pressure gauge, and rotameter was negligible, because they had been calibrated. The theory of the propagation of uncertainty was applied to evaluate the 95% confidence uncertainty of the average heat fluxes. The maximum uncertainties associated with the heat flux were obtained to be 6% at  $40 \text{ W/cm}^2$  and 4% at  $100 \text{ W/cm}^2$ . The maximum uncertainties of Weber and Strouhal number calculations were estimated to be less than 3% and 5%, respectively. Both numbers are calculated based on subcooled water temperature. Heat flux calculation based on one-dimensional heat conduction assumption was generally 5% lower than the net power supplied to the heater cartridges. It is consistent with expected losses due to the free convection from the heated surface.

Table 1. The precision error associated with measured parameters

Measurement Parameter( $x_i$ )	$x_i$	$U_{x_i}$
$T_\infty$	298.5 K	$\pm 0.1 \text{ K}$
$P_\infty$	101 KPa	1 KPa
$f$	0.5-5.5 Hz	$\pm 0.15 \text{ Hz}$
$D_h$	7.874 mm	$\pm 2 \times 10^{-5} \text{ m}$
$s$	4-85 mm	$\pm 0.7 \text{ mm}$
$d_p$	2.39 – 3.71 mm	$\pm 0.1 \text{ mm}$
$\dot{V}$	1-4.8 cc/min	$\pm 0.1 \text{ cc/min}$
$V$	0.28 – 1.3 m/s	$\pm 0.01 \text{ m/s}$

### 3.4 Results and Discussion

In order to check the accuracy of the experimental procedure and the data reduction method, the boiling curves of droplet cooling for capillary 17g with impact velocity of  $\sim 1.3 \text{ m/s}$  were obtained at different mass fluxes and average CHF's were compared with the unadjusted CHF data reported by Halvorson [6]. It should be noted that Halvorson [6] used tissue around the experimental test section in order to suck up excess water by capillary action. These previous experiments were reproduced by applying various tissues around the experimental test section to mimic the physical conditions of Halvorson's experiments and the new CHF's were obtained. Although the repeatability of the previous

experiments [6] depends on the physical properties of the applied tissue and its dimensions, the CHF can be reproduced by applying some dense cotton tissue. However, after eliminating the cotton tissue a significant discrepancy can be observed between the measured CHF and those reported by Halvorson [6]. The previous experiments [6] overestimated the average CHF by a factor of  $\sim 2$ . Fig. 4 shows the average CHFs obtained by Halvorson [6] versus the current experimental results with and without cotton tissue. The cotton tissue presumably introduces additional physical complications. It acts as a physical block, particularly when it becomes saturated by excess water, and this may enhance the droplet resident time over the heated surface, which would result in artificially higher CHF measurements. It is concluded that the cotton tissue interferes with the data collection and makes the result highly dependent on the cotton tissue condition including size, material, porosity, and the amount of water absorbed by the tissue.

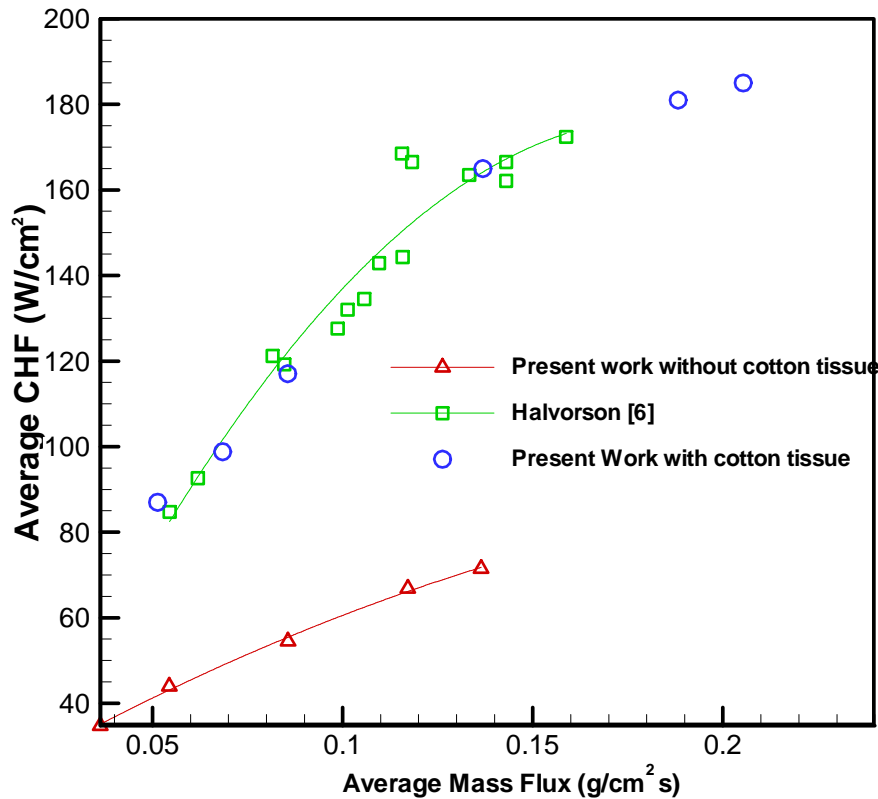


**Figure 4: Variation of droplet cooling CHF with mass flux of capillary 17g compared with previous studies**

There is one more complication regarding to the previous experimental setup, which may lead to the mentioned discrepancy. In Halvorson's setup [6], the bare capillary was fixed above the heated surface and it was in direct contact with the hot saturated vapor produced by boiling process. This resulted in condensation heat transfer occurrence at the capillary surface and significant increments in inlet water temperature. Accordingly, the inlet temperature varies depending on the coolant mass flux and the condensation rate. Although they reported the vigorous condensation at the capillary wall, they did not report any measure to reduce this undesired heat transfer at the wall.

In the current experimental setup, the condensation heat transfer was reduced by adding a 10-mm diameter Teflon block insulation around the capillaries. The inlet water temperature was monitored by a thermocouple junction installed just upstream of the capillary outlet and controlled to be  $25^{\circ}\text{C} \pm 2^{\circ}\text{C}$  during the experiment. The experimental runs were performed at least 20 minutes apart from each other to ensure proper insulation cooling.

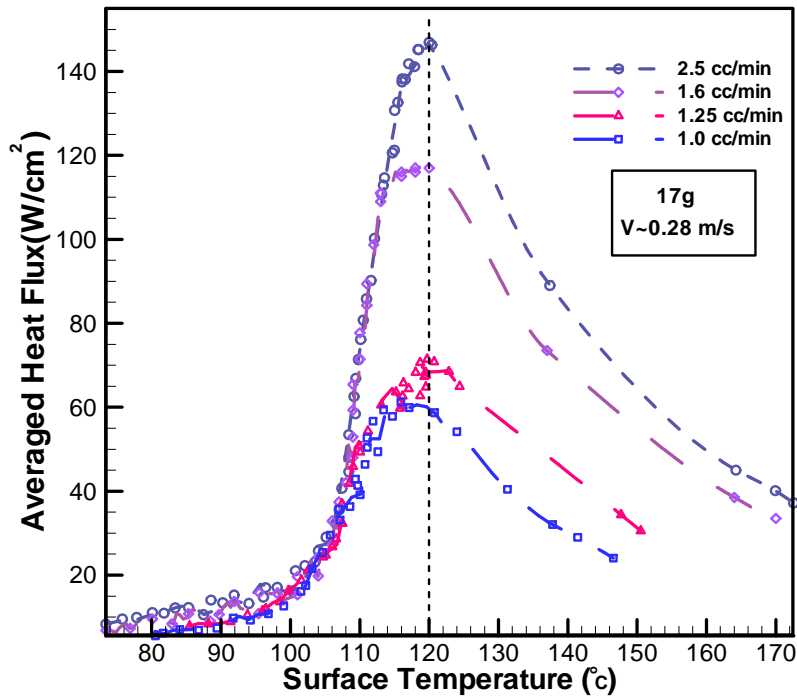


**Figure 5: Boiling curves of 17g capillary at various volumetric flow rates**

In order to investigate the droplet cooling at very low Weber numbers, the CHFs were found at low impact velocities, where the spreading process is theoretically more stable. The capillary was fixed at the distance in the order of the initial droplet diameter, approximately 3-4 mm. The acquired velocity of the droplet was estimated to be  $\sim 0.28$  m/s. Based on the impact velocity and droplet size, the Weber number varies in the range between 3 and 4 for volumetric flow rates in the range of 1-2.5 cc/min. Since the trend of boiling curves for various capillary gauges is similar, the boiling curves for only smallest and largest capillaries used in these experiments are presented.

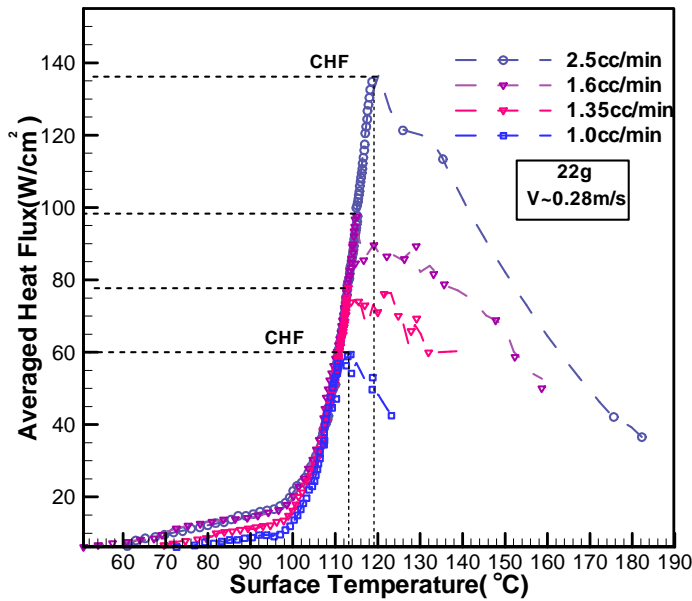


**Figure 6: Boiling curves for 22g capillary at different volumetric flow rates**



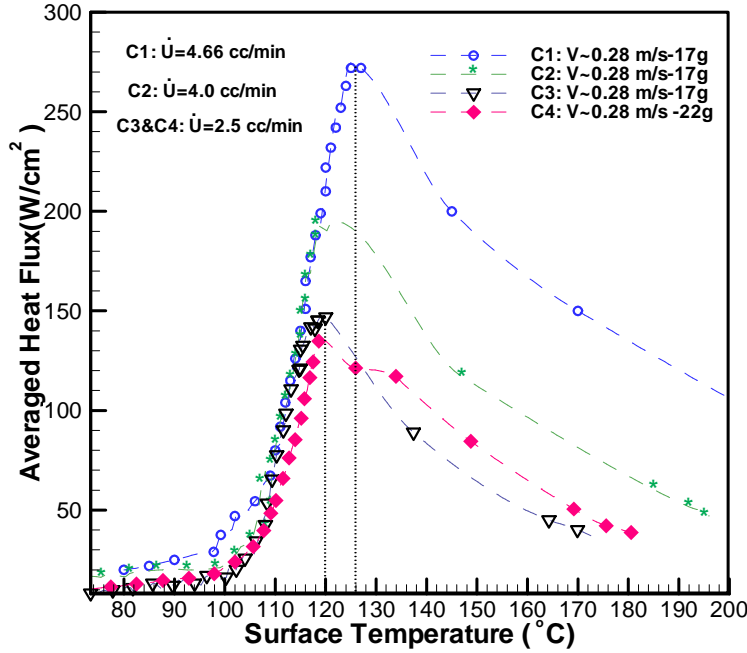


**Figure 7: Boiling curves for 22g and 17g capillaries at different volumetric flow rates**

Figures 5, 6 and 7 depict boiling characteristics of droplets with impingement velocity  $\sim 0.28 \text{ m/s}$  at four different flow rates for 17g and 22g capillaries, respectively. As it can be seen, the magnitude of the measured heat dissipation in the two-phase regime using different capillaries, ranged between 17g-22g, is in the order of tens of  $\text{W/cm}^2$ . For instance, average heat fluxes as much as  $60 \text{ W/cm}^2$  and  $138 \text{ W/cm}^2$  with  $16^\circ\text{C}$  and  $19^\circ\text{C}$  superheat can be removed through the impacted droplets generated by a 22g capillary with initial diameter size of  $\sim 2.39 \text{ mm}$  at  $1 \text{ cc/min}$  and  $2.5 \text{ cc/min}$ , respectively. This significant heat removal improvement is mainly attributed to the boiling heat transfer enhancement, due to the stagnation point flow-like pattern of the coolant after droplet impact and the resulting thin film establishment during the spreading process.

Departing from the single-phase regime, a relatively sharp transition to the two-phase regime is observed for both capillaries in Figs. 5-7 at around the saturated temperature. At lower volumetric fluxes ( $\sim 1 \text{ cc/min}$ ), the transition to the nucleation regime is slightly sharper due to the smaller rate of droplet formation and resulting thinner liquid film over the heated surface. Comparing the two-phase characteristics for fine and coarse capillaries, the boiling curves approximately fall on a universal graph in the nucleation

boiling regime regardless of the mass flux. The CHF values obtained at a given mass flow rate for low impact velocities using various capillaries is almost identical. This suggests that at low impact velocities the CHF is only influenced by flow rate of the coolant rather than the initial droplet size variation or frequency. As expected, by increasing the flow rate the CHF increases and dry out occurs at higher surface superheats for both capillaries. The dry-out occurs between  $\sim 114^\circ\text{C}$  and  $120^\circ\text{C}$  for 1 cc/min and 2.5 cc/min.

Figure 8 depicts the boiling curves of droplet cooling at various impact velocities for the 22g needle. The boiling curves for different impact velocities ranging between 0.28 and 1.3 m/s show a similar trend. The prominent feature of the boiling curves is their steep departure from single-phase regime and sharp transition to two-phase regime. The sharp transition around the saturation temperature is primarily due to the thin film evaporation and onset of nucleate boiling in the thin liquid film. The trend of the boiling curves in the nucleation boiling regime is identical regardless of impact velocity. The mono-dispersed droplet impingement featured for single-phase regime also results in higher amount of heat dissipation, which can be as high as  $\sim 19\text{ W/cm}^2$  around the saturated temperature. By increasing the flow rate from 1 cc/min to 1.6 cc/min, single-phase heat transfer augmentation  $\sim 60\%$  is obtained due to the mean radial velocity increment over the heated surface. However, changing volumetric flow rates between 1.6 cc/min and 2.5 cc/min through the 22g needle, the single-phase heat transfer enhancement asymptotically reaches to maximum  $19\text{ W/cm}^2$  at slightly below the saturated temperature. This asymptotic behavior for single-phase convective heat transfer at high flow rates is believed to be due to the increased loss of the supplied coolant flooding off the heated surface in the spreading process.

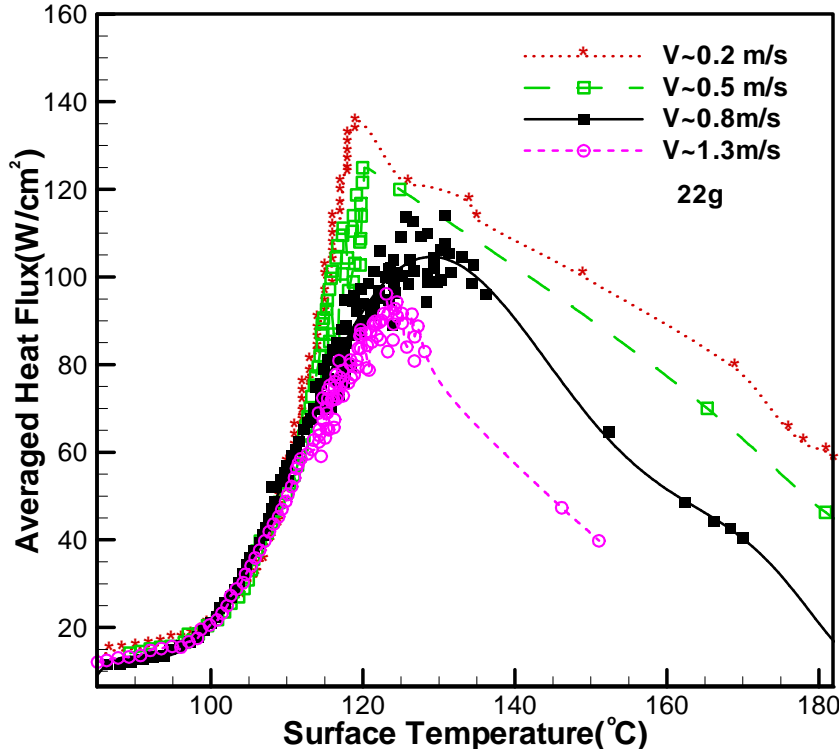
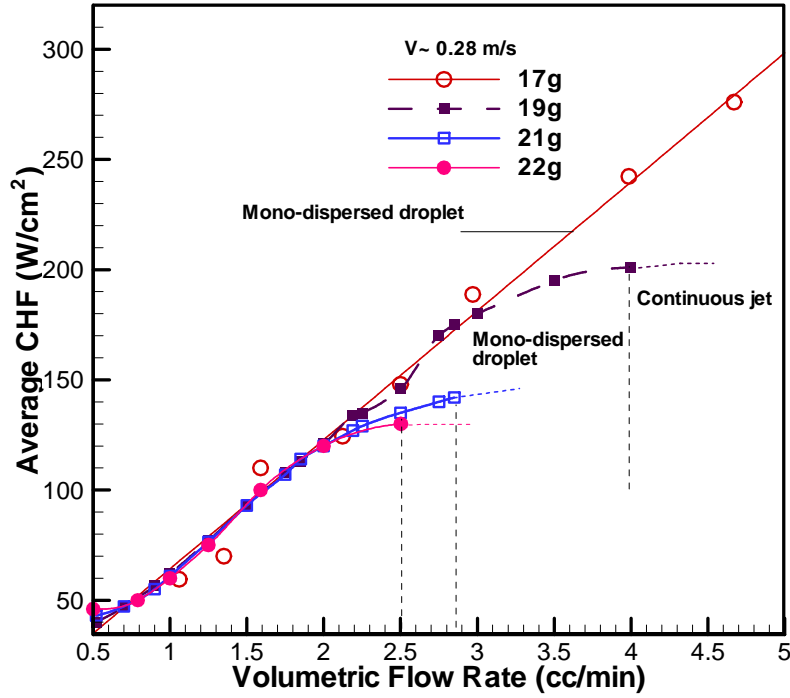


**Figure 8: Boiling curves of droplet cooling of 22g capillary at various impact velocities**

As shown in Fig. 8, by increasing the spacing between the capillary and heated surface, the impact velocity increases, the CHF reduces significantly (~240%) and occurs at higher superheats (~124 °C). For an individual capillary, increasing the droplet impact velocity unexpectedly resulted in lower heat transfer and CHF. It should be noted that, theoretically, thinner liquid film provides higher convective single-phase and two-phase heat transfer rates. Although this contradicts the theoretical expectation for the heat transfer trend, the results are consistent with those presented previously [3,10,14]. A higher impact velocity results in a higher Weber number, corresponding to a less stable spreading process. Both the film thickness and the stable droplet spreading dynamics have a significant influence on the droplet cooling process. For example, at lower impact velocity ( $V < 0.6 \text{ m/s}$ ) corresponding to  $We < 20$ , comparatively thick continuum liquid film is preserved and the residential time increases. The fingerprint for the film continuity can be explored comparing Figs. 5-7 with Fig. 8. The heat transfer curves for  $V \sim 0.28 \text{ m/s}$  ( $We \sim 5$ ) show small fluctuations approximately at all superheats including the critical

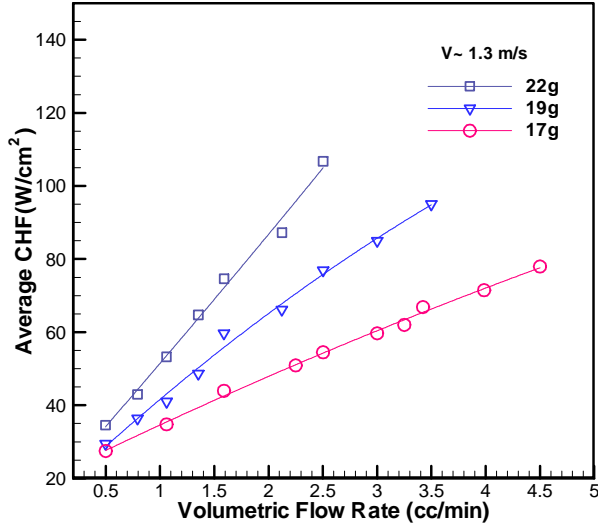
temperature. At low Weber numbers, the fresh droplet lands on the heated surface, when the previous droplet volume is still engaged in the boiling process. The fresh sub-cooled droplet is mixed vigorously with the liquid film and the temperature rises up to the saturation point and the boiling process resumes quickly. Therefore, the heat transfer for the stream of droplets impacted on the heated surface at lower impact velocities is more stable, likely due to the continuity of liquid film. For very low impacted velocities ( $We < 10$ ), slightly increased impact velocity enhances CHF due to higher kinetic energy of the impact. Moreover, for very low Weber numbers (below 10), the resulting film is comparatively thick and hydrodynamically stable, thus it is less likely to develop semi-dry spots at low superheats and CHF postponed to higher values. However, by increasing the impact velocity ( $V > 0.7 \text{ m/s}$ ), corresponding to  $We > 20$ , the impacted droplet breaks up to tiny droplets. The film continuity is not preserved during the spreading process and characteristic curves show appreciable fluctuations. For high impact velocities ( $We > 20$ ), thinner film formation decreases residential time. Therefore, the fresh droplet lands on the heated surface, when the most volume of the previous droplet was evaporated. Thus, the heated surface more likely becomes locally semi-dried in a time period between two landings. The local lack of coolant on the surface due to the disintegration of the liquid film and reduced residual time may cause early dry-out.

Figure 9 shows the variation of CHF with respect to the volumetric flow rate ranged between  $1 \text{ cc/min}$  and  $4.67 \text{ cc/min}$  at low Weber numbers  $We < 20$ . This CHF variation is nearly universal and independent of capillary gauge size at low volumetric flow rates, but it shows deviation from the universal trend at higher flow rates. This indicates that at low Weber numbers,  $We < 20$ , the CHF is a dominant function of mass flow rate rather than the initial droplet size or frequency. Although the variation of the CHF is approximately universal at low flow rates, asymptotic behavior using 19-22g needles at higher flow rates can be observed in Fig. 9. The asymptotic trend may have been due to the flooding of the high frequency sub-cooled droplets, which do not have enough time to contribute the heat transfer process.



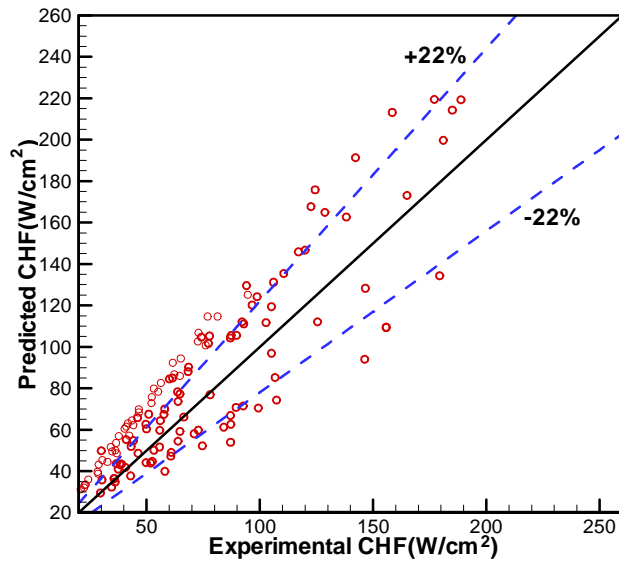
**Figure 9: Variation of average CHF for various capillaries at different volumetric flow rates**

Figure 10 shows the variation of average CHF with respect to the volumetric flow rate for droplet impact velocity of  $\sim 1.3$  m/s using different capillaries. As it can be clearly seen, the CHF variation strongly depends on the size of capillary. Comparing the coarse (17g) and fine capillaries (22g), the rate of increase in resulting CHF is significantly steeper for fine capillaries. The CHFs obtained for coarse capillaries (17g and 19g) show nearly linear trend for  $\sim 1.6$  cc/min, but at moderate and high flow rates (above  $\sim 1.6$  cc/min) an asymptotic trend in CHF is observed. The CHF generally enhances nearly linearly with respect to the volumetric flow rate for fine capillaries (22g and 21g).



**Figure 10: Variation of average CHF at different volumetric flow rates**

Qualitative observations confirmed that supplying coolant with higher flow rates causes the liquid film to be swept away by fresh droplets and prevents temperature rise over the heated surface at moderate superheats, and results in suppression in bubble generation mechanism and nucleate boiling regime. Similar asymptotic behavior of two-phase characteristic curves was reported for spray cooling at high mass flow rates [11, 12].



**Figure 11: Comparison between the experimental and the predicted CHF evaluated by Sawyer et al.'s correlation [3].**

Through this extensive set of experiments it was confirmed that the CHF can be correlated to initial droplet size, impact velocity and frequency by considering two dimensionless groups, Weber and Strouhal numbers. However, comparing the current result for the range of low Weber number,  $10 < We < 100$ , shows that the Sawyer et al.'s correlation [3] shows some deviations (see Fig.11); the current deviation with Sawyer et al.'s correlation is significantly lower than that of Halvorson's experimental data [1]. This evidence is consistent with the earlier discussion on validity of the CHF reported by Halvorson [6]. The appearance of the current correlation,  $CHF/\rho_L h_{fg} V = m \cdot We^a \cdot St^b$ , is similar to the previous correlation given by Sawyer et al. [3]. The correlation and the range of applicability for Weber numbers between 10 and 100 and Strouhal numbers between  $1.81 \times 10^{-3}$  and  $3.86 \times 10^{-2}$  based on 150 data points are given as:

$$\frac{\overline{CHF}}{\rho_L h_{fg} V} = 6.46 \times 10^{-2} We^{-0.2} St^{0.9} \quad (4)$$

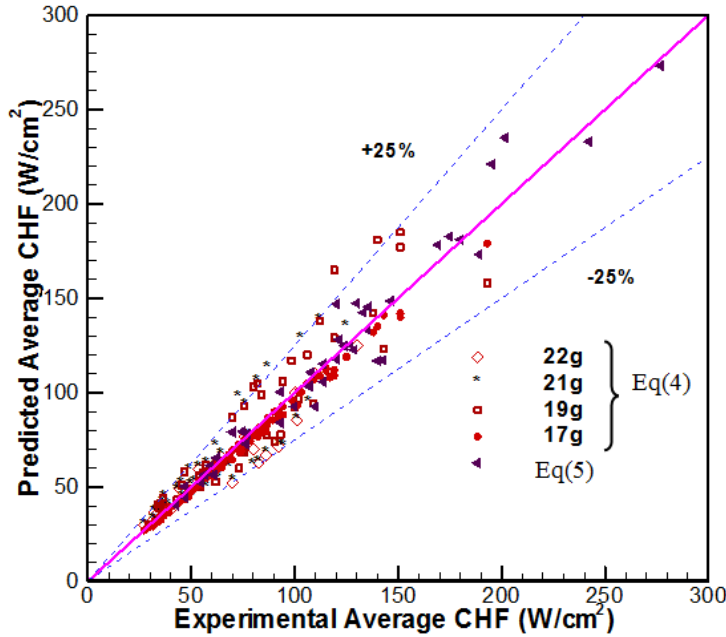


**Figure 12: Comparison between the all experimental and the predicted CHF evaluated by Eq.(4) and Eq.(5).**

As seen in Fig. 12, the proposed correlation predicts the current experimental CHF with an absolute error of less than  $\pm 25\%$  for any combination of the droplet size, frequency and velocity of impacts. Dashed lines represent 95% confidence interval for the correlation given in Eq (4).

It should be noted that the data points collected for  $We < 10$  are not presented in Fig. 12. Fig. 13 compares the measured CHF data for  $We < 10$  and the proposed correlation given in Eq (4). The blue dash lines correspond to the error margins of  $\pm 25\%$ . The average CHF shows considerable deviations at the range of very low Weber number ( $We < 10$ ). This suggests that the droplet spreading dynamics and two-phase characteristics behavior have distinctive differences at very low Weber numbers ( $We < 10$ ).

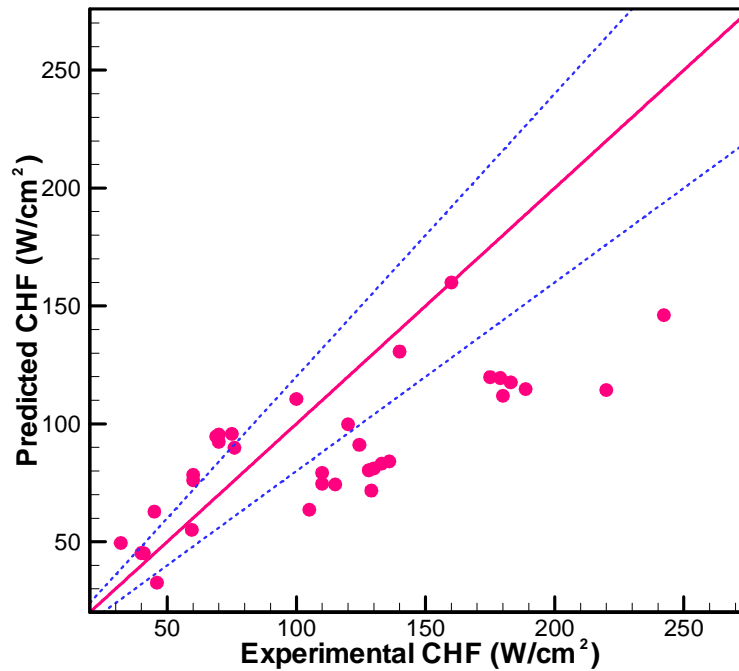


**Figure 13: Comparison between the experimental CHF and the predicted values using Eq.(4) for low Weber numbers ( $We < 10$ )**

As it was shown in Fig. 9, at very low Weber numbers, the CHF varies linearly with respect to the mass flow rate and it is an increasing function of both Weber and Strouhal numbers. It should be noted that by increasing the mass flow rate, both the droplet size and frequency increase and result in higher Weber and Strouhal numbers. Since the mass



flow rate is proportional to impact frequency and the volume of the single droplet is proportional to  $f \cdot d_p^3$ , the appearance of the correlation is expected to be  $\overline{CHF} / \rho_L h_{fg} V = n \cdot We^a St^b$ , where,  $a = 2$ ,  $b = 1$  or  $a = 1$ ,  $b = 2$ . Assuming  $a = 2$ ,  $b = 1$  preserves the dependency of CHF to the impacted velocity and provides more accurate correlation (see Fig. 14). The CHF correlation and the range of its applicability for Weber numbers between 3 and 10 and Strouhal numbers between  $6.35 \times 10^{-3}$  and  $3.88 \times 10^{-2}$  based on 42 data points is given as:

$$\frac{\overline{CHF}}{\rho_L h_{fg} V} = 4.588 \times 10^{-3} We^2 St \quad (5)$$

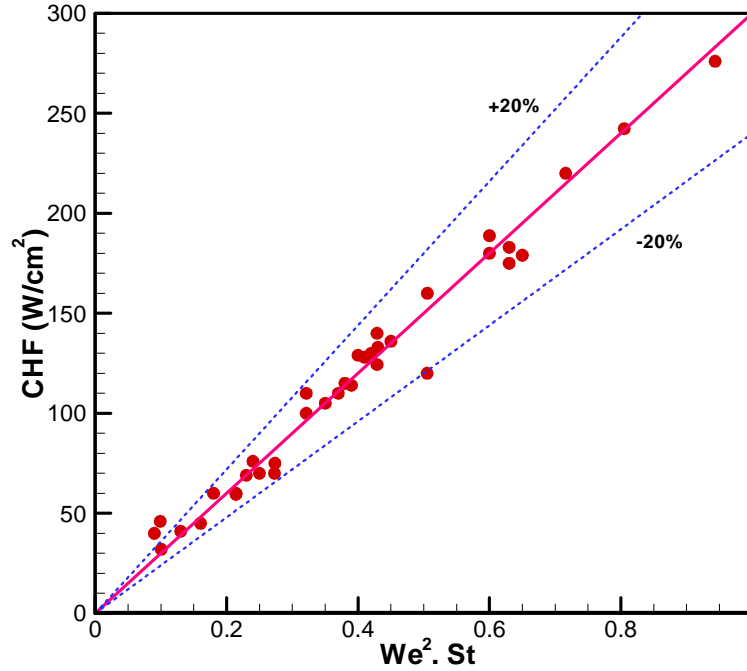


**Figure 14: Comparison between the experimental and predicted CHF data obtained by the dimensionless groups presented in Eq.(5) for  $We < 10$ .**

Fig. 14 shows the ability of Eq.(5) to predict the CHF data at very low Weber numbers. The determination factor is 0.957, indicating that 95% of the measured CHF can be predicted by the correlation given by Eq.(5) with accuracy of 20%. The direct comparison of the proposed correlation is depicted in Fig. 14.

### 3.5 Conclusions

The cooling characteristics of mono-dispersed water droplet impacting a circular heated disk were investigated. The boiling curves were obtained for various impact velocities volumetric fluxes and capillary sizes, ranged between 0.28 *m/s* and 1.3 *m/s*, 1 and 4.8 *cc/min*, and 17 and 22g, respectively. The size and frequency of droplets were varied through the volumetric flux variation. The prominent feature of the boiling curves is their steep departure from the single-phase regime and sharp transition to the two-phase regime. The nucleation boiling regime of the boiling curves is approximately identical regardless of impact velocity and droplet parameters. The CHF obtained at a given mass flow rate for low impacted velocities using various capillaries is almost identical. Through collecting 150 data points it was also confirmed that the average CHF of mono-dispersed droplet cooling can be fitted using a correlation based on Weber numbers ranged between 10 and 100 and Strouhal numbers between  $1.81 \times 10^{-3}$  and  $3.86 \times 10^{-2}$ , respectively. Since the droplet dynamics and heat transfer characteristics show significant changes at very low Weber number, a separate CHF correlation based on the 42 data points was developed for  $We < 10$ . It should be noted that the proposed correlations are only valid for water and one may use different working fluids to adapt more general correlations applicable for the broader range of thermo-physical properties.

### Nomenclature

$\overline{CHF}$	Average critical heat flux ( $Wcm^{-2}$ )
$d_p$	Initial diameter of droplet ( <i>m</i> )
$f$	Impact frequency ( $s^{-1}$ )
$h_{fg}$	Latent heat of vaporization ( $Jkg^{-1}$ )

$k$	Thermal conductivity ( $Wm^{-1}K^{-1}$ )
$q''$	Heat flux ( $Wcm^{-2}$ )
$Re = \frac{\rho_L V d_p}{\mu}$	Reynolds number
$St = \frac{f d_p}{V}$	Strouhal number
$\dot{U}$	Volumetric flux ( $ccmin^{-1}$ )
$v$	Impact velocity ( $ms^{-1}$ )
$We = \frac{\rho_L V^2 d_p}{\sigma}$	Weber number
$\rho_L$	Density ( $kgm^{-3}$ )
$\sigma$	Surface tension ( $Nm^{-1}$ )
$\mu$	Viscosity ( $Nm^{-2}s$ )

## References

- [1] W.M. Healy, P.J. Halvorson, J.G. Hartley, S.I. Abdel-Khalik, "A critical heat flux correlation for droplet impact cooling at low Weber numbers and various ambient pressures", *International Journal of Heat and Mass Transfer*, 41(6-7), 1998, pp.975-978.
- [2] S.G. Kandlikar, M. Steinke, "Contact angle of droplets during spread and recoil after impinging on a heated surface", *Chemical Engineering Research and Design*, A(79), 2001, pp.491-498.
- [3] M.L. Sawyer, S.M. Jeter, S.I. Abdel-Khalik, "A critical heat flux correlation for droplet impact cooling", *International Journal of Heat and Mass Transfer*, 40(9), 1997, pp.2123-2131.
- [4] M. Monde, T. Inoue, "Critical heat flux in saturated forced convective boiling on a heated disk with multiple impinging jets", *Journal of Heat Transfer*, 113, 1991, pp.722-727.
- [5] J. Kim, "Spray cooling heat transfer: The state of the art", *International Journal of Heat and Fluid Flow*, 28(4), 2007, pp.753-767.
- [6] P.J. Halvorson, "On the heat transfer characteristics of spray cooling", PhD thesis, Georgia Inst. of Technology, Atlanta, GA, 1993.
- [7] P.J. Halvorson, R.J. Carson, S.M. Jeter, S.I. Abdel-Khalik, "Critical heat flux limits for a heated surface impacted by a stream of liquid droplets", *Journal of Heat Transfer*, 116(3), 1994, pp.679-685.
- [8] F.K. McGinnis, J.P. Holaman, "Individual droplet heat transfer rates for splattering on hot surfaces", *International Journal of heat and mass transfer*, 12, 1969, pp.95-108.

- [9] L.H.J. Watchers, N.A.J. Westerling, "The heat transfer from a hot wall to impinging water drops in the spheroidal state", *Chemical Engineering Science*, 21, 1966, pp.1047-1056.
- [10] M.L. Sawyer, "High intensity heat transfer to a stream of monodispersed water droplets", PhD thesis, Georgia Inst. of Technology, Atlanta, GA, 1996.
- [11] J.S. Coursey, J. Kim, K. T. Kiger, "Spray cooling of high aspect ratio open microchannels", *Journal of Heat Transfer*, 129, 2007, pp.1052-1059.
- [12] J.C Chen, "Correlation for boiling heat transfer to saturated fluids in convective flow", *Ind. Eng. Chem. Prod. Res. Dev.*, 5(3), 1966, pp.322-339.
- [13] C. Ukiwe, D.Y. Kwok, "On the maximum spreading diameter of impacting droplets on well-prepared solid surfaces", *Langmuir*, 21(2), 2005, pp.666-673.
- [14] J.D. Bernardin, C. J. Stebbins, I. Mudawar, "Mapping of impact and heat transfer regime of water drops impinging on a polished surface", *International Journal of Heat and Mass Transfer*, 40(2), 1997, pp.247-267.
- [15] J.D. Bernardin, C.J. Stebbins, I. Mudawar, "Effect of surface roughness on water droplet impact history and heat transfer regime", *International Journal of Heat and Mass Transfer*, 40(1), 1996, pp.73-78.
- [16] B.S. Kang, D.H. Lee, "On the dynamic behavior of a liquid droplet impacting upon an inclined heated surface", *Experiments in Fluids* 29, 2000, pp.380-387.
- [17] H. Chaves, A.M Kubitzek, F. Obermeyer, "Dynamic processes occurring during the spreading of thin liquid films produced by drop impact on hot walls", *International Journal of Heat and Fluid Flow*, 20(5), 1999, pp.47-476.
- [18] P. Tartarini, G. Lorenzini, M.R. Randi, "Experimental study of water droplet boiling on hot, on-porous surfaces", *Heat and Mass Transfer*, (34), 1999, pp.437-447.

- [19] S.L. Manzello, J.C. Yang, "An experimental investigation of water droplet impingement on a heated wax surface", *International Journal of Heat and Mass Transfer*, 47(8-9), 2004, pp.1701-1709.
- [20] J.S. Coursey, J. Kim, K. Kiger, "Spray Cooling of High aspect ratio open microchannels", *Journal of Heat Transfer*, 129(8), 2007, pp.1052-1060.
- [21] B. Horacek, K.T. Kiger, J. Kim, "Single nozzle spray cooling heat transfer mechanisms", *International Journal of Heat and Mass Transfer*, 48, 2005, pp.1425-1438.
- [22] B. Horacek, K.T. Kiger, J. Kim, "Spray cooling using multiple nozzles: visualization and wall heat transfer measurements", *IEEE Transactions on Device and Materials Reliability*, 4(4), 2004, pp.614-625.
- [23] T.A. Shedd, A.G. Pautsch, "Spray impingement cooling with single-and multiple-nozzle arrays. Part II: Visualization and empirical models", *International Journal of Heat and Mass Transfer*, 48(15), 2005, pp.3176-3184.
- [24] A.G. Pautsch, T.A. Shedd, "Spray impingement cooling with single-and multiple-nozzle arrays. Part I: Heat transfer data using FC-72", *International Journal of Heat and Mass Transfer*, 48(15), 2005, pp.3167-3175.
- [25] E.A. Silk, E.L. Golliher, R.P. Selvam, "Spray cooling heat transfer: Technology overview and assessment of future challenges for micro-gravity application", *Energy Conversion and Management*, 49(3), 2008, pp.453-468.
- [26] S.G. Kandlikar, M.E. Steinke, "Contact angles and interface behavior during rapid evaporation of liquid on a heated surface", *International Journal of Heat and Mass Transfer*, 45, 2002, pp.3771-3780.
- [27] S. Chandra, C.T. Avedisian, "On the collision of a droplet with a solid surface", *Proc. R. Soc. London A*(432), 1991, pp.13-41.
- [28] S. Chandra, C.T. Avedisian, "Observations of droplet impingement on a ceramic porous surface", *International Journal of Heat and Mass Transfer*, 35, 1992, p.2377-2388.

- [29] S.G. Kandlikar, M. Steinke, "Contact angle of droplets during spread and recoil after impinging on a heated surface", *Chemical Engineering Research and Design*, A (79), 2001, pp.491-498.
- [30] Y. Takata, S. Hidaka, J.M. Cao, T. Nakamura, H. Yamamoto, M. Masuda, T. Ito, "Effect of surface wettability on boiling and evaporation", *Energy*, 30(2-4), 2005, pp.209-220.
- [31] M. Pasandideh-Fard, S.D. Aziz, S. Chandra, J. Mostaghimi, "Cooling effectiveness of a water drop impinging on a hot surface", 22(2), 2001, pp.201-210.
- [32] W.J. Yang, "Theory on vaporization and combustion of liquid drops of pure substances and binary mixtures on heated surface", Technical report, 553,1975, Inst. Space Aero. Sci., University of Tokyo.

## Chapter 4

# Two-phase cooling characteristics of a saturated free falling circular jet of HFE7100 on a heated disk in the presence and absence of electric field

### 4.1 Introduction

The two-phase jet-impingement method is typically used to dissipate moderate and high concentrated heat loads in the order of 100-1000 W/cm<sup>2</sup> at relatively low superheats [1, 2]. Such heat fluxes are encountered in several specialized applications such as cooling of high-energy x-ray devices, high power laser diode arrays, Si-C based photonic devices and the recent solid-state photonic components, such as optical scaling power elements [3]. The jet impingement technique has also found extensive applications in the transient quenching of alloys to accurately control the material phase-microstructure curves in metal industries. In several recent applications [1-3], the heated targets are delicate structures where their performance is sensitive to the mechanical stresses. Although high momentum jets are remarkably effective for the cooling of such localized heated targets, this aggressive technique may yield unwanted deformations or mechanical failure. This suggests the operation of the jets at low flow rates particularly for moderate heat fluxes. This decrease in operating flow rate may also lead to reduction in the size of auxiliary elements such as pump and condenser in the cooling circuit.

Jets can be produced from either a rectangular or a circular orifice. Jet impingement cooling might be used in three different forms: (i) free jet (jets in vapor/gas), (ii) submerged jet (jet flow in the ambient liquid) and (iii) confined jet (jet axis is positioned in parallel with the heated wall) [13-17]. The present study is focused only on free circular jets. Here, the circular jet strikes the heated target and forms a radial liquid sheet. As a general principal, a high momentum jet may improve the contact between the coolant and the heated target around the impingement zone. Typically, for the low or



moderate heat flux ranges, the momentum of the liquid sheet is high enough to sweep the generated vapor bubbles away from the target; thus the contact between the liquid and vapor is mostly preserved for a large range of superheats. By increasing the heat flux, the generated vapor next to the heated surface may blow through the liquid sheet rupturing it and creating several holes in it. This eventually leads to the formation of semi-dry spots around the rim of the heater. With a further increase in the heat flux, several dry regions may propagate inwards towards the impingement zone and the liquid sheet can be splashed away in the form of micro-droplets. Under these conditions, the liquid sheet is divided into two identifiable portions. One portion is a spray of micro droplets, which acquires significant surface energy and fly upward from the sheet at a some angle with respect to the heated wall plane. The other portion is the original sheet which remains mostly attached to the target and moves horizontally in a radial direction [18]. At a high enough heat flux, but slightly below the burnout condition, the contact of the original liquid sheet is preserved, the droplets become finer and their upward departure angle slightly increases. At burnout, the liquid sheet is suddenly interrupted since the kinetic energy of the bulk liquid is not enough to supply an adequate liquid to preserve its balance with the rate of evaporation and upward micro-droplet formation. Thus, the sprayed droplets become coarser and the liquid sheet no longer maintains its contact with the heated target. This picture of the burnout (the critical heat flux (CHF) regime) has been verified both theoretically and experimentally at comparatively high flow rates [7,8,9].

Several studies have been performed to investigate the influence of the free jet parameters on CHF [4,5,18] at comparatively high flow rates. Based on these studies, various authors have correlated the saturated critical heat flux with the relevant dimensionless groups:

$$\frac{q_{CHF}}{\rho_g h_{fg} U} = f \left( \frac{\rho_g}{\rho_f}, \frac{\rho_f U^2 d}{\sigma}, \frac{g(\rho_f - \rho_g)d}{\rho_f U^2}, \frac{\mu_g}{\mu_f}, \frac{\rho_f U d}{\mu_f} \right) \quad (1)$$

Further modifications were carried out by Haramura and Katto [6] to adopt Eq.(1) to consider the effect of liquid subcooling. Their proposed model, based on the burnout picture described earlier, has shown remarkable success in correlating the data of high velocity impingement jets (0.5 *m/s* to 12 *m/s*). In the course of generalizing the CHF correlation, Monde and Okuma [8] recognized two distinct regimes (i) V-regime: high impingement velocity with small target and (ii) L-regime: jets with low impingement velocity and comparatively large heated targets.

The theoretical model based on the Mechanical Energy Stability Criterion (MESC) proposed by Lienhard and Eichhorn [18] predicted that the CHF for the V-regime varies with the cube root of the velocity, while for the L-regime the CHF is linearly proportional to the impingement velocity. The theoretical model was verified for both ranges by slightly perturbing the exponents to 0.343 and -0.364 for the V-regime which were originally 1/3 and -1/3 in the theoretical model. They also found boundaries for the two different correlations between the L- and V-regimes. Sharan and Lienhard [9] also proposed a more complicated unified correlation for both L and V-regimes based on the MESC. The unified correlation provides the same accuracy  $\sim \pm 20\%$  for both L- and V-regimes.

In the case of free falling jets with a small impingement velocity the boiling characteristic is rather complicated. The thickness and the stability of the liquid sheet are the two most important factors that play a pivotal role, particularly at the CHF regime. Although the heat transfer coefficient is inversely proportional to the thickness of the film, the thinner film is more likely to be ruptured in multi locations due to the hydrodynamic instabilities. Several semi-dry spots can be created at even small superheats due to such instabilities, which may lower the magnitude of the CHF. These qualitative observations suggest that both film thickness and the layer stability determine the boiling curve characteristics.

A complication for low speed jets is that the cross sectional area of the free falling jet is influenced by gravity/surface tension interactions at low flow rates. As the jet length increases, the liquid volume is accelerated by the gravitational force and since the flow

rate is constant, the cross sectional area reduces. It is expected that the jet length determines the boiling curves since both velocity and jet diameter change. In the previous studies, authors did not consider such an effect since the jets were typically operated at high flow rates, so that the cross section and velocity of the jet were not affected by gravity/surface tension interaction. For high momentum jets, gravity /surface interaction is dominated by the jet inertia.

The reduction of the cross section and increase in velocity of a free falling circular jet can be analytically obtained by applying Bernoulli's theorem between the exit point and a desired axial position  $z$ . Considering a circular jet with radius  $r_{ext}$  and exit velocity of  $V_{ext}$  of a liquid with mass density of  $\rho$  and surface tension  $\sigma$ , one may find an expression for velocity increase in the  $z$  direction as:

$$\frac{V(z)}{V_{ext}} = \left( 1 + \frac{2gr_{ex}}{V_{ext}} \left( \frac{z}{r_o} \right) + \frac{2\sigma}{\rho V_{ex}^2 r_{ext}} \left( 1 - \frac{r_{ext}}{r} \right) \right)^{1/2} \quad (2)$$

By rearranging the above equation and considering the Froude and Weber numbers,

$$Fr = \frac{V_{ext}^2}{gr_{ext}} \text{ and } We_{r_{ext}} = \frac{\rho V_{ext}^2 r_{ext}}{\sigma}, \text{ the following expression for velocity variation in axial}$$

direction can be obtained:

$$\frac{V(z)}{V_{ext}} = \left( 1 + \frac{2}{Fr} \left( \frac{z}{r_{ext}} \right) + \frac{2}{We_{r_{ex}}} \left( 1 - \frac{r_{ext}}{r} \right) \right)^{1/2} \quad (3)$$

At a given jet length,  $S$ , it is useful to define the reduction coefficient as  $\Gamma = r(S)/r_{ext}$ . Since the mass flow rate is continuous in the free falling jet, the cross section of the jet due to the gravitational acceleration can be expressed as:

$$\Gamma = \frac{r(z)}{r_{ext}} = \left( \frac{V_{ext}}{V(z)} \right)^{1/2} = \left( 1 + \frac{2}{Fr} \left( \frac{z}{r_{ext}} \right) + \frac{2}{We_{r_{ex}}} \left( 1 - \frac{r_{ext}}{r} \right) \right)^{-1/4} \quad (4-a)$$

In this derivation, the jets were assumed to be hydrodynamically stable and  $z$  is smaller than the critical length, where the jet becomes unstable,  $z_{crit}$ . The normalized critical length of the jet can be obtained by dimensional analysis:

$$\frac{z_{crit}}{r_{ext}} \approx V_{ext} \left( \frac{\rho_f r_{ext}}{\sigma} \right)^{1/2} \quad (4-b)$$

For the present volumetric flow rates, the minimum critical length for the falling jets is calculated to be 70 mm, which is larger than the largest jet length of this study.

For high-speed jets, both the Froude and Weber numbers tend to infinity. According to Eq. (4-a), the falling jet shows no significant change in its diameter since the inertia force is dominant. In contrast, for low speed jets, the cross sectional area may be decreased since both Froude and Weber numbers take moderate values.

The effect of jet length might be more understandable if one considers an extreme case, where the jet length is large enough so that the capillary-driven instability (Plateau-Rayleigh instability) of the falling jet forms mono-dispersed droplets from the continuous jet. Boiling curves obtained for a mono-dispersed stream of droplets impacted on a heated target differ from that of a continuous jet and other dimensionless groups might be used to predict the measured CHF. However, one may find several commonalities between the jet impingement and the mono-dispersed droplet cooling technique [19, 20]. In mono-dispersed cooling, both the film thickness after the impact and the hydrodynamic stability of the film contribute in determining the CHF. For instance, for increased impact velocity one may expect CHF enhancement due to the convection enhancement. However, significantly reduced CHF has been reported due to the hydrodynamic instabilities of the resulting liquid film at higher impact velocity [19].

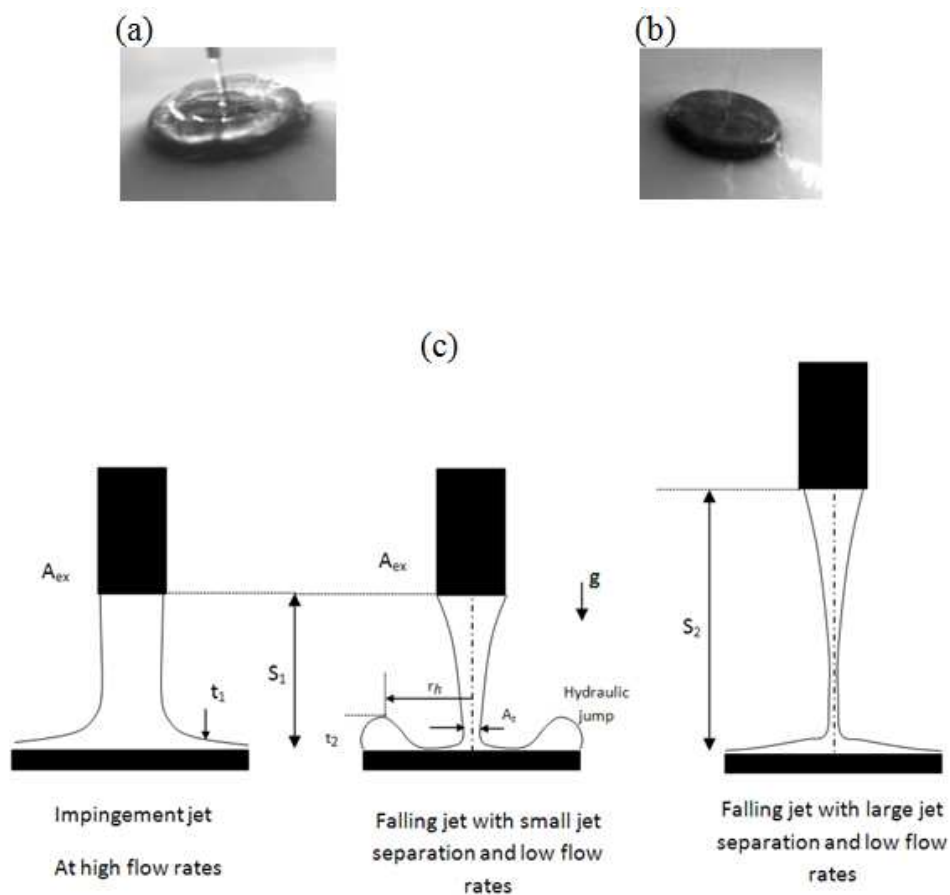


**Figure 1 (a):** Radial spreading of an impingement jet striking on an upward facing disk at (low) volumetric flow rates 20 cc/min and (b)(high) flow rates 60 cc/min. (c) Figurative description of the effect of the jet length at different flow rates.



**Figure 2:** Falling jets of HFE7100 at different jet lengths. Hydraulic jump position varies by varying the jet length. Jet lengths are: (a) 5 mm, (b) 10 mm (c) 20 mm at 20 cc/min volumetric flow rate using 15g needle as nozzle.

For low speed jets, an additional complexity arises due to the development of the circular hydraulic jump over the heated target (see Figs.1 and 2) [10,11,12]. As qualitatively shown, the circular hydraulic jump position in a falling jet varies for different jet lengths.

It has been proven that applying the standard theory of the hydraulic jump to the uniform supercritical flow model may lead to large disagreements in predicting the hydrodynamics of the circular hydraulic jumps [12]. Unlike the classical theory of the hydraulic jump in open channels, which can be found in fluid mechanics textbooks, one cannot find a complete analytical model for circular hydraulic jump resulting from impingement jets. The complete mathematical model should include several physical effects describing both the upstream and downstream flow evolution including velocity of the jet, jet diameter, local and overall Froude numbers, jump position, possible flow separations and parameters describing the stability of the jump surface and the jump types [12].

In general, for high-speed jets striking on small targets, the circular hydraulic jump does not occur within the heater area. For moderate and high-speed jets, the thickness of the liquid sheet is approximately uniform since the hydraulic jump occurs typically at radial distances larger than the target size. The hydraulic jump formation within the heater size may suddenly increase the liquid layer thickness. The complexities in flow patterns in the hydraulic jump region may significantly change the boiling characteristics. For example, the recirculation that occurs within a hydraulic jump may decrease the heat transfer. Since the jet length may determine the location of the hydraulic jump, the boiling curves may be considerably influenced due to the changing distance between the jet and target.

The literature review suggests that the two-phase characteristics of free falling jets at very low flow rates has not been extensively studied. This is mainly because the previous studies have been more interested in maximizing the heat transfer by increasing the jet velocity. However, as mentioned earlier, increasing the momentum of the jet can introduce several drawbacks including aggressive mechanical stress. In this case, it makes more sense to consider a less aggressive cooling method in which the dielectric coolant is directly used to cool down the heat sources. The direct method is advantageous

since the heat sink and its bonding thickness is eliminated and thus the thermal resistance and the temperature increase across their thickness can be reduced significantly. This is especially important for high power solid-state devices in which high densities of generated heat should be dissipated at low operating temperatures.

To the best of the knowledge of the authors, the effect of jet length at low flow rates has not been yet considered. This paper is intended to demonstrate the importance of jet length in determining the CHF at low volumetric flow rates. The boiling curves of the free falling circular jets of HFE7100 striking on an upward facing disk were obtained at different volumetric flow rates and jet lengths. The ranges of jet length and flow rates were chosen so that the jet remains continuous. The mono-dispersed droplet generation mode was avoided for all of the boiling curves presented in this paper. The dielectric fluid HFE7100 was selected as the working fluid since it possesses relatively good thermophysical properties and its low electrical conductivity makes it a reasonable candidate for direct electronic cooling applications. In order to understand the experimental results, some flow visualization of the jets is also presented. In order to include the effect of the length of the falling jets at low flow rates, the previous CHF correlation [9] was adjusted for the variable cross sectional area obtained by the analytical model. The current CHF results were predicted with the revised correlation.

## 4.2 Experimental setup and procedure

The experimental setup was designed to determine the heat transfer from a horizontal, upward-facing, heated disk impacted by the jets. The experimental apparatus consisted of three major components: (I) heat surface, (II) measurement system and instrumentation (III) fluid delivery system. The schematic diagram of the experimental circuit is presented in Fig.3-a. The heat transfer surface was circular and consisted of nickel-plated copper base joined to a heated cylinder. The heated cylinder was made of copper, coated with a protective layer of 30 micron nickel. The heat transfer surface was fully polished

and coated with an additional layer of 25  $\mu\text{m}$  nickel. Surface measurement after the coating process showed its arithmetic average roughness was less than 200  $\text{nm}$ .

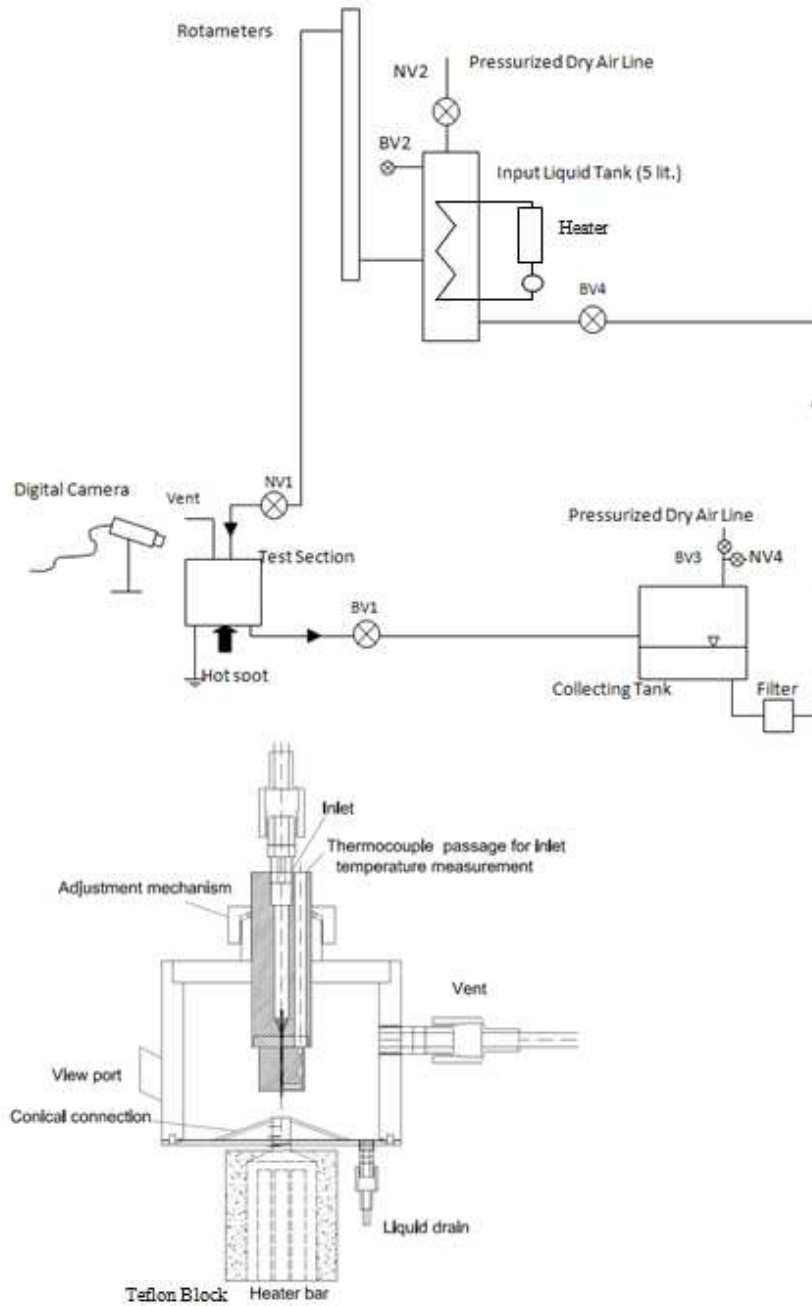


**Figure 3: Schematic view of experimental setup**



Four identical cavities were drilled in the cylinder and four identical 300 W-cartridge WATLOW heaters were inserted axially into the cavities, connected in parallel and supplied with a programmable power supply (QuadTech Model:42000). The upper end of the heated cylinder was tapered to a smaller diameter (8 mm) to increase the surface heat flux and this formed the heat transfer surface. The effective heat transfer area was a disk with a diameter of 8 mm. It was instrumented with 12 calibrated K-type thermocouples with a 0.25 mm bead (Omega K-type thermocouples 0.25 mm- 5SRTC series Kapton®). The calibrations estimated the fixed and bias errors of each thermocouple. The calibration was performed in a constant-temperature water bath for 50–100 °C. During the calibration, the constant temperature bath was maintained at the calibration temperature to within  $\pm 0.05$  °C using PT100 thermocouples. The bath temperature was measured by a thermistor diode. The thermocouples to be calibrated were immersed simultaneously in the water bath and were kept close to the probe and the temperature measured by each thermocouple was recorded by a Data Acquisition System for 30 min maintaining a span of 10 s between two successive readings. The entire process was repeated one more time, and the average of the two readings was taken. The difference between the actual water bath temperature and the average of the measured temperatures gave the bias error. Precision error was estimated as twice the standard deviation of the thermocouple readings. The average values of precision and bias errors for all thermocouples used in the experiments were  $2\sigma=0.06$  and 0.1 °C, respectively, where  $\sigma$  is the standard deviation. The thermocouples were embedded in the neck of the heat transfer surface and fixed using a mixture of ultrafine copper powder and high thermal conductive adhesive epoxy (OMEGABOND 200®). The heated cylinder was inserted into a Teflon block to minimize the heat losses. Extra slag wool with thermal conductivity  $\sim 0.04$  W/m.K was used in the neck region to reduce the radial heat transfer.

The heated surface was fitted to a truncated Teflon ring to seal the neck of the heat transfer surface and to direct the excess liquid to the drain. The rim of the impacted surface was insulated using a conical ceramic connection and sealed with a thin strip of a

high temperature resistant silicone rubber. An adjustable holder was used to precisely align the heated surface in  $x$ - $y$ - $z$  direction.

Table. I Thermophysical properties of HFE7100 at 61°C and 0.1 MPa [21].

$\rho_f(kg/m^3)$	$\rho_g(kg/m^3)$	$\nu(cSt)$	$\sigma(mN/m)$	$h_{fg}(kg/kJ)$
1370	9.8	0.27	10.1	11.60

Table.II Uncertainty of the measured parameters

Measured Parameters ( $x_i$ )	$x_i$	$U_{x_i}$
$T_\infty$	297.3 K	$\pm 0.1$ K
$P_\infty$	101 KPa	$\pm 1$ KPa
$S$	5-50 mm	$\pm 0.5$ mm
$D_h$	7.98 mm	$\pm 5$ $\mu m$
$r_{ext}$	0.686-0.301 mm	$\pm 1$ $\mu m$
$\dot{V}$	20-60 cc/min	$\pm 0.05$ cc/min
$T_s$	334-369 K	$\pm 0.1$ K

In order to examine the uniformity of temperature over the heated surface at different levels and to allow accurate heat flux calculation, the 12 calibrated thermocouples were placed at three different levels and in four different radial depths and peripheral angles, and connected to a 16-channel data acquisition system NI-DAQ 9213. A LABVIEW code was developed to calculate the heat flux and surface temperature from the thermocouple readings. The average heat flux was calculated from 1-D steady state Fourier's law of conduction for the cylinder neck. The reported heat transfer and surface temperature were obtained by averaging the calculated heat fluxes and thermocouple readings. The surface temperature was obtained by linear extrapolation. The thermophysical properties of saturated HFE7100 are presented in Table. I. The volumetric flow rate of the jet was measured using pre-calibrated rotameters. A CCD camera was used for the visualization and measurement of the jet cross section variation along the axial direction.

The fluid delivery system consisted of a recycling circuit with the following components: hydrostatic pressurized reservoir with a closed loop heating circuit, pressure vessel, universal nozzle holder, standard hypodermic needles, and fine thread needle valves. The

coolant in the reservoir was preheated to around saturation temperature by an immersed helical heat exchanger. The reservoir was thermally isolated with a layer of slag wool. The temperature of the liquid in the reservoir was monitored at three different levels. In order to avoid cavitation at the nozzle, the coolant was heated to  $59^{\circ}\text{C} \pm 1$  ( $\sim 2^{\circ}\text{C}$  below the saturation). The saturated liquid was directed to the nozzle holder by pressurizing the reservoir. The jets were formed by directing the working fluid through two different hypodermic needles 15g and 20g having inner diameters of 1.37 mm and 0.41 mm, respectively. A thermocouple was inserted into the Teflon block and fixed at the needle wall 2-mm away from its tip to measure the inlet coolant temperature. The nozzle holder was equipped with a universal fitting to easily mount the various needles and center them above the heat transfer surface. An axial guide was designed to vary the distance between the tip of the nozzle and heated target.

Before starting heat transfer experiments, the target was aligned and leveled, and the jet was applied. The radial symmetry of the flow field over the target was visually examined. The experiments were started by applying a low heating power of about 20 W, while the thermocouple readings were recorded in 1 second intervals. The heating power was gradually increased. It was assumed that the steady-state was reached at the heated surface when the calculated time-spaced averaged surface temperature changed by  $< 0.1^{\circ}\text{C}$  over a 30 s period. It took generally less than 5 s per 1 W input power increment to reach the steady-state condition. After reaching steady-state condition, the space-time averaged heat flux and surface temperature were recorded for a 30-second period. The data acquisition process was initiated when the surface temperature reached around the steady-state saturation temperature. By increasing the electrical power, the surface temperature increased and heat transfer showed a relatively sharp increase due to the initiation of the boiling process. By further increasing the input power, the heat transfer increases in the nucleation boiling regime, the heat flux approaches a maximum value and is followed by a steep decrease and rapid temperature rise. After reaching the post-CHF boiling regime, the electrical power was switched off and the heated surface and insulation was allowed to cool down. The procedure was repeated for the next run. The coolant flow rate and the quality of the jet were monitored periodically during the test.

All of the experiments were repeated three times to verify the reproducibility of the results.

### 4.3 Experimental uncertainty and error analysis

Three sources of error contribute to the heat flux calculation: errors in thermocouple readings, uncertainty in thermal conductivity of copper, and uncertainty in thermocouple locations. The propagation equation of Kline-McClintock for heat flux calculation can be expressed as:

$$\delta q'' = \left( \left( \frac{\partial q''}{\partial (dT/dx)} \delta \left( \frac{dT}{dx} \right) \right)^2 + \left( \frac{\partial q''}{\partial k} \delta k \right)^2 \right)^{\frac{1}{2}} \quad (5)$$

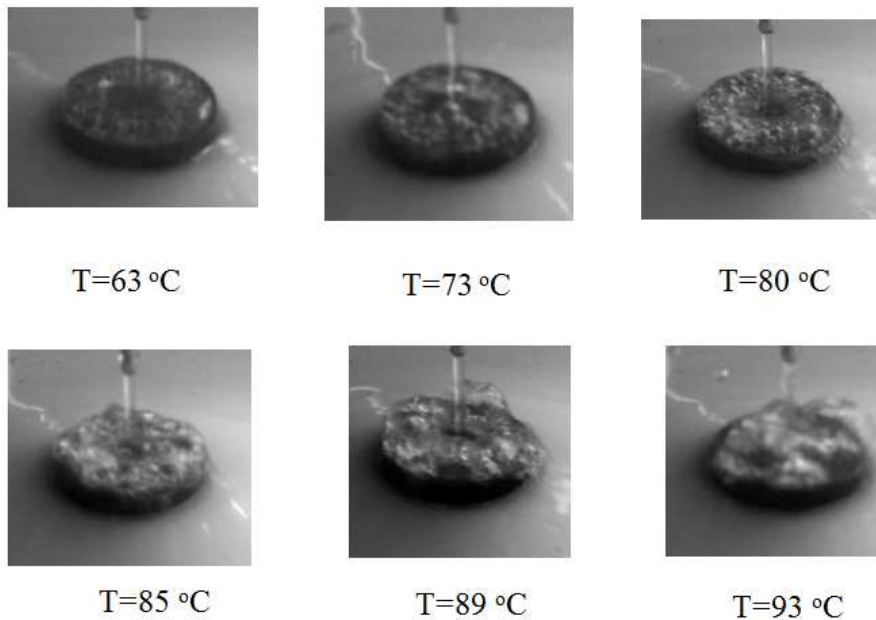
The precision errors,  $U_{x_i}$ , associated with the various measured quantities,  $x_i$ , are summarized in Table II. The bias errors for the thermocouples, pressure gauge, and rotameter were assumed to be negligible, because they had been calibrated. The theory of the propagation of uncertainty was applied to evaluate the 95% confidence uncertainty of the average heat fluxes. The maximum uncertainties associated with the heat flux were obtained to be 4% at 50  $W/cm^2$  and 3% at 100  $W/cm^2$ . Heat flux calculation based on one-dimensional heat conduction assumption was generally 5% lower than the net power supplied to the heater cartridges. It is consistent with expected losses due to the free convection from the heated surface.

## 4.4 Results and discussion

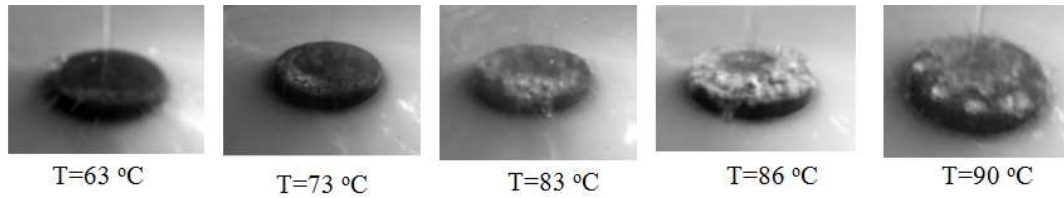
### 4.4.1 In the absence of electric field

Flow visualization may reveal the difference between the liquid sheets at small and large jet lengths. Fig. 4 shows photographs of the jet of HFE7100 striking the upward facing heated disk at different surface temperatures. In this case the saturated jet is issued from a 15g needle at 20  $cc/min$  volumetric flow rate. The jet length is small (only 5  $mm$ .) The

calculated exit velocity is about  $0.23 \text{ m/s}$  and the measured diameter decreases to 91%. This corresponds to an increase in the axial velocity of less than 10%. For such a small jet length, the thin liquid sheet is developed in a limited area around the stagnation point. This small region around the stagnation zone with the thin sheet is followed by a suddenly thick layer region generated by the circular hydraulic jump formation. The position of the hydraulic jump moves towards the center of the target as the surface temperature increases. The generated vapor bubbles in the nucleation boiling process around the rim of the disk serve as a physical barrier and boost the hydraulic jump with a larger increase in thickness. By increasing the surface temperature, as more nucleation sites are activated, the number of bubbles increases and this physical barrier extends to the center of the heater. Thus, the hydraulic jump occurs at smaller radial distances. At the CHF regime, the coolant layer around the rim is comparatively thick and the liquid sheet momentum is not large enough to push the bubbles off the target.



**Figure 4: Photographs of saturated jet of HFE7100 issued from 15g needle striking a heated disk at different surface temperatures. The volumetric flow rate is 20 cc/min and the jet length is 5 mm. The heat transfer area is 8 mm.**



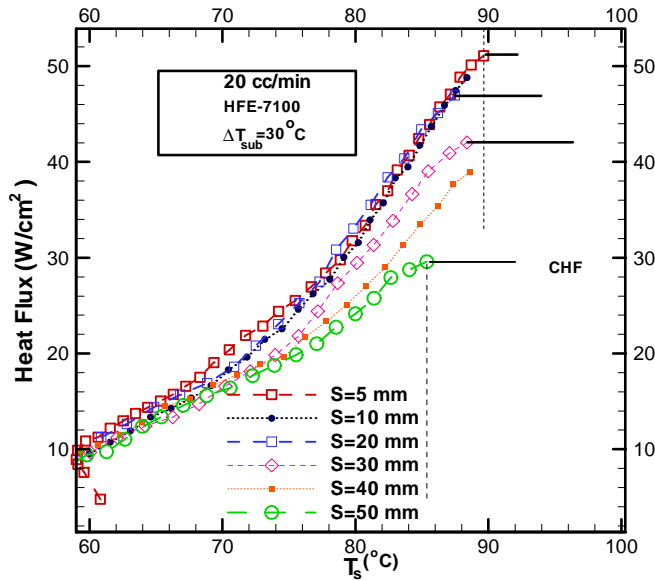
**Figure 5: Photographs of saturated jet of HFE7100 issued from 15g needle striking a heated disk at different surface temperatures. The volumetric flow rate is 20 cc/min and the separation between the jet and heated disk is 50 mm.**

Fig.5 shows photographs of a saturated jet of HFE7100 striking the disk with ten times larger jet length (50 mm) at different surface temperatures. All the experimental conditions were identical except the distance between the jet and heated target. The measured effective diameter of the falling jet over the target shows a 53% decrease with respect to the exit jet diameter at a volumetric flow rate of 20 cc/min. This corresponds to increase in impingement velocity of more than 400%. These measured reductions in the cross sections were consistent with the theoretical expectations presented in Eq. (4-a). In general, a clear difference between the appearance of the liquid sheet presented in Fig.4 and Fig.5 is noticeable. For the large jet lengths, the effective diameter of the jet is considerably reduced and the effective velocity of the striking jet becomes higher. This may result in thin sheets with high momentum. Since the momentum in the sheet is comparatively large, the circular hydraulic jump occurs at radial distances larger than the heater diameter for a wide range of surface temperature and has virtually no effect on the boiling characteristic curves. Thin sheets resulting from the jets with large lengths are hydrodynamically unstable. The thin films are more likely to be ruptured, particularly around the rim of the target. This leads to the local formation of several semi-dry spots and early burnout at low superheats. As another qualitative difference, for jets with large lengths, their associated liquid sheet escapes off the heated target and creates a spray of tiny droplets, while for the small lengths the excess liquid smoothly flows off the heated surface.

Fig.6 presents the boiling characteristics of falling jet of HFE7100 issued from a 15g needle for various jet lengths ranging between 5 to 50 mm at 20 cc/min volumetric flow

rate. Variation of the jet length from 5 mm to 50 mm shows only a slight change in boiling curves at low superheats. However, the boiling curves in both the nucleation and CHF regimes varies for different jet lengths. For example, the CHF as high as  $50 \text{ W/cm}^2$  at  $90^\circ\text{C}$  can be achieved at 5 mm jet length. By increasing the jet length to 50 mm, the CHF decreases to  $28 \text{ W/cm}^2$  and occurs at  $86^\circ\text{C}$ . For instance, comparing the CHF measured for 5 mm –length jet with the CHF of 50 mm-length jet shows that the CHF enhances 78% for reduced length at 20 cc/min flow rate.

In order to study the effect of jet length on boiling characteristics, the volumetric flow rate was slightly increased to 30 cc/min. Fig.7 shows the boiling curves for HFE7100 jets produced by a 15g needle with different jet length at higher volumetric flow rate.



**Figure 6: HFE7100 Boiling curves obtained by 15g needle for different jet lengths at 20 cc/min.**

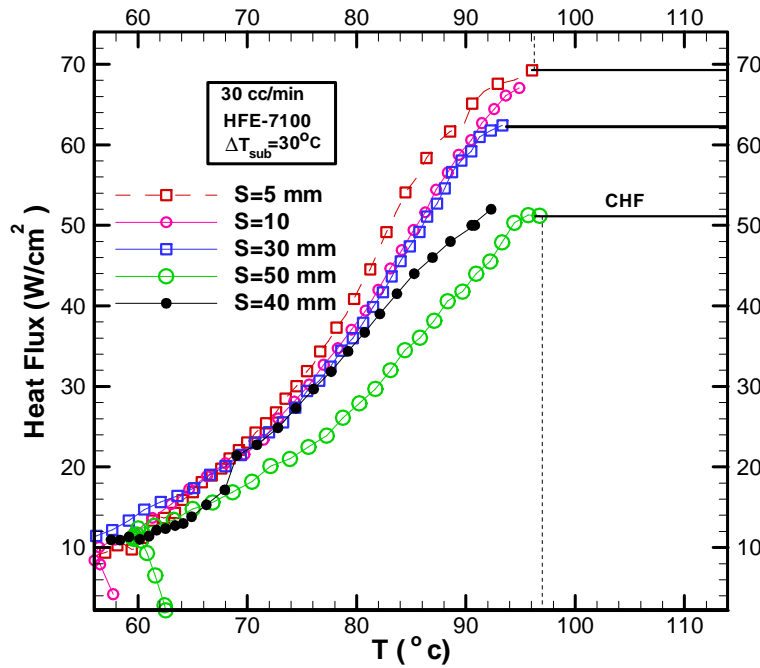


**Figure 7: HFE7100 Boiling curves of falling jets issued by 15g needles for different jet lengths at 30 cc/min.**

Decreasing the jet length leads to CHF enhancements of about 40% for identical length reductions (from 50 mm to 5 mm) at 30 cc/min. By increasing the flow rate the CHF enhancement due to the effect of reduced jet length decreases. In order to explain this decrease in CHF enhancement for increased flow rates, one should note that the effect of cross section reduction due to the gravitational acceleration becomes smaller. Moreover, since the heated target area is typically small, the hydraulic jump occurs at radial distances larger than the heater diameter for all jet lengths. Therefore, the thickness of the liquid sheet shows only small changes for various tested range of jet lengths. Consequently, the CHF enhancement due to the jet length variation is smaller at higher flow rates. According to this explanation, it is expected that the boiling curves show no appreciable change by variation of jet length at high enough flow rates.



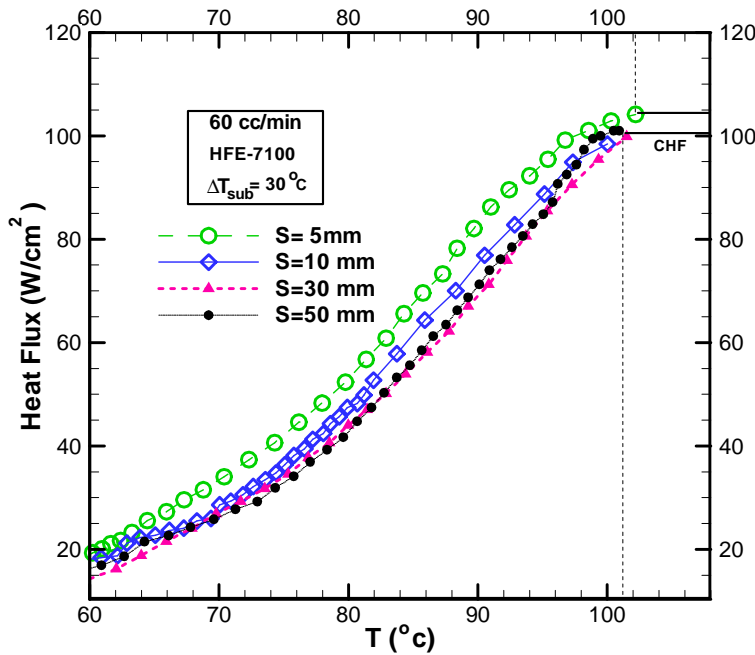
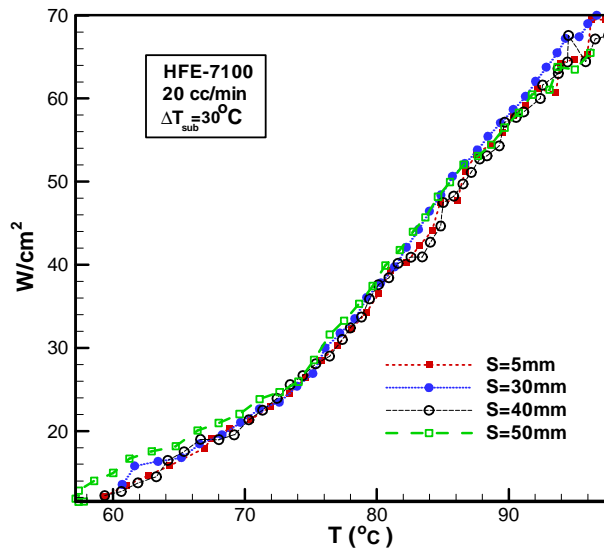


**Figure 8: HFE7100 Boiling curves of jets issued by 15g needle for different jet lengths at 60 cc/min.**

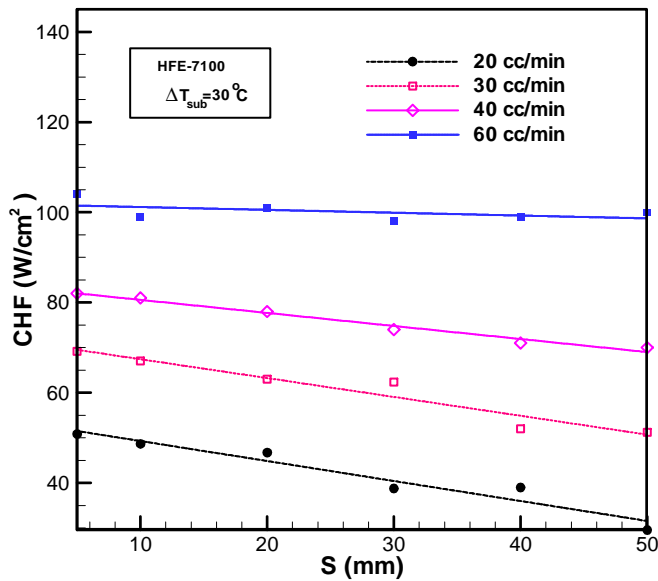
In order to test the above hypothesis, the experiments were repeated at 60 *cc/min* volumetric flow rate and the boiling curves obtained are given in Fig. 8. For such high volumetric flow rate, the boiling curves fall approximately on a universal graph for different jet lengths thus the CHF regime is clearly not sensitive to the jet length. Visual observations of the liquid sheet at these high flow rates show that the liquid sheet uniformity is qualitatively not a function of jet length. This is expected since the inertia of the high momentum jet is dominant and the cross section of the falling jet shows no measurable change. Accordingly, the boiling curves become approximately identical for all different jet lengths. The burnout mechanism elaborated in [18] is consistent with our current observations at 60 *cc/min*.

Fig. 9 presents the boiling curves of the HFE7100 jet issued from a smaller needle diameter (20g) for various jet lengths at 20 *cc/min*. The boiling curves for all jet lengths ranging from  $S=5\text{ mm}$  to 50 *mm* fall on a universal graph. The cross section of the jet produced by a 20g needle is not affected by gravity/surface tension interactions and it cannot be considered as a “free-falling jet”, thus, the boiling curves corresponding to the

jet are not influenced by variation of jet length. Therefore, we use the term “impingement jet” instead of “falling jet” for such circular high-speed jets.



**Figure 9: HFE7100 Boiling curves of jets issued by 20g needle for different jet lengths at 20 cc/min.**



**Figure 10: Effect of jet lengths on measured CHF at different volumetric flow rates using 15g needle.**

Fig.10 summarizes the measured CHF for different jet lengths at different volumetric flow rates. As expected, the slope of the variation at lower flow rates is steeper than that of higher flow rates. The impinging jet behavior at low flow rates is similar to the falling jets and its velocity and cross section are affected by gravity/surface tension interaction. In contrast, for higher flow rates, the inertia of the jet becomes significant so that the effect of gravity/surface tension interaction becomes negligible for the tested jet heights.

In order to compare the current results with the previous studies, the Sharan and Lienhard correlation (S-L) [9] was selected. The correlation was able to predict extensive sets of previous measured CHF within  $\pm 20\%$  of accuracy.

In order to consider the effect of jet length in S-L correlation, the cross sectional jet radius reduction coefficient,  $\Gamma r_{ext}$ , is used instead of the exit jet radius,  $r_{ext}$  as:

$$\frac{CHF}{\rho_g h_{fg} V_{ext}} = \left( 0.21 + 0.0017 \rho_f / \rho_g \left( \frac{\Gamma r_{ext}}{r_{heater}} \right)^{1/3} \left( \frac{1000 \rho_g / \rho_f}{We_{D_{heater}}} \right)^A \right) \quad (6)$$

$$A = 0.486 + 0.06052 \ln r - 0.0378 (\ln r)^2 + 0.00362 (\ln r)^3$$

where  $r = \rho_f / \rho_g$ . For HF7100 working fluid the value of  $A$  was calculated to be 0.299. It should be noted that the increase in velocity magnitude is not included in the correlation given by Eq. (6). If one includes the velocity increase factor of  $\Gamma^{-1/2}$ , the CHF becomes proportional to  $\Gamma^{-0.76}$ . With this analysis, the CHF is expected to increase by increasing the jet length. However, the experimental observations revealed that the CHF decreases by increasing the jet length. In order to resolve this inconsistency with the S-L correlation, it was postulated that the effective ratio of the jet diameter to the heater diameter is of first order importance and the velocity is second order parameter for very small flow rates. This postulation comes from the presented earlier observation and measurements. For instance, for jets with large lengths the increase in the impact velocity due to the cross sectional reduction was reported to be more than 400%. According to the Lienhard and Eichhorn model [18] one may expect CHF enhancement in the order of 400%, while measured CHF for large lengths showed more than 70% suppression. This highlights the effect of cross sectional area reduction for large lengths and its impact on

liquid sheet stability. Based on this discussion, the reduction coefficient is only applied for  $\frac{\Gamma r_{ext}}{r_{heater}}$ . For this case, the CHF is proportional to  $\Gamma^{1/3}$ , where  $\Gamma \leq 1$ , and the correlation is consistent with the observations.

The earlier postulation of the effect of hydraulic jump intervention in affecting the boiling characteristics can be further confirmed by comparing the current results and the adjusted S-L correlation. Referring to Fig. 3, for volumetric flow rates of 20 *cc/min*, the hydraulic jump occurs within the diameter of the disk for jet length smaller than 20 *mm*. For jet lengths of 20 *mm* and longer, the hydraulic jump position is located at the rim. For all the flow rates, by increasing the jet length to the values larger than 25 *mm*, the hydraulic jump occurs virtually beyond of the test section, thus it has no effect on the boiling characteristics. As shown in Fig. 11, the measured CHF of jets with lengths smaller than 25 *mm* can be predicted by the adjusted correlation within 20% of accuracy with more than 97% confidence. However, for jet lengths larger than 25 *mm* and flow rates smaller than 40 *cc/min*, the CHF predictions show larger disagreement. The measured values of CHF in the presence of hydraulic jump are also found to be systematically lower than that of predicted by the S-L correlations.

This may support the earlier postulation that the hydraulic jump increases the liquid sheet thickness around the impingement zone and this may lead to heat transfer suppression. Moreover, the liquid sheet instability rather than radial velocity plays the primary role in determining the CHF magnitude for low flow rate jets with large lengths. Thus, the S-L correlation must be further revised for large jet lengths at low flow rates with a more complicated model including the upstream stability of the film and the hydraulic jump effect. The hydraulic jump issue may cause significant suppression in CHF for larger heater diameters at moderate or even high flow rates. Therefore, similarly to Sharan and Lienhard's semi-empirical approach, one may develop a more complicated model and consider the effect of upstream liquid sheet instability and hydraulic jump effect in the energy balance equation to determine the kinetic energy of the liquid sheet upstream and downstream of the sheet over the heated target.

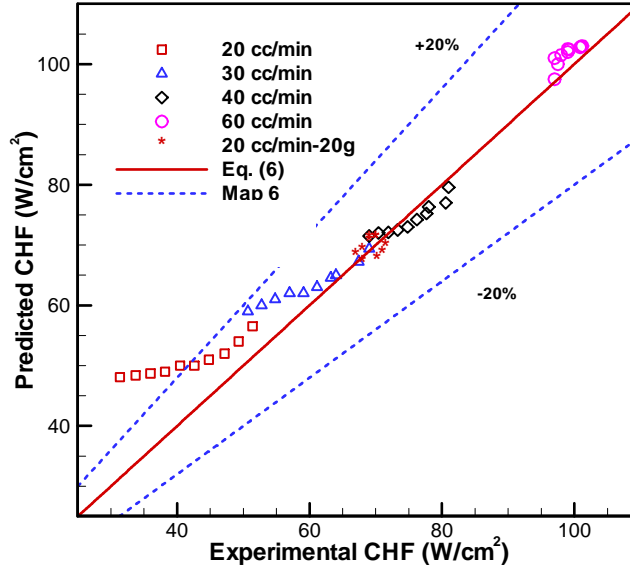


**Figure 11: Comparison between all measured CHFs in the present work and the adjusted correlation Eq. (6).**

#### 4.4.2 Effect of electric field on CHF for jet impingements

According to the our experimental observations for falling jets, as burnout is approached, the horizontal sheet of liquid around the rim of circular disk remains intact and spray above the liquid sheet is fine. The horizontal flow suddenly stops and spray above the sheet becomes coarse, and the angle between the plate and the spray increases. The liquid sheet ceases to absorb kinetic energy and to protect the heated surface, which is insulated by the vapor around its periphery.

Supplying kinetic energy to the edges of the circular liquid sheet around the rim of the disk is essential to enhance the critical heat flux. As shown above, a simple way to increase the momentum of liquid sheet around the rim is to increase the volumetric flow rate. Increasing the flow rate may cause critical heat flux deferral, however, the main drawback of the mass flow rate increment is increasing the size and dimensions of the cooling circuit elements such as pumps and condenser and wasting a large volume of coolant since significant part of the coolant just provide larger momentum to the liquid sheet and does to contribute in heat transfer enhancement. An alternative way to enhance

the momentum of the liquid sheet around the edge is to introduce EHD forces. A visualization of the boiling heat transfer in the presence of electric field is presented in Fig. 12. Here EHD flow helps to enhance the momentum transportation to the rim of heated target and improve the rewetting process. As it can be observed in Fig. 12, in the pre-CHF regime (at surface temperatures around 92 °C), the electrostatic forces tend to keep the coolant over the heated surface by establishing a cone-shape structure over the heated disk. Compared with the case that the electric field is absent, the hydraulic jump effect does not appear and the coolant layer is more uniform. Fig. 13 compares typical boiling curves in the presence and absence of electric field for the jet lengths of 4 mm at 6 cc/min volumetric flow rate. In the presence of electric field, CHF shows more than 100% enhancements at applied voltage about 11 kV. Moreover, the CHF occurs at higher superheats of about 92 °C. Comparing Fig. 13 with Figs. 6 and 7 shows that approximately the same CHF enhancements (achieved by applying electric field) can be obtained by supplying two to three times larger volumetric flow rates of the coolant. It is worthy to note that although higher heat transfer enhancements may be expected for thinner liquid films over the surface, these results show that the more hydrodynamically stable liquid films, which are typically thicker, cause significant heat transfer enhancements for the CHF regime. Vigorous rewetting of the heated surface in the presence of electric field is believed to be the main mechanism for electric field-assisted CHF enhancements. The present results are consistent with the previous results for mono-dispersed droplet cooling. Rewetting of the surface with thick layer of coolant is of primary importance in CHF heat transfer enhancement rather than developing thinner films over the heated target.

Fig. 14 shows the effect of electrostatic forces on heat transfer enhancement at CHF regime. By increasing the volumetric flow rate, the effect of electrostatic forces in heat transfer enhancement is reduced. This is attributed to the fact that the main flow resulting from the jet is dominant at high flow rates and the electrostatic forces cannot further intervene in hydrodynamics of the jet. Therefore, the CHF heat transfer enhancement in the presence of electrostatic forces is only promising for relatively small or intermediate range of volumetric flow rates.

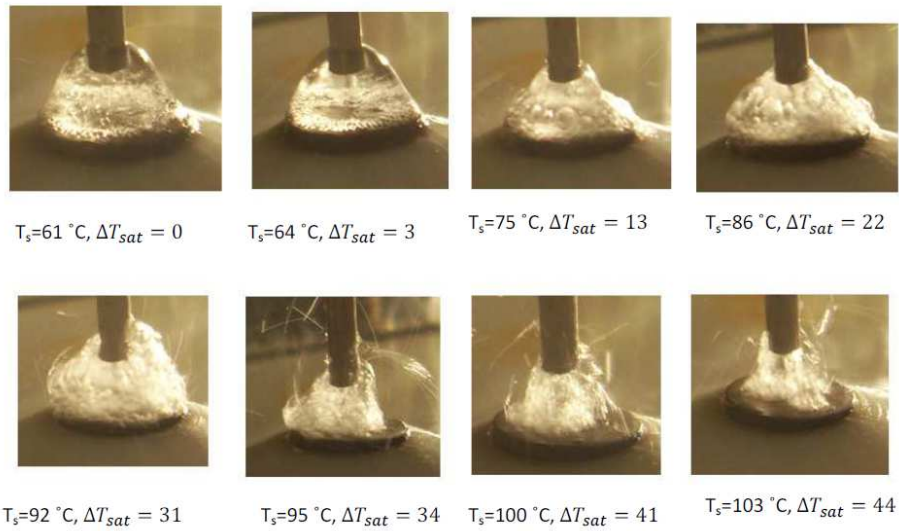


**Figure 12: Experimental visualization of boiling heat transfer enhancement of HFE-7100 in the presence of strong electric field. The needle was 15g hypodermic needle. The volumetric flow rate was 6 cc/min. Applied voltage is 9 kV DC and separation between electrode was measured to be 4 mm.**

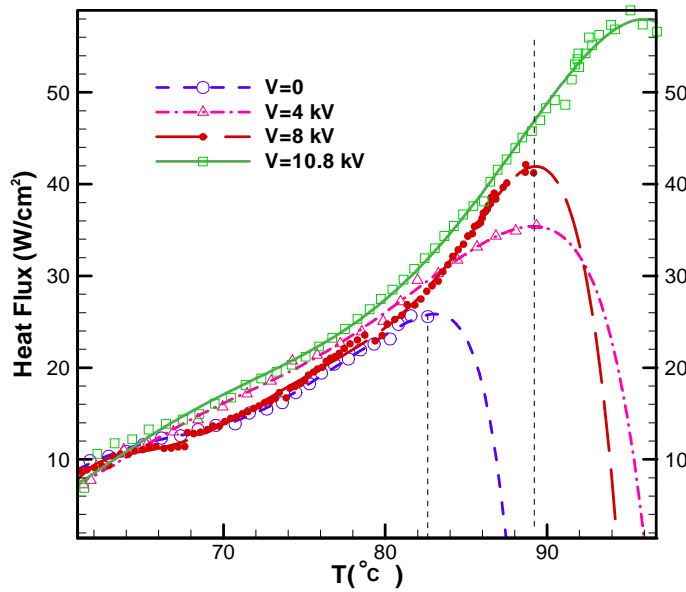


**Figure 13: Boiling curves of HFE-7100 at different applied voltages. Jets were issued using 15g hypodermic needle. The separation between the target and jet was 4 mm and volumetric flow rate kept constant at 6 cc/min.**

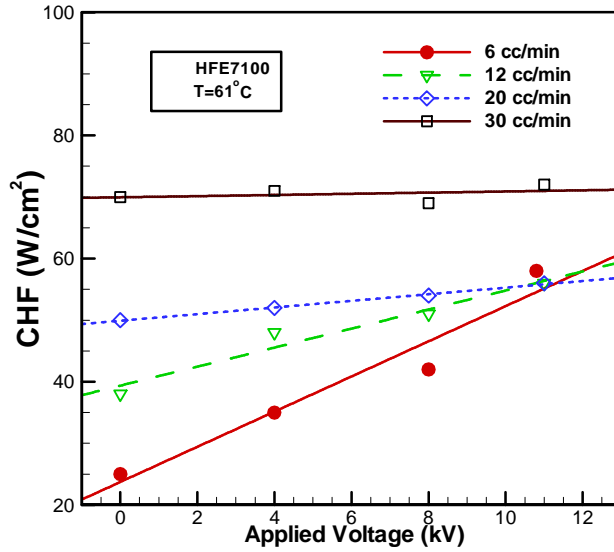


**Figure 14: Variation of CHF with applied voltage at different volumetric flow rates. Jets were issued using 15g hypodermic needle. The separation between the target and jet was 4 mm.**

## 4.5 Conclusions

The effect of jet length on two phase free falling circular jet of HFE7100 striking on an upward-facing heated disk was experimentally investigated. It was demonstrated that for low speed jets, the jet length is a key parameter in determining the boiling curve, particularly at the CHF regime. By increasing the jet length at low flow rates, the cross section of the jet reduces due to surface tension/gravity interactions while the effective velocity increases and this may result in thinner liquid sheets. The thinner sheet can be ruptured more easily and this may lead in a pre-mature CHF. For high-speed jets, the jet cross section and axial velocity do not show measurable change for various jet lengths. In this case,  $\Gamma \sim I$  and the original S-L correlation and the revised correlation are identical. Comparing the present measured values of CHF with the previous correlation revealed that good agreement can be achieved by considering the cross sectional reduction coefficient in the correlation; however, for those CHF results where the hydraulic jump occurs within the heater diameter, the S-L correlation systematically predicts higher CHF. This suggests that the S-L correlation must be revised based a new model including the hydraulic jump suppression effect. The electrostatic effect showed



significant effect on the hydrodynamics of the falling jet and the amount of heat removal at relatively low flow rates. More than 100% CHF enhancement was achieved with 10.8 kV applied voltage at 6 cc/min volumetric flow rate. The electric field heat transfer enhancement effect reduces by increasing the flow rate. This suggests that the EHD enhancement through electric field for falling jets is more effective at low flow rates.

## References

- [1] K.A. Estes and I. Mudawar, Comparison of two-phase electronic cooling using free jets and sprays, *J. of Electronic Packaging* 117 (1995) 323–332.
- [2] I. Mudawar, Assessment of high-heat-flux thermal management schemes, *Component and Packaging Technologies*, 24(2) (2001) 122-141.
- [3] A. Giesen, H. Hugel, A. Voss, K. Wittig, U. Brauch and H. Opower, Scalable concept for diode-pumped high-power solid-state lasers, *Applied Physics B: Lasers and Optics* , 58(5) (1994) 365-372.
- [4] Y. Katto and S. Yokoya, Critical heat flux on a disk heater cooled by circular jet of saturated liquid impinging at the center, *Int. J. of Heat and Mass Transfer*, 31(2) (1988) 219-227.
- [5] M. Monde and Y. Katto, Burnout in a high heat-flux boiling system with an impingement jet, *Int. J. of Heat and Mass Transfer*, 21 (1978) 295-305.
- [6] Y. Haramura and Y. Katto, A new hydrodynamic model of critical heat flux, applicable widely to both pool and forced convection boiling on submerged bodies in saturated liquids, *Int. J. of Heat and Mass Transfer*, 26 (1983) 389–399.
- [7] I. Mudawar and D. E. Maddox, Critical heat flux in subcooled flow boiling of fluorocarbon liquid on a simulated electronic chip in a vertical rectangular channel, *Int. J. of Heat and Mass Transfer* ,32 (1989) 379–394.

- [8] M. Monde and Y. Okuma, Critical heat flux in saturated forced convective boiling on a heated disk with an impinging jet—CHF in L-regime, *Int. J. of Heat and Mass Transfer*, 28(8) (1985) 547–552
- [9] A. Sharan and J.H. Lienhard, On predicting burnout in the jet-disk configuration, *J. of Heat Transfer*, 107(2) (1985) 398-401.
- [10] J.W.M Bush, J.M. Aristoff and A.E. Hosol, An experimental investigation of the stability of the circular hydraulic jump, *J. of Fluid Mech.*, 558 (2006) 33-52.
- [11] E.J. Watson, The radial spread of a liquid jet over a horizontal plane, *J. of Fluid Mech.*, 20 (1964) 481-499.
- [12] X. Liu and J.H. Lienhard, The hydraulic jump in circular jet impingement and in other thin liquid films, *Exp. in Fluids*, 15 (1993) 108-116.
- [13] M. Masanori and O. Yoshiaki, Critical heat flux in saturated forced convective boiling on a heated disk with an impinging jet—CHF in L-regime, *Int. J. of Heat and Mass Transfer*, 28(3) (1985) 547-552.
- [14] M. Monde and T. Inoue, Critical heat flux in saturated forced convective boiling on a heated disk with multiple impinging jets, *J. of Heat Transfer*, 113(3) (1991) 722-727.
- [15] Y. Qiu and Z. Liu, Critical heat flux in saturated and subcooled boiling for R-113 jet impingement on the stagnation zone, *App. Thermal Eng.*, 25(14-15) (2005) 2367-2378.
- [16] D.E. Hall, F.P. Incropera and R. Viskanta, Jet impingement boiling from a circular free-surface jet during quenching: part 2-two-phase jet, *J. of Heat Transfer*, 123(5) (2001) 911-917.
- [17] S.G. Kandlikar and A.V. Bapat, Evaluation of jet impingement, spray and microchannel chip cooling options for high heat flux removal, *Heat Transfer Eng.*, 28(11) (2007) 911-923.

- [18] J.H. Lienhard and R.Eichhorn, On predicting boiling burnout for heaters cooled by liquid jets, *Int. J. of Heat and Mass Transfer*, 19 (1976) 1135-1142.
- [19] M.L. Sawyer, S.M. Jeter and S.I. Abdel-Khalik, A critical heat flux correlation for droplet impact cooling, *Int. J. of Heat and Mass Transfer*, 40(9), 1997, pp.2123-2131.
- [20] M.L. Sawyer, High intensity heat transfer to a stream of monodispersed water droplets, PhD thesis, Georgia Inst. of Technology, Atlanta, GA, 1996.
- [21] M.S. El-Genk and H. Bostanci, Saturation boiling of HFE-7100 from a copper surface, simulating a microelectronic chip, *Int. J. of Heat and Mass Transfer*, 46, 2003, pp.1841-1854.

## Chapter 5

### Study of Electrohydrodynamic Micropumping Through Conduction Phenomenon

#### 5.1 Introduction

The operation of electrohydrodynamic (EHD) micropumps is based on the interaction between electric fields and electric charges in a dielectric fluid. The electric body force  $\vec{f}$  in a dielectric liquid that results from an imposed electric field  $\vec{E}$  can be expressed as [1]:

$$\vec{f} = \rho_c \vec{E} - \frac{1}{2} \vec{E}^2 \nabla \epsilon + \frac{1}{2} \nabla \left[ \vec{E}^2 \rho \left( \frac{\partial \epsilon}{\partial \rho} \right)_T \right] \quad (1)$$

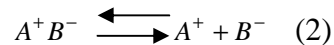
where  $\rho_c$  is volume charge density,  $\epsilon$  is the fluid permittivity and  $\rho$  is the fluid density,  $T$  is the fluid temperature.

The first term on the right hand side of the Eq.(1) is the electrophoretic, or Coulombic, force that results from the net free space charges in the fluid. The second term, known as the dielectrophoretic force, arises from the permittivity gradient. The last term, called the electrostrictive force, is important only for compressible fluids and two phase flows. Free space charges in dielectric liquids can be generated by three different mechanisms. I) Induction: occurs in dielectric liquid with variable electrical conductivity, which can be caused due to the presence of a thermal gradient, or in two or multi phase flows, II) Conduction: through dissociation-recombination reactions in the areas adjacent to the electrodes, III) Injection: by direct charge injection from the solid/liquid interface. These three distinctive mechanisms for free space charge generation can be exploited to create induction, conduction and injection EHD pumping effects [4].

For an isothermal single phase dielectric liquid, the last two terms of Eq.(1) vanish and EHD pumping operation requires the existence of net space charge in the presence of an electric field to produce a Coulombic force. Because an induction EHD pump requires a fluid non-homogeneity for its operation, it cannot be utilized for isothermal single phase

liquid pumping purposes. Therefore, there are only two possibilities to produce free space charge: ion injection and dissociation mechanisms. Ion drag pumps are based on direct ion injection from a charged electrode surface to the liquid. As a main disadvantage, these pumps cause degeneration of the working fluid and its electrical properties, thus, they are not reliable for long term operation [2]. The typical electrode life time in ion injection pump was reported to be less than one hour [3]. The chemical reactions cause serious electrode damages, which affect the static head generation produced by the micropump. In contrast, conduction pumping is based on interaction between the electric field and charge carriers, which result from the dissociation-recombination reactions around the electrodes submerged in a low conductivity dielectric liquid. A similar effect in liquids with high electrical conductivity, such as electrolytes, is called electroosmosis. The feasibility of conduction pumps has been proven for non-isothermal liquids and two phase flow applications [4]. Elimination of the direct ion injection and their operation in both isothermal and non-isothermal dielectric liquids makes them potentially attractive in many applications.

The conduction mechanism in weakly conductive dielectric liquids is a complicated phenomenon. When a relatively small electric field (below  $0.1\text{V}/\mu\text{m}$ ) is established between a low potential and a high potential electrode immersed in a dielectric liquid, the ion injection is negligible, but the liquid impurities adjacent to the electrodes may begin to dissociate. The process of dissociation of the neutral species and recombination of the created ion pairs can be schematically written as follows [5]:



By increasing the applied voltage, but before reaching some threshold value of electric field (approximately  $0.1\text{ V}/\mu\text{m}$ ), the existing ions due to the dissociation of neutral species experience strong enough electrical Coulomb force, which concentrates the positive and negative ions around counter-polarized electrodes. The concentrated ions around each electrode form charge layers around them. The ion density distributions in the dielectric liquid bulk can be determined on the basis of the conservation law of neutral species. The attraction between the electrodes and the charges results in a net

fluid flow from the blunt electrode towards the electrode having smaller radii of curvature. The conduction mechanism in this regime is mainly due to the ionic dissociation and is referred to as EHD conduction pumping. Further increasing of the electric field (in the order of  $10\text{V}/\mu\text{m}$ , depending on the liquid characteristics and impurity concentration), results in ion injection from the liquid/metal interface and produces a reverse pressure. Beyond this threshold, the ion-injection pumping mechanism will be dominant [6] and the pumping direction is reversed.

The concept of the charge generation through the dissociation phenomenon has been known for long time [1], but the idea of using this phenomenon for pumping dielectric liquids is comparatively new [20]. Several theoretical [6,17], numerical [12,15,18,19] and experimental works [5,13,21,16] were carried out to determine the feasibility of EHD pumping through the conduction phenomenon. In all of the previous studies, commercial refrigerants R-123, R-134a and N-Hexane were introduced as working fluids to a single or multi-stage pump with the electrode spacing in the order of millimeter and the steady-state static pressure generation of the pump was determined. Furthermore, several geometries for high voltage electrodes were investigated to increase pressure generation [21]. The initiation of a typical macro-scale conduction pumping for R-123 was observed for voltages in the order of 5 kV DC.

The main motivation in miniaturization of the EHD pumps is to shrink the separation between the electrodes in order to generate an intense electric field over a small volume of the working fluid even with reduced applied voltage for lab-on-a-chip applications. In this article, an EHD micropump is referred to a device with an electrode spacing,  $d$ , in the order of  $d \leq 10^{-4}\text{m}$ . Typically, scaling down an EHD pump electrode spacing from macro- to micro-scale reduces the level of applied voltage required for the operation as much as one or even two orders of magnitude. This significant change in the operating voltage eliminates the need for a high voltage power supply. Moreover, EHD pumping of the dielectric liquids used for heat transfer, such as high Prandtl number liquids (transformer oils), fluorinert dielectric liquids [10] with low boiling temperature and high latent heat of vaporization, cryogenic liquids [32] and other commercial refrigerants,

shows promising performance in recent advanced cooling systems. Accordingly, scaling of the EHD pumps to smaller sizes can be potentially attractive in microfluidic devices.

A survey of the literature for micro-scale EHD pumps shows that the miniaturization of ion drag pumps has been the subject of many investigations [28,33]. Bart et al. [7] and Richter et al. [8] proposed preliminary designs for an ion injection micropump. Ahn [9] studied an ion drag micropump with 30-mm channel length and a planar electrode pair on a glass substrate. Two different designs with emitter-collector spacing of 100 and 200  $\mu\text{m}$  were fabricated. The device was operated in the range of applied voltages between 20 and 130 V DC. Static pressure heads up to 200 Pa at 110 V applied voltage was achieved with 100  $\mu\text{m}$  gap spacing using ethylene glycol. Darabi et al. [10] developed an ion drag pump consisting of 50-90 pumping stages with 100  $\mu\text{m}$  electrode gaps fabricated on an alumina substrate. They used HFE-7100 (3M Co.) as a dielectric working fluid and obtained static pressure heads up to 700 Pa at 300 V applied voltage. Recently, several attempts were carried out to find a suitable high resistivity material to protect the electrodes and working fluid against oxidation and aging due to the ion injection at the solid-liquid interface. Yang et al. [3] fabricated an ion drag micropump with indium-tin oxide (ITO) as a material resistant against corrosion for the electrodes instead of using conventional electrode materials, such as evaporated Cr/Au [10]. More stable operation of the micropump without visible damages of the ITO electrodes was initially observed and looked promising. However, in subsequent tests the life-time of the electrodes at 15 V DC applied voltage was only 6 minutes. This short life-time of the electrodes and deterioration of the thermophysical properties of the working fluid due to the significant electrochemical effects during the operation [2] are the main disadvantages of the ion drag micropumps and recently fewer investigations have been carried out to improve such designs.

Although there have been these several attempts to scale down the ion injection pumps and decrease the operating voltage level, there were no similar attempts to miniaturize the conduction pumps mainly because they have been proposed just recently. Also, to the best of the authors' knowledge, few investigations have been carried out to match the experimental results and the numerical simulations for the conduction pumping [14].

Moreover, in all of the numerical and experimental studies, the effect of conduction pumping has been reported with only three dielectric liquids, R-123, R-134a and N-Hexane [15, 17-21,16]. In the present work, an axisymmetric single-stage micro-scale conduction pump in the vertical configuration was designed, fabricated and tested using three different working fluids: 10-GBN Nynas and Shell Diala AX transformer oils, and N-hexane. At steady-state operation and in the absence of the fluid flow, the static generated pressure and electric current of the device were measured at different applied voltages. In order to find an estimate for the charge density distribution and the electric field variation in the micropump, and further verify the experimental results, a numerical study based on the double-species bipolar conduction model was performed. The pressure generation was predicted numerically and compared with experimental results at different applied voltages.

## 5.2 Electrode design for a conduction micropump

In order to exploit charge carriers generated by the conduction mechanism for pumping purposes, the electrode geometry should be designed properly to form an effective hetero-charge layer. For conduction pumping, high voltage electrodes are needed to provide a large projected area perpendicular to the flow direction or pressure gradient [21]. Moreover, in order to mitigate the ion injection effect at the metal/liquid interface, sharp edges should be avoided. If an imposed electric field is applied to a pair of parallel-plates, a hetero-charge layer is formed adjacent to both electrodes. The Coulombic forces exerted on the heterocharge layers near both electrodes are balanced. Therefore, net flow cannot be produced in this geometry [6]. However, by implementing some small changes in the configuration of the electrodes, one may increase the projected area and achieve a conduction pumping effect. For example, the high voltage electrode may have the form of a series of concentric annuli, fixed parallel to the planar grounded electrode, which is immersed in a dielectric liquid, a section of which is shown in Fig. 1. Heterocharge layers, adjacent to each electrode, are formed and the non-uniform field distribution near the high voltage electrode creates an attraction toward the upper electrode. In this particular configuration, the radial component of the electric force exerted on the hetero-charge layer is balanced and the axial component of the electric



force generates a pressure gradient, eventually causing a net flow in the axial direction. Since the electric field is more intense near the edges of the annuli, the thickness of the corresponding heterocharge layer will be larger and the static pressure across it will be high. Therefore, the flow direction in the micropump is from the grounded electrode towards high-voltage electrode.

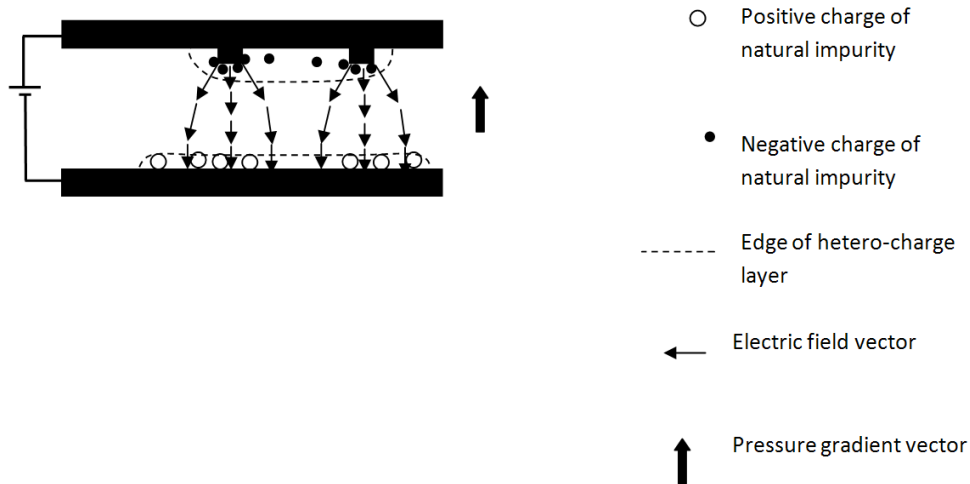


**Figure 1: Qualitative description of electrode design**

In this study, the proposed conduction micropump consists of four components: high voltage electrode, grounded electrode, insulator spacer, and inlet/outlet ports. The printed circuit board technology (PCB) was adapted to pattern the electrode geometries for the micropump. The PCB technology was recently implemented to fabricate several devices such as a magnetic fluxgate sensor [23], RF switch [35] and microfluidic devices [22, 34]. The schematic configuration of the high voltage electrode and grounded electrode of

the micropump patterned on the two substrates are presented in Fig. 2.

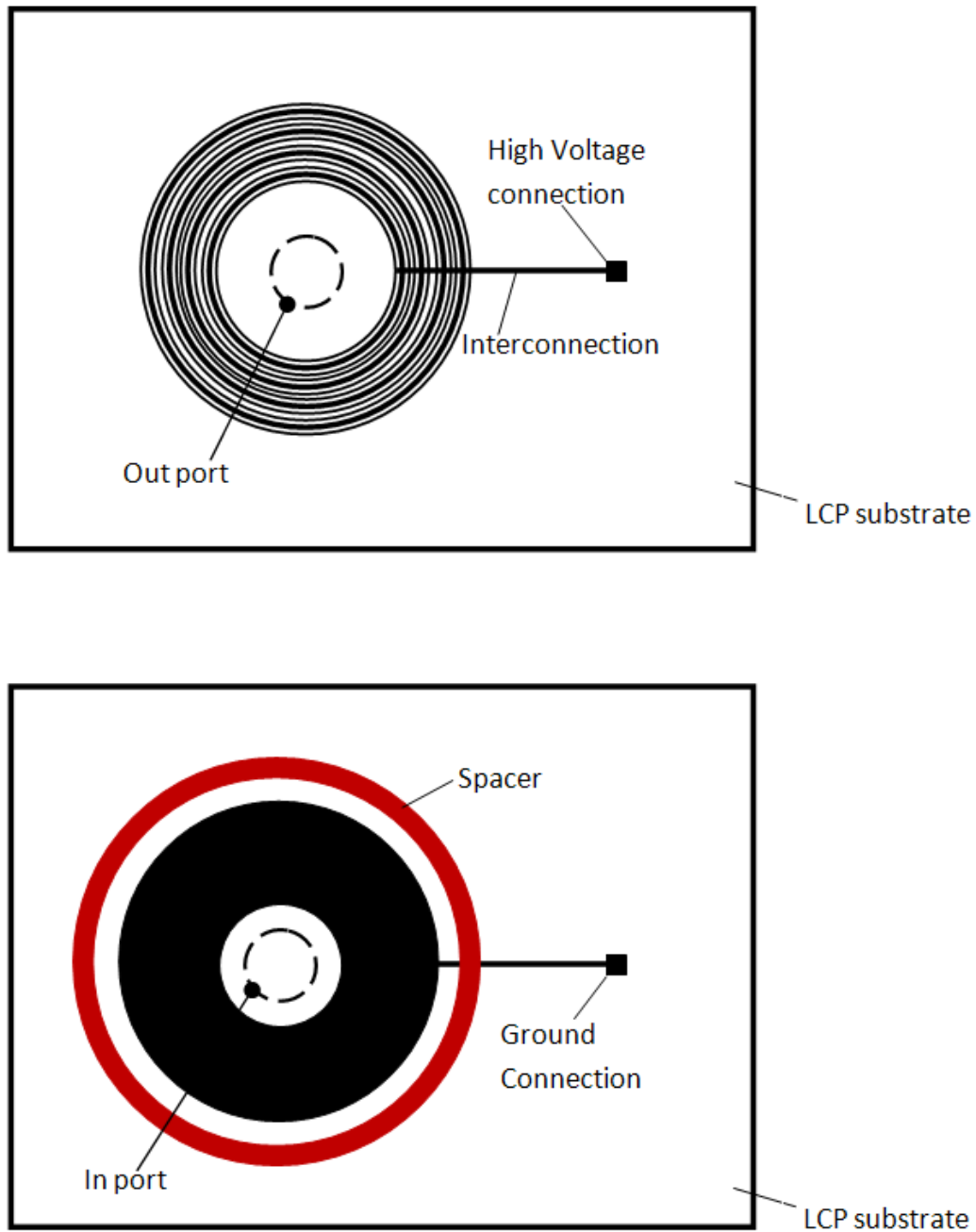
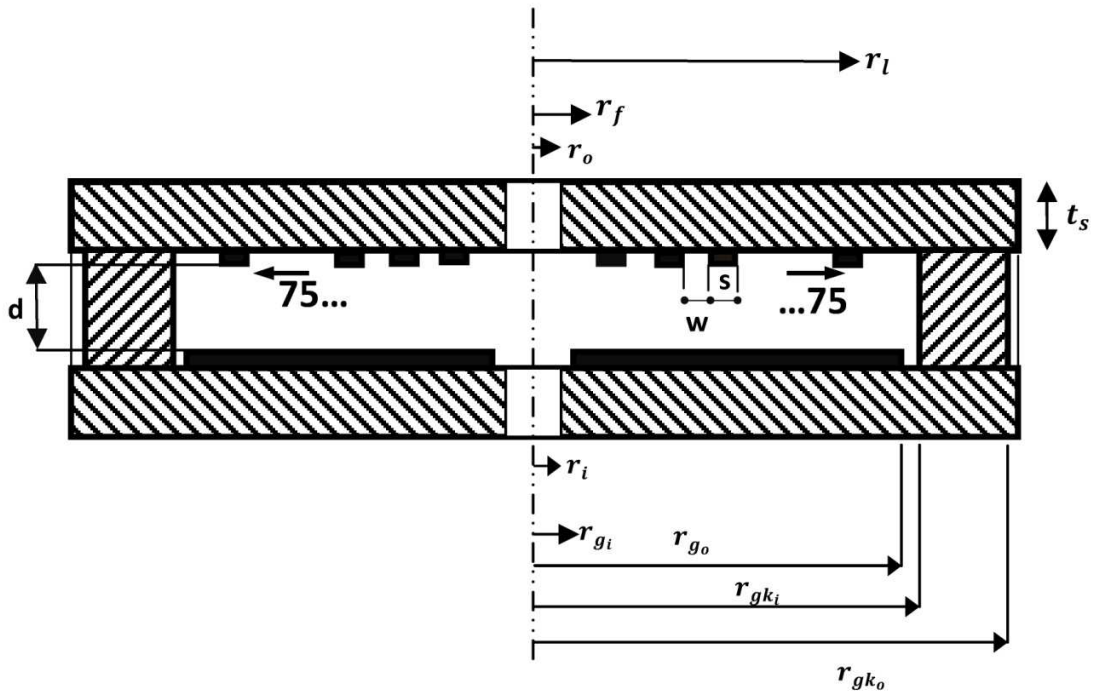


**Figure 2: Top view of (a) high voltage annulus electrodes and (b) grounded electrode patterned on two separate substrates. (Not scaled)**

The high voltage electrode, shown in Fig. 2a, consists of a series of concentric annulus rings patterned on a commercial Liquid Crystal Polymer (LCP) substrate coated with copper cladding using standard lithographic techniques.

A total of 75 concentric annuli each  $25\mu\text{m}$  wide and spaced  $75\mu\text{m}$  apart, were electrically connected together. Considering the 75 ring structures with a thickness of  $30\mu\text{m}$  as a high voltage electrode provides the projected area perpendicular to the axial direction in the order of  $1\text{cm}^2$ . Furthermore, this radial symmetric electrode design helps to minimize the number of sharp points and edges, which are usually encountered in a rectangular planar electrode design, thus minimizing any undesired ion injection. A disc-shaped grounded electrode was patterned on another piece of LCP substrate with the cladding using the same technique. A  $230\mu\text{m}$  thick annulus LCP spacer was utilized to position the two substrates parallel to each other. In order to seal the micropump, a layer of resin epoxy was used on both sides of the spacer. The final spacing between the two electrodes and the total volume of the fluid in the micropump was measured to be  $d=286\mu\text{m}$  and  $0.8\mu\text{L}$ , respectively. Comparing the electrode separation of this device ( $d < 0.3\text{ mm}$ ) with previous macro-scale design ( $d\sim 2\text{ mm}$ ), the current device is expected to operate at one order of magnitude smaller applied voltage. Two identical holes on both substrates, 2-mm in diameter, serve as inlet/outlet ports. The details of the geometry and dimensions are shown in Fig. 3. The performance of EHD micropumps is temperature dependent. Temperature rise in the pumping volume can be induced by Joule heating of the working fluid particularly at higher applied voltages. Therefore, one should be cautious about the thermal effects which may significantly affect the performance of EHD pump. For the presented packaged device, since the total surface area of the pump is comparatively large ( $\sim 60\text{ cm}^2$ ) with respect to the total volume of the micropump, the temperature rise in working fluid is expected to be small. Therefore, in the present work, the variation of ion mobility, permittivity, and electrical conductivity of the working fluid due to thermal effects was assumed to be negligible.



Parameter	dimension(m)
$d$	$2.86 \times 10^{-4}$
$s$	$2.5 \times 10^{-5}$
$w$	$7.5 \times 10^{-5}$
$r_o$	$1.0 \times 10^{-3}$
$r_i$	$1.0 \times 10^{-3}$
$t_s$	$2.1 \times 10^{-3}$
$r_{gi}$	$1.82 \times 10^{-3}$
$r_{go}$	$1.50 \times 10^{-2}$
$r_{gk_i}$	$3.15 \times 10^{-2}$
$r_{gk_o}$	$8.15 \times 10^{-2}$
$r_f$	$8.25 \times 10^{-3}$
$r_l$	$1.41 \times 10^{-2}$

Figure 3: Details of packaged conduction micropump

### 5.3 Experimental apparatus and procedure

The packaged micropump was investigated using three different working fluids. The two transformer oils mentioned earlier were selected due to their low electrical conductivity. Commercial grade Normal Hexane (N-hexane) was also used and it was chosen because it showed no significant pumping effect in the previous macro-scale studies. The  $V$ - $I$  characteristics and the magnitude of generated pressure for this micropump were obtained for each of the different working fluids. The electrical and thermophysical properties of the fluids are tabulated in Table I.

Table.I Electrical and thermophysical properties of the working fluids used in this study at 296.7 K.					
Dielectric liquid	Density $\rho(kg/m^3)$	Viscosity $\nu(cSt)$	Electric Conductivity $\sigma_{eq} \times 10^{12}(S/m)$	Permittivity $\epsilon(pF/m)$	Surface Tension (mN/m)
Shell Diala AX [27]	842.5	20.7	0.47	19.48	27
10-GBN Nynas [26]	860.6	11.44	0.5	19.46	31
N-Hexane [27]	659	0.4	63.9	16.82	18

The charge relaxation time of the dielectric liquids used in this study is typically long. Therefore, the mobility of ions [11], charge density distribution, electric field variation and resultant pressure of the device may be affected by even a weak streaming of the fluid. The vertical positioning of the micropump enabled us to minimize the impact of disturbance and to measure the static pressure generation in the absence of fluid flow. The grounded side of the micropump was positioned at the bottom of a bath of working fluid and the HV side of the pump with the patterned ring structures was positioned at the top.

The micropump was completely submerged in the bath of working fluid and a hypodermic syringe was used to fill it. A variable 0- 3600 V DC power supply with a resolution of 10 V was connected to the upper electrode to provide the necessary voltage for the operation of the micropump. A microammeter was connected between the lower electrode and ground to measure the electric current. In the present work, only the static

operation of the micropump at steady-state condition has been investigated; therefore, no mass flow rate measurement was carried out. In order to measure the generated static pressure at different values of applied voltage, a transparent tube 2mm in diameter and 20mm long was perpendicularly connected to the pump outlet. After reaching the steady-state condition, the column of working fluid is at a position where the electric body force is balanced with the weight of the column. Both the column rise due to the capillary action and conduction pumping were measured for different working fluids at different applied voltages with a CCD camera. Before starting the image processing, the measurement system was calibrated using an external object with known sizes. Its size in pixels, both in vertical and horizontal directions, was obtained at a specific focal length. In order to minimize the optical aberration, the liquid column is adjusted to be at the center of the image. A MATLAB code was used to convert the number of pixels directly to the liquid height and static pressure. In order to find the net liquid column rise due to EHD conduction pumping, the experimental column rise due to the capillary action was subtracted from the generated head ( $H = h_{\text{generated}} - h_c$ ). The total static pressure generation was calculated from the equation  $P = \rho g H$ . The measured column rise due to the capillary action was approximately 2mm, 3mm, and 3.5mm for N-hexane, Shell Diala AX and 10 GBN Nynas, respectively. In order to verify the experimental observation of liquid column rise due to the capillary forces, the height of liquid was calculated for a narrow tube from the relation  $h_c = 2\gamma / \rho g r$ , where  $\gamma$  is the surface tension and  $r$  is radius of the tube. The comparison showed consistency between experimental observation and the formula with  $\pm 0.5$  mm difference.

The experimental uncertainty of the calculated pressure generation was mainly due to the column level measurement. Although the conduction pressure generation relies on the electrical and thermophysical properties of the working fluid, which may vary significantly with small changes in concentration of contaminants, in the present study, the numerical values of these properties were obtained from the literature (Table I). The uncertainties associated with the measured parameters are summarized in Table II. The electrical permittivity of other materials used in this study is presented in Table III. Each

experiment was repeated three times to ensure the repeatability of experiments and error bars are affixed to all the data in the graphs presented.

Table. II Uncertainty of each quantity which was measured in the present work

Measurement Parameter( $x_i$ )	$x_i$	$U_{x_i}$
<b><math>T</math></b>	296.7 K	$\pm 0.1$ K
<b><math>V</math></b>	286-1500 V	$\pm 10$ V
<b><math>I</math></b>	0.5-15 $\mu$ A	$\pm 0.5$ $\mu$ A
<b><math>d</math></b>	$2.86 \times 10^{-4}$ m	$\pm 2 \times 10^{-5}$ m
<b><math>H</math></b>	1-33 mm	$\pm 0.7$ mm

Table. III Electrical permittivity of materials

medium	Permittivity $\epsilon(pF/m)$ [30]
Air	8.85
Liquid Crystal Polymer (LCP)	24.78
Resin epoxy	31.86

## 5.4 Numerical analysis

In this study, the system of governing equations is formulated based on the previous assumptions [12]. The electric field,  $\vec{E}^*$ , around the electrodes, which is responsible for the charge generation, is distorted by the net free charges,  $\rho_c^*$ , in the dielectric liquid and is governed by Poisson's equation:

$$\nabla^* \cdot \vec{E}^* = C_o \rho_c^* \quad (3)$$

where:

$$\rho_c^* = p^* - n^* \text{ and } \vec{E}^* = -\nabla^* \phi^* \quad (4)$$

$p^*$  and  $n^*$  are positive and negative charge densities, respectively.

The charge transport equations of positive and negative charge carriers for the simplest conduction model [5] are:

$$\nabla^* \cdot \left( p^* \vec{E}^* - \alpha \nabla^* p^* \right) = 2C_o (1 - p^* n^*) \quad (5)$$

$$-\nabla^* \cdot \left( n^* \vec{E}^* + \alpha \nabla^* n^* \right) = 2C_o (1 - p^* n^*) \quad (6)$$

$C_o$  in Eqs.(5) and (6) is a non-dimensional conduction parameter which can be interpreted as ratio of charge relaxation time,  $\tau_T = \epsilon / \sigma$ , to charge transit time,  $\tau = d / bE$ ,  $C_o = \frac{\tau_T}{2\tau} \approx (n_{eq} d^2) / (\epsilon V) = (\sigma_{eq} d^2) / (2b\epsilon V) \frac{\tau_T}{2\tau}$ . The subscript eq indicates thermal equilibrium condition. The momentum balance equation can be expressed as:

$$-\nabla^* P^* + C_o \rho_c^* \vec{E}^* + \rho^* \vec{g}^* = 0 \quad (7)$$

where  $\rho^*$  and  $P^*$  are dimensionless mass density and the generated pressure, respectively.

The definition of the dimensionless parameters appearing in the above equations are

$$z^* = \frac{z}{d}, \quad E^* = \frac{E}{\frac{V}{d}} \quad (8)$$



$$\begin{aligned}
r^* &= \frac{r}{d}, & \varphi^* &= \frac{\varphi}{V} \\
p^* &= \frac{p}{n_{eq}}, & P^* &= \frac{P}{\varepsilon \cdot \left(\frac{V}{d}\right)^2}, \\
n^* &= \frac{n}{n_{eq}}, & \rho^* g^* &= \frac{\rho g}{\varepsilon \cdot \left(\frac{V}{d}\right)^2 \left(\frac{1}{d}\right)}
\end{aligned}$$

The diffusion coefficient  $\alpha$  in (5) and (6) is equal to  $\frac{D}{bV} = \frac{kT}{eV} \approx \frac{1}{40V}$ .

The order of magnitude analysis shows that the contribution of the hydrodynamic convection and diffusion terms are negligible compared with that of the electric body force at steady state condition and static operation of the device. This assumption is consistent with the previous numerical model proposed by Atten and Yagoobi [5], and Jeong et al. [12]. Therefore, the charge convection terms in (5) and (6) can be neglected. The applied boundary conditions are summarized in Table IV.

Table. IV Summary of boundary conditions

HV electrodes	ground electrode	truncating boundaries	liquid/solid interface	axis of symmetry
$\varphi^* = 1$ $p^* = 0$ $\vec{n} \cdot \nabla n^* = 0$	$\varphi^* = 0$ $n^* = 0$ $\vec{n} \cdot \nabla p^* = 0$	$\varphi^* = 0$ $n^* = 0, p^* = 0$	$\varepsilon_s \vec{n} \cdot \nabla \varphi_s^* - \varepsilon_l \vec{n} \cdot \nabla \varphi_l^* = 0$ $\vec{n} \cdot \nabla p^* = \vec{n} \cdot \nabla n^* = 0$ Continuous potential: $\varphi_s^* = \varphi_l^*$	$\frac{\partial \varphi^*}{\partial r^*} = 0$ $\frac{\partial p^*}{\partial r^*} = 0, \quad \frac{\partial n^*}{\partial r^*} = 0$

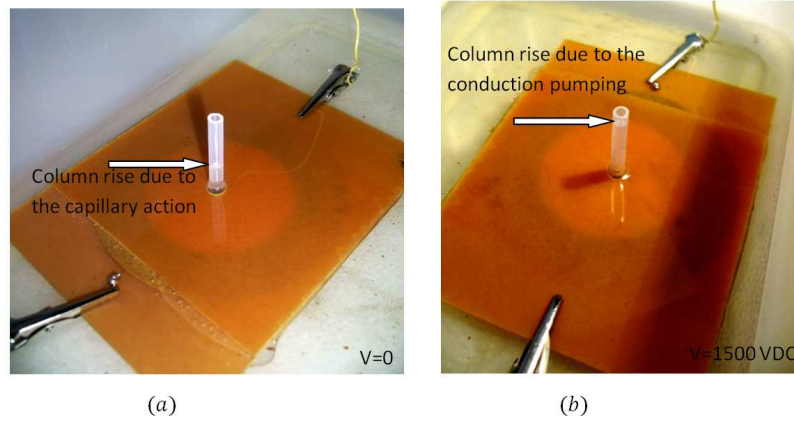
An unstructured triangular mesh with increased mesh density in the area of the intense electric field around the high voltage electrodes and in the hetero-charge layer region around the grounded electrodes was used. In order to ensure that the numerical results are independent of the computational grid, a grid sensitivity analysis was performed for different working fluids at different applied voltages. The criterion for the grid independency analysis was that the total pressure generation calculations were to be constant to the second decimal.

## 5.5 Results and discussion

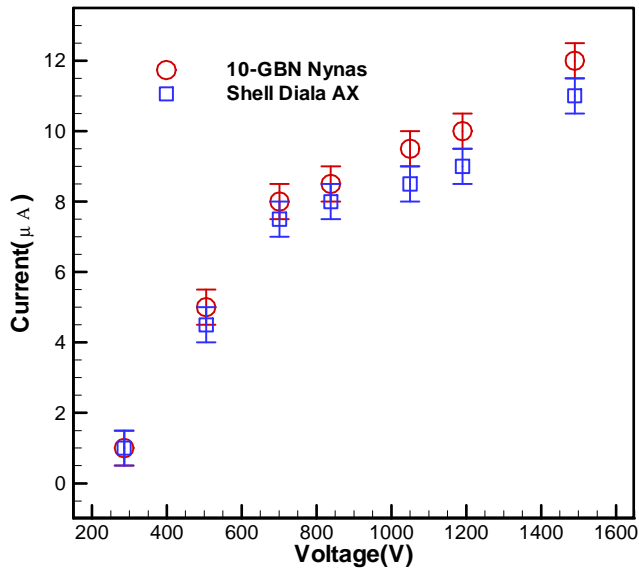
Fig. 4 shows a photograph of the micropump submerged in a bath of 10-GBN Nynas transformer oil during its operation. By increasing the applied voltage and before reaching the steady-state conditions, the electric current passing through the micropump increases and a liquid column rise is generated in the vertical direction. In all experiments before reaching steady-state conditions, the direction of the net flow was from the grounded (blunt) electrode towards the high voltage electrode, which confirms that the current micropump predominantly operates based on conduction phenomenon. It takes a few seconds, depending on the magnitude of applied voltage, to reach the steady-state conditions. At the steady state conditions, the electric current of the micropump shows no measurable fluctuation and the liquid column rise in the capillary tube remains static. Both the electric current and static pressure generation measurements presented in this paper were performed at the steady-state conditions.

The presented device was tested at 1500VDC for a 14 hour continuous operation and the static generated pressure and electric current were monitored frequently. No appreciable change was observed in the pressure and electric current during the time. This suggests that the chemical reaction in the electrode/liquid interface due to the direct ion injection is not appreciable and the electrodes remain relatively unchanged during this period. Comparing the direct ion injection micropump and conduction pumping, one can conclude that the conduction micropumps are remarkably reliable and suitable for long term operations.

By increasing the applied voltage, the current through the conduction micropump increases. Fig. 5 shows  $V$ - $I$  characteristics for the micropump with 10-GBN Nynas and Shell Diala AX transformer oils. At the fixed gap spacing between the electrodes of 286 $\mu$ m, the level of applied voltage for initiation of the conduction pumping is reduced to a few hundred volts. Changing the working fluid results in only small variations in the  $V$ - $I$  characteristics, because the electrical properties of these two fluids are very similar.

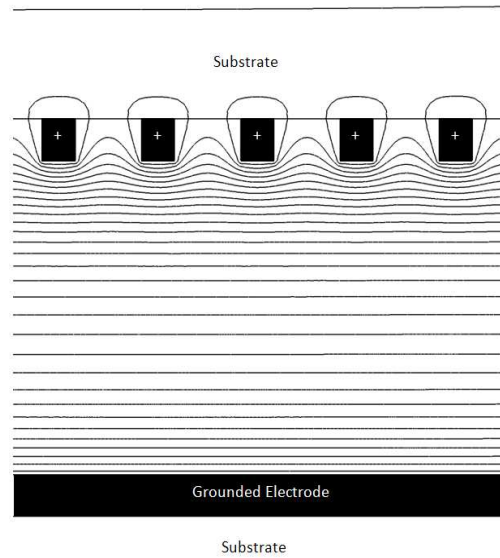


**Figure 4: Demonstration of the column rise for a conduction micropump in a bath of 10-GBN Nynas transformer oil at  $V=0$  (a) and  $V=1500$  VDC applied voltages (b).**



**Figure 5: V-I characteristics for conduction micropump measured for two different working fluids.**

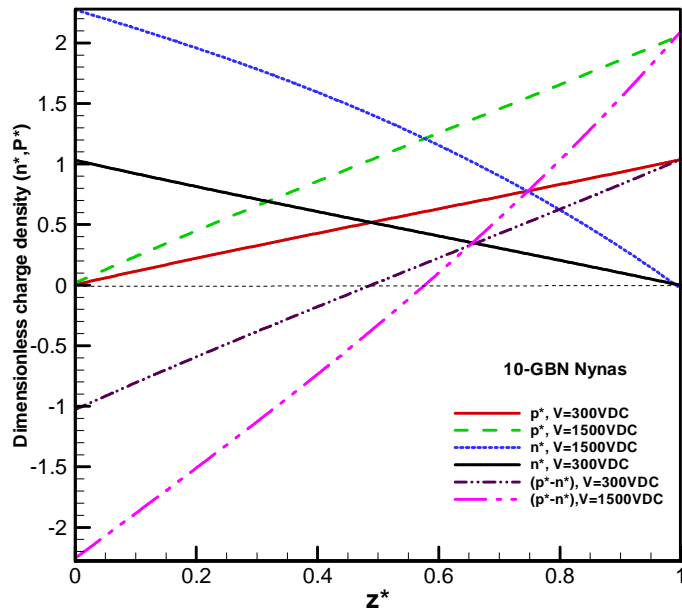
The numerically calculated equipotential lines for the conduction micropump submerged in the bath of 10 GBN Nynas transformer oil are depicted in Fig. 6. Potential difference between two adjacent lines is 50V. The equipotential lines are distorted by the charge distribution near to the electrodes and they are closer to each other adjacent to the high voltage and grounded electrodes.



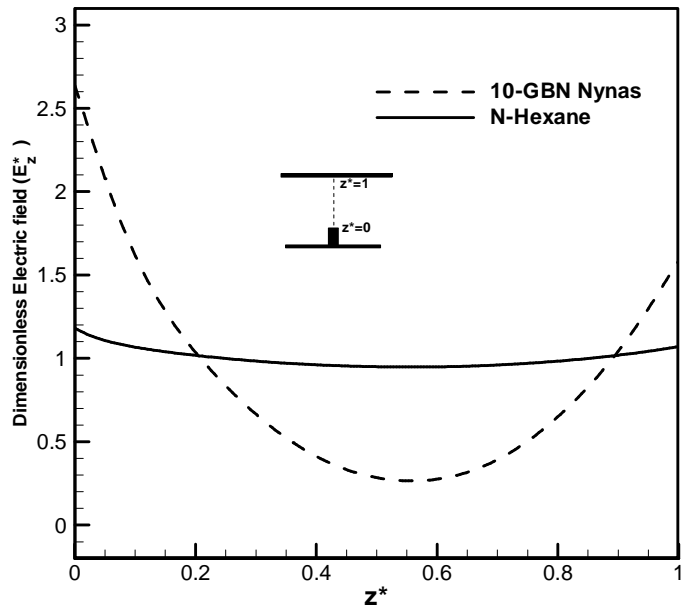
**Figure 6: Distribution of equipotential lines of micro-scale conduction pumping calculated for 10-GBN Nynas at 1500 VDC applied voltage. Potential difference between two adjacent lines is 50V.**

The solution of the charge transport equations yields the spatial variation of charge carriers. Fig. 7 shows the numerical results for the concentration of positive and negative charges at 300 and 1500 VDC applied voltage with 10-GBN Nynas transformer oil as the working fluid. Because the thermophysical properties of the two the transformer oils are very similar, the distribution of charges for Shell Diala AX is not presented. It can be seen that the hetero-charge layers extend into entire the gap spacing at both lowest and highest applied voltages.

Figure 8 shows the electric field distribution between the electrodes for 10 GBN and N-hexane. The integration of electric field along a given path between the two electrodes should be equal to the electric potential difference,  $V$ , because the applied voltage is constant. Therefore, the model predicts electric field enhancement in the whole space over the electrode gap especially adjacent to the electrodes due to the existence of charge excluding a depression in a narrow band in the equilibrium region.

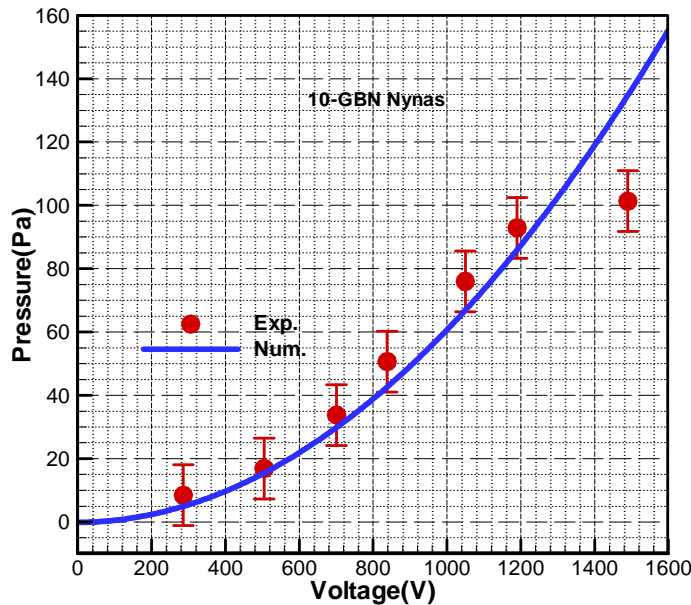


**Figure 7: Calculated positive and negative charge densities in micro-scale conduction pump with 10GBN-Nynas oil transformer.**



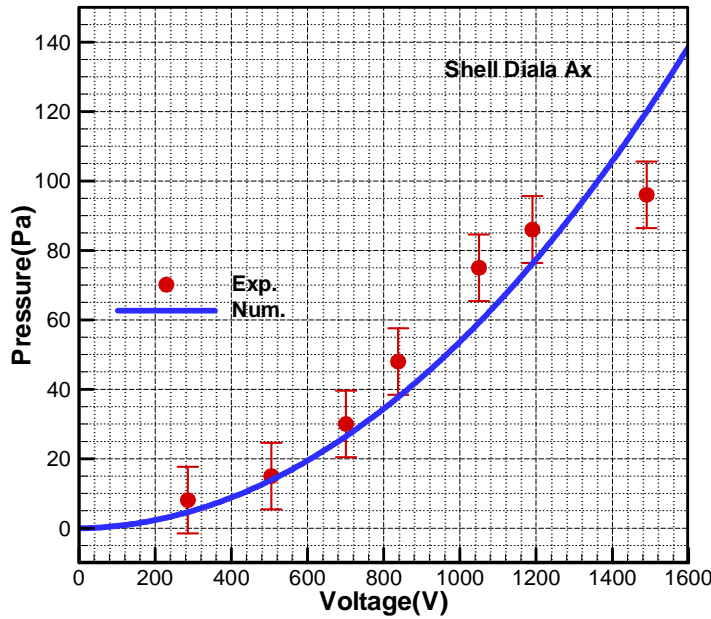
**Figure 8: Axial electric field in micro-scale conduction pump calculated for different working fluids.**

A much smaller enhancement of the electric field near both electrodes can be observed for N-hexane due to its lower concentration of charges.



**Figure 9: Comparison of calculated and experimental static pressures for conduction micropump using 10GBN-Nynas oil transformer.**

The comparison between the numerical results and experimental pressure generation for 10-GBN Nynas as the working fluid is presented in Fig. 9. The conduction pumping effect was started at the average field strength of  $1 \text{ V}/\mu\text{m}$  and a maximum 101 Pa pressure was achieved at the average field strength of  $5.24 \text{ V}/\mu\text{m}$ . The comparison between numerical prediction and experimental results for pressure generation shows a good agreement with an average 8% deviation. The numerical results fall in the band of experimental uncertainty except at highest applied voltage. It is of interest to note that at 1500 VDC the pressure generation of the device is overestimated. This corresponds to the average field strength of  $5.24 \text{ V}/\mu\text{m}$ , a condition where the ion injection phenomenon may produce a back pressure, reducing the pressure generated by the conduction micropump. This interpretation is confirmed when it is realized that the local field strength around the high voltage electrode is approximately twice as that of the average value of field strength and is in the order of the theoretical threshold,  $10 \text{ V}/\mu\text{m}$ , where ion injection can occur.



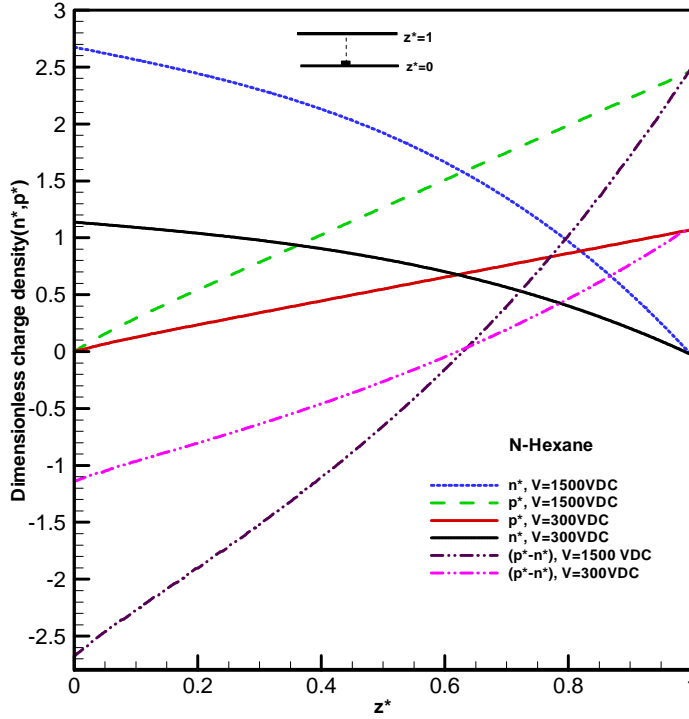
**Figure 10: Comparison of calculated and experimental static pressures for conduction micropump using Shell Diala AX oil transformer.**

Figure 10 shows the comparison between the experimental and numerical results for the pressure generation of the micro-pump using Shell Diala AX indicating a good agreement with an average deviation of 12%. Similarly to the 10GBN Nynas, the numerical model overestimates the pressure generation. Comparing the numerical results of the pressure generation in micro-scale for 10-GBN Nynas and Shell Diala AX shows that there is a small difference between the experimental and numerical results. The main reason for this difference is believed to be the uncertainty associated with the ion mobility calculation. In this study, the ion mobilities of negative and positive charges were assumed to be identical and calculated based on Walden's rule, which relates the ion mobility to dynamic viscosity. Referring to the thermophysical and electrical properties of these two working fluids shows that the electrical properties of the fluids are very similar, whereas there is appreciable difference between their dynamic viscosities and ion mobilities. It should be noted that the dynamic viscosity of both transformer oils are exponential function of temperature and small changes in temperature may significantly change their viscosity and ion mobility [24,26]. It should be noted that in the present numerical analysis, the field enhancement coefficient was assumed to be negligible. This

assumption is particularly valid at low-field regimes ( $E < 4 \text{ V}/\mu\text{m}$ ). However, it was shown that neglecting the field enhancement coefficient for even moderate electric fields ( $4\text{-}6 \text{ V}/\mu\text{m}$ ) still provides good agreements between experimental and numerical pressure generation [6].

By submerging the micropump in the bath of N-Hexane and applying the voltage, an electric current was measured, but no appreciable pressure generation was produced. A similar effect has been reported in the literature for a macro-scale conduction pump with N-Hexane as working fluid using various configurations of the electrodes [5]. Because of its shorter relaxation time, thicker hetero-charge layer and the associated enhancement of the electric field in the gap, one should expect higher numerical pressure generation for N-Hexane based on the thermophysical properties tabulated in Table. I. However, N-Hexane is proven to be particularly sensitive to the effect of contaminations and the electrical conductivity of values on the order of  $10^{-8}$  to  $10^{-17}$  (nine orders of magnitude difference) can be found throughout the literature [5,25,31]. Implementing the tabulated value of conductivity,  $\sigma = 63.9 \times 10^{-12} \text{ S/m}$ , agreement between experimental and numerical pressure generation cannot be achieved. In order to obtain agreement, a numerical value of  $\sigma = 1 \times 10^{-12} \text{ S/m}$  for electrical conductivity of N-Hexane must be assumed. The dimensionless positive and negative charge densities and the electric field were calculated and shown in Fig. 11. The charge distribution is very similar to that of 10-GBN Nynas, but the N-hexane charge distribution profile is more diffusive due to its two order of magnitude higher ion mobility. Assuming the numerical value for electrical conductivity  $\sigma = 1 \times 10^{-12} \text{ S/m}$ , the thermal equilibrium charge density for N-hexane,  $n_{\text{eq}} = 4.17 \times 10^{-5} \text{ C/m}^3$ , becomes two order of magnitude lower than  $n_{\text{eq}} = 1.91 \times 10^{-4} \text{ C/m}^3$  for 10-GBN Nynas. With this assumed value of electrical conductivity for N-Hexane the numerical solution predicts pressure generations about 0.1Pa at applied voltages up to 1500 kV, which is consistent with the experimental observations of negligible column rise.





**Figure 11: Distribution of positive and negative charge densities in micro-scale conduction pump calculated for N-Hexane.**

A typical distribution of charge density over the micro-scale gap for a given dielectric fluid spacing slightly differs from that of macro-scale spacing. By increasing the applied voltage, the weakly conductive liquid around the electrodes experiences the bipolar ionization and heterocharge layers develop. By further increasing the electric field strength, the heterocharge layers extend over the entire gap spacing. Generally, at macro-scale the gap is larger than the thickness of the heterocharge layer. The conduction parameter,  $C_o$ , determines the regime of charge concentration distribution. The different regimes of heterocharge layer distribution are demonstrated in Fig. 12.

In order to show the impact of  $C_o$  on the charge distribution patterns, the growth of the heterocharge layer is qualitatively demonstrated at different scales of  $C_o$  for macro-scale gap spacing (Figs. 12a and 12b) and for micro-scale gap spacing (Figs. 12c and 12d). The conduction parameter is a function of the electric field strength, thermophysical properties of dielectric fluid and the square of electrode spacing. By decreasing the gap space from order of centimeters to microns,  $C_o$  becomes very small. Thus, depending on

the dielectric fluid properties, the heterocharge layers around the opposite polarity electrodes extend to the gap spacing and no definitive equilibrium region can be identified. For the operating voltage of 300-1500 VD, the  $C_o$  varies between  $10^{-4} < C_o < 10^{-3}$  for transformer oils and  $1 \times 10^{-2} < C_o < 5 \times 10^{-2}$  for N-hexane. Therefore, the operation of the device falls in the regime depicted in Fig. 12d. Moreover, by shrinking the distance between the electrodes, the required voltage to initiation of the conduction pumping effect decreases. Because the diffusion coefficient is inversely proportional to the applied voltage, it becomes one or two order of magnitude higher for the micro-scale device.

It should be noted that the theoretical static pressure generation obtained for a macro-scale conduction pump overestimates the resulted static pressure generation of the micropump. The quadratic relation between the pressure generation and the electric field,  $P = 0.85\epsilon V^2/d^2$ , was derived by Feng and Yagoobi[6] for a conduction pump with macro-space separation between the electrodes, where  $\lambda \ll d$ . This cannot be applied for the device tested here with micro-scale gap spacing, where  $\lambda$  is in the order of  $\sim d$ . This equation can be applied only for the conduction macro pump, where the thickness of the heterocharge layer near the electrode is smaller (or much smaller) than the electrode spacing (see Fig. 12 -a). In the present conduction micropump with an electrode gap spacing in the order of few hundred microns, the heterocharge layers, formed around two opposite charged electrodes, extend to the entire gap spacing (compare Fig. 12 -a and 12-d). Therefore, the theoretical analysis based on the simplifications due to the small heterocharge layer thickness is not applicable to the present study. Furthermore, in the previous theoretical model, it has been assumed that ion diffusion has a negligible contribution in the carrier transport process. According to the discussion given by Atten and Yagoobi [5], the ion diffusion term should be taken in to account for  $V < 2500 \text{ VDC}$ . Therefore,  $P = 0.85\epsilon V^2/d^2$  cannot describe the static pressure generation at micro-scale gap spacing with heterocharge layers extended to the length of electrode separation.

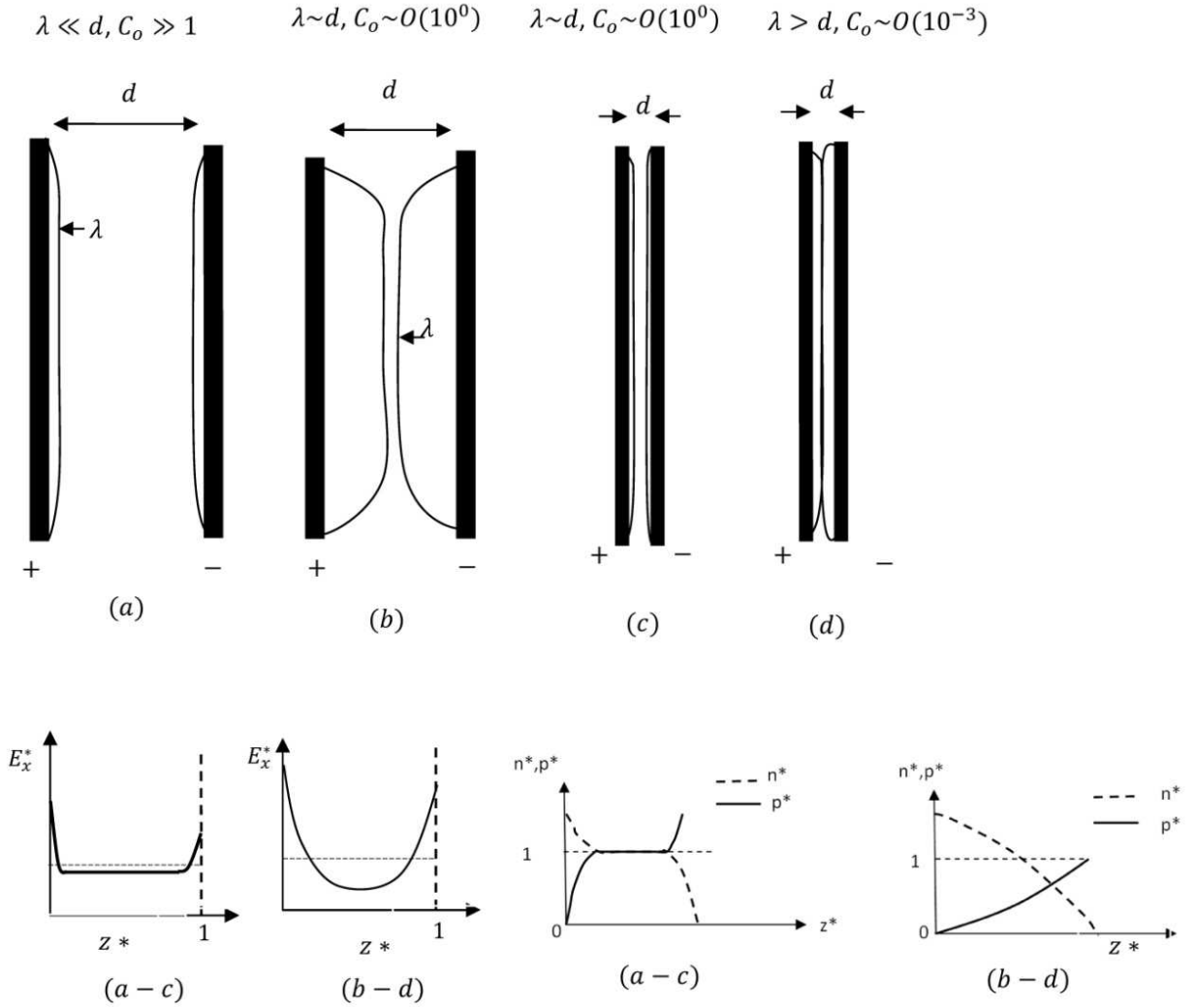


**Figure 12: Space charge density and electric field in macro- and micro-gaps and (b)-impact of space averaged conduction parameter on formation of hetero-charge layers in parallel plate geometry filled with a low conductive dielectric liquid, (c) Extension of hetero-charge to the length of gap spacing for micro-scale gap spacing in parallel plate geometry filled with low conductive electrodes at comparatively lower applied voltages, (d) hetero-charge extension for micro-scale gap spacing in parallel plate geometry filled with low conductive electrodes at comparatively higher applied voltages.**

## 5.6 Conclusions

In the present work, an axisymmetric EHD conduction micropump with 286 $\mu\text{m}$  gap spacing between electrodes was proposed. The micropump was tested in the vertical configuration with three different working fluids: two transformer oils and N-Hexane. The static pressure generation due to the conduction pumping was measured at different applied voltages. As an important result, the initiation of conduction pumping was reduced to 300 VDC applied voltage, which is one order of magnitude lower than that of the typical macro-scale conduction pumps. In order to verify the experimental results, the 2D axisymmetric model of the micropump was developed based on a double species conduction model. The static pressure generations were calculated and compared with the experimental results in steady-state static operation at different applied voltages. The numerical static pressure generations of the device are generally in a good agreement with the experimental data except for an overestimation at 10 V/ $\mu\text{m}$  local field strength (1500 VDC). This overestimation is believed to be related to the reversed pressure generation due to the initiation of the direct ion injection at the corresponding field strength threshold predicted by the theory.

## References

- [1] J.R. Melcher, *Continuum electromechanics*, Cambridge, MIT Press, 1981, Chaps.3 and 5.
- [2] V. Betis, "Experimental and computational investigation of planar ion drag micropump geometrical design parameters", PhD Thesis, 2005, University of Maryland-College Park.
- [3] L.-J. Yang, J.-M. Wang and Y.-L. Huang "The micro ion drag pump using indium-tin-oxide (ITO) electrodes to resist aging" *Sens. Actuators A* (2003) 111, pp. 118–122.
- [4] J. Seyed-Yagoobi, "Electrohydrodynamic pumping of dielectric liquids" *J. of Electrostat.* (2005) 63(6-10), pp. 861-869.
- [5] P. Atten and J. Seyed-Yagoobi, "Electrohydrodynamically induced dielectric liquid flow through pure conduction in point/plane geometry," *IEEE Trans. Dielect. Elect. Insul.* (2003) 10(1), pp. 27–36.
- [6] Y. Feng and J. Seyed-Yagoobi, "Understanding of electrohydrodynamic conduction pumping phenomenon" *J. Phys. Fluids* (2004) 16 pp.2432–2441.
- [7] S.F. Bart, "Microfabricated electrohydrodynamic pumps" *Proc. of the 5th Int. Conf. on Solid-State Sensors and Actuators and Eurosensors III. Part 2*, Jun 25-30 1989, Montreux, Switzerland.
- [8] A. Richter, A. Plettner, K.A. Hofmann and H. Sandmaier "Electrohydrodynamic pumping and flow measurement" *Proc. of the 1991 IEEE Micro Electro Mechanical Systems - MEMS '91*, Jan 30-Feb 2 1991, Nara, Japan.
- [9] S. H. Ahn and Y. K. Kim, "Fabrication and experiment of planar micro ion-drag pump," *Sens. Actuators A* 70, (1998), pp. 1–5.

- [10] J. Darabi, M. Rada, M. Ohadi and J. Lawler “Design, fabrication, and testing of an electrohydrodynamic ion-drag micropump” *J. of Electromech. Syst.* (2002)11 (6), pp.684-690.
- [11] E. Gray, T.J. Lewis “The effect of liquid motion on ion mobility in hexane” *Brit. J. App. Phys.* (1969), 2(2), pp.93-100.
- [12] S.I Jeong, J. Seyed-Yagoobi and P. Atten, “Theoretical/numerical study of electrohydrodynamic pumping through conduction phenomenon” *IEEE Trans. Ind. Appl.* (2003) 39 pp. 355–361.
- [13] S.I Jeong and J. Seyed-Yagoobi, "Experimental study of electrohydrodynamic pumping through conduction phenomenon", *J. of Electrostat.* (2002) 56 , pp.123-133.
- [14] M. Yazdani and J. Seyed-Yagoobi, “Electrically induced dielectric liquid film flow based on electric conduction phenomenon,” *IEEE Trans. Dielect. Elect. Insul.* (2009) 16(3), pp.768-777.
- [15] S. Dini, “Electrohydrodynamic induction and conduction pumping of dielectric liquid film: theoretical and numerical studies”, PhD Thesis, 2005, Texas A&M University.
- [16] S.I Jeong, J. Didion, “Performance characteristics of electrohydrodynamic conduction pump in two-phase loops”, *J. Therm. Heat. Trans.* (2008) 2, pp.90-97.
- [17] Y. Feng and J. Seyed-Yagoobi “Electrical charge transport and energy conversion with fluid flow during electrohydrodynamic conduction pumping”, *Phys. of Fluids*, (2007) 19, pp.057102-1.
- [18] M. Yazdani and J. Seyed-Yagoobi “Thermal homogenization in spherical reservoir by electrohydrodynamic conduction phenomenon”, *J. of Heat Transfer*, (2009) 131 pp.094502-1.

- [19] M. Yazdani and J. Seyed-Yagoobi “Numerical investigation of electrohydrodynamic-conduction pumping of liquid film in the presence of evaporation”, J. of Heat Transfer, (2009) 131, pp. 011602-1.
- [20] J. Seyed-Yagoobi and J. E. Bryan, “Electrohydrodynamic conduction pump,” U.S. Patent 6 932 580, August 23, 2005.
- [21] S.I. Jeong and J. Seyed-Yagoobi “Innovative electrode designs for electrohydrodynamic conduction pumping”, IEEE Trans. Ind. Appl., (2004) 40, pp.900-904.
- [22] L. Pagel and S. Gabmann, "Microfluidic systems in PCB technology", Industrial Electronics Society, 2005, IECON 2005, 31 Annual Conf. of IEEE, 10.1109/IECON.2005.1569274.
- [23] O. Dezuari, E. Belloy, S.E. Gilbert and M.A.M. Gijs, "Printed circuit board integrated fluxgate sensor", J. Sen. and Actuators. Phys A, (2000) 81, pp.200-203.
- [24] C. Yeckel, R. D. Curry and P. Norgard, “A comparison of the AC breakdown strength of new and used poly- $\alpha$  Olefin coolant”, IEEE Trans. Dielect. Elect. Insul. (2007) 14(4), pp. 820–824.
- [25] J. M. Crowley, G. S. Wright and J. C. Chato, “Selecting a working fluid to increase the efficiency and flow rate of an EHD pump,” IEEE Trans. Ind. Appl. (1990) 26, pp.42–49.
- [26] K. M. Takami, “Process control and simulation of ferromagnetic strip in the power transformers and electrical machines applications”, PhD thesis, Mälardalen University, 2009.
- [27] J.E. Bryan and J.Seyed-Yagoobi, “Experimental study of ion-drag pumping using various working fluids”, IEEE Trans. Dielect. Elect. Insul. (1991) 26(4), pp.647-655.
- [28] D.J Laser, J.G Santiago, “A review of micropumps”, J Micromech Microeng (2004) 14(6):R35-R64.

- [29] P. Debye, "Reaction rates in ionic solutions," *Trans. Electrochem. Soc.* (1942) 82 pp.265-272.
- [30] C.R. Paul, *Introduction to electromagnetic compatibility*, 2nd Edition, John wily & sons, 2006.
- [31] I. Adamczewski, *Ionization, conductivity and breakdown in dielectric liquids*, Taylor & Francis, 1969.
- [32] P. Foroughi, "Design and characterization of an electrohydrodynamic (EHD) micropump for cryogenic spot cooling application", PhD Thesis, 2008, University of Maryland-College Park.
- [33] B. D. Iverson, S. V. Garimella, "Recent advances in microscale pumping technologies: a review and evaluation", *J. Microfluid. Nanofluid.* (2008) 5: pp.145–174
- [34] Wego, L. Pagel, "A self-filling micropump based on PCB technology" ", *J. Sen. and Actuators. Phys A*, (2001) 88, pp.220-226.
- [35] B.A. Centiner, J.Y. Qian, H.P. Chang, M. Bachman, G.P. Li, F. Flaviis, "Monolithic integration of RF MEMS switches with a diversity antenna on PCB substrate", *IEEE Trans. on Micro. Theo. and Tech.* (2003) 51(1) pp. 332-335.
- [36] P. Langevin, "Recombmaison et mobilites des ions dans les gag," *Ann. Chim. Phys*, (1903) . (28), pp. 433.



## Chapter 6

### Spreading of a dielectric droplet through an interfacial electric pressure

#### 6.1 Introduction

Spreading of a liquid droplet over a solid surface is important for a wide variety of applications, such as coating and deposition processes [1-3], spray cooling of heated surfaces [4,5] and thin film evaporation [6]. The active control of the droplet deposition process is still challenging and the current techniques highly depend on the fluid properties and surface condition. The conventional way to increase the spreading ratio of a droplet is to increase the impact velocity. However, high speed impact causes some drawbacks, such as non-uniformity of the resulting film thickness, micro-satellite droplet formation due to violent breakup, and recoiling/rebounding phenomenon. In most of the listed above applications, the droplet spreading process needs to be uniform since the non-uniform film thickness leads to other complications [7,8]. Moreover, preserving the contact between the resulting liquid film and the solid surface during the spreading process leads to efficient deposition with reduced material wastage and environmental pollution. Therefore, new methods are demanded to enhance the deposition efficiency and mitigate the drawbacks of high speed droplet impact.

The corona discharge process has been found to be advantageous for several scientific and industrial applications. It creates a partially ionized gaseous medium with free space charge carriers drifting towards a grounded electrode. These free charge carriers can be deposited as surface charge on the targets. Although the corona discharge has been extensively applied to create net motion in gaseous media, little effort has been expended to obtain a net flow in dielectric liquids. Recently, perpendicular corona discharge was applied to liquid/vapor interface to investigate a new type of interfacial electrohydrodynamic instability, which is so-called rose-window instability [9, 10]. The dielectric liquid was placed in a container and charge carriers injected through the gaseous phase towards the dielectric interface using a high voltage corona needle

electrode fixed at some height above the liquid surface. The surface charge density accumulates on the interface and creates strong electrical pressure, so that the thickness of dielectric layer locally reduces. Subsequently, the electric field in the thin film region increases and the surface charge easily migrates to the ground electrode due to conduction phenomenon. The charge migration mitigates the electrical pressure and the local thickness of the liquid film increases. The process is resumed by charge accumulation over the interface and rose-window instability patterns are generated. Although several experimental and theoretical studies have focused on understanding the interaction of corona discharge with dielectric liquid interface and the induced instabilities [11, 12], no effort can be found in literature to generate a net pressure gradient through interfacial corona discharge exposure.

In the present work, a new technique for forced spreading of a dielectric droplet over a conductive substrate is proposed. In order to generate a strong enough electrical pressure, the droplet interface was exposed to a corona discharge. The interfacial electrical pressure resulting from the ion deposition on the liquid/vapor interface was used to actively control the liquid film spreading process. In order to understand the physics of spreading in the presence of corona discharge, a simplified mathematical model based on theoretical postulations is proposed. In this model, the dynamic expansion of the droplet is correlated to the corona discharge parameters, physical/electrical properties of the dielectric liquid and gaseous medium, in which the discharge occurs. The theoretical postulations of the mathematical model were verified through further demonstrative experiments. A comparison between theoretical predictions and measured spreading dynamics is provided.

## 6.2 Experimental setup and procedure

A schematic view of the experimental setup is shown in Fig. 1. In order to develop the perpendicular corona discharge, a universal fitting with a precise adjustable mechanism was constructed. This fitting was electrically insulated and connected to a XYZ holder.

The position of the substrate with respect to the high voltage electrodes was adjusted using a laser pointer and the XYZ holder.

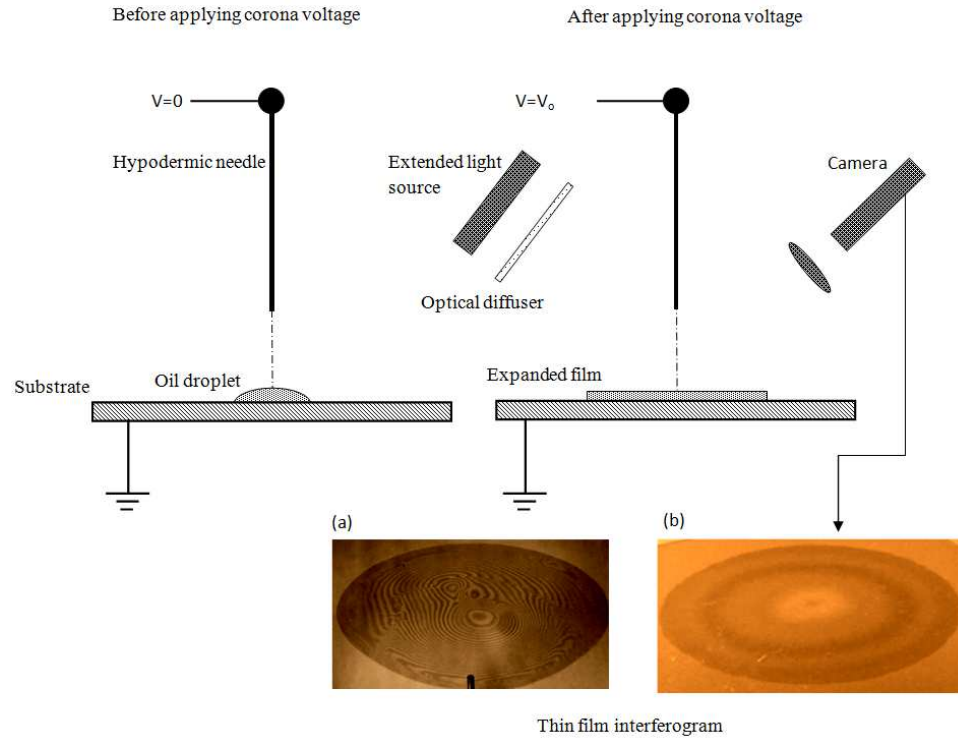


**Figure 1: Schematic view of the experimental setup and a sample of Fizeau fringes observed after 6min (a) and 60min (b) corona discharge exposure.**

In order to confirm the pivotal role of the ion injection process due to corona discharge in the film spreading phenomenon, two sets of experiments were performed with two different electrode configurations (i) parallel plate geometry and (ii) needle-plate geometry. For parallel plate electrode experiments, a mirror finished stainless steel disk was chosen and all the sharp edges, including the rim of electrode, were rounded and fully finished to minimize the back corona discharge. For needle-plate experiments, two standard hypodermic needles, 15g and 22g, were selected as emitter electrodes. The inner and outer diameters for 15g were 1.37 mm and 1.83 mm, respectively. For 22g, the inner diameter was measured to be 0.41 mm and the outer diameter was 0.72 mm. The length of both needles was identical and chosen to be 40 mm. The tips of needles were cut off perpendicularly to their axis with a laser cutter. No particular irregularity in the needle cross section was found after the preparation process.

The needles were connected to a positive polarity of a dc high voltage power supply (Spellman Model: SL-600) and the substrate was grounded. The unipolar ion injection strength was controlled through variation of the applied voltage using these two emitter electrodes. Since oxidation due to the ozone generation may affect the sharpness of electrodes, the  $V$ - $I$  characteristics for both needles was monitored. The corona discharge characteristics for these emitter electrodes was found to be stable during the experiments.

The substrate was a mirror-finished stainless steel plate. In the present study, silicone oil was chosen to be the main dielectric working fluid. The dielectric droplet was gently deposited on the grounded substrate using a micro-syringe. A few additional qualitative experiments were performed using glycerin, deionized water and solution of silicone oil with different concentrations of di-2-ethylhexyl sodium sulfosuccinate (AOT).

The initial size of the deposited droplet,  $D_o$ , was evaluated by converting the droplet weight to its equivalent spherical size. Droplets with different sizes were obtained using the two different hypodermic needles and with various injected volumes. It should be noted that immediately after the droplet deposition, some spontaneous spreading occurs due to its own weight and capillary effects. Thirty seconds after deposition, the high voltage power supply was switched on and the droplet evolution was recorded using a digital camera (SONY DCR-SX43) at 30 fps. A typical set of photographic sequential frames for a silicone oil droplet shown in Fig. 2(a) were used to plot the dynamic evolution of the film diameter,  $D(t)$  (Fig. 2(b)). The measurement system converts the number of pixels directly to the dimensions of the spreading film. In order to check the uniformity of expansion, the film diameters were measured at different peripheral angles.

The non-uniformity of the measured droplet spreading ratio,  $\beta = \frac{D(t)}{D_o}$ , never exceeded

1%. In order to diagnose the onset of any interfacial deformation due to the ion injection, an additional optical system including a laser beam and photodiode detector was used. For a fixed incident angle, any changes in the mirror angle simply produce a detectable electric signal. All the experiments were repeated three times to ensure the reproducibility of the experimental data.

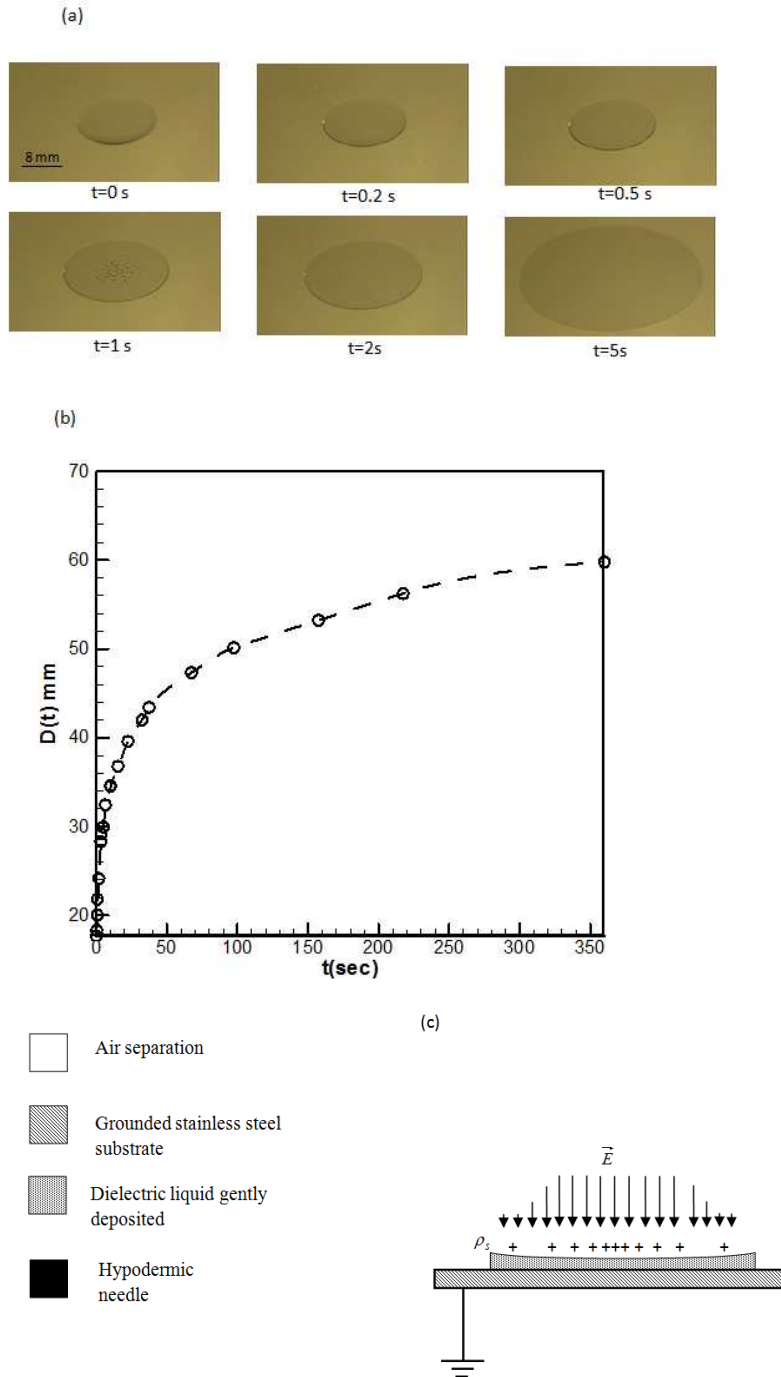


**Figure 2: Typical photographic sequence of a silicone oil spreading process on a mirror finished stainless steel grounded substrate in the presence of corona discharge (a). Typical evolution diagram obtained from the above photographic sequential frames (b). The corona discharge emitter electrode was 15g hypodermic needle separated 40 mm from the grounded substrate. The initial diameter of the oil droplet was 3.78 mm. (c) Figurative explanation of the dielectric liquid spreading phenomenon in the presence of corona discharge.**

## 6.3 Results and discussion

In order to prove that interfacial charging is responsible for the spreading phenomenon, we studied the spreading behavior of a silicone oil droplet in a uniform and strong electric field in the absence of ion injection. Two parallel disks with smooth rounded edges enabled us to achieve high electric field close to the air breakdown limit with negligible ion injections. For this extreme case, where the principal radii of curvature of the high voltage electrodes tend to infinity, monitoring the oil droplet shape using laser diode and photodiode detectors showed no noticeable change in its surface or the contact line. The range of applied voltage was 0 to 40 kV dc and no measurable electric current was recorded during these experiments. This shows that the Laplacian electric field in the absence of corona discharge yields no changes either in droplet shape or contact line position. Therefore, the electrical pressure generation due to the permittivity and static field difference across an air/dielectric liquid interface does not influence the deposited droplet shape. However, by introducing a series of mini-grooves on the high voltage electrode and repeating the experiment, a weak corona discharge was established between the parallel plates and a noticeable electric current in the order of  $\sim 0.1 \mu\text{A}$  was measured at the highest possible applied voltage, which was close to the breakdown limit. At these conditions, a minor depression on the droplet interface was detected. These observations suggest that the spreading mechanism is governed by ion deposition on the droplet surface. In order to obtain significant film spreading, one should locally enhance the strength of ion injection to create localized surface charge density and electric field on the droplet interface. The needle-plate configuration was adopted to provide more significant spreading.

The typical evolution of a silicone oil droplet exposed to the corona discharge (applied voltage  $V=15 \text{ kV}$  and total corona current of  $I=15 \mu\text{A}$ ) is shown in Fig. 2(b). It can be observed that the droplet is squeezed to a pancake shape and spreads axisymmetrically in the radial direction. The expansion process is uniform and the spreading ratio increases monotonically with the discharge exposure time.

It is noticeable that the evolution process involves two distinct regimes: short and long time. In the short term evolution (for  $t < 10$  s), when the ratio of the film diameter to the film thickness is moderate, the spreading proceeds very rapidly, but its rate decreases quickly with time. For the long term exposure (for  $t > 10$  s), as the diameter of the squeezed droplet increases and the liquid film thickness dramatically decreases, the spreading rate becomes significantly slower.

The mechanism of droplet spreading in the presence of unipolar ion injection is rather complicated. A figurative explanation of the spreading mechanism is shown in Fig. 2(c). The electric charge carriers are generated due to the locally intense electric field. The charge cloud drifts towards the liquid layer and grounded electrode. The surface charge density,  $\rho_s$ , accumulates over the liquid interface until it asymptotically saturates. Under the quasi-steady state conditions, the supplied and migrated charges reach equilibrium. The normal component of the electric field produces an interfacial electrophoretic pressure,  $\rho_s E$ , acting towards the substrate. This electric pressure, resulting from the surface charge/electric field interaction, creates a uniform pressure gradient in the radial direction. The net visible effect of this phenomenon is the axisymmetric radial spreading of the droplet. This hypothetical explanation of the spreading mechanism will be discussed through various experiments in this paper.

In order to investigate the effect of ion injection strength on the spreading process, two different hypodermic needles were used to create different corona currents at the same gap spacing. Fig. 3 shows a comparison between the  $V$ - $I$  characteristics obtained for the modified 15g and 22g hypodermic needles with  $S=25$  mm electrode gap spacing. Since the sum of the two principal radii of the corona electrode curvature affects the strength of ion injection and corona current, the  $V$ - $I$  characteristics of both needles at a given electrode separation are different. It should be noted that the  $V$ - $I$  characteristics does not show measurable changes in the presence and absence of a thin dielectric film. Therefore, Fig. 3 represents universal  $V$ - $I$  characteristics for all experimental data presented in this paper.

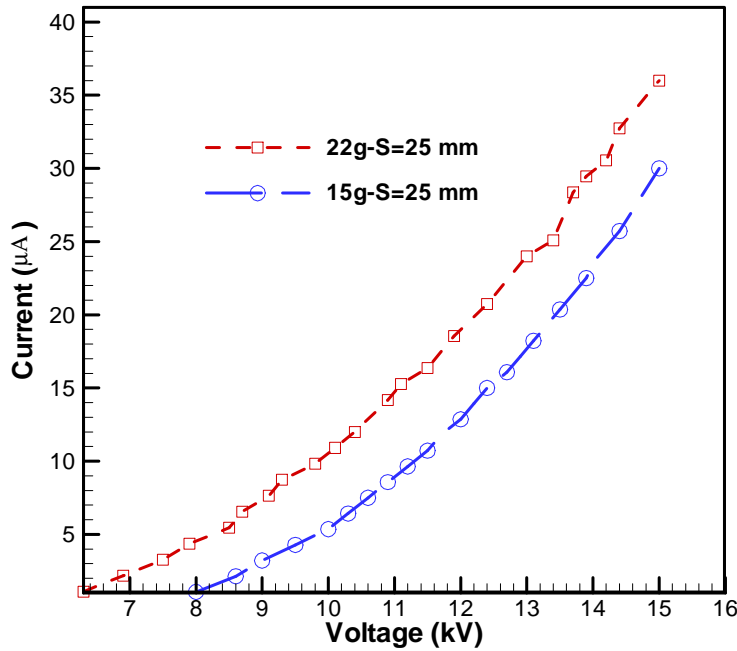


**Figure 3: V-I characteristics of needle-plate geometry using 15g and 22g hypodermic emitter electrode with S=25 mm gap spacing.**

Figure 4 shows the dynamic evolution of a large and medium silicone oil droplet in the presence of corona discharge for both the 15g and 22g hypodermic needles. According to Fig. 4, a significant expansion can be achieved at 15 kV applied voltage using both needles. Comparing the corona characteristics for these needles at the same applied voltage and electrode gap spacing, one can notice that the corona current becomes almost double when the 22g electrode is used. Therefore, using a fine needle at a fixed applied voltage leads to a higher electric field, increased ion injection strength and thus a larger corona current, which corresponds to a larger rate of interfacial charge accumulation and droplet spreading ratio. As it was shown before, the spreading process for both needles has two distinct regions, (i) rapid expansion at the beginning of discharge exposure and (ii) long term evolution, which is remarkably slower. The experimental observations revealed that the fine emitter needle, 22g, gives faster expansion rate in both regions, while the coarser needle, 15g, results in a lower rate of expansion.



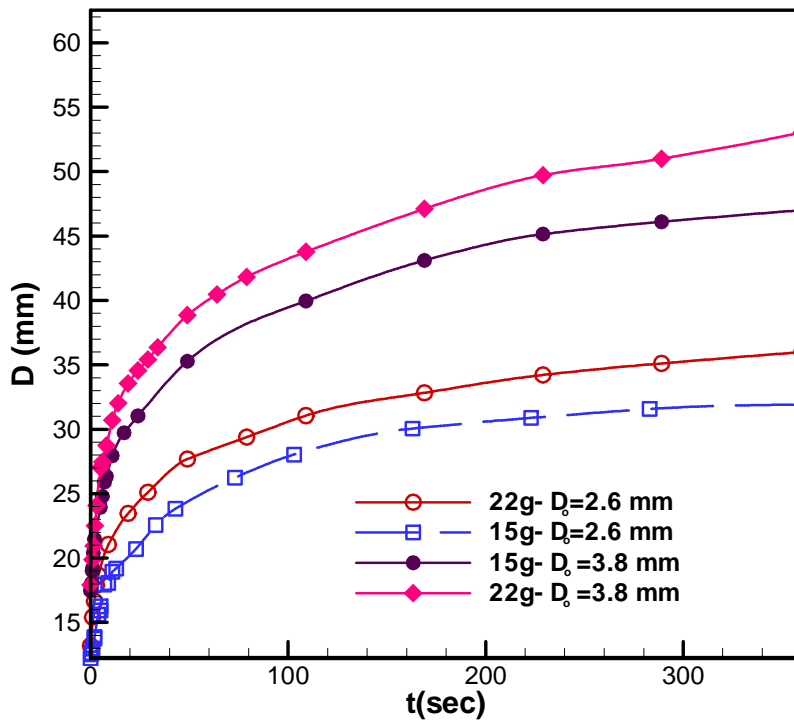


**Figure 4: Dynamic evolution of medium ( $D_0=2.6$  mm) and large ( $D_0=3.8$  mm) silicone oil droplets in the presence of corona discharge at  $V=15$  kV. The electrode separation in both cases was  $s=62$  mm. The corona currents for 15g and 22g are  $7.5 \mu\text{A}$  and  $13 \mu\text{A}$ , respectively.**

### 6.31 Effect of electric field strength

The effect of electric field strength on droplet spreading dynamics is shown in Fig. 5. The electrode voltage was kept constant ( $V=15$  kV) during the experiment and the electrode spacing was varied between 25 mm to 62 mm. As it can be seen in Fig. 5, decreasing the electrode separation results in faster spreading process. Here the enhanced electric field increases the current, elevates the rate of interfacial charging, produces higher electrical pressure and increases spreading rate. However, since for the reduced gap spacing, the effective region of discharge (corona cone) becomes narrower, the electric field and surface charge deposition is more concentrated around the center region (Warburg's law [13, 14]), and weaker at the rim of the film [15]. Therefore, it may be expected that the

corona discharge at reduced gap spacing leads to a less uniform expanded films. Qualitative observation of Fizeau interferograms confirmed that for the larger gap spacing, the fringe patterns become more regular and a more uniform film spreading was obtained. Furthermore, for the smaller electrode separations ( $S < 25$  mm), the random irregularities of the high voltage emitter electrode and its associated non-uniformities in electric field presumably become of increasing importance and the resulting film is more likely to be non-uniform.

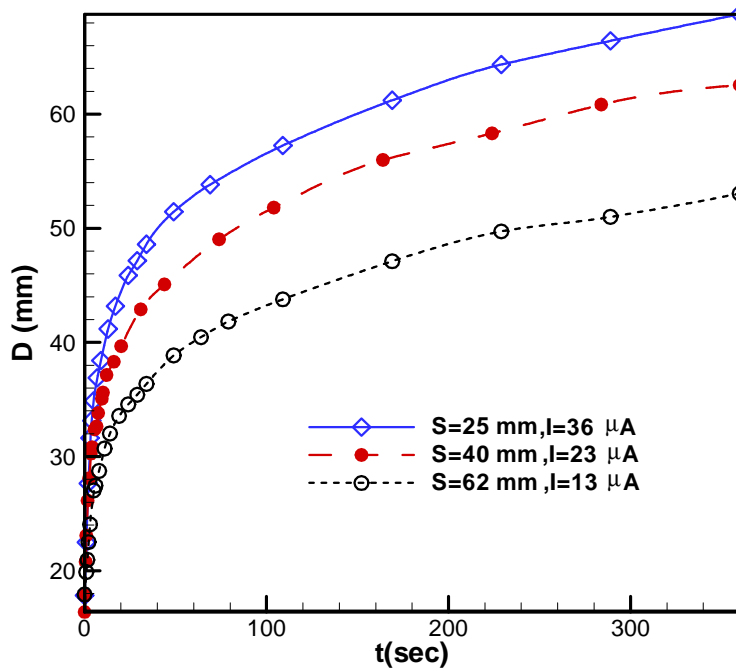


**Figure 5: Dynamic evolution of large silicone oil droplet ( $D_0=3.8$  mm) in the presence of corona discharge for various gap spacings. The emitter electrode was 22g needle and its voltage was kept constant at 15 kV.**

### 6.3.2 Effect of droplet size and electrical conductivity on the spreading process

Figures 6 and 7 depict the dynamic evolution of droplets with different sizes at different electric field strengths. Since the capillary length,  $\ell_c = \sqrt{\sigma/\rho g}$ , is approximately 1.5 mm, droplets with initial size  $D_0 > 3$  mm can be classified as large droplets. In order to

investigate the effect of droplet dimension, small, medium and large droplets were generated and expanded. The spreading ratio of different size droplets falls approximately on a universal curve for both electric field strengths. This means that the spreading rate in the presence of corona discharge is not sensitive to the droplet volume. Later, we will revisit this experimental observation analytically.

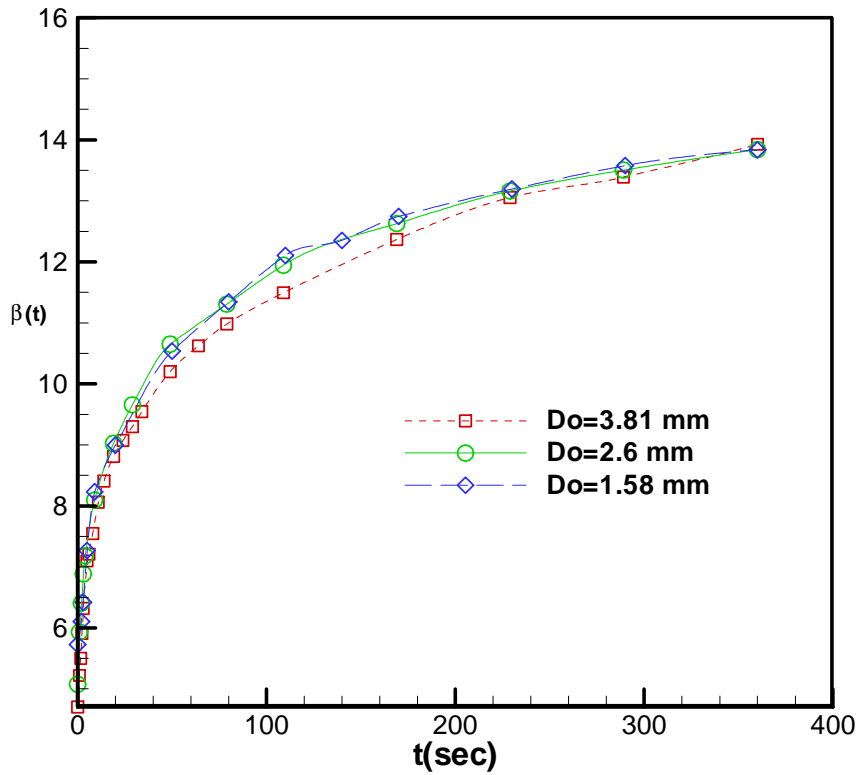


**Figure 6: Dynamic spreading ratio of silicone oil droplets with different initial sizes in the presence of corona discharge ( $V=15$  kV,  $I=13$   $\mu$ A,  $S=62$  mm).**

In order to investigate the importance of the physical properties of the dielectric liquid, such as electrical conductivity and viscosity some additional demonstrative experiments were performed. To increase the electrical conductivity of silicone oil from  $5.5 \times 10^{-9}$  S/m to  $\sim 5 \times 10^{-5}$  S/m, a solution of silicone oil and  $10^{-1}$  mol di-2-ethylhexyl sodium sulfosuccinate (AOT) was prepared. When using 22g electrode at  $V=15$  kV,  $I=23$   $\mu$ A,  $S=40$  mm, only a minor depression over the droplet interface was observed, but the droplet contact line remained unchanged and no spreading was recorded.

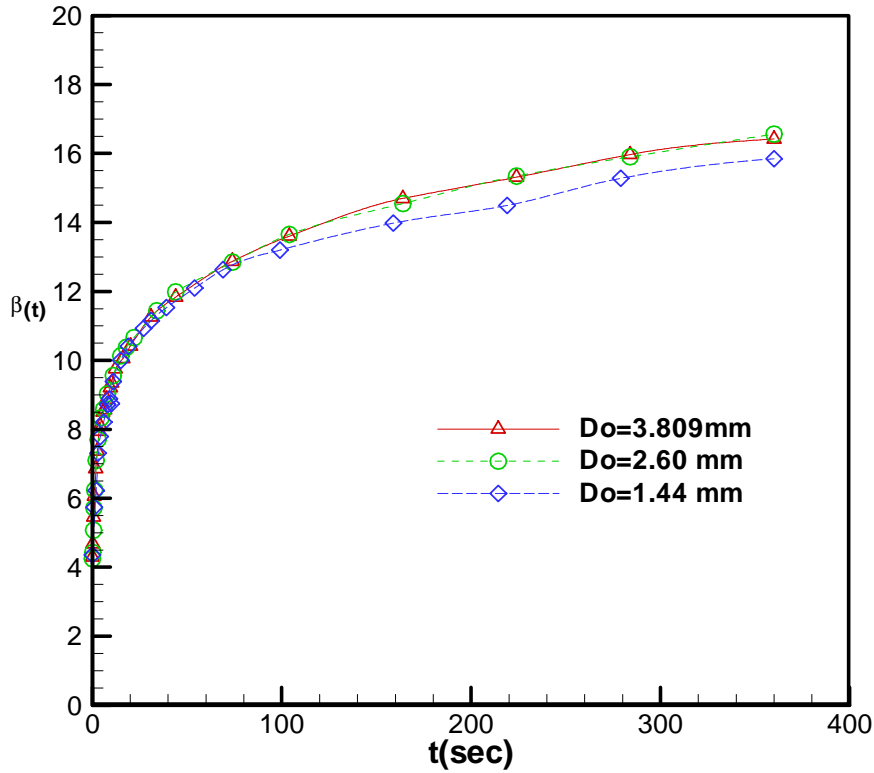


**Figure 7: Dynamic spreading ratio of silicone oil droplets with different initial sizes in the presence of corona discharge ( $V=15$  kV,  $I=23$   $\mu$ A ,  $S=40$  mm).**

The minor depression of interface at the center region can be an indication of a slight electrical pressure, which weakly affects the semi-conductive liquid interface. Repeating the above experiment using silicone oil solution with  $10^{-2}$  mol AOT ( $\sigma \sim 1 \times 10^{-6}$  S/m), one can obtain very slow film spreading. As shown in Fig. 8, the spreading rate in both short term and long term regimes is significantly slower than that of pure oil with the same corona discharge parameters. These observations confirm the effect of elevated electrical conductivity on scaling down the electrical pressure generation and reduced rate of spreading explained earlier. The same experiment was repeated with a glycerin droplet, which has a viscosity one order of magnitude higher than that of silicone oil and its electrical conductivity is near the conductivity of  $10^{-2}$  mol AOT solution. The corona discharge at 15 kV showed no change of glycerin droplet interface. However, after increasing the applied voltage to 18 kV, a similar minor interfacial depression was detected and contact line position was slightly changed. For an extreme case, where the

liquid is electrically conductive (water droplet), even the strongest corona discharge showed no measurable interfacial distortion.

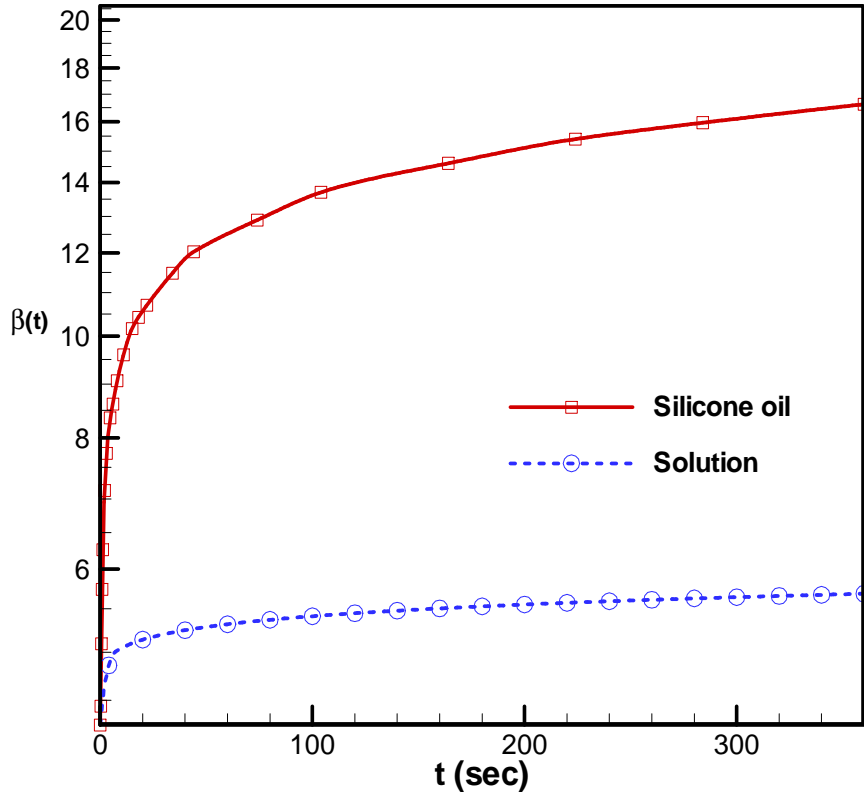


**Figure 8. Dynamic spreading ratio of silicone oil droplet and drop of silicone oil with surfactant in the presence of corona discharge ( $V=15$  kV,  $I=23$   $\mu$ A,  $S=40$  mm). Open circle-symbols represent the dynamic evolution of silicone oil solution with 0.01 mol surfactant (electrical conductivity  $\sigma \sim 1 \times 10^{-6}$  S/m) and squares are for silicone oil ( $\sigma \sim 5.5 \times 10^{-9}$  S/m).**

As observed with the glycerin droplet, both electrical conductivity and viscosity of the liquid play important roles in determining the spreading rate of a film exposed to the corona discharge. All of these evidences confirm the effect of elevated electrical conductivity on scaling down the electrical pressure generation and reducing rate of spreading as postulated earlier.

### 6.3.4 Mathematical model

In order to understand the spreading mechanism, the hydrodynamics of the droplet distortion in the presence of corona discharge was simplified to the classical Stefan's squeezing flow of a fluid between two parallel disks through an external force [16]. An analogy between the current problem and classical squeeze flow can be made by replacing the external mechanical pressure with the electric pressure (see Fig. 9). One minor difference is the boundary condition imposed at the droplet interface. For the classical Stefan problem, no-slip conditions are applied over both plates, whereas in the current problem the boundary conditions at the interface can be primarily assumed to be free boundary conditions (stress free boundary). Due to the symmetry of the squeezing flow between parallel disks, all other aspects of both problems can be considered identical. The simplifying assumptions are as follows:

- 1 – the film thickness  $h(t)$  is uniform in the radial direction,
- 2 - according to the approximation normally assumed in lubrication theory, the spreading process is quasi-steady [17],
- 3 - the electric pressure,  $\rho_s E$ , is uniformly distributed over the liquid surface and is treated as an external pressure exerted on the liquid film interface.
- 4 - all the edge effects, including the effect of surface charge migration from the contact line to the ground, are neglected,
- 5 - convection terms are assumed to be negligible,
- 6 - the inertia effect is important for large droplets only in short time evolution,
- 7 - in the first approximation, the effect of surface tension and droplet interfacial curvature are assumed to be negligible,
- 8 - the electrohydrodynamic instabilities due to the surface charge are neglected,

9- the film thickness was assumed to be very small with respect to the gap length during the evolution process. However, the corona discharge over the interface was assumed to be strong enough, so that the current density change due to the film thickness variation becomes negligible. Applying both conditions, the implicit current density expression presented in [18] is reduced to well-known Mott's steady-state space-charge-limited conduction [19],

10- the electric pressure has two components. (i) electric pressure due to the surface charge (electrophoretic component) and (ii) electric pressure due to the interfacial jump in  $1/2\epsilon E^2$  (dielectrophoretic component). According to the observations, since the electrostatic field in the absence of ion injection does not influence the interface, the dielectrophoretic component was neglected,

11- the main voltage drop is assumed to occur in air gap. Since the liquid layer is thin, the voltage drop across the dielectric film is assumed to be small with respect to that of electrode spacing.

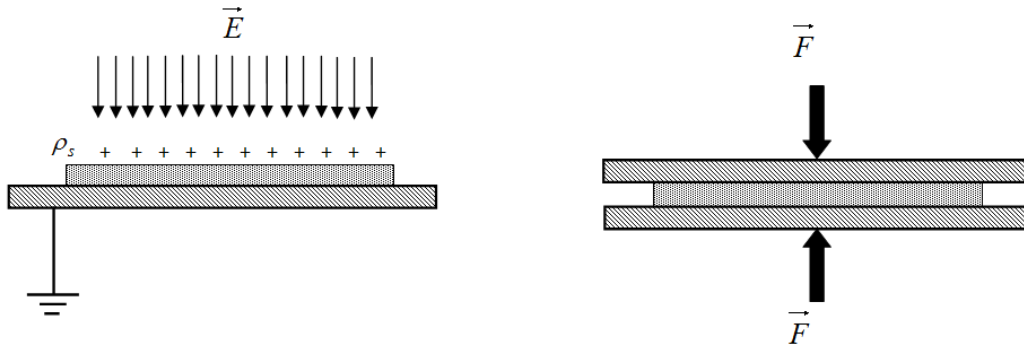


**Figure 9: The similarity of the investigated problem to the squeeze flow between two parallel disks (Stefan's classical problem).**

The Stephan's equation for squeezing flow assuming a constant force  $F$ , Newtonian liquid of viscosity  $\mu$  and a constant volume  $V_0$ , and partially filled between two parallel disks with separation  $h$  is as follows [20]:

$$F = \frac{3\mu V_0^2 \dot{h}}{2\pi h^5} \quad (1)$$

The differential Eq.(1) has been obtained from the simplified lubrication theory for quasi-steady state neglecting the inertia effects [21]. Assuming that the net electric pressure,  $\rho_s E_n$ , resulting from the surface charge density,  $\rho_s$ , and the normal electric field,  $E_n$ , are uniform, and considering the hydrodynamic analogy between the mechanical and electrical pressures:

$$\rho_s E_n = \frac{3\mu V_0 \dot{h}}{2\pi h^4} \quad (2)$$

Since the droplet volume,  $V_0$ , is constant during the evolution, the dynamic spreading diameter,  $D(t)$ , can be obtained as:

$$D(t) = 2D_o \sqrt[6]{\frac{\rho_s E_n t}{9\mu}} + D_s \quad (3)$$

Knowing the electric pressure exerted on the interface and maximum spontaneous spreading of the droplet deposited over the solid substrate,  $D_s$ , the dynamic behavior of the droplet having an initial diameter of  $D_o$  can be predicted from Eq.(3). However, estimation of the electric pressure is difficult since a portion of the deposited surface charge density migrates towards the grounded substrate through the conduction mechanism as the liquid was assumed to be an ohmic (“leaky”) dielectric. Moreover, the current density, surface charge and electric field have a non-uniform distribution over the interface. An additional difficulty is the fact that the thickness of dielectric layer may affect this distribution. As a first approximation, the surface charge density distribution can be assumed to be uniform over the interface (see Appendix A). For moderate or strong ion injections, the interfacial charge and current density rapidly reach the saturation level and become constant. This regime is so-called space charge limited current regime (SCLC [18]). Since the voltage drop mainly occurs across the air gap, the voltage drop in the thin film is assumed to be much smaller than that across the air gap. Therefore, the effect of film thickness on the current density and electric pressure can be neglected. This assumption is particularly valid for thin dielectric liquid films ( $h \ll S$ ), which are exposed to stronger corona discharge at larger electrode separations [19] (See



Appendix B). Current density, surface charge density and electric field in the presence of uniform electric field are saturated and they can be expressed as [18, 19]:

$$j = \frac{9\alpha K_a \varepsilon_a}{8} \left( \frac{V^2}{S^3} \right) \quad (4)$$

$$\rho_s = \frac{9\alpha K_a \varepsilon_a^2}{8\sigma_f} \left( \frac{V^2}{S^3} \right) \quad (5)$$

$$E_n = \frac{9\alpha K_a \varepsilon_a^2}{8\sigma_f \varepsilon_f} \left( \frac{V^2}{S^3} \right) \quad (6)$$

where  $V$  is the voltage applied to the corona electrode,  $S$  is electrode gap spacing,  $K_a$  and  $\varepsilon_a$  are ion mobility of the positive ions and electrical permittivity of the air, respectively, and  $\sigma_f$  is electrical conductivity of the dielectric liquid. The electric field enhancement coefficient,  $\alpha$  equals to 1 for strong uniform ion injection in an infinite film layer (Mott's steady-state space-charge-limited conduction [18,19]). Substituting the surface charge density and the electric field expressions into Eq.(4), the dynamic behavior of the film diameter can be expressed as:

$$D(t) = \Gamma t^{1/6} + D_s \quad (7)$$

$$\Gamma^3 = \frac{3\alpha K_a \varepsilon_a^2}{\sigma_f \sqrt{\mu \varepsilon_f}} \left( \frac{V^2}{S^3} \right) D_o^3$$

The spreading ratio can be calculated as:

$$\beta(t) = \Gamma' t^{1/6} + \beta_s \quad (8)$$

$$\Gamma'^3 = \frac{3\alpha K_a \varepsilon_a^2}{\sigma_f \sqrt{\mu \varepsilon_f}} \left( \frac{V^2}{S^3} \right)$$

According to Eq.(8), the dynamic spreading ratio is not function of the droplet initial size. This conclusion is consistent with the universal spreading ratio for different droplet sizes presented earlier in Figs. 6 and 7.

### 6.3.5 Analytical results versus experimental measurements

A typical comparison between the analytical and experimental behavior of the film diameter,  $D(t)$ , is presented in Fig. 10. The predicted trend of the dynamic evolution of the film diameter is very similar to the experimental results. The comparison between the analytical and experimental diameters for the long term regime shows a maximum 4% difference, while for the short term the deviation is less than 16%. The analytical overestimation of the film diameter in the short term range is believed to be due to the fact that Eq.(7) is sensitive to the model simplifications at the very beginning of evolution process. These assumptions are for instance, neglecting of the surface tension force and dynamic contact angle effects, temporal/convective inertia, spatial variation of surface charge density and electric field and the effect of dielectric film thickness (which is larger in the early stage of spreading). It should be also mentioned that the electric pressure is slightly overestimated due to neglecting the voltage drop across the film. This leads to an overestimation of current density, and consequently electric pressure and dynamic spreading, particularly when the dielectric layer is comparatively thicker. Better agreement could be found by applying the Vega's and Pérez's approach [19] for current density and interfacial charge estimation at the very beginning of evolution ( $t < 5$  s). Considering so many idealizations of the model, the analytical expression shows relatively good agreement with the experimental results and supports the above spreading mechanism hypothesis.

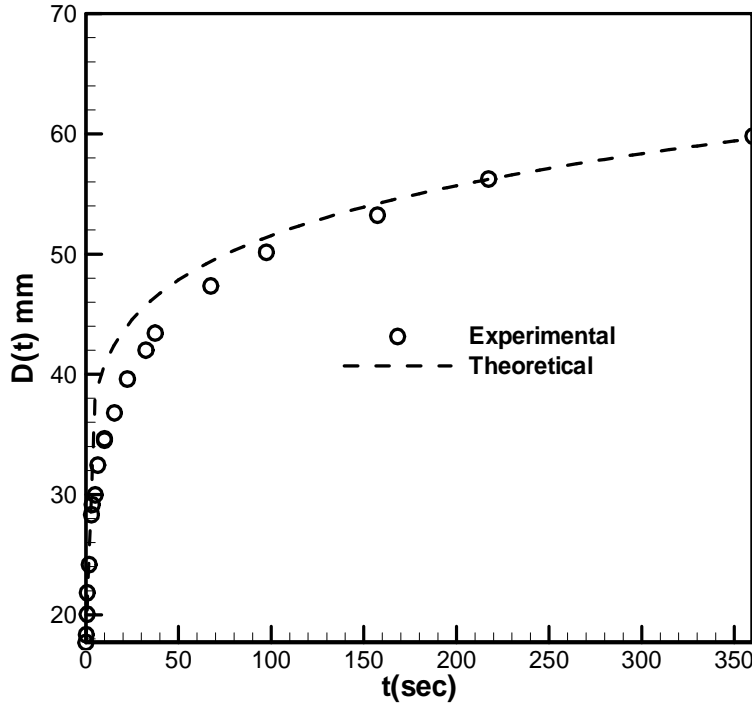


**Figure 10: Evolution of the diameter of a silicone oil droplet exposed to corona discharge. The circles represent the measured expansion of film diameter. The dashed line represents the theoretical predictions of droplet evolution given by Eq. (7). The electrical conductivity of the oil was measured to be  $\sigma \sim 5.5 \times 10^{-9}$  S/m. The kinematic viscosity of the silicone oil was 50 cSt. The calculated field enhancement parameter was calculated to be  $\alpha = 2.25$ . The experimental error bars are smaller than the symbol size.**

## 6.4 Conclusions

A corona discharge-assisted technique for uniform spreading of a dielectric droplet is reported. The mechanism of the spreading process was investigated through several qualitative and quantitative experiments. It was found that the spreading process is governed by the interfacial charge accumulation resulting from the imposed corona discharge. We also demonstrated that the current problem is analogous to the classical Stefan's lubrication theory for squeezing liquid flow between parallel disks. Using this analogy, dynamic spreading ratio was correlated to the electrical pressure and the electrical/thermophysical properties of the fluids. The analytical model showed good

agreement with the experimental results especially for long term film expansion and supports the postulated spreading mechanism.

## Appendix A

### Mathematical model for spreading of a dielectric droplet through an interfacial electric pressure

The dynamic spreading of a droplet in the presence of corona discharge can be predicted through understanding the analogy between the investigated problem and the classical squeezing liquid flow between two parallel disks (Stefan's problem [16]). Figs. A-1 (a) and (b) depict the schematic of a realistic and simplified model of the spreading process in the presence of corona discharge, respectively.

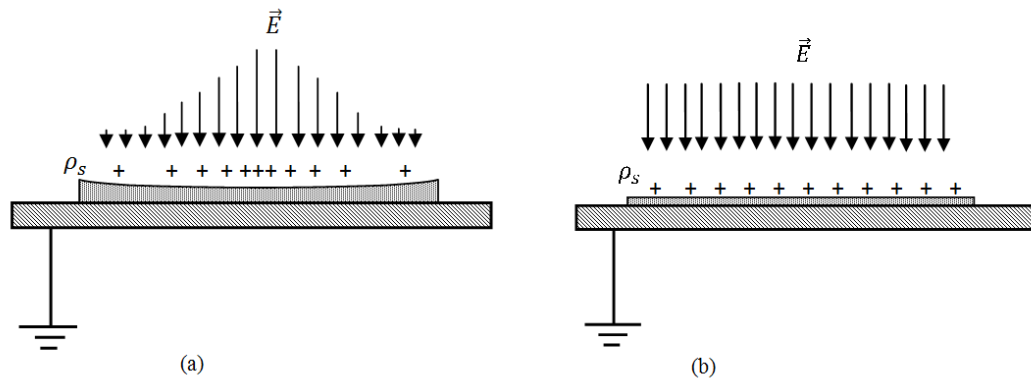


Figure A1: Schematics of the dielectric liquid spreading in the presence of corona discharge. (a) Realistic model before simplifications (b) Simplified model for current analysis.

The simplifying assumptions are as follows:

- 1 - film thickness  $h(t)$  is uniform in the radial direction,
- 2 - according to lubrication approximation theory, the spreading process is assumed to be quasi-steady,

Appendix A was published in Proc. R Soc. A 2011 (467) pp.3257-3271 as a supplementary document.

3 - electric pressure,  $\rho_s E$ , is uniformly distributed over the liquid surface. It will be treated as an external pressure exerted on the liquid film interface. This consequently creates a pressure gradient in the radial direction, which is responsible for a flow field in the liquid volume. Moreover, the volume charge density is assumed to be negligible; this is particularly valid when the film thickness is very small,

4 - all the edge effects, including the effect of surface charge migration from the contact line to the ground, are neglected,

5 - convection terms are assumed to be negligible (full analysis of this assumption is given in chapter 6),

6 - the inertia effect is important for large films in short time evolution; the validity of the assumption will be discussed,

7 - in the first approximation, the effect of surface tension and droplet interfacial curvature are assumed to be negligible (This is valid when the interface curvature tends to infinity. This assumption is not true for the short term evolution, where the curvature is finite around the rim. It can be relevant for long term hydrodynamically stable spreading process),

8 - the electrohydrodynamic instabilities due to the surface charge are neglected,

9- the film thickness is assumed to be very small with respect to the gap length during the evolution process. However, the corona discharge over the interface was assumed to be strong enough, so that the current density change due to the film thickness variation becomes negligible. Applying both conditions, the implicit current density expression presented in [19] is reduced to well-known Mott's steady-state space-charge-limited conduction [18],

10- the electric pressure has two components. (i) electric pressure due to the surface charge (electrophoretic component) and (ii) electric pressure due to the interfacial jump in  $0.5\epsilon E^2$  (dielectrophoretic component). According to the observations, since the

electrostatic field in the absence of ion injection does not influence the interface, the dielectrophoretic component was neglected,

11- The main voltage drop is assumed to occur in the air gap. Since the liquid layer is thin, the voltage drop across the dielectric film is assumed to be small with respect to that of electrode spacing.

The spreading phenomenon through interfacial electric pressure is analogous to the classical problem of squeezing flow between parallel disks, the so-called Stefan problem [16]. Fig. 2 presents a figurative explanation of this analogy. The solutions of the velocity and pressure fields for the Stefan problem have been derived by several authors [20, 21]. This has been the interest of rheologists to obtain the response of a given liquid between two parallel disks for either Newtonian or non-Newtonian fluids under a constant force or constant velocity disk movement. The details of a model for the squeezing of a Newtonian liquid between parallel disks with constant force can be found in [21]. Fig. 3 demonstrates the geometry of the simplified model used in this study.

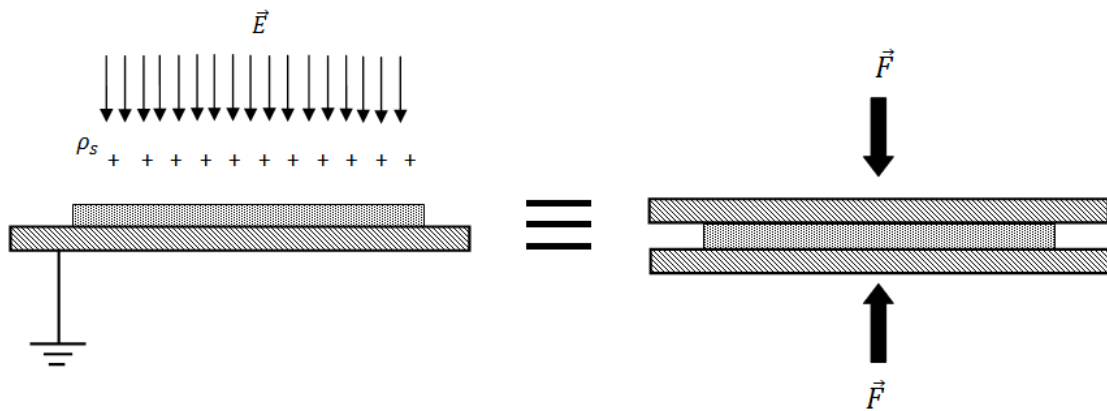


Figure A-2: The similarity of the investigated problem to the squeeze flow between two parallel disks (Stefan's classical problem).

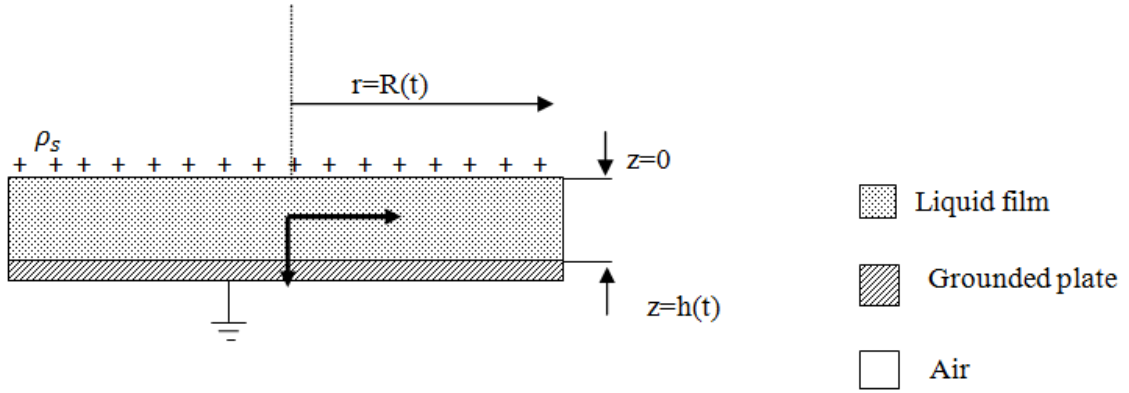


Fig. A-3 Idealized model in the cylindrical coordinates assumed in the present analytical approach

Starting with the conservation of mass equation in cylindrical coordinates:

$$\frac{1}{r} \frac{\partial}{\partial r} (ru_r) + \frac{\partial u_z}{\partial z} = 0 \quad (1)$$

The problem depends on two spatial dimensions,  $r$  and  $z$ . The  $r$ -dependence can be eliminated by applying von Karman similarity transformation:

$$\begin{aligned} \Psi(r, z, t) &= r^2 G(z, t), \quad \text{and } u_r \\ &= r \frac{\partial G(z, t)}{\partial z} \end{aligned} \quad (2)$$

Substituting (2) in the continuity Eq.(1), we have:

$$2 \frac{\partial G(z, t)}{\partial z} + \frac{\partial u_z}{\partial z} = 0 \quad (3)$$

$$u_z = -2G(z, t) \quad (4)$$

Assuming the temporal inertia is negligible, the  $r$ -momentum balance equation can be written as:

$$u_r \frac{\partial u_r}{\partial r} + u_z \frac{\partial u_r}{\partial z} = \frac{\mu}{\rho} \left( \nabla^2 u_r - \frac{u_r}{r^2} \right) - \frac{1}{\rho} \frac{\partial p}{\partial r} \quad (5 - a)$$

By performing order of magnitude analysis and considering the liquid film thickness is very small, the convective terms are found to be as small as  $O(\frac{u_r^2}{R})$ , while the viscous force is in the order of  $O(\frac{u_r}{h^2})$ . Neglecting the convection terms, the  $r$ -momentum balance equation can be expressed as:

$$\frac{\mu}{\rho} \left( \frac{\partial^2 u_r}{\partial z^2} \right) = \frac{1}{\rho} \frac{\partial p}{\partial r} \quad (5 - b)$$

Using the von Karman similarity transformations, the balance equation in  $r$ -direction reduces to the following ordinary linear differential equation:

$$\mu G'''(z, t) = \frac{1}{r} \frac{\partial p}{\partial r} \quad (5 - c)$$

The boundary conditions can be expressed as:

- at  $z=0$  (the film surface),  $G''(z, t) = 0$
- at  $z = h(t)$  (substrate),  $G'(z, t) = G(z, t) = 0$ .

The general solution of Eq.(5-c) can be obtained as:

$$G(z, t) = \left( \frac{1}{\mu r} \frac{\partial p}{\partial r} \right) \frac{z^3}{6} + C_1 z^2 + C_2 z + C_3 \quad (6 - a)$$

Using three boundary conditions, the unknown coefficients  $C_1$ ,  $C_2$  and  $C_3$  can be calculated as:

$$C_1 = 0 \quad (6 - b)$$

$$C_2 = - \left( \frac{1}{\mu r} \frac{\partial p}{\partial r} \right) \frac{h(t)^2}{2} \quad (6 - c)$$

$$C_3 = \left( \frac{1}{\mu r} \frac{\partial p}{\partial r} \right) \frac{h(t)^3}{3} \quad (6 - d)$$

The radial velocity is equal to:



$$u_r = \frac{h^2}{2\mu} \left( \frac{\partial p}{\partial r} \right) \left( \left( \frac{z}{h} \right)^2 - 1 \right) \quad (6 - e)$$

In order to find the pressure field in the liquid film, we used the integral form of the mass continuity:

$$\int_0^h u_r dz = \int_0^{2\pi} \int_0^r u_z r dr d\theta \quad (7)$$

The velocity in the  $z$ -direction,  $u_z = -2G(z, t)$ , is not a function of  $r$ . Since the film thickness was assumed to be uniform (assumption 1) and substituting  $u_z = \dot{h}$ , the integration of the continuity equation gives:

$$\int_0^{2\pi} \int_0^h u_r r d\theta dz = \pi r^2 \dot{h} \quad (8)$$

$$\int_0^{2\pi} \int_0^h \frac{h^2}{2\mu} \left( \frac{\partial p}{\partial r} \right) \left( \left( \frac{z}{h} \right)^2 - 1 \right) r d\theta dz = \pi r^2 \dot{h} \quad (9)$$

$$\frac{2h^3}{3\mu} \left( \frac{\partial p}{\partial r} \right) = r \dot{h} \quad (10)$$

$$\left( \frac{\partial p}{\partial r} \right) = \frac{3\mu r \dot{h}}{2h^3} \quad (11)$$

$$p = \frac{3\mu r^2 \dot{h}}{4h^3} + P_o \quad (12)$$

$P_o$  can be found by applying the contact line condition: at  $r = R(t)$ ,  $P = P_{atm}$

$$P_{atm} = \frac{3\mu R^2 \dot{h}}{4h^3} + P_o \quad (13)$$

$$P(r, t) = \frac{3\mu R^2 \dot{h}}{4h^3} \left( \left( \frac{r}{R} \right)^2 - 1 \right) + P_{atm} \quad (14)$$

$$\int \rho_s E dA = \int (P - P_{\text{atm}}) dA = \int_0^{2\pi} \int_0^R \frac{3\mu R^2 \dot{h}}{4h^3} \left( \left( \frac{r}{R} \right)^2 - 1 \right) r dr d\theta \quad (15)$$

If we assume that the electric pressure,  $\rho_s E$ , is uniformly distributed over the droplet surface, then the above differential equation provides the evolution of film thickness:

$$\rho_s E \pi R^2 = -2\pi \frac{3\mu R^4 \dot{h}}{4h^3} \quad (16)$$

Equation (16) is exactly the same as the Stefan's equation for squeezing flow exerting constant force to the parallel disks.

$$-\frac{\rho_s E dt}{\mu R_0^3} = \frac{dh}{h^4}$$

$$-\int_{t=0^+}^t \frac{\rho_s E}{\mu R_0^3} dt = \int_{h_s}^h h^{-4} dh$$

$$\frac{\rho_s E t}{\mu R_0^3} = \frac{1}{3h^3} + C \quad (17)$$

where  $h_s$  is the film thickness of droplet, spontaneously expanded on the substrate at  $t = 0^+$ . The constant  $C$  can be determined by applying the initial conditions:

$$h(t) = \frac{1}{\sqrt[3]{\frac{3\rho_s E t}{\mu R_0^3} + \frac{1}{h_s}}} \quad (18)$$

The evolution of  $R(t)$  can be obtained assuming the volume of the droplet is kept constant during the evolution process:  $R^2 h = \frac{4}{3} R_0^3$

$$R(t) = \sqrt{\frac{4}{3} R_0^3} \sqrt[6]{\frac{3\rho_s E t}{\mu R_0^3}} + R_s \quad (19)$$

$$R(t) = 2R_0 \sqrt[6]{\frac{\rho_s E t}{9\mu}} + R_s$$

$$D(t) = 2D_0 \sqrt[6]{\frac{\rho_s E t}{9\mu}} + D_s \quad (20)$$

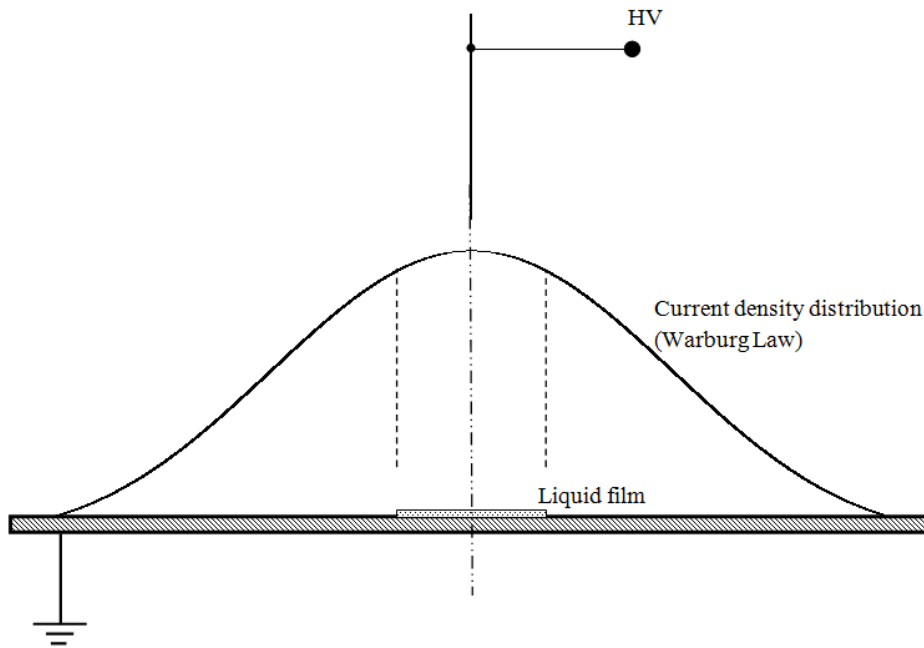


Figure A-4: Distribution of current density in the point-plane corona discharge. For thin film liquid,  $h \ll S$ , deposited on the substrate, the current density distribution is similar to the Warburg law. The current density variations in the radial direction can be assumed to be negligible for relatively small droplet spreading ratios.

Equation (20) describes the dynamic evolution of a deposited droplet on a grounded substrate in the presence of corona discharge. An analytical expression for the interfacial electric pressure,  $\rho_s E$ , can be obtained by considering several simplifications. The initial condition,  $t = 0^+$ , is defined as an arbitrary instant of time, when the film thickness is measured after a spontaneous spreading process due to the inertia effect. Therefore, initial conditions for  $h_s$  and  $D_s$  can be obtained experimentally.

Since the electrical pressure calculation is difficult due to the complicated physics and non-uniform distribution of surface charge density and electric field, additional idealizations based on experimental observation are necessary. The experimental observation revealed that at quasi steady-state conditions the corona current density and measured total corona current remain approximately unchanged in the presence of the film regardless of its dimensions.

$$I_{film,exp} = I_{corona,exp} \quad (21)$$

This observation is consistent with conservation of charge density and saturation condition derived in [19]. Also, it can be proven from Warburg's law that for  $S > 4R(t)$ , the current density distribution on the surface of substrate and liquid film varies slightly (15% variations) [13-15] and it can be assumed constant over the dielectric interface (see Fig. 4). Assuming a strong ion injection, the maximum charge density at  $r = 0$  and its neighborhood can be approximated as [14,18]:

$$j_{max} = \frac{9\alpha K_a \epsilon_a}{8} \left( \frac{V^2}{S^3} \right) \quad (22)$$

where  $\alpha$  is a function of electrode shape. For parallel plate geometry  $\alpha$  equals to 1, which corresponds to the well-known Mott's steady-state space-charge-limited conduction [18,19]. For a specific emitter electrode, the coefficient  $\alpha$  in Eq.(22) can be determined by integrating the current density over the grounded electrode. Therefore, the field enhancement coefficient is correlated to the experimental value of the total corona current  $I_{exp}$ :

$$\int j_{max} \cos^5 \theta dA = \int \frac{9\alpha K_a \epsilon_a}{8} \left( \frac{V^2}{S^3} \right) \cos^5 \theta dA = I_{exp}$$

According to [19], the current density saturates rapidly and remains constant at quasi-steady state condition. For ohmic dielectric liquid, the accumulated surface charge density and resulting electric field can be obtained as:

$$\rho_s = \frac{9\alpha K_a \varepsilon_a^2}{8\sigma_f} \left( \frac{V^2}{S^3} \right) \quad (23)$$

$$E_n = \frac{9\alpha K_a \varepsilon_a^2}{8\sigma_f \varepsilon_f} \left( \frac{V^2}{S^3} \right) \quad (24)$$

Substituting the surface charge density and the electric field, the dynamic behavior of the film diameter can be expressed as:

$$D(t) = \Gamma t^{1/6} + D_s, \quad \Gamma^3 = \frac{3\alpha K_a \varepsilon_a^2}{\sigma_f \sqrt{\mu \varepsilon_f}} \left( \frac{V^2}{S^3} \right) D_o^3 \quad (25)$$

According to Eq.(25), the dynamic evolution of the droplet depends on the strength of the ion injection, the medium in which the unipolar ion injection occurs, the strength of the electric field, permittivity, electrical conductivity and viscosity of the dielectric fluid.

## Appendix-B

### Validity of the hydrodynamic model

The essence of droplet spreading in the presence of corona discharge introduces two different length scales, the film thickness,  $h$ , and spreading diameter,  $D$ . These two length scales are used to normalize the governing equation as follows:

$$\{\bar{r}, \bar{z}\} = \left\{ \frac{1}{D} r, \frac{1}{h} z \right\}$$

The velocity field can be normalized by the radial velocity as following:

$$\{\bar{u}_r, \bar{u}_z\} = \left\{ \frac{u_r}{U^*}, \frac{u_z}{U^* \left( \frac{h}{D} \right)} \right\}$$

The normalized pressure and time can be expressed as:

$$\bar{p} = \frac{p}{\rho U^{*2}} \left( \frac{h}{D} \right) \text{Re}, \quad \bar{t} = \xi t$$

$\xi = \frac{1}{t_{1/n}}$ ,  $t_{1/n}$  is the time of evolution to reach  $\frac{1}{n} h_s$ . The Reynolds number is defined as:

$$\text{Re} = \frac{U^* h}{\nu}.$$

The mass and momentum continuity equation can be written as:

$$\xi^* = \frac{h^2 \xi}{\nu}, \quad \text{Re}^* = \frac{h}{D} \text{Re} = \frac{h^2 U^*}{\nu D}$$

$$\xi^* \frac{\partial \bar{u}_r}{\partial t} + \text{Re}^* \left( \bar{u}_r \frac{\partial \bar{u}_r}{\partial r} + \bar{u}_z \frac{\partial \bar{u}_r}{\partial z} \right) = -\frac{\partial \bar{p}}{\partial r} + \frac{\partial^2 \bar{u}_r}{\partial z^2}$$

The left-hand side in the last equation is in the order of  $O(h^2)$ . As an initial approximation, the LHS (temporal inertia and convective inertia) can be assumed negligible and viscous force is balanced only with the pressure gradient in the radial direction. However, the effect of inertia becomes important, particularly for the short term evolution studies. Temporal inertia becomes important and the convective inertia might be ignored, when  $\text{Re}^* \rightarrow 0$  and  $\xi^* \geq 1$ . This condition corresponds to  $\frac{h^2}{\nu} \geq t_{1/n}$

(very beginning of the slow evolution process). For the limiting case  $\xi^* \rightarrow 0$  and  $\text{Re}^* \geq 1$ , the convective term should be considered and temporal convection can be neglected. This corresponds to the long term behavior investigation of a relatively rapid evolution. For short term behavior,  $t_{1/n} \leq \frac{h^2}{\nu}$ , where the evolution is rapid,  $U^* \geq \frac{\nu D}{h^2}$ , both convective inertia and temporal inertia effects should be considered. Therefore, the previous model more accurately describes the long term evolution behavior.

## References

- [1] Bergeron, V., Bonn, D., Yves Martin, J., Vovelle, L., 2000, Controlling droplet deposition with polymer additives, *Nature* **405**, 772-774.
- [2] Carré, A., Gastel, J., Shanahan, M., 1996, Viscoelastic effects in the spreading of liquids, *Nature* **379**, 432-434.
- [3] Schiaffino, S., Sonin, A., 1997, Molten droplet deposition and solidification at low Weber numbers, *Phys. Fluids* **11**, 3172-3187.
- [4] Bernardin, J.D., Stebbins, C. J., Mudawar, I., 1997, Mapping of impact and heat transfer regimes of water drops impinging on a polished surface, *Int. J of Heat and Mass Trans.* **40(2)**, 247-267.
- [5] Frohn, A., Roth, R., 2000, *Dynamics of Droplets* Springer, Berlin.
- [6] Mang, T., Dresel, W., 2007, *Lubricants and Lubrication* Wiley, Weinheim.
- [7] Bussmann, M., Chandra, S., Mostaghimi, J., 2000, Modeling the splash of a droplet impacting a solid surface, *Phys. Fluids* **12**, 3121-3132.
- [8] Mehdizadeh, N.Z., Chandra, S., Mostaghimi J., 2004, Formation of fingers around the edges of a drop hitting a metal plate with high velocity, *J. Fluid Mech.* **510**, 353-373.
- [9] Vega, F., Pérez, A.T., 2003, Corona-induced electrohydrodynamic instabilities in low conducting liquids, *Exp. Fluids* **34**, 726-735.
- [10] Vega, F., García, F., 2006, Pattern imaging of primary and secondary electrohydrodynamic instabilities, *J. Fluid Mech.* **549**, 61-69.
- [11] Atten, P., Moreau, R., 1972, Stabilité électrohydrodynamique des liquides isolants soumis à une injection unipolaire, *J. Mécanique.* **11(3)**, 471-520.



- [12] Koulova-Nenova, D., Atten, P., 1997, EHD instability of air/liquid two liquid layer system under unipolar charge injection, J. Electrostat. **40–41**, 179-174.
- [13] Warburg, E., 1899, Über die spitzenentladung, Wied. Ann. **67**, 69-83.
- [14] Warburg, E., 1927, *Handbuck der Physik* Springer, Berlin.
- [15] Jones, J.E., 1997, A theoretical explanation of the laws of Warburg and Sigmond, Proc. R. Soc. A: Math. Phys. Eng. Sci **453**, 1033-1052.
- [16] Stefan, J., 1874, Versuche über die scheinbare adhäsion, Sitzungber. K. Akad. Wiss. Math. Natur. Wien **69**, 713-735.
- [17] Cameron, A., 1966, *The Principles of Lubrication*, Longmans, London.
- [18] Mott, N.F., Gurney, R.W., 1964, *Electronic Processes in Ionic Crystals* Dover, New York.
- [19] Vega, F., Pérez, A.T., 2002, Instability in a non-ohmic/ohmic fluid interface under a perpendicular electric field and unipolar injection, Phys. Fluids **14**, 2738-2751.
- [20] Dienes, G.J., Klemm, H.F., 1946, Theory and application of the parallel plate plastometer, J. Appl. Phys. **17**, 458-471.
- [21] Leider, P.J., Bird, R.B., 1974, Squeezing flow between parallel disks. I. Theoretical analysis, Ind. Eng. Chem. Fund. **13**, 336–341.

## Chapter 7

### Different regimes of corona discharge spreading of dielectric liquid films

#### 1.2 Introduction

Dielectric liquid films are encountered in numerous industrial and scientific applications, such as coating, deposition, wetting and adhesion, nano-lubrication of ultra-fast rotary systems [1], recent thin film electronic devices in molecular electronics [2,3], and several biological processes [4]. Fundamental study in the characterization of the thermophysical and electrical properties of these thin films may lead to better understanding of both the energy and charge carrier transport processes across the films in the listed applications [5,6]. An important first step for such studies would be the study of the deposition of such as dielectric thin films on a substrate. Since the number of techniques for spreading of dielectric liquids is limited, new techniques for liquid film deposition and control over the substrate could be of great interest.

It has been demonstrated that the electrostatic forces can be used for spreading of dielectric layers [7,8]. Recently, several studies were performed to show the spreading of the liquid layers using an external electric field. It was found that both interfacial components of the electrostatic forces, normal and tangential, can be used to produce liquid films over a substrate. A selective spreading of a dielectric liquid due to the tangential component of electric forces was demonstrated which accompanies with formation of a Taylor cone and periodic jetting occurring during the process [7]. Very recently, it was demonstrated that a dielectric droplet exposed to a perpendicular corona discharge expands uniformly over the grounded substrate due to the normal component of the electric pressure. The corona discharge moves the ionic cloud towards the substrate and develops a surface charge over the droplet interface. The normal component of electric field produces a squeezing electric pressure over the dielectric interface and the droplet expands uniformly over the substrate in the radial direction. It was found that the dynamics of the liquid film formation for intermediate corona discharge exposure time obeys  $D(t) \sim t^{1/6}$  law, where  $D(t)$  is the diameter of the film and  $t$  is the corona discharge

exposure time. In this case, the ohmic conduction model was assumed to be a valid charge transport mechanism across the film whose thickness was comparatively thick (in the order of  $10^{-4}$ - $10^{-5}$  m).

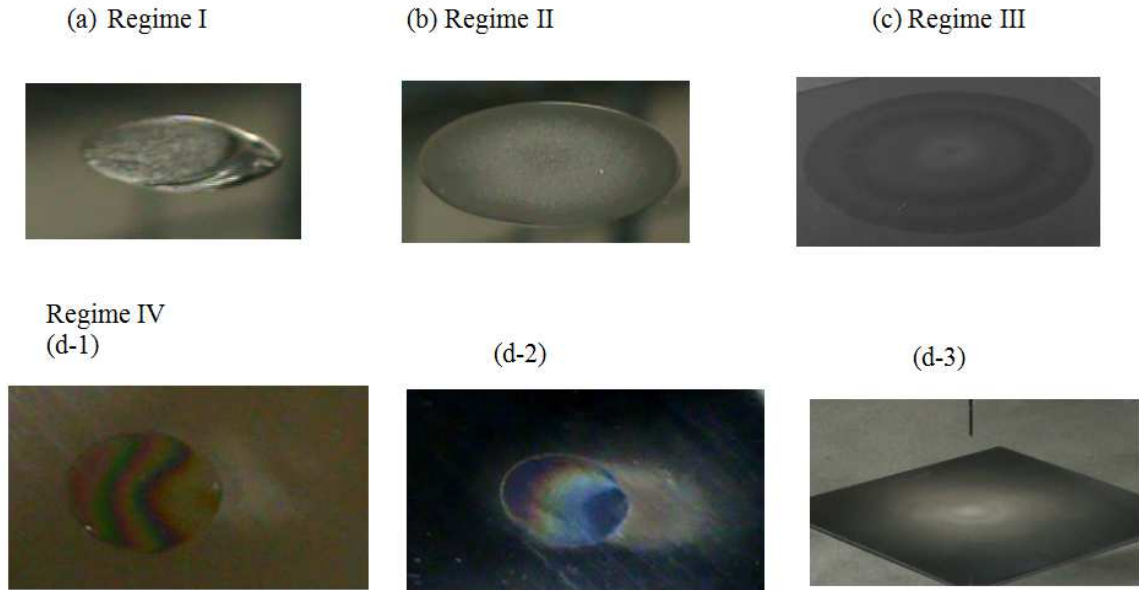


**Figure 1: Silicone oil film spreading over a conductive substrate through corona discharge exposure. Different regimes of spreading are depicted using different size of droplets. (a) Regime I (transient corona charging): 2ms after corona discharge exposure (b) Regime II (quasi-steady state corona charging): after 300 sec corona discharge exposure. (c) Regime III (hetero-charge interaction): after 1000 sec exposure. (d) Regime IV (corona accelerated precursor film): (d-1) silicone oil film after 2400 sec, (d-2) after 7200 sec (d-3) after  $1.7 \times 10^5$  seconds of corona discharge exposure. The electrode was a modified needle and the separation between the corona needle and substrate for all cases was 25 mm. The corona voltage and total current was measured to be 17 kV and 40  $\mu$ A, respectively.**

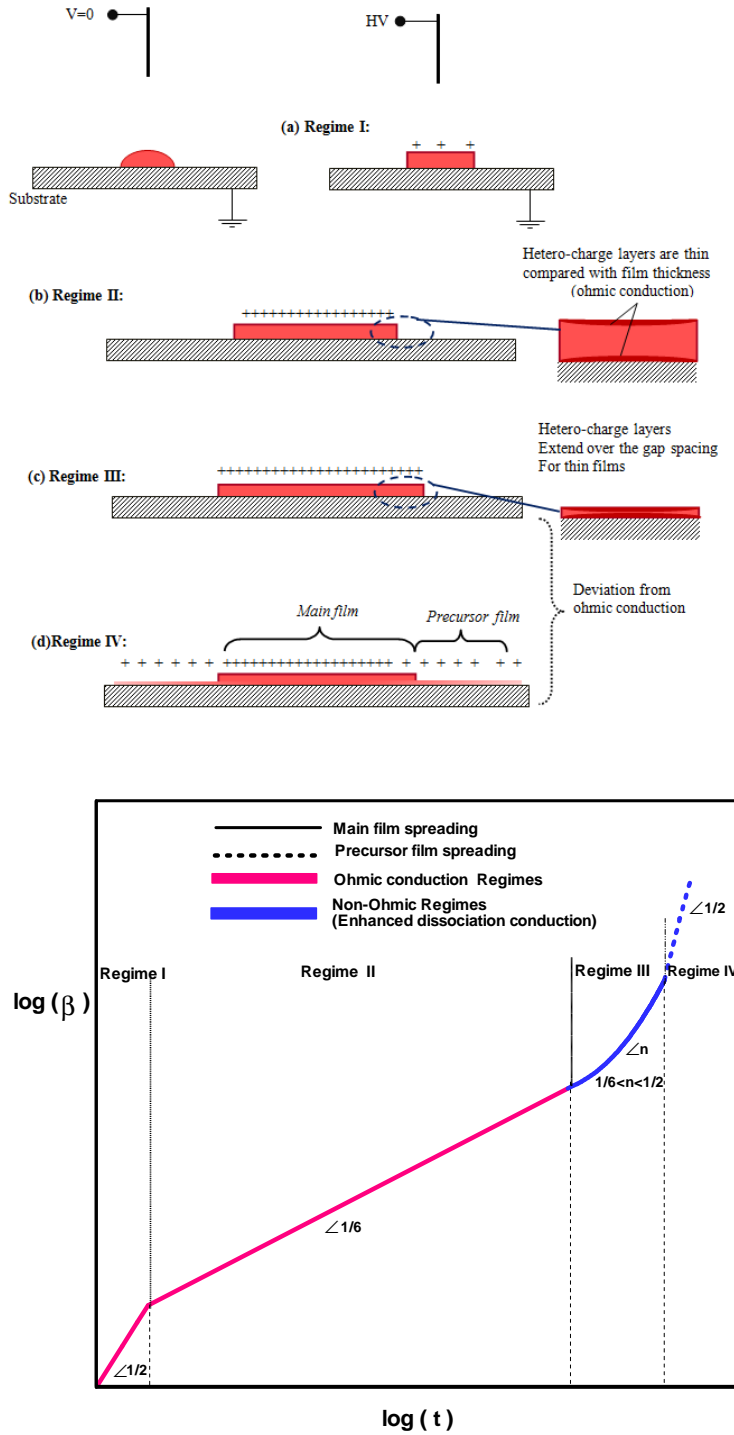


**Figure 2: (a-d) Figurative description of charge carrier transport and (e) qualitative demonstration of dielectric film spreading ratio variation,  $\beta(t)$ , versus corona discharge exposure time. Four different regimes of spreading are identified.**

In the present work, we demonstrate that the corona discharge spreading technique can be effectively used to produce uniform ultra thin films. Four different regimes in the film spreading due to the long term corona exposure have been identified and characterized (see Figs. 1 and 2). Since the charge transport mechanism across the film determines the dynamics of expansion, different regimes of charge carrier transport have been postulated and implemented into the analytical expansion model. These postulated charge transport mechanisms were confirmed experimentally and theoretically. For each regime, a theoretical hydrodynamic model along with a description of the charge carrier transport mechanism have been proposed to predict the observed dynamics of spreading. Fig. 2 (a-d) shows a figurative description of the different regimes and the charge transport mechanism across the liquid thin films. The regimes of liquid film spreading are summarized in Fig. 2-e. The measured spreading dynamics for these different regimes was verified by these mathematical models. At the very beginning of the corona exposure (Regime I), the dielectric film expansion is governed by the transient surface charge accumulation. After the interfacial charging of the dielectric layer reaches a quasi-steady state, the spreading enters the second regime, which was discussed in detail in [8]. In this regime, the film expands monotonically with  $D(t) \sim t^{1/6}$  and the thickness of the film decreases. When the thickness of the film reaches some specific value, a transition to Regime III is observed and the spreading is accelerated. The acceleration is found to be related to the electrostatic component of the disjoining pressure due to the hetero-charge layer attraction force. The transition to the fourth and most interesting regime appears when the corona discharge exposure time is extended further and the thickness of the liquid film reaches sub-micrometer levels. In this regime, a new type of “precursor film” with thicknesses in the order of nanometer occurs ahead of the main film. This precursor film is diffused and rapidly expands from the main film over the substrate due to the electrostatic component of the disjoining pressure until it reaches the area, where the corona discharge is no longer effective (beyond the corona cone region). This is the first time that we report formation of a precursor film due to the electrostatic forces, as all previously reported precursor films were created due to the dispersion component of disjoining pressure due to van der Waals forces [16-18]. The expansion rate of the new precursor film is much faster than the previous one and it can cover much larger area

depending on the size of the corona cone. Deposition of such nanometer thin films through the corona discharge forced-spreading may create a platform for further fundamental studies, such as dielectric phenomena in thin films, hydrodynamics of the thin films, accelerated wetting process, and coating and deposition. Several industrial applications may benefit from such investigations.

## 7.2 Experimental setup and procedure

The schematic diagram of the experimental setup is depicted in Fig. 3. All the experiments start with the deposition of a single silicone oil droplet over a dry and clean mirror-finished stainless steel substrate. In order to generate a corona discharge over the droplet interface, a modified hypodermic needle was used as a high voltage electrode. The end of this needle was cut flush and connected to the positive polarity 0-50 kV DC power supply and the stainless steel substrate with the deposited droplet was grounded. The hypodermic needle was centered with respect to the deposited droplet using a precise XYZ holder. The corona discharge voltage and the current were measured using a pre-calibrated voltmeter (80K-40 Fluke high voltage probe) and electrometer (Keithley electrometer Model 602). In order to record the liquid film spreading dynamics at the early stages of corona discharge exposure, a high speed CCD camera was used. An additional camera was used to record the liquid film spreading for intermediate and long term corona discharge exposures. An image-processing code was developed for post-processing of the collected frame-shots. In order to estimate the thickness of the dielectric thin films smaller than  $5\mu\text{m}$ , a monochromatic interferometer with an extended sodium light source was employed. For film thicknesses below  $2\mu\text{m}$ , a white light interferometer was pre-calibrated using the monochromatic interferometer. In order to measure the thicknesses below  $1\mu\text{m}$  and to further verify the accuracy of the film thickness measurements with interferometers, an automated Variable Angle Spectroscopic Ellipsometer (VASE) M2000V was employed.

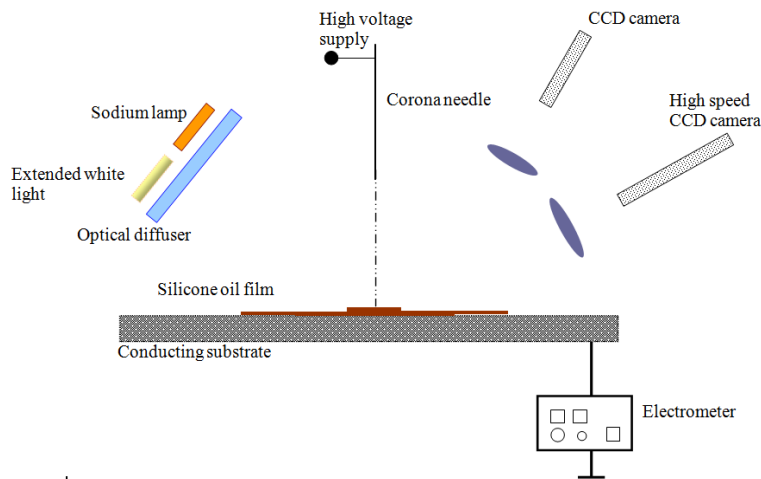


**Figure 3: Schematic view of the experimental setup**

Since the different regimes of the film spreading may be linked to the charge carrier transport across the thin film, an additional experimental setup was prepared (see Fig. 4) to determine the relationship between the surface potential and local current density across the film. For this additional setup, another mirror-finished stainless steel substrate with a hole at its center was fabricated. A stainless steel wire with 0.9 mm diameter was inserted into the hole and it was electrically insulated from the substrate. The wire, which serves as a probe for local current measurement, was connected to the electrometer. The dielectric droplet was deposited at the center of the wire and the corona discharge high voltage needle was mounted perpendicular above the droplet interface and the center of the wire. The corona discharge was applied and the thin film was expanded over the substrate. When the film reached a desired thickness, the corona current across the film was measured. For thin liquid films with thicknesses less than 10  $\mu\text{m}$ , the corona current measurements showed only minor changes with respect to the case when the substrate is clean. In order to confirm the local current density measurement procedure, the radial distribution of the current density was obtained and compared with Warburg's law.

### 7.3 Experimental procedure

To fully characterize the charge transport characteristics across the thin film, the surface potential of the dielectric film subjected to the corona discharge should also be

determined. It is rather difficult to measure the surface electric potential in the presence of corona discharge. In order to estimate this potential, a probe was constructed by micro-welding a zinc particle with diameter equal to the thickness of the film to the top of the stainless steel wire. This was electrically insulated using a solution of 95% plastic paint - 5% n-Heptane. A small droplet of this solution was applied to the wire and particle and the corona discharge was applied to cover the dielectric layer uniformly over the probe. A sharp needle was used to scratch the coating off the particle tip which is needed for surface potential measurements. Choosing a small particle is advantageous since it minimizes the physical size of the measurement probe and reduces the level of the interference in the surface potential measurement and hydrodynamics of the film. (Schematic details are shown in Fig 4.) In order to measure the interfacial electric potential, a variable 0-100 V DC power supply (QuadTech Model: 42000) was used to apply a bias voltage to the probe. An electrometer was used to measure the small currents in the circuit. The bias voltage was applied to the probe and increased until the measured current in the circuit reached approximately zero. At this condition, the bias voltage applied to the probe was assumed to equal the surface potential of the liquid film. In practice, for the surface potential measurements, a silicone oil droplet was placed over the center of the probe and the perpendicular corona discharge was applied. The dielectric film of silicone oil was established over the probe and substrate due to the electrostatic forces. At the beginning, the tip of the probe is totally immersed in the oil and the measured voltages were very small. When the thickness of the thin film reached the probe height, a jump in the potential measurement was detected. The jump corresponds to the enhancement of the electric field due to presence of the interface and the deposited interfacial charge over the surface through the corona discharge. Moreover, in order to further confirm that the film thickness reached the height of the zinc particle probe, a simple setup with a laser diode and detector was employed. When the tip of the zinc particle was immersed in the oil film, no specific signal can be detected. When the film thickness reached to the height of the zinc particle, the reflected light is scattered and a signal could be detected. This signal corresponds to the jump in bias voltage and confirmed that the film thickness equals to the height of the probe. Immediately after the jump was detected, the bias voltage applied to the probe was adjusted so that the current



through the probe tends to zero. This bias voltage was assumed to be equal to the air-oil film interfacial electric potential. The thickness of the film was also monitored through the interferometer. All the experiments were repeated at least twice to ensure the repeatability of the experiments. The room temperature, absolute pressure and the relative humidity were monitored frequently during the tests at 1 m distance from the experimental test section. The uncertainty of the collected experimental data was smaller than the symbols shown in all graphs.

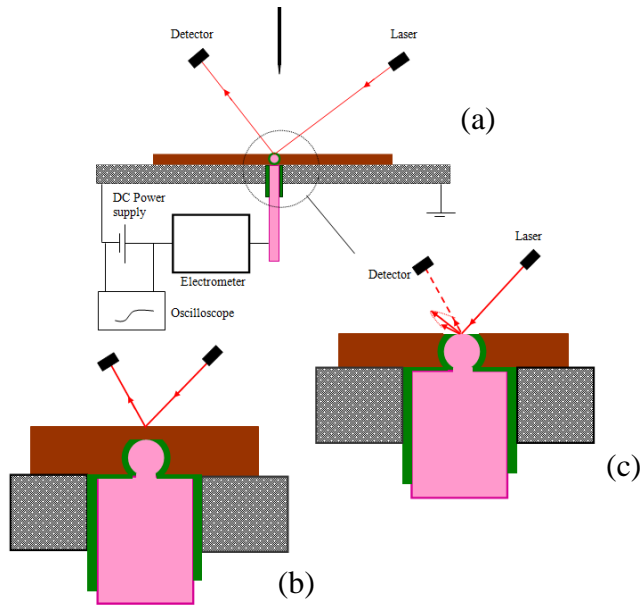


**Figure 4: Schematics of additional experimental setup for measurement of the surface potential of the oil interface subjected to corona discharge. (a) The schematics of the experimental setup. (b) The laser irradiation is completely reflected from the liquid surface while the liquid film thickness is larger than the height of the probe. (c) The reflected laser irradiation from the surface reduces due to the beam scattering when the thickness of the liquid becomes smaller than the height of the probe.**

## 7.4 Results and discussion

### 7.4.1 Regime I and Regime II: Ohmic conduction across the liquid film

High speed imaging of the silicone oil droplet spreading with different initial sizes enabled us to detect the earliest stage of the corona discharge-assisted spreading process. Immediately after corona discharge exposure, the droplet expansion is much more rapid. Fig. 5 depicts the spreading dynamics of two different size silicone oil droplets subjected to the corona discharge for an intermediate exposure time.

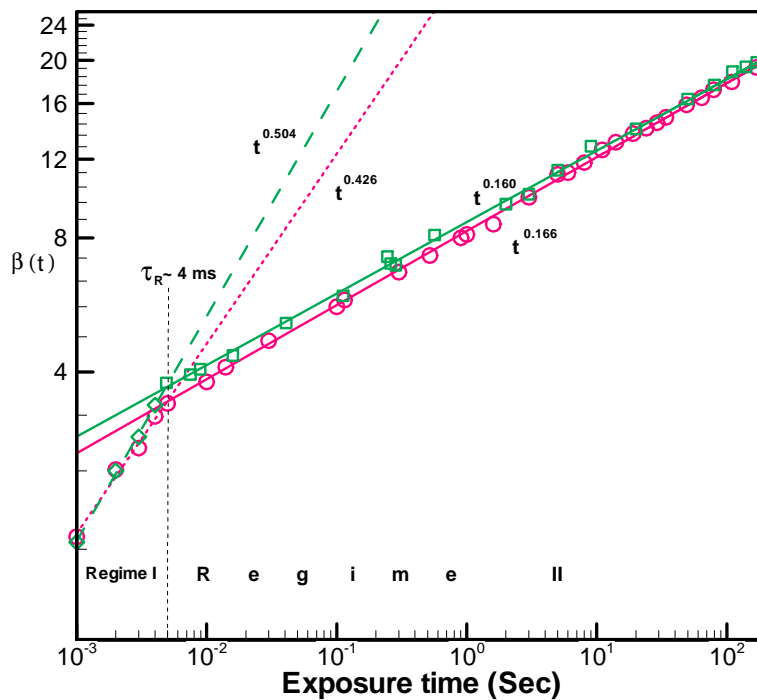


**Figure 5:** Spreading dynamics of two different silicone oil droplets subjected to the corona discharge. The initial size of the droplet is  $D_o=1.44$  mm (green) and  $D_o=2.64$  mm (red). The applied voltage is 17 kV and total corona current 40  $\mu$ A. The gap spacing was kept constant at  $S=25$  mm.

At the beginning of the corona discharge exposure (Regime I), the expansion is fast and it is governed by a  $D(t) \sim t^{1/2}$  law. However, after about 4 milliseconds of exposure, the spreading ratio shows a cross-over to Regime II where the rate of spreading becomes much slower. The dynamic spreading ratio of Regime II is governed by  $D(t) \sim t^{1/6}$ , and was studied in detail in our previous paper [8]. The crossover time relaxation was found to be equal to the charge relaxation time of Silicone oil ( $\tau_R = \frac{\epsilon_f}{\sigma_f} \sim 4 \text{ ms}$ ) (see Fig. 5). Since the crossover time is comparable with the charge relaxation time, we postulated that the Regime I occurs due to the transient interfacial charging. Based on this postulation, the previous model [8] is no longer valid since the charge transport across the film was assumed to be steady state. This assumption is only valid for longer corona discharge exposure (Regime II), but it might be questioned for earliest stages exposure times, for example, milliseconds after exposure (Regime I). In order to understand the early stages of the expansion and confirm this hypothesis, a simplified mathematical model based on an energy balance approach was developed. In order to validate the new energy balance approach, the energy balance approach was first applied for steady state charge transport across the film (Regime II). The spreading law derived with the new approach was shown to be identical to the previous spreading law presented in [8]. After the validation, the proposed energy balance approach is applied to the Regime I where the interfacial charging of the silicone oil film is transient and the dynamic spreading ratio is calculated immediately after the corona discharge exposure. Based on the analysis, it was found that the spreading law for the Regime I obeys  $D(t) \sim t^{1/2}$ . The mathematical model predicts the spreading rates of the droplet expansion in Regime I and further confirms the hypothetical explanation of transient charging of the droplet interface at the earliest stage of the spreading. In the next section, the energy balance approach is presented and discussed.

#### 7.4.2 Energy balance approach: Verification

Using energy balance is an alternative analytical technique to investigate the dynamic spreading of a droplet subjected to corona discharge. Assuming the liquid film after expansion is uniform and the evaporation is negligible:

$$\frac{\pi}{4} D(t)^2 h(t) = \frac{1}{6} \pi D_o^3 = Cte \text{ (droplet volume)} \quad (1)$$

$$D(t)^2 = \frac{2}{3h} D_o^3 \quad (2)$$

where the diameter of the film,  $D(t)$ , and its thickness,  $h(t)$ , are both functions of time. It is also assumed the dielectric liquid is not volatile and the droplet preserves a thin cylindrical shape during evolution.

The derivative of the eq. (1) provides the rate of expansion (contact line velocity) and the rate of thickness variation.

$$2D\dot{D}h + D^2\dot{h} = 0 \quad (3)$$

$$\dot{D} = \frac{-D\dot{h}}{2h} \quad (4)$$

The negative sign in Eq.(4) is due to the fact, that when  $D$  increases,  $h$  must decrease ( $\dot{D} > 0$  and  $\dot{h} < 0$ ).

The contact line velocity is:

$$u = \frac{\dot{D}}{2} = \frac{-D\dot{h}}{4h} \quad (5)$$

$$u = \frac{\dot{D}}{2} = \frac{-D\dot{h}}{4h} = -\left(\frac{D_o^3}{24}\right)^{1/2} \frac{\dot{h}}{h^{3/2}} \quad (6)$$

Since the droplet is deposited over the substrate, the initial kinetic energy of the droplet is zero,  $KE1 = 0$ . The potential energy of the droplet in state 1 is

$$PE1 = \pi D_o^2 \sigma$$

The potential energy of the droplet in state 2 is:

$$PE2 = \frac{\pi}{4} D(t)^2 \sigma (1 - \cos \theta)$$

The electrical energy can be expressed as:

$$WE = \frac{1}{2} \varepsilon_f (E_n)^2 \left( \frac{1}{6} \pi D_o^3 \right)$$

According to the [8], the electric field can be calculated from the formula

$$E_n = \frac{9\alpha K_a \varepsilon_a^2}{8\sigma_f \varepsilon_f} \left( \frac{V^2}{S^3} \right) \quad (7)$$

During the expansion process, a portion of energy is lost due to the viscous dissipation.

The viscous dissipation function,  $\phi$ , can be expressed as [9]:

$$\phi \sim \mu \left( \frac{u}{L} \right)^2 \quad (8)$$

where  $L$  and  $u$  are length scale and characteristic velocity, respectively. The dimension of the function is  $[W/m^3]$ . If we assume that the resulting film is thin, it would be relevant to assume characteristic velocity and length scales as  $u$  and  $h$ , respectively. Energy loss due to the viscous dissipation can be estimated as:

$$EL = \phi \left( \frac{1}{6} \pi D_o^3 \right) t \sim \mu \left( \frac{u}{h} \right)^2 \left( \frac{1}{6} \pi D_o^3 \right) t \quad (9)$$

The energy balance equation can be expressed as:

$$PE1 + WE = PE2 + EL$$

$$\pi D_o^2 \sigma + \frac{1}{2} \varepsilon_f \left( \frac{V_o}{h} \right)^2 \left( \frac{1}{6} \pi D_o^3 \right) = \frac{\pi}{4} D(t)^2 \sigma (1 - \cos \theta) + \mu \left( \frac{u}{h} \right)^2 \left( \frac{1}{6} \pi D_o^3 \right) t$$

By conducting an order of magnitude analysis, the surface tension energy can be neglected.

$$\pi D_o^2 \sigma + \frac{1}{2} \varepsilon_f \left( \frac{V_o}{h} \right)^2 \left( \frac{1}{6} \pi D_o^3 \right) = \frac{\pi}{4} D(t)^2 \sigma (1 - \cos \theta) + \mu \left( \frac{u}{h} \right)^2 \left( \frac{1}{6} \pi D_o^3 \right) t$$

$$O(h^{-2})$$

$$O(h^{-2})$$

The second terms in LHS and RHS have the same order of magnitude and it can be assumed these terms are balanced particularly in our experiments, where the surface tension is small and the substrate is a complete-wetting surface. By substituting the velocity and converting  $D(t)$  to  $h(t)$  using the mass continuity we have:

$$\frac{1}{2} \varepsilon_f \left( \frac{9 \alpha K_a \varepsilon_a^2 \left( \frac{V^2}{S^3} \right)}{8 \sigma_f \varepsilon_f} \right)^2 \left( \frac{1}{6} \pi D_o^3 \right) \approx \mu \left( \frac{D_o^3}{24} \right) \frac{\dot{h}^2}{h^5} \left( \frac{1}{6} \pi D_o^3 \right) t \quad (10)$$

The equation above is an ordinary differential equation. In simplified form we have:

$$\varepsilon_f \left( \frac{9 \alpha K_a \varepsilon_a^2 \left( \frac{V^2}{S^3} \right)}{8 \sigma_f \varepsilon_f} \right)^2 \approx \mu \left( \frac{D_o^3}{12} \right) \frac{\dot{h}^2}{h^5} t \quad (11)$$

The solution of the above ordinary-first order differential is as follows

$$h(t) = \frac{1}{\left( \frac{24 \varepsilon_f \left( \frac{\alpha K_a \varepsilon_a^2 \left( \frac{V^2}{S^3} \right)}{\sigma_f \varepsilon_f} \right)^2}{\mu D_o^3} \right)^{1/3} t^{1/3} + \frac{1}{h_s}} \quad (12)$$

Substituting Eqn. (1) to the above formula, the dynamic spreading of the droplet can be obtained as:

$$D(t) = \Gamma t^{1/6} + D_s \quad \text{where} \quad \Gamma^3 = \frac{3 \alpha K_a \varepsilon_a^2 \left( \frac{V^2}{S^3} \right)}{\sigma_f \sqrt{\mu \varepsilon_f}} D_o^3 \quad (13)$$

This analysis of the dynamics of the spreading using an energy balance method gives a similar result as presented in [8].

### 7.4.3 Energy balance approach: Regime I

In order to obtain the dynamics of spreading of a dielectric film subjected to corona discharge for the Regime II, it was assumed the surface charge is immediately developed over the dielectric liquid interface. Experimental observations revealed that the film expansion at the very beginning of the expansion shows deviation from the  $t^{1/6}$  law (Fig. 5). One reason for such deviation may be due to the naive assumption of “immediate constant surface charge”. It would be interesting to investigate the effect of the “transient charging” of the dielectric interface instead of assuming the surface charge density as a step function. The Taylor expansion of the surface charge density around  $t=0$  yields:

$$\rho_s = \rho_{s0} + \frac{d\rho_s}{dt} t + \frac{d^2\rho_s}{dt^2} t^2 + \frac{d^3\rho_s}{dt^3} t^3 + \dots \quad (14)$$

For a dielectric layer without corona discharge exposure, the initial surface charge density at the oil-air interface,  $\rho_{s0}$ , is negligible and can be assumed to be zero. Then:

$$\rho_s = C t + C_1 t^2 + C_3 t^3 + \dots \quad (15)$$

As a first-order approximation, the surface charge density can be estimated as:

$$\rho_s = C t \quad (16)$$

Assuming the film thickness is small enough, the constant  $C$  can be calculated as:

$$C = \frac{1}{\int_0^\theta dA} \cdot \int_0^\theta j \cdot dA \quad (17)$$

The electric field jump across the dielectric film can be related to the accumulation of surface charge density:

$$\varepsilon_a E_a - \varepsilon_f E_f = \rho_s \quad (18)$$

Immediately after the corona discharge is exposed to the film, the electric field on the oil side of interface can be assumed to be smaller than the external electric field due to the corona discharge. Therefore:

$$\varepsilon_a E_a = \rho_s \quad (19)$$

The electric field on the air side of interface can be estimated as:

$$E_a = \frac{\rho_s}{\varepsilon_a} \quad (20)$$

$$= \left[ \frac{1}{\varepsilon_a A} \cdot \int_0^\theta j \cdot dA \right] t \quad (21)$$

In order to obtain the approximation for total current  $\int_0^\theta j \cdot dA$ , the current density profile can be considered to have Warburg's law distribution.

$$j = j_{max} \cos^5(\theta) - \sigma_f E_f \quad (22)$$

$j_{max}$  can be obtained experimentally as [19]:

$$j_{max} = \xi K_a \varepsilon_a \frac{V(V - V_{onset})}{S^3} \quad (23)$$

where  $\xi$  is a scaling factor and it varies for different configurations of electrodes. For a uniform corona discharge generated by mesh-like electrode  $\xi$  approximately equals to 1. For sharp needles typically  $\xi > 1$ . Current density can be expressed as:

$$j = \xi K_a \varepsilon_a \frac{V(V - V_{onset})}{S^3} \cos^5(\theta) - \sigma_f E_f \quad (24)$$

Therefore, the electrical pressure can be obtained as:

$$\rho_s E = \left\{ \frac{1}{\varepsilon_a \int_0^\theta dA} \cdot \int_0^\theta \left[ \left( \xi K_a \varepsilon_a \frac{V(V - V_{onset})}{S^3} \cos^5(\theta) \right) - \sigma_f E_f \right] \cdot dA \right\}^2 t^2 \quad (25)$$

Accordingly, the electric pressure over the interface at the beginning is quadratic function of time:



$$\rho_s E = \sqrt{\hat{C}} t^2 \quad (26)$$

Assuming the surface charge density migration to the ground for  $t \ll 1$  is small, the second term tends to zero:

$$\hat{C} = \left[ \frac{1}{\varepsilon_a \int_0^\theta dA} \cdot \int_0^\theta \left( \xi K_a \varepsilon_a \frac{V(V - V_{onset})}{S^3} \cos^5(\theta) \right) \cdot dA \right]^4 \quad (27)$$

From the energy balance equation:

$$\frac{1}{2} \varepsilon_f \hat{C} t^2 \left( \frac{1}{6} \pi D_o^3 \right) = \frac{1}{2} \rho u^2 \left( \frac{1}{6} \pi D_o^3 \right) \quad (28)$$

$$\sqrt{(\varepsilon_f \hat{C} t)} dt = \sqrt{\mu \left( \frac{D_o^3}{12} \right)} h^{-5/2} dh \quad (29)$$

$$h = -D_o \left( \frac{\mu}{18 \varepsilon_f \hat{C}} \right)^{1/3} t^{-1} + h_s \quad (30)$$

From Eqn. (1), the dynamic size of the film can be determined as:

$$D(t) = D_o \left( \frac{16 \varepsilon_f \hat{C}}{3 \mu} \right)^{\frac{1}{6}} \sqrt{t} + D_s \quad (31)$$

and the spreading ratio,  $\beta(t) = \frac{D(t)}{D_o}$ , is:

$$\beta(t) = \left( \frac{16 \varepsilon_f \hat{C}}{3 \mu} \right)^{\frac{1}{6}} \sqrt{t} + \beta_s \quad (32)$$

Eqn. (32) describes the dynamic spreading of the droplet at the early stages of corona discharge exposure for an insulating liquid with a very small electrical conductivity,  $\sigma_f \ll 1$ .

The present energy balance approach based on the transient surface charge accumulation may predict the law of  $D(t) \sim t^{1/2}$  for earlier stages of corona discharge exposure (Regime I) which is in agreement with experimental observations (Fig. 5). Moreover, similarly to Regime II, the spreading ratio in Regime I shows universal behavior for all droplet sizes, which is consistent with the experimental results. Previously, it was found that the law  $t^{1/6}$  overestimates the dynamics of spreading immediately after exposure. This can be attributed to the assumption in the derivation [8] that the surface charging immediately reaches to the steady state condition, which is not realistic immediately after the discharge exposure. In the current model, the surface charging was assumed to be transient and first order analysis predicts slower law of  $t^{1/2}$  at  $t \ll 1$ . Compared with experimental results, the theoretical prediction is in agreement with for exposure times smaller than the dielectric liquid relaxation time  $t < \tau_R = \frac{\epsilon_f}{\sigma_f} \sim 4 \text{ ms}$ . This is believed to confirm that the first regime of corona discharge spreading occurs due to the transient charging of the interface. It is worthy to note that the conduction mechanism across the liquid film in the first two regimes is mainly due to ohmic conduction. In these cases, the liquid layer thickness is comparatively thick and since the voltage drop in the dielectric film is smaller than that of electrode separation (particularly in Regime I), the charge transport mechanism across the thin film remains ohmic conduction. In order to support this postulation, it is useful to calculate the conduction parameter [20, 21], which is the ratio of ion transit time,  $\tau_T$ , to relaxation time,  $\tau_R$ :

$$C_o = \frac{1}{2} \frac{\tau_T}{\tau_R} = \left( \frac{h}{2K_f E} \right) / \left( \frac{\epsilon_f}{\sigma_f} \right) \sim \frac{\sigma_f h^2}{2K_f \epsilon_f V_o} \quad (33)$$

Substitution of the experimental values for interface potential, film thickness, ion mobility, permittivity and the measured electrical conductivity of the bulk liquid, one may obtain typically of  $C_o \sim O(10^2)$ . For  $C_o \gg 1$ , the conduction mechanism remains in slightly perturbed equilibrium condition where the ohmic conduction model can be applied confidently [21].

### 7.4.4 Regime III: Field-enhanced Dissociation conduction regime

When the corona discharge exposure is continued for a longer period of time, another cross-over may be observed. Figs. 6-8 show the spreading dynamics of the liquid film subjected to corona discharge for three different droplet sizes. For all tested droplets, by increasing the time of the corona discharge exposure, the liquid film expanded and the film thickness monotonically decreases. As just shown for the intermediate corona discharge exposure time, the spreading dynamics obeys  $D(t) \sim t^{1/6}$  law.

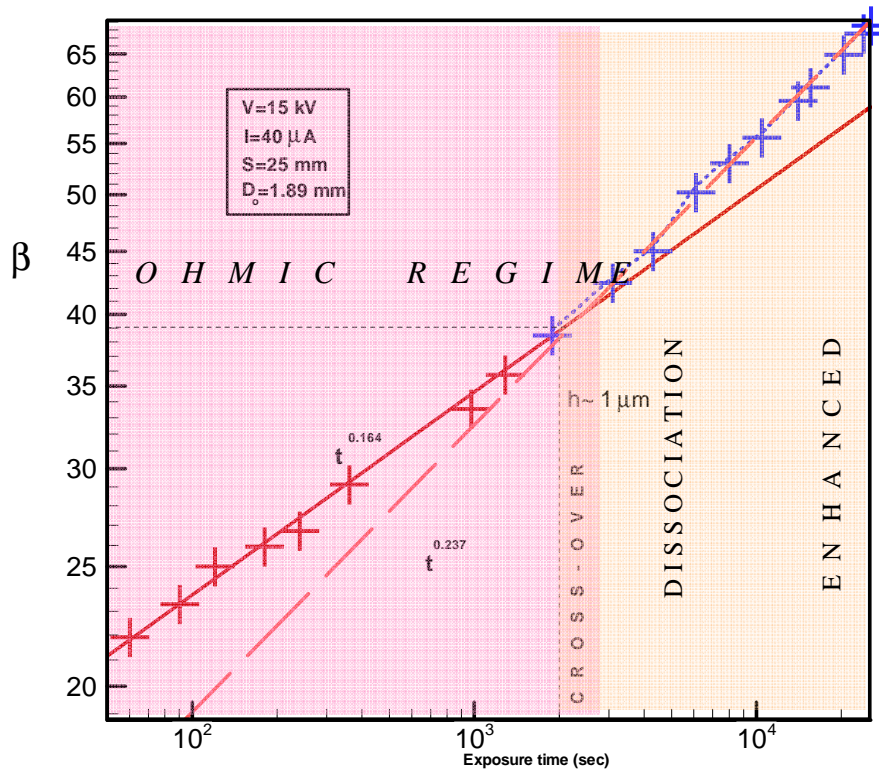


**Figure 6: Spreading dynamics of a silicone oil film subjected to corona discharge. The film was produced by expansion of a silicone oil droplet with initial size of  $D_o=1.89$  mm. Second and third regimes of expansion are mapped to the ohmic conduction and enhanced dissociation conduction mechanism, respectively. The applied voltage was 17 kV and the total corona current was 40  $\mu$ A. The gap spacing was kept constant at  $S=25$  mm.**

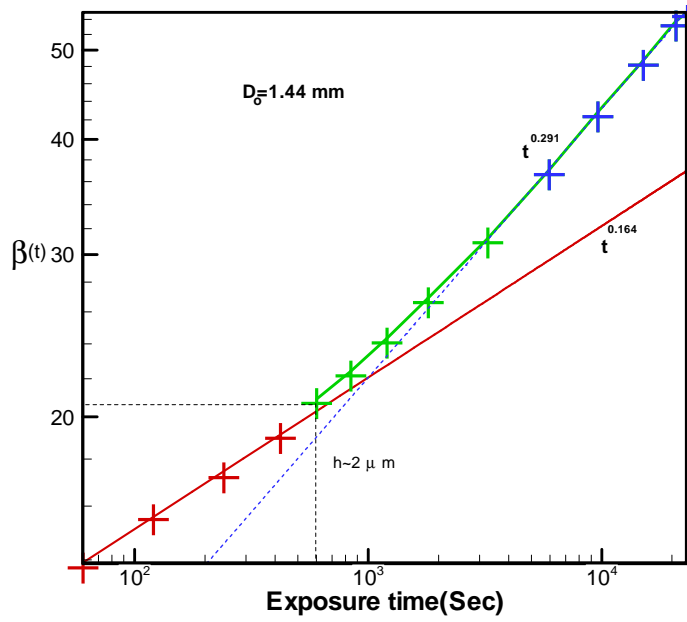


**Figure 7: Spreading dynamics of a silicone oil film produced by expansion of a small droplet with initial diameter of  $D_0=1.44$  mm. The applied voltage was 17 kV and the total corona current was 40  $\mu$ A. The gap spacing was kept constant at  $S=25$  mm.**

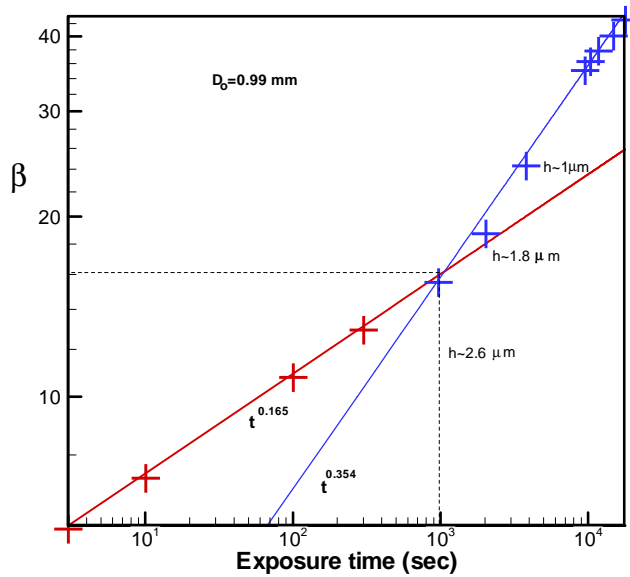


**Figure 8: Spreading dynamics of a silicone oil film produced by expansion of a very small droplet with initial diameter of  $D_0=0.99$  mm. The applied voltage was 17 kV and the total corona current was 40  $\mu$ A. The gap spacing was kept constant at  $S=25$  mm.**

However, when the film thickness reaches a critical thickness in the order of  $\sim 2 \mu m$ , the spreading law is accelerated and starts deviating from the  $t^{1/6}$  law. This mode of droplet spreading is called Regime III. According to the experimental observations, transition to this Regime starts after reaching almost an identical critical film thickness for all droplet sizes, but the spreading dynamics is no longer universal and the rate of expansion for smaller droplets is faster. For instance, after  $10^4$ s of exposure, the spreading law for  $D_0=1.89$  mm is  $D(t) \sim t^{0.237}$ , while for the smallest tested droplet with an initial diameter of 0.99 mm, the spreading law becomes  $D(t) \sim t^{0.354}$ . This indicates that below the critical thickness, the thickness of the film may affect the spreading dynamics. In the previous regimes of expansion (Regimes I and II) it has been confirmed from experimental and theoretical investigations that the spreading dynamics is universal for all droplet sizes. This suggests that for Regimes I and II the variation of film thickness is not important in the spreading process, while in Regime III thickness of the film determines the spreading law.

It has been realized that different conduction mechanisms may simultaneously contribute to charge carrier transport across the thin films [12, 13]. When ohmic conduction is the dominant charge transport mechanism, the spreading dynamics gives universal behavior for all droplet sizes (Fig. 5 and [8]). This is due to the fact that the ohmic conduction charge transport is not a function of film thickness and the spreading dynamics is similar for different droplet sizes. However, as seen in Figs. 6-8, below the critical thickness, the spreading dynamics is no longer universal and it depends on the initial size of the droplet. This may imply that the conduction mechanism across the thin film deviates from ohmic conduction since the film thickness becomes important and the ohmic model cannot describe the carrier transport in such a case. This surprising behavior of the nature of the spreading dynamics below the critical film thickness in Regime III might be attributed to a deviation in the charge carrier transport mechanism across the thin film. We examine this hypothesis through experimental observations and mathematical modeling. In the mathematical model, it is postulated that the field-enhanced dissociation conduction model can describe the transport mechanism across the film here and this hypothesis will be examined experimentally and theoretically.

In the thermodynamic equilibrium state where the electric field is absent, neutral electrolyte impurities dissolved in dielectric liquids dissociate into counter-ions, while the dissociated ions can recombine back into the neutral electrolyte. There is an equilibrium between the dissociation and recombination processes anywhere in the liquid except close to the interfaces. Due to the electrochemical effects adjacent to the interfaces, the space charge layers, known as the double-layer, are established where their thickness is approximately equal to the Debye length. When the external electric field is established across the dielectric liquid, these dissociated ions experience an electric force. Close to the interfaces, the ions with the interface polarity are repelled due to the Coulomb force and concentrate the positive and negative ions around the counter-polarity interfaces. These space charge layers are known as hetero-charge layers; a gradient of space charge exists in these layers (Fig. 9) and the thermodynamic equilibrium is destroyed. The hetero-charge layers can be considered in dielectric liquid when their thickness is higher than the Debye length [10, 20, 21]. For the low-electric field regime, the hetero-charge layers are so thin that the net charge in the bulk might be assumed to be zero and only ohmic conduction need be considered [21]. However, when the interfaces approach each other, which may happen for larger electric fields in thin films, the hetero-charge layers may extend into the bulk. For such a regime, the ohmic model is no longer valid since a net charge exists in the bulk [10].

In the field-enhanced dissociation conduction model, the relation between current density and applied electric field is more complicated. According to [14], the current density varies exponentially with square root of applied electric field:

$$J = 2cD(E)h = 2chD_o \exp\left\{-U_o + 2e^{3/2}(E/4\pi\epsilon_r\epsilon_o)^{1/2}\right\}/k_B T \quad (34)$$

where  $D_o$  is the dissociation coefficient at  $E=0$  (thermal equilibrium).

In the Regime III, where the thickness of the film is below some critical value, experimental results suggested that the spreading dynamics may depend on thickness of the film (Figs. 6-8). Based on the field-enhanced dissociation model, the thickness of the film,  $h$ , appears in the current density-applied field relation Eq. (34). This indicates that

the field-enhanced dissociation conduction model is an appropriate mechanism for carrier transport across the film [10,11].

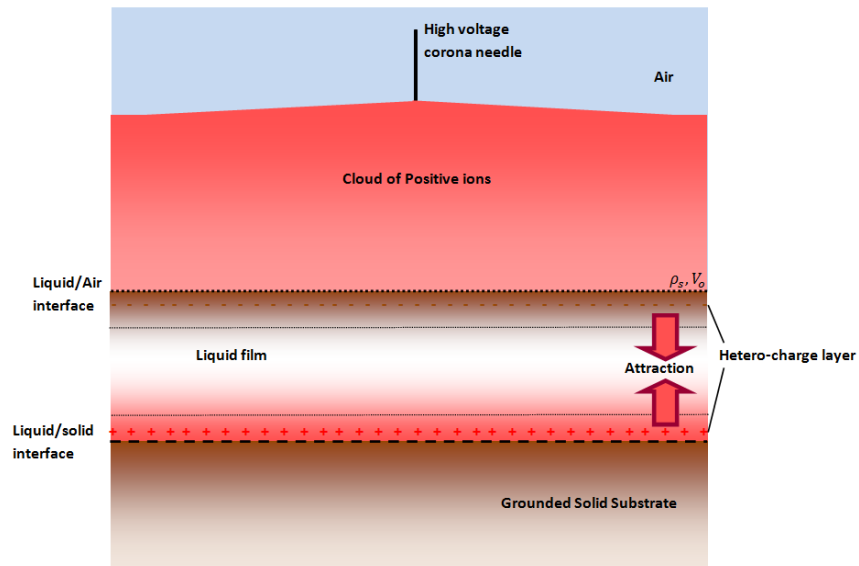


**Figure 9: Demonstration of hetero-charge layers formation around the solid/liquid and liquid/air interfaces.**

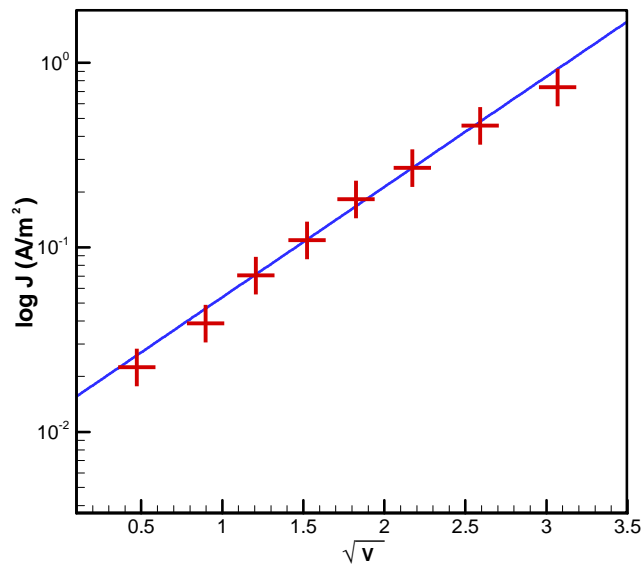


**Figure 10:  $\log J$ -  $\sqrt{V}$  characteristics obtained for a 2 $\mu\text{m}$ -thick silicone oil film.**

In order to confirm that the conduction mechanism across the thin film is due to the dissociation model,  $\log J$  was plotted versus the square root of surface potential  $\sqrt{V}$  for 2 $\mu\text{m}$ -thick silicone oil film at different corona discharge strengths (Fig. 10). The current density across the film and the surface potential of the interface were measured through the additional experimental setup presented in Fig. 3 and the procedure explained in the previous section. A broad range of current densities was obtained through applying various corona discharge voltages to the corona needle at various electrode separations. This combination enabled us to cover two orders of magnitude variation in the current density across the film. It can be noticed from Fig. 10 that the current density,  $J$ , is proportional to  $\exp(\sqrt{V})$  and the slope of variation is  $\sim 1.376$ . Substituting the experimental values into the Eq. (34) the theoretical slope is  $\sim 1.261$ . Thus the theoretical slope of variation in the field-enhanced dissociation model agrees with the experimental results within 10%. Moreover, calculation of the conduction parameter  $C_o$  using the experimental measured values immediately after the transition ( $V_o \sim 1$  V and  $h \sim 2\mu\text{m}$ ) gives magnitudes in the order of unity. This may suggest that the ion transit time across the thin film becomes in the same order as the charge relaxation time ( $\tau_T \sim O(\tau_R)$ ) at the critical film thicknesses. At the initiation of the deviation, the calculated hetero-charge layer thickness ( $\lambda \sim K_f \tau_R E$ ) is in the order of 1  $\mu\text{m}$ . Therefore, the hetero-charge thickness becomes comparable with the film thickness at the regime transition point. These evidences may further support the postulated field-enhanced dissociation charge transport mechanism across the thin film [10,11].

In order to explain the accelerated expansion observed in Regime III, it was postulated that the attraction of the hetero-charge layers developed around both interfaces is responsible for such accelerated spreading (Fig. 9). This attractive force in the dielectric film may create a new electrostatic component of disjoining pressure. The analysis is similar to that of aqueous solution of salts or electrolytes. In an electrolyte solution, the attraction in the electric double layers created adjacent to the interfaces may result in an electrostatic component of disjoining pressure [15]. However, for weak electrolytes or dielectric liquids, the ion diffusion coefficient,  $D$ , is very small ( $D = \frac{K_f k_B T}{e} \sim 10^{-11} \text{ m}^2 \text{ s}^{-1}$ ) and the double layer thickness ( $D_L \sim \sqrt{D\tau} \sim 10^{-7} \text{ m}$ ) is



typically thinner than the hetero-charge layer thickness. Therefore, it is reasonable to consider hetero-charge layer attraction as the electrostatic component of disjoining pressure in dielectric liquids.

The Standard Thin Film Model (TFM) [15] along with the concept of disjoining pressure due to the hetero-charge layer attraction was employed to investigate the proposed spreading mechanism in Regime III. Let's assume the extreme case where only the substrate interactions govern the spreading. The mass continuity equation can be derived from lubrication theory [16,18]:

$$\frac{\partial h}{\partial t} = -\frac{1}{3r\eta} \frac{\partial}{\partial r} \left( rh^3 \frac{d\Pi}{dh} \frac{\partial h}{\partial r} \right) \quad (35)$$

where  $\Pi$  is the disjoining pressure in the film. In general, disjoining pressure in dielectric films may have two components:

$$\Pi = \Pi_{\text{vww}} + \Pi_{\text{el}}$$

The first component,  $\Pi_{\text{vww}}$ , is dispersion component of the disjoining pressure due to the van der Waals (VW) force and second component,  $\Pi_{\text{el}}$  is the electrostatic component of the disjoining pressure due to the attraction of the hetero-charge layer. It should be noted that the disjoining pressure due to the van der Waals force interactions can be neglected for the thin films in the order of few microns [22].

If the thickness of the film is close to that of the hetero-charge layer, the disjoining pressure has only the electrostatic component due to the attraction between the hetero-charge layers. Moreover, since below the critical thickness, the relationship between the current density and electric field across the film is exponential, small changes in surface potential correspond to a large change in current density. According to the  $\log J - \sqrt{V}$  characteristics presented in Fig. 10, it was confirmed that the surface potential shows small variations during the expansion process in regime III. Therefore, the electrostatic component of disjoining pressure can be calculated as:

$$\Pi = \Pi_{el}(h) = \alpha \varepsilon_{oil} \frac{V_o^2}{h^2} = \frac{\chi}{h^2} \quad (36)$$

where  $\alpha > 1$  is an enhancement coefficient. The detailed calculation of electric field enhancement coefficient due to the presence of hetero-charge layers can be found in [21]. For a detailed derivation of the electrostatic component of disjoining pressure see the ref [22]. Considering the Eq.(36), the conservation equation becomes:

$$\frac{\partial h}{\partial t} = -\frac{1}{3r\eta} \frac{\partial}{\partial r} \left( -2r\alpha \varepsilon_{oil} V_o^2 \frac{\partial h}{\partial r} \right) \quad (37)$$

Based on the field-enhanced dissociation conduction model, at fixed ion injection conditions (constant corona discharge voltage and gap spacing), after decreasing the film thickness the changes in surface potential might not be significant (see also Fig. 10). For instance, for 10 times thinner film, the surface potential changes less than 10%. Therefore, the mass conservation equation can be simplified to:

$$\frac{\partial h}{\partial t} = \frac{2\alpha \varepsilon V_o^2}{3r\eta} \frac{\partial}{\partial r} \left( r \frac{\partial h}{\partial r} \right) \quad (38)$$

Considering the non-dimensional parameters:

$$t^* = \frac{3\eta r^{*2}}{\chi}, \quad h^* = \frac{V}{2\pi r^{*2}}$$

Eq.(38) can be written as:

$$\frac{\partial \bar{h}}{\partial \bar{t}} = \frac{1}{\bar{r}} \frac{\partial}{\partial \bar{r}} \left( \bar{r} \frac{\partial \bar{h}}{\partial \bar{r}} \right) \quad (39)$$

In order to find the similarity solution for the spreading dynamics due to the hetero-charge layer attraction let us consider the following parameter:

$$\Omega = \bar{r} f(\bar{t})$$

where  $\bar{f}(\bar{t})$  is an unknown function. Since the volume of the film is constant during the evolution, then:

$$\int_0^{\bar{R}(\bar{t})\bar{f}(\bar{t})} \left( \Omega \frac{\bar{h}}{(\bar{f}(\bar{t}))^2} \right) d\Omega = 1 \quad (40)$$

The tested dielectric liquid (silicone oil) is not volatile and the volume of the film is preserved during the expansion process thus the above equation should not be a function of time. Therefore,

$$\bar{R}(\bar{t})\bar{f}(\bar{t}) = cte \quad \text{and} \quad \bar{h} = g(\Omega)(\bar{f}(\bar{t}))^2$$

Considering  $\bar{h} = g(\Omega)(\bar{f}(\bar{t}))^2$  as a similarity solution for governing equation and using

$\bar{r} = \frac{\Omega}{\bar{f}(\bar{t})}$ , the governing equation becomes:

$$\bar{f} \frac{d\bar{f}}{d\bar{t}} \left\{ \left( \Omega \frac{dg}{d\Omega} \right) + 2g \right\} = -\bar{f}^4 \frac{1}{\Omega} \frac{d}{d\Omega} \left( \Omega \frac{dg}{d\Omega} \right) \quad (41)$$

From eq. (41), the following differential equation can be derived:

$$\bar{f} \frac{d\bar{f}}{d\bar{t}} = -\bar{f}^4 \quad \text{or} \quad \frac{d\bar{f}}{d\bar{t}} = -\bar{f}^3$$

Therefore:

$$\bar{f}(\bar{t}) \sim c^* \bar{t}^{-1/2}$$

Since  $\bar{R}(\bar{t})\bar{f}(\bar{t}) = cte$

$$\bar{R}(\bar{t}) = C^* \bar{t}^{1/2} \quad (42)$$

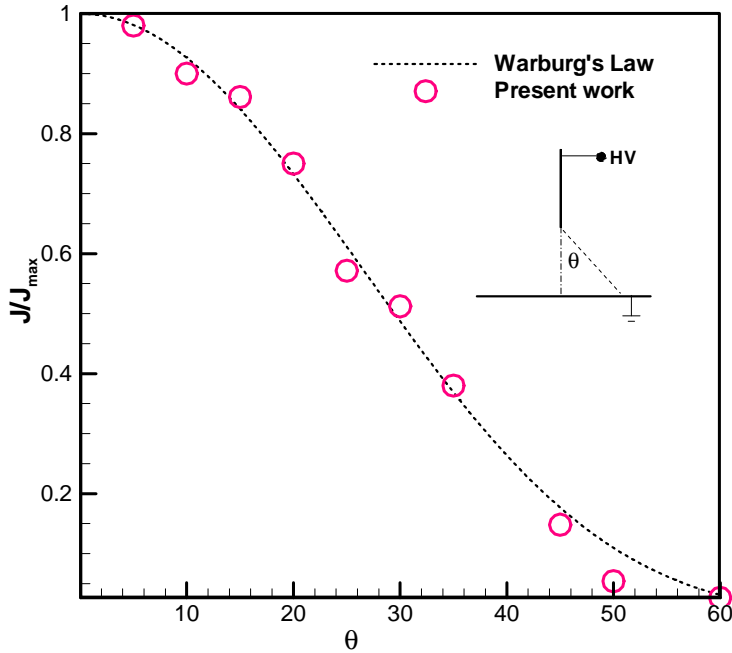


**Figure 11: Radial distribution of the relative current density for the hypodermic needle used in this study. The applied voltage was 17 kV and the total corona current was 40  $\mu$ A. The gap spacing was kept constant at  $S=25$  mm.**

The spreading law of  $t^{1/2}$  has been predicted by considering the electrostatic component of hetero-charge layer. For comparatively larger droplets, it was found experimentally that the transition occurs smoothly and the exponent of the law increases slowly (compare Fig. 6 with Fig. 8). This might be due to the fact that the transition to Regime III starts when the initial film size is large and the local corona current density shows only slight variation in radial direction. This corresponds to slight variation in surface potential that was theoretically assumed to be constant earlier. In order to confirm this hypothesis, the same experiments were repeated with droplets whose initial diameter was one order of magnitude smaller. In this case, the theoretical assumption of uniform surface potential is more likely to be met since the expansion of the film for such small droplets occurs well within the corona cone and the spreading dynamics is closer to the predicted law of  $t^{1/2}$ . For instance, for droplet  $D_0=0.99$  mm (Fig. 8), the spreading dynamics in Regime III was measured to be  $t^{0.354}$  while for largest tested droplet of  $D_0=1.89$  mm (Fig. 6) the spreading law of  $t^{0.237}$  was obtained. According to the measured

current density profile presented in Fig. 11, the current density variation within the size of the film is about 40%, which corresponds to the surface potential variation of below 15%. Based on this analysis, it has been confirmed that the substrate interactions due to attraction of hetero-charge layer may accelerate the spreading process in Regime III. It is important to note that as the film thickness decreases below the critical thickness, the interaction with the substrate due to the hetero-charge layers attraction become more significant and the spreading law approaches the predicted law of  $t^{1/2}$ . At the beginning of the transition, the spreading law is governed by the interfacial electric pressure, while below the critical thickness when the carrier transport mechanism due to the enhanced-dissociation becomes dominant, the substrate interaction may govern the spreading dynamics due to the attraction of hetero-charge layer. Since the transition is smooth, the spreading dynamics law is observed to be bounded between the  $t^{1/6}$  and  $t^{1/2}$  (See Appendix C-2). More general solutions for the Regime II, Regime III and Regime IV can be obtained in Appendices C-1 C-2 and C-3, respectively.

#### 7.4.5 Regime IV: “Precursor film”

Continuing the corona discharge exposure to the accelerated film in Regime III reveals an additional interesting regime of the film spreading. It was observed that when the dielectric film reaches sub-micron thicknesses, an ultra-thin film in the order of tens of nm diffuses from the main film, and spreads ahead of the apparent contact line. The appearance of the thin film resembles the previously reported precursor film expanding ahead of the main film during long term spontaneous spreading [24]. Fig. 1-d shows a dielectric droplet with initial size of 0.5 mm after 40 and 500 and 2500 minutes of corona discharge exposure with 17 kV applied voltage and total corona current of 40  $\mu$ A. The blue dark fringe in right side of the main film corresponds to sub-micron liquid film thickness. The thickness of ultra-thin film is so small that the white light interferometry shows only a gray fringe in this regime. It should be noted that the slight non-uniformity in the thickness of the main film results in asymmetric ultra-thin film formation around the main film. Uniform thin films with such thicknesses are difficult to achieve since it depends on several factors such as precise adjustment of needle with respect to the center of the film, micro-irregularities on the tip of the needle, etc. Moreover, small local

impurities in the dielectric volume may result in such non-uniformities. It was observed that the dynamics of the ultra-thin film is de-coupled from the main film and it spreads much faster than the main film. According to our ellipsometry studies, the thickness of the secondary diffusive film is tens of nanometers (Fig.12).

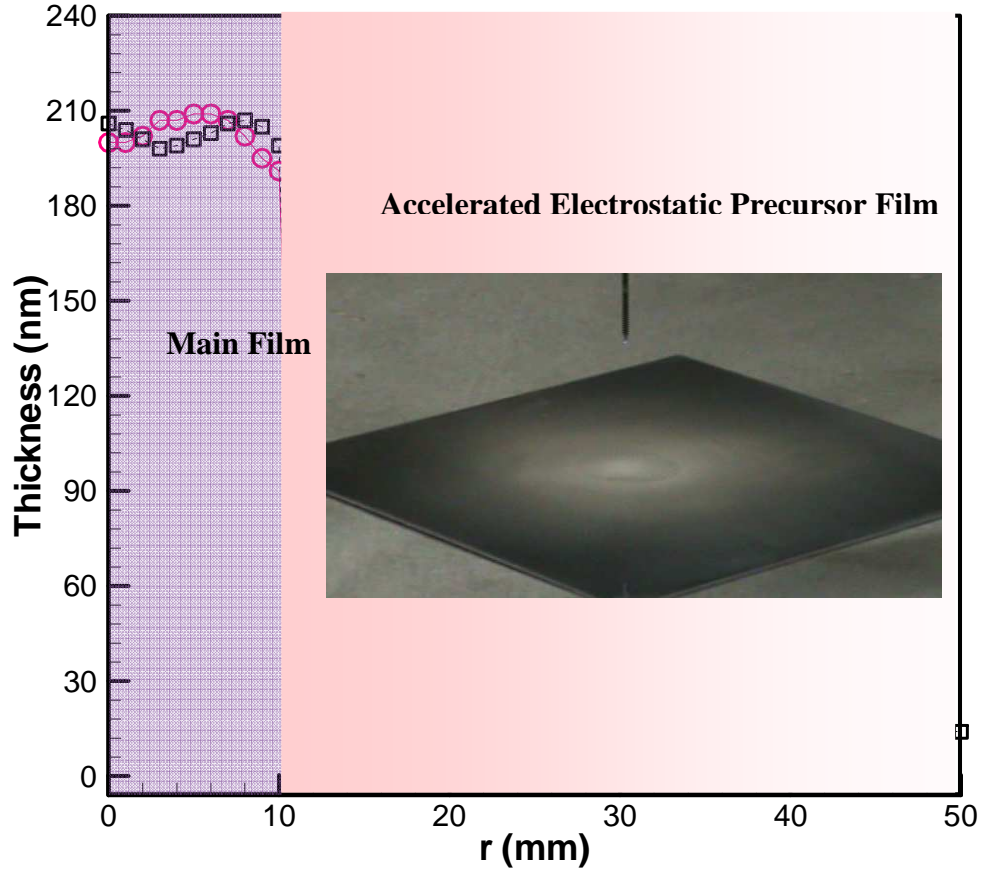


**Figure 12: Ellipsometric measurement of silicone oil film thickness after  $1.7 \times 10^5$  seconds of corona discharge exposure. The measurement performed at two different peripheral angles. The applied voltage was 17 kV and the total corona current was 40  $\mu$ A. The gap spacing was kept constant at  $S=25$  mm.**

Compared with the normal precursor film formation around the main film under spontaneous spreading in the absence of corona discharge, the length of the film created by the forced spreading corona discharge-assisted technique is typically two orders of magnitude faster, but the thickness of the film is in the same order of magnitude. Due to the several commonalities between the observed thin film and the conventional

previously reported precursor film [15-16], we use a similar terminology, “accelerated electrostatic precursor film”, for the present observed film resulting from the post-forced–spreading corona discharge assisted technique

The process of the precursor film formation is complicated. The attraction between the hetero-charge layers accelerates the spreading process until the film thickness becomes sub-micron. For regions with submicron thicknesses, a transition from Regime III to Regime IV occurs due to the stronger substrate interactions. In Regime IV, the van de Waals force might contribute in initiating of the precursor film, whose thickness is typically five times smaller than the main film. In this stage, according to the field-enhanced dissociation conduction model, the surface potential is expected to show only minor changes, which corresponds to an electric field enhancement of at least 5 times larger as compared with that of the main film. Since the electrostatic component of disjoining pressure is scaled with  $E^2$ , this abrupt variation in electric field across the thin film may lead to a significant gradient in disjoining pressure, which accelerates the expansion of the precursor film.

In order to mathematically describe the film expansion in regime IV and further confirm the above postulated mechanism, let us consider the standard Thin Film Model (TFM) and assume that the expansion of the film is based on two components of disjoining pressure: (i) dispersion component,  $\Pi_{vww}$  (ii) electrostatic component,  $\Pi_{el}$  [22]:

$$\Pi = \Pi_{vww} + \Pi_{el} \quad (43)$$

Using the first approximation of the direct summation of all molecular interaction in the thin film, the dispersion component of the disjoining pressure can be simplified as:

$$\Pi = \Pi_{vww} = \frac{A_H}{6\pi h^3} \quad (44)$$

where  $A_H$  is referred to as the Hamaker constant. According to the lubrication approximation:

$$\frac{\partial h}{\partial t} = \frac{\partial}{\partial r} \left( D_e(h) \frac{\partial h}{\partial r} \right) \quad (45)$$

The diffusion coefficient has two components as:

$$D_e(h) = D_{vww} + D_{el} = \frac{-h^3}{3\mu} \frac{d(\Pi_{vww} + \Pi_{el})}{dh} = \frac{-h^3}{3\mu} \left( \frac{-A_H}{2\pi\mu h^4} + \frac{-2\chi}{h^3} \right) = \frac{A_H}{6\pi\mu h} + \frac{2\chi}{3\mu} \quad (46)$$

Assuming the precursor film thickness starts at  $h(r, t) = h_s$  [16], the similarity solution yields:

$$r(t) = \left( \frac{A_H}{3\pi\mu h_s} + \frac{4\chi}{3\mu} \right)^{1/2} \sqrt{t} \quad (47)$$

In the absence of corona discharge  $\chi$  is zero and the above equation becomes:

$$r(t) = \left( \frac{A_H}{3\pi\mu h_s} \right)^{1/2} \sqrt{t} \quad (48)$$

The above analysis of the spreading dynamics in the absence of corona discharge was obtained theoretically in [16,23] and experimentally confirmed in [17]. Eq. (47) predicts that the spreading length of the precursor film in the presence of corona discharge is much faster than the previously reported precursor films produced only due to the dispersion component of the disjoining pressure (spontaneous spreading). For example, typical spreading of the precursor film of a silicone oil droplet in the spontaneous mode is in the order of 100  $\mu\text{m}$  after about three days. This shows that precursor film spreading through spontaneous spreading can take a very long time (perhaps in the order of years or more [16]). However, in the presence of corona discharge, the spreading length for the precursor film was demonstrated to be in the orders of tens of millimeters after only a day of corona discharge exposure. This suggests that the precursor film spreading is mainly governed by electrostatic forces and it is accelerated by electrostatic component of disjoining pressure rather than the presence of the dispersion component of disjoining pressure. This can be qualitatively confirmed by discontinuing the corona discharge exposure and monitoring the rate of spreading. It was observed that when the spreading



was interrupted by disconnecting the corona discharge voltage no visible precursor film expansion was recorded during two days of monitoring. The importance of the electrostatic component of disjoining pressure can be further confirmed by repeating the experiments for an identical test period in the presence of corona discharge. It was observed that the precursor film is monotonically expanded and it can be extended to radial distances equal to the distances where the corona discharge is no longer effective (corona cone). The expansion of the precursor film within the corona cone region confirms the role of corona discharge in the expansion of the precursor film.

The above experimental observations and the explained mechanism for precursor film spreading can be further confirmed by evaluation of the diffusion coefficients. The diffusion coefficient due to the dispersion component of disjoining pressure (assuming thicknesses  $h_s=10^{-7}$  m),  $D_e(h)$ , is in the order of  $10^{-12}$  m<sup>2</sup>/s, while the diffusion coefficient due to the electrostatic component of the disjoining pressure is in the order of  $10^{-9}$  m<sup>2</sup>/s. As it is depicted in Fig. 13, the best fit power law curve for the experimental data using 1-D precursor film length measurements, reveal that the experimental value of the diffusion coefficient should be in the order of  $10^{-9}$  m<sup>2</sup>/s, which is very close to the calculated electrostatic component of the disjoining pressure. This further confirms the pivotal role of the electrostatic component of disjoining pressure in acceleration of the precursor film.

It is worthy to note that, in the proposed mathematical model, we only considered the long-range attractive component of van der Waals forces. The short-range repulsive component of the van der Waals forces becomes important when the thickness of the film goes below the typical thicknesses of 5 nm. Such small thicknesses may only occur at the early stages of the precursor film development. Since we neglected the early stages of the precursor film dynamics, repulsive short-range van der Waals forces are not effective. Note that the short-range repulsive van der Waals force may act only on few molecules adjacent to the interfaces. In the present work, the typically reported thickness was 30 nm where the repulsive forces have negligible contribution in film spreading dynamics.

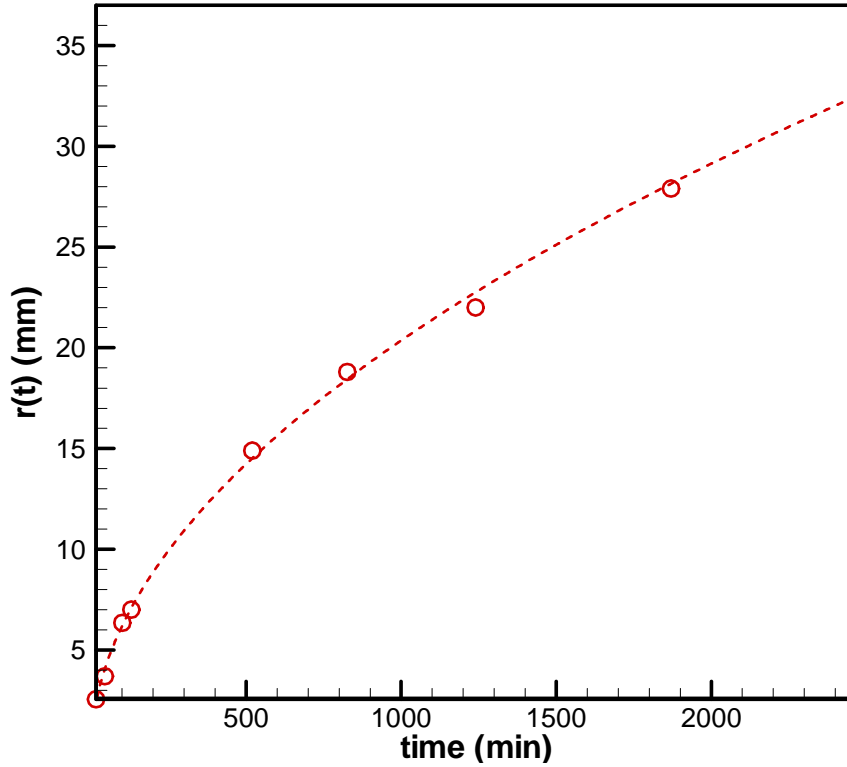


**Figure 13: Fit line of the experimental data (circles) for the dynamics of the accelerated precursor film. The curve is in the form of  $r(t) - r_0 = \delta t^n$ . When  $n$  fixed at 0.5, the fitness parameter and the standard errors are as following:  $\delta = 7.74 \times 10^{-5} \text{ m/s}^{1/2} \pm 2.06 \times 10^{-6} \text{ m/s}^{1/2}$  which corresponds to diffusion coefficients of  $D_e = 3.01 \times 10^{-9} \text{ m}^2/\text{s} \pm 1.7 \times 10^{-12} \text{ m}^2/\text{s}$ . The equation is valid for times after 40 min of corona discharge exposure where the accelerated precursor film length was measured to be  $r_0 = -2.556 \times 10^{-3} \text{ m} \pm 4.32 \times 10^{-5} \text{ m}$ .**

## 7.6 Conclusions

In the present work, we demonstrated four different regimes of dielectric film expansion, when it is subjected to the corona discharge. It was found that the spreading dynamics in the different regimes is related to the charge transport mechanism across the film. For the two first regimes, the interfacial electric pressure squeezes the dielectric film and the charge carrier transport follows ohmic conduction. Below some critical layer thickness, where the hetero-charge layer thickness is comparable to that of the dielectric film, a

transition to the third regime occurs and the attractive force resulting from the electrostatic component of disjoining pressure in the dielectric film accelerates the expansion. In this case, the charge transport mechanism deviates from the ohmic conduction model and it is governed by the field-enhanced dissociation conduction mechanism. By extending the corona discharge exposure time, a fourth regime of expansion was observed, where the precursor film is ejected from the main film. This precursor film is found to be accelerated due to the electrostatic component of disjoining pressure. Although the precursor film expansion shows commonalities with traditional precursor film dynamics, resulting from the dispersion component of disjoining pressure, its expansion is much faster. It was also demonstrated that the precursor film having thickness of the order of nanometers may cover a large area of the substrate within the corona discharge effective region, which is in the order of tens of millimeters. Further study of the new precursor film is required to understand its formation and dynamics of spreading. The results of the current work could be useful for several scientific and industrial applications.

## Appendix C

In appendix C, we are looking for a more general solution for the different regimes of spreading II, III, IV. The regime I cannot be included in this approach since it arises from dynamic surface charging and highly transient disjoining pressure.

If we define the disjoining pressure in the following form:

$$\Pi = \Pi_{el}(h) = \frac{B}{h^n} \quad (1)$$

The case considered here is to the final stage of the spreading of a film in which the substrate is completely wetted. The film profile can be described as:

$$\frac{\partial h}{\partial t} = -\frac{1}{3r\mu} \frac{\partial}{\partial r} \left( rh^3 \Pi'(h) \frac{\partial h}{\partial r} \right) \quad (2)$$

The conservation equation becomes:

$$\frac{\partial h}{\partial t} = -\frac{nB}{3r\mu} \frac{\partial}{\partial r} \left( rh^{2-n} \frac{\partial h}{\partial r} \right) \quad (3)$$

Considering the non-dimensional parameters:

$$t^* = \frac{3\mu r^{*2}}{nBh^{*2-n}} \quad , \quad h^* = \frac{V}{2\pi r^{*2}}$$

$$\frac{\partial \bar{h}}{\partial \bar{t}} = \frac{1}{\bar{r}} \frac{\partial}{\partial \bar{r}} \left( \bar{r} \bar{h}^{2-n} \frac{\partial \bar{h}}{\partial \bar{r}} \right) \quad (4)$$

In order to find the similarity solution for the spreading dynamics due to the hetero-charge layer attraction let us consider the following parameter:

$$\Omega = \bar{r} f(\bar{t})$$

where  $\bar{f}(\bar{t})$  is an unknown function. Since the volume of the film is constant during the evolution, then:

$$\int_0^{\bar{R}(\bar{t})\bar{f}(\bar{t})} \left( \Omega \frac{\bar{h}}{(\bar{f}(\bar{t}))^2} \right) d\Omega = 1 \quad (5)$$

The tested dielectric liquid (silicone oil) is not volatile and the volume of the film is preserved during the expansion process thus the above equation should not be a function of time. Therefore,

$$\bar{R}(\bar{t})\bar{f}(\bar{t}) = cte \quad \text{and} \quad \bar{h} = g(\Omega)(\bar{f}(\bar{t}))^2$$

Considering  $\bar{h} = g(\Omega)(\bar{f}(\bar{t}))^2$  as a similarity solution for governing equation and using

$\bar{r} = \frac{\Omega}{\bar{f}(\bar{t})}$ , the governing equation becomes:

$$\bar{f} \frac{d\bar{f}}{d\bar{t}} \left\{ \left( \Omega \frac{dg}{d\Omega} \right) + 2g \right\} = -(\bar{f})^{8-2n} \frac{1}{\Omega} \frac{d}{d\Omega} \left( \Omega g^{2-n} \frac{dg}{d\Omega} \right) \quad (6)$$

Since the above equation should not be a function of time:

$$\bar{f} \frac{d\bar{f}}{d\bar{t}} = -(\bar{f})^{8-2n} \quad \text{or} \quad \frac{d\bar{f}}{d\bar{t}} = -(\bar{f})^{7-2n}$$

Therefore:

$$\bar{f}(\bar{t}) \sim c^* t^{1/(-6+2n)}$$

Since  $\bar{R}(\bar{t})\bar{f}(\bar{t}) = cte$

$$\bar{R}(\bar{t}) = C^* t^{1/(6-2n)} \quad (7)$$

substituting the  $\bar{f}(t) \sim c^* t^{1/(-6+2n)}$ , Eq.(6) becomes in the following form:

$$\left\{ \left( \Omega \frac{dg}{d\Omega} \right) + 2g \right\} = -\frac{1}{\Omega} \frac{d}{d\Omega} \left( \Omega g^{2-n} \frac{dg}{d\Omega} \right) \quad (8)$$

$$\Omega \left\{ \left( \Omega \frac{dg}{d\Omega} \right) + 2g \right\} = -\frac{d}{d\Omega} \left( \Omega g^{2-n} \frac{dg}{d\Omega} \right)$$

$$\frac{d}{d\Omega} \{ (\Omega^2 g) \} = -\frac{d}{d\Omega} \left( \Omega g^{2-n} \frac{dg}{d\Omega} \right)$$

Therefore, the profile of the film can be obtained by the following differential equation:

$$\Omega = -g^{1-n} \frac{dg}{d\Omega}$$

Let us construct the concept of disjoining pressure for the charged liquid interfaces. The disjoining pressure can be defined as the negative derivative of the Helmholtz free energy. The excess Helmholtz free energy can be caused by excess charge at the interface.

$$\Pi = -\frac{1}{A} \frac{dF}{dx} \Big|_{T,P} = -\frac{dF_s}{dx} \Big|_{T,P}$$

$$dF_s = \rho_s d\phi$$

Therefore, the disjoining pressure due to adding excess charge over the liquid interface can be defined as:

$$\Pi = -\frac{1}{A} \frac{dF}{dx} \Big|_{T,P} = -\frac{dF_s}{dx} \Big|_{T,P} = -\rho_s \frac{d\phi}{dx} = -\rho_s (-E_f) = (\epsilon_f E_f) E_f$$

The disjoining pressure can be simplified as:

$$\Pi = \epsilon_f \frac{V_f^2}{h^2}$$

The presented concept of disjoining pressure helps to apply the general solution conveniently.

## C-1 Similarity solution for Regime II

In the regime (II), the conduction mechanism mainly remains in the ohmic regime. Since the current density is constant during the spreading process, the electric field must remain constant. In this case, electric pressure is constant and  $V_f \propto h$ , therefore,  $n$  in equation (1) must equal to zero.

According to Eq.(7), the spreading dynamics obeys:

$$\bar{R}(\bar{t}) = C^* \bar{t}^{-1/(6-2n)}$$

Substituting  $n = 0$  :

$$\bar{R}(\bar{t}) = C^* \bar{t}^{-1/6}$$

This is the spreading law we obtained previously by two different methods: (i) Stephan's analogy (ii) energy balance method.

## C-2 Similarity solution for Regime III

For Regime III, the relationship between the surface potential and thickness variation is more difficult. Based on the experimental results, the J-V characteristics shows reasonable agreement with Onsagar's model.

$$J = 2cD(E)h = 2chD_o \exp\left\{-U_o + 2e^{3/2}\left(E / 4\pi\epsilon_r\epsilon_o\right)^{1/2}\right\} / k_B T \quad (1)$$

As it can be implied, at a given corona discharge condition (constant applied voltage and electrode separation), the current density is constant and:

$$\exp(a\sqrt{E}) = \frac{H}{h}$$

Since the V-J measurements for thin liquid film is difficult, from the existing data for the range of thicknesses  $4 \times 10^{-6} - 8 \times 10^{-7} m$ , the following inequalities can be written based on the experimental data:

$$E < \left(\frac{1}{a^2}\right) \frac{H}{h} \text{ or } E < \frac{H^*}{h}$$

$$E^2 > \left(\frac{1}{a^2}\right) \frac{H}{h} \text{ or } E^2 > \frac{H^*}{h}$$

Therefore, the electrostatic component of disjoining pressure due to the interfacial excess charge is bonded between  $1/h$  and  $1/h^2$ .

$$\frac{B_1}{h} < \Pi < \frac{B_2}{h^2}$$

Therefore, the spreading dynamics can be calculated by Eq.(7) by substituting  $n=1$  for lower value and upper value  $n=2$ . The spreading dynamics can be varied between:

$$\bar{t}^{-1/4} < \bar{R}(\bar{t}) < \bar{t}^{-1/2}$$

### C-3 Similarity solution for Regime IV

Reconsidering the late stage of the spreading of a film which the substrate is completely wetted by the precursor film:



$$\frac{\partial h}{\partial t} = -\frac{1}{3r\mu} \frac{\partial}{\partial r} \left( rh^3 \Pi'(h) \frac{\partial h}{\partial r} \right) \quad (1)$$

In this regime, the change in surface potential during the spreading process becomes negligible and the liquid interface tends to adapt intermediate values of electric potential between zero (at solid conductive substrate) and a finite value of surface potential at slightly above the solid boundary where the interface is located. Therefore, thin film tends to creep along the substrate and conserve surface potential at a finite value of  $V_f^*$ . This is thermodynamically preferable since the jump from finite voltage to zero is not physical and creeping along the solid interface with reduced thicknesses may minimize the energy in the film. For this case, it would be reasonable to consider the electrostatic disjoining pressure as following:

$$\Pi = -\epsilon_f \frac{V_f^{*2}}{h^2} \quad \text{where } V_f^* \sim \text{cte} \quad (2)$$

Considering the van der Waals disjoining pressure:

$$\Pi_{vw} = \frac{A}{6\pi h^3} \quad (3)$$

$$\Pi_t = \Pi + \Pi_{vw} = \frac{A}{6\pi h^3} - \epsilon_f \frac{V_f^{*2}}{h^2} \quad (4)$$

Let's assume the case where the electrostatic forces are absent.

The diffusion coefficient for van der Waals forces:

$$D_{vw} = -\frac{1}{3\mu} \left( h^3 \Pi'_{vw}(h) \right) = \frac{A}{6\mu\pi h} \quad (5)$$

Assuming the precursor film thickness is cut at  $h(r, t) = h_s$ ,

$$D_{vw} = -\frac{1}{3\mu} \left( h^3 \Pi'_{vw}(h) \right) = \frac{A}{6\mu\pi h_s} \quad (6)$$

The solution of Eq.(6) becomes in the following form:

$$\bar{R}(\bar{t}) = C^* \bar{t}^{1/2} \quad (7)$$

The classical solution for precursor film in the presence of repulsive van der Waals forces is:

$$\left( \frac{A}{3\mu\pi h_s} \right)^{1/2} \sqrt{t} \quad (8)$$

Considering the molecular length scale,  $a = \sqrt{\frac{A}{6\pi\gamma}}$ , the cut thickness,  $h_s$ , can be calculated as

$$h_s = a \left( \frac{3\gamma}{2S} \right)^{1/2} \quad (9)$$

Substituting the Eq.(9) to Eq.(8), the constant  $C^*$  in eq.(7) is determined. The solution presented in eq.(7) presents the dynamics of conventional diffusive precursor films.

## References

- [1] B. Bhushan, J.N. Israelachvili, U. Landman, 1995, Nanotribology: friction, wear and lubrication at the atomic scale, *Nature*, **374**, 607-616.
- [2] A. Laiho, L. Herlogsson, R. Forchheimer, X. Crispin, M. Berggren, 2011, Controlling the dimensionality of charge transport in organic thin-film transistors, *Proc. of the Nat. Acad. of Sci. of the USA*, 1107063108v1-5.
- [3] T. Mills, L.G. Kaake, X.Y. Zhu, 2009, Polaron and ion diffusion in a poly(3-hexylthiophene) thin-film transistor gated with polymer electrolyte dielectric, *Appl. Phys. A Mat. Sci. and Proces.*, **95**, 291–296.
- [4] G. Xie, J. Luo, S. Liu, D. Guo, C. Zhang, 2011, Nanoconfined liquid aliphatic compounds under external electric fields: roles of headgroup and alkyl chain length, *Soft Matter*, **7**, 4453-4460.
- [5] C. Iacob, J. R. Sangoro, W. K. Kipnusu, R. Valiullin, J. Kärger, F. Kremer, 2011, Enhanced charge transport in nano-confined ionic liquids, *Soft Matter*, DOI: 10.1039/c1sm06581e.
- [6] F. Dinelli, M. Murgia, P. Levy, M. Cavallini, F. Biscarini, D. M. Leeuw, 2004, Spatially correlated charge transport in organic thin film transistors, *Phys. Rev. Let.*, **92**, 116802-1-4.
- [7] P. Kim, C. Duprat, S.S.H. Tsain, H.A Stone, 2011, Selective spreading and jetting of electrically driven dielectric films, *Phys. Rev. Let.*, **107**, 034502-1-4.
- [8] S. R. Mahmoudi, K. Adamiak, G. S. P. Castle, 2011, Spreading of a dielectric droplet through an interfacial electric pressure, *Proc. of the Royal Soc. A*, **467**, 3257-3271.
- [9] M. Pasandideh-Fard, Y.M. Qiao, J. Mostaghimi, 1996, Capillary effects during droplet impact on a solid surface, *Phys. of Fluids*, **8**, 650-659.

- [10] L. Onsagar, 1934, Deviations from Ohm's law in weak electrolytes, *J. of Chem. Phys.*, **2**, 599-615.
- [11] A. I. Zhakin, *Conduction Phenomena in Dielectric Liquids, EHD Models, Linear and Nonlinear Effects on the Charged Interface*, Vienna, Austria: Springer, 1998.
- [12] D.R. Lamb, *Electrical Conduction Mechanisms in Thin Insulating Films*; Methuen and Co.: London, 1968.
- [13] J. G. Simmons, *DC Conduction in Thin Films*, London, UK: Mills and Boon Ltd., 1971.
- [14] T. J. Sluckin, D.A. Dunmur, H. Stegmeyer, *Crystals that flow: Classical papers from the history of liquid crystals*, London, UK: Taylor and Francis, 2004.
- [15] V. M. Starov, M. G. Velarde, C. J. Radke, *Wetting and Spreading Dynamics*, Boca Raton, FL, USA: CRC Press, 2007.
- [16] L. Leger, J.F. Joanny, 1992, Liquid spreading, *Reports on Progress in Physics*, **55**, 431-486.
- [17] A. Hoang, H. P. Kavehpour, 2011, Dynamics of nanoscale precursor film near a moving contact line of spreading drops, *Phys. Rev. Let.*, **106**, 254501-1-4.
- [18] P.G. de Gennes, 1985, Wetting: statics and dynamics, *Rev. of Modern Phys.*, **57**, 827-863.
- [19] R.S. Sigmond, 1982, Simple approximate treatment of unipolar space-charge-dominated coronas: the Warburg law and the saturation current, *J. of Appl. Phys.*, **53**, 891-898.
- [20] J. J. Thomson, G. P. Thomson, *Conduction of Electricity through Gases*, 3rd, London, UK: Cambridge University Press, 1928.

- [21] F. Pontiga, A. Castellanos, 1996, The effect of field-enhanced injection and dissociation on the conduction of highly-insulating liquids, *IEEE Trans. on Dielectr. and Electr. Insul.*, **3**, 792-799.
- [22] B.V. Derjaguin, *Theory of Stability of Colloids and Thin Films*, Plenum Press, New York: Consultants Bureau, 1989.
- [23] J.F. Joanny, P.G. de Gennes, 1986, Upward creeping a wetting fluid: a scaling analysis, *J. de Phys.*, **47**, 121-127.
- [24] P. Ball, 1989, Spreading it about, *Nature*, **338**, 624-625.

## Chapter 8

### Retraction control of an impacted dielectric droplet through electric pressure

#### 8.1 Introduction

Controlling the deposition of impacted droplets on a non-wetting solid substrate is important for numerous industrial and scientific applications, such as deposition and coating techniques, ink jet printing, rapid spray cooling of a heated target, thin film evaporation, and pharmaceutical processes [1,2]. High-speed droplets colliding with a non-wetting substrate expand and subsequently retract [5,11,15] (see Fig.1a). Compared with the expansion phase investigations [17,18], the retraction dynamics have received less attention in the literature, primarily due to the complexity of the fluid dynamics [14,16]. It was recently demonstrated that polymer additives in water [5,12] significantly slow down the retraction rate through the non-Newtonian rheological effects [6,11]. Although adding such agents is remarkably successful in suppressing the retraction phenomenon for water droplets, these polymers are not soluble in dielectric liquids, thus new techniques for retraction inhibition of such liquids are potentially of interest.

When a deposited dielectric droplet is exposed to a strong enough unipolar ion injection in a gaseous medium, an electric pressure can be developed over its interface. At and above the onset of corona discharge, the charge carriers, generated due to the ionization process, drift towards the grounded substrate and the deposited dielectric droplet (see Fig. 1b). Interaction of the strong electric field and the surface charges deposited on the droplet creates an interfacial electrical pressure. The electrical pressure exerts a net squeezing force towards the substrate and the droplet spreads axisymmetrically in the radial direction [13]. This positive interfacial electric force creates a resistance against the capillary forces acting to retract the impacted droplet.

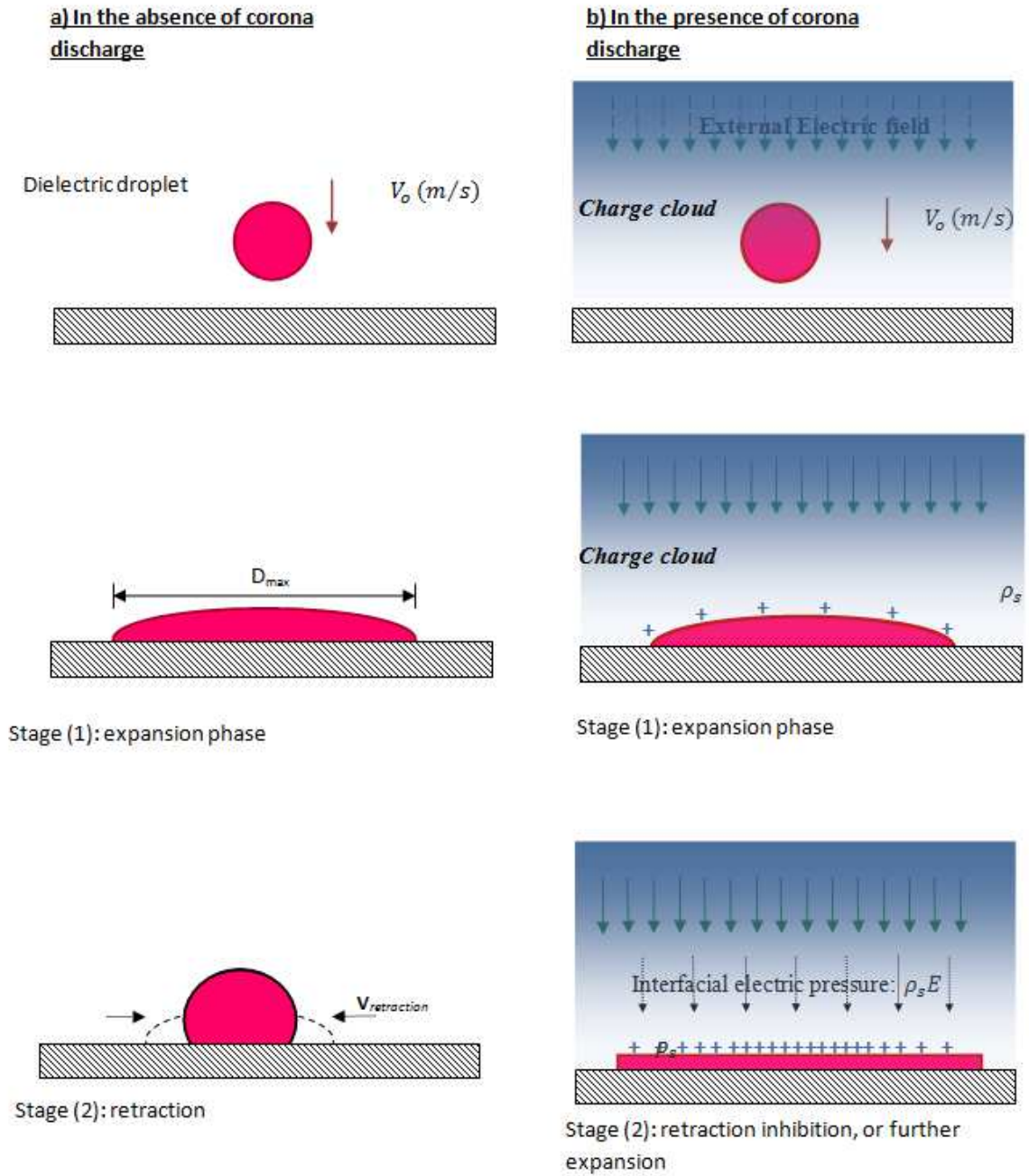


**Figure 1: Stages of droplet evolution in the absence of corona discharge (a) and in the presence of corona discharge (b).**

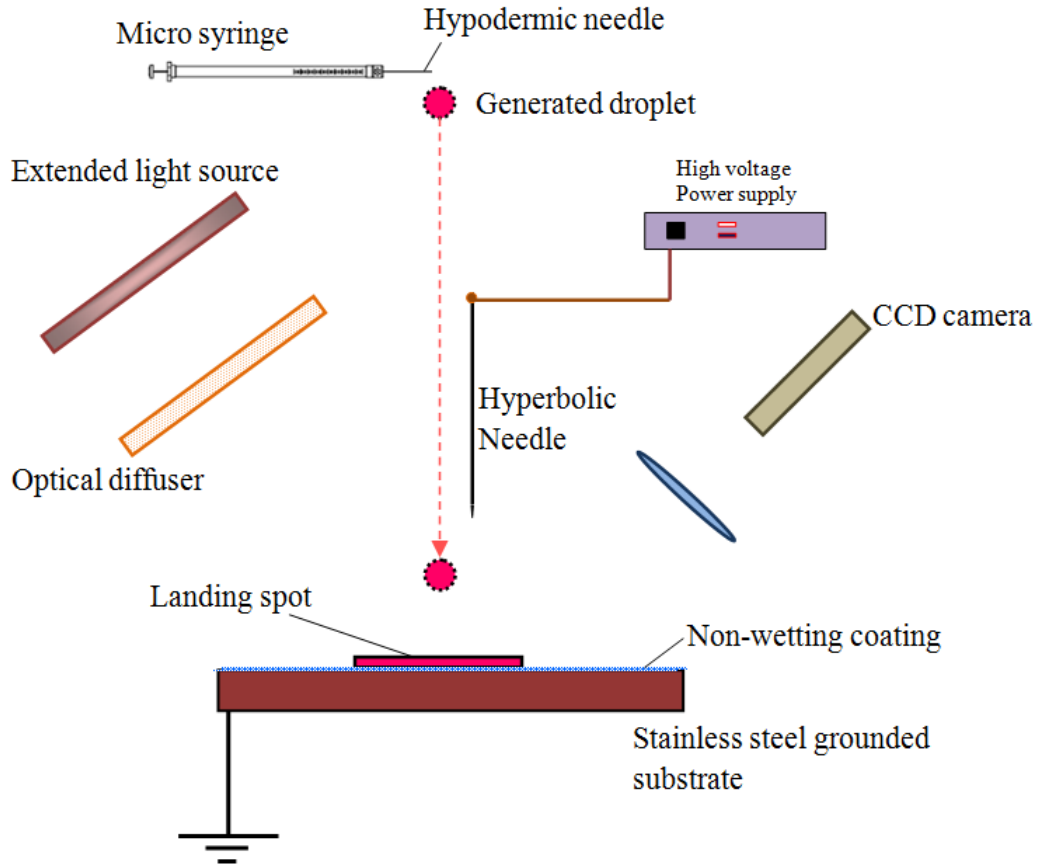


**Figure 2: Schematics of experimental setup**

The charging of a dielectric film through unipolar ion injection is a transient phenomenon, but in the quasi-equilibrium condition, where the surface charge asymptotically reaches its saturation limit, the electric pressure over a dielectric interface can be estimated from a simplified model as [7,13]:

$$\rho_s E_n = \frac{1}{\epsilon_f \sigma_f^2} \left( \frac{9\alpha K_a \epsilon_a^2}{8} \right)^2 \left( \frac{V^4}{S^6} \right) \quad (1)$$

where  $V$  is the voltage applied to the corona electrode,  $S$  is electrode gap spacing,  $K_a$  and  $\epsilon_a$  are ion mobility of the positive ions and electrical permittivity of the air, respectively, and  $\sigma_f$  is electrical conductivity of the dielectric liquid. The electric field enhancement



coefficient  $\alpha$  equals 1 for strong uniform ion injection in an infinite film layer (Mott's steady-state space-charge-limited conduction [7,8]), but it has higher values for sharp emitter electrodes.

In the presence of a moderate or strong corona discharge, a typical value of the capillary force,  $\vec{F}_c$ , and electric force,  $\vec{F}_{EP}$ , resulting from the electrical pressure,  $\rho_s E$ , established over a dielectric interface with the electrical conductivity of  $\sim 10^{-9}$  S/m can be estimated as:

$$|\vec{F}_c| = 2\pi R(t)\gamma[1 - \cos(\theta_R)] = 2 \times 3.14159 \times (1 - 2 \times 10^{-2} \text{ m}) \times (20 \times 10^{-3} \text{ Nm}^{-1}) \times [1 - \cos \approx 90^\circ] \sim O(10^{-4} - 10^{-3} \text{ N})$$

$$\begin{aligned} |\vec{F}_{EP}| &= \rho_s E A_s \\ &\approx (10^{-6} - 10^{-5} \text{ C m}^{-2}) \times (10^5 - 10^6 \text{ N C}^{-1}) \times 3.14159 \\ &\times (1 - 2 \times 10^{-2} \text{ m}) \sim O(10^{-3} - 10^{-2} \text{ N}) \end{aligned}$$

This crude order of magnitude analysis suggests that the interfacial electric forces and capillary forces are of the same order at a moderate corona discharge. For an intense unipolar ion injection, the interfacial electric force can be even an order of magnitude stronger than the capillary force. This implies that the electric force may be strong enough to intervene in interfacial capillary-driven retraction phenomena.

Although conventional passive retraction inhibition techniques for aqueous droplets on hydrophobic surfaces have been the subject of several theoretical and experimental works [5,6,11,12], to the best of the author's knowledge the corona discharge inhibition technique for dielectric liquid droplet has not been considered. In this paper, we propose a new active technique to suppress, or inhibit, the retraction of a dielectric droplet impacted on a non-wetting solid dry substrate. Different dielectric liquids, silicone oil, ISOPAR-L and its solution with a surfactant, were used to demonstrate the effectiveness of the proposed technique. The prominent feature of the proposed method is that the

retraction speed can be actively controlled by changing the ion injection strength through variation of the electric field.

## 8.2 Experimental Setup

The schematic diagram of the experimental setup is presented in Fig. 2. The two different fluids, silicone oil and ISOPAR-L, were chosen for this study based on their electrical and thermophysical properties as summarized in Table. I. The non-wetting substrate was developed by applying a solution of silica nanoparticles and n-Heptane over the mirror finished stainless steel substrate.

Table.I Electrical and thermophysical properties of the working fluids used in this study at 296.7 K.

Dielectric liquid	Density $\rho(kg/m^3)$	Viscosity $\nu(cSt)$	Electric conductivity $\sigma_{eq} \times 10^{-9}(S/m)$	Permittivity $\epsilon(pF/m)$	Surface tension (mN/m)
Silicone oil	961	50	5.5	23.9	22
ISOPAR-L®	763	2	4	16.82	24
ISOPAR-L® 3.3×10 <sup>-3</sup> M AOT	763	2	10	16.82	24

In the normal situation, the droplet strikes the surface, spreads out and subsequently undergoes rapid retraction. The initial size of the droplet,  $D_o$ , and its impact velocity were measured to be  $\sim 3.3$  mm and 2.8 m/s, respectively. Both the initial droplet size and impact velocity were kept constant during all the experiments. The corona discharge was generated between a high voltage emitter electrode and grounded substrate. The high voltage emitter electrode was a stainless steel needle with a well-defined hyperbolic tip profile with a radius of 50  $\mu m$ . The high voltage emitter electrode was mounted perpendicularly above the grounded substrate with a separation of 38 mm. The axis of emitter electrode was adjusted 5 mm off the center of the landing spot over the substrate. The applied voltage and corona current were measured using a high voltage voltmeter (80K-40 Fluke high voltage probe) and a Keithley® 610B electrometer. An extended light

source, an optical diffuser, and a high-speed CCD camera were used to record the dynamics of the droplet behavior during and after the impact process. The accuracy of the dynamic film diameter measurements was determined to be  $\pm 0.2$  mm. All the experiments were repeated at least twice to ensure the reproducibility of the presented results.

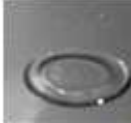
### 8.3 Results

Fig. 3 shows examples of the photographic sequences of evolution of different dielectric droplets obtained after the droplet impact at different applied voltages. For the silicone oil droplet in the absence of corona discharge ( $V=0$ ), the expansion stage takes place during  $\sim 5$  ms after the impact. This stage is followed by retraction of the droplet, which typically starts a few tens of milliseconds after the impact. Compared with the expansion stage, the rate of retraction stage is an order of magnitude slower than the expansion stage.

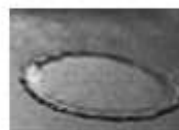
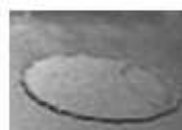
The effect of moderate and strong corona discharge on dynamic spreading ratio,  $\beta(t) = D(t)/D_o$ , of the impacted droplet is presented in Fig. 4. By increasing the corona voltage to  $V=12.5$  kV, a total corona current of  $9 \mu\text{A}$  was measured, the electric pressure increases and the droplet retraction is eliminated. By further increasing the applied voltage to 16 kV, the current increases to  $18 \mu\text{A}$  and not only is the droplet retraction prevented, but also further spreading can be achieved. This is attributed to the fact that increased applied voltage causes more ionization adjacent to the high voltage electrode and elevates the rate of charging due to the increased corona current. Compared with the electrical pressure given by Eq.(1) at the onset of corona discharge, the calculated electrical pressure is augmented at least 50 times at 16 kV, assuming that the field enhancement coefficient is identical at both applied voltages. Consequently, this impressive augmentation of electrical pressure at 16 kV applied voltage would explain the continued droplet spreading without retraction.

Silicone oil:

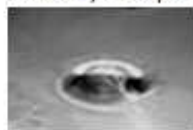
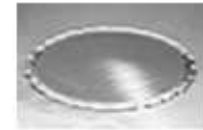
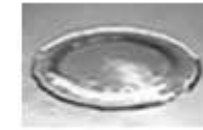
V=0 kV

 $t \sim 0 \text{ ms}$  $t=5 \text{ ms}$  $t=100 \text{ ms}$  $t=1000 \text{ ms}$ V=16 kV, I=18  $\mu\text{A}$  $t \sim 0 \text{ ms}$  $t=5 \text{ ms}$  $t=100 \text{ ms}$  $t=1000 \text{ ms}$ Pure ISOPAR-L:

V=0

 $t \sim 0 \text{ ms}$  $t=5 \text{ ms}$  $t=10 \text{ ms}$  $t=30 \text{ ms}$  $t=100 \text{ ms}$ V=20 kV, I=33  $\mu\text{A}$  $t \sim 0 \text{ ms}$  $t=5 \text{ ms}$  $t=10 \text{ ms}$  $t=30 \text{ ms}$  $t=100 \text{ ms}$ ISOPAR-L with  $3 \times 10^{-3} \text{ M AOT}$ :

V=0 kV

 $t \sim 0 \text{ ms}$  $t=5 \text{ ms}$  $t=10 \text{ ms}$  $t=30 \text{ ms}$  $t=100 \text{ ms}$ V=24 kV, I=54  $\mu\text{A}$  $t \sim 0 \text{ ms}$  $t=5 \text{ ms}$  $t=10 \text{ ms}$  $t=30 \text{ ms}$  $t=100 \text{ ms}$ 

**Figure 3: Comparison of droplet spreading using different fluids at different applied voltages and corona currents. The electrode spacing was 38 mm.**

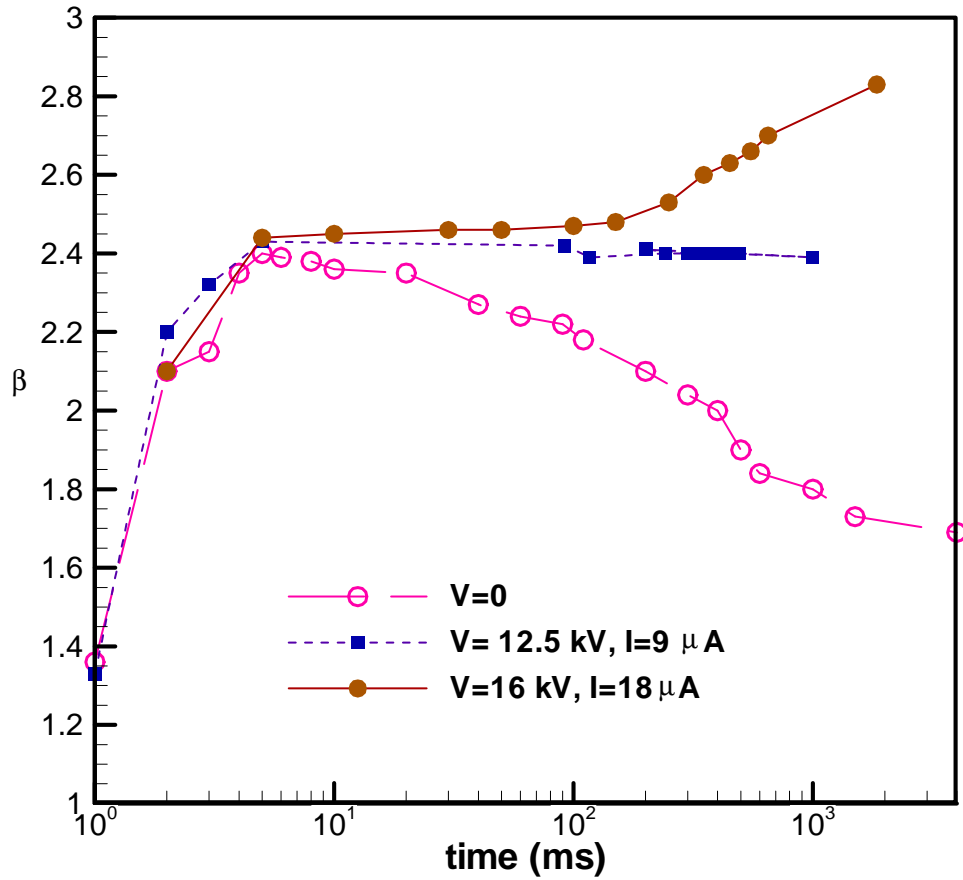


**Figure 4: Dynamic spreading ratio of an impacted silicone oil droplet in the presence of corona discharge**

Fig.5 presents the results for ISOPAR-L whose molecular viscosity is 25 times lower than the silicone oil, while both the surface tension and electrical conductivity are in the same order of magnitude (See the Table. I). Compared with silicone oil, the retraction process for ISOPAR-L in the absence of corona discharge is one order of magnitude faster since its molecular viscosity is one order of magnitude lower and the surface tension of both liquids is approximately the same.

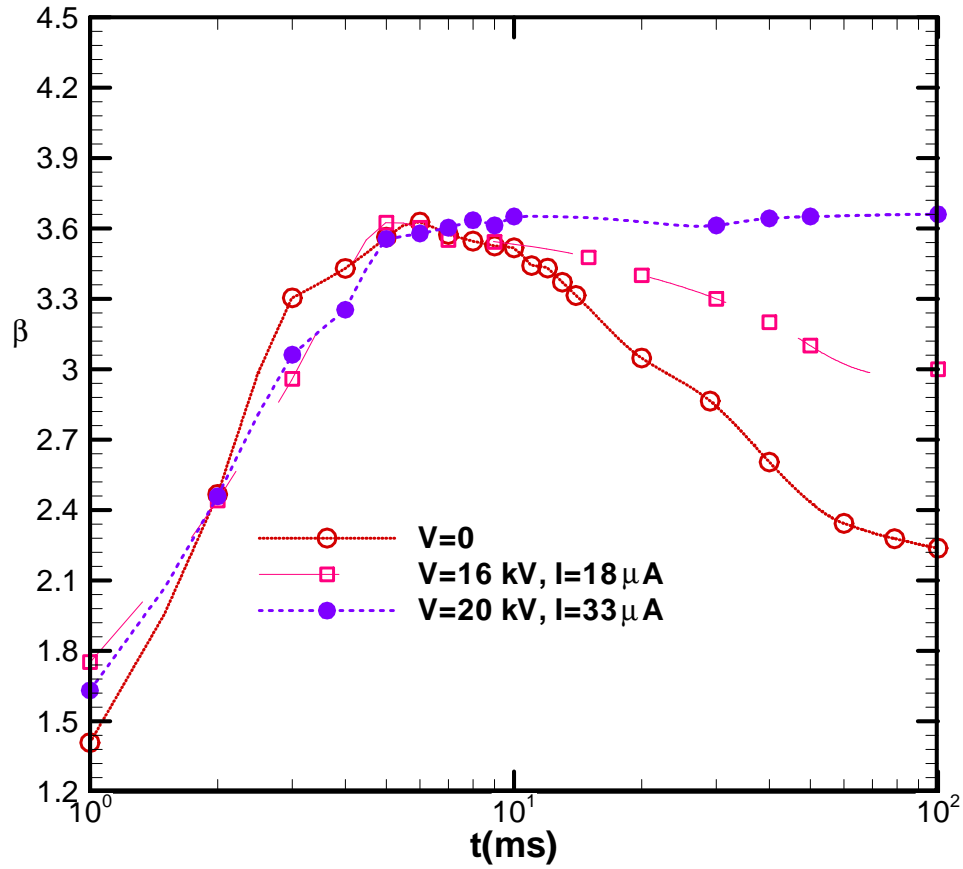


**Fig. 5 Dynamic spreading ratio for ISOPAR-L at different applied voltages. Droplet spreading ratio  $\beta = \frac{D}{D_0}$  versus time in the presence of corona discharge.**

Similarly to the silicone oil, by increasing the corona voltage the retraction process is suppressed. However, for ISOPAR-L, a comparatively larger electric pressure is required to mitigate the retraction process. For instance, by increasing the applied voltage to 16 kV, the retraction speed is still significant. By further increasing the applied voltage to 20 kV, the ion injection is strengthened and the corona current increases to  $I=33\mu\text{A}$ , so that the retraction is completely inhibited. These results show that higher applied voltage and interfacial electric pressure are required to overcome the capillary forces, when the retraction resistance due to the viscous force is weaker. Moreover, the experimental observations for both liquids revealed that the corona discharge has no appreciable effect on the droplet expansion phase. This implies that during the expansion stage the impacted

droplet remains practically unchanged. The inertia force is the only dominant force during the expansion and contribution of the interfacial electric force is not appreciable at the very beginning of the evolution, where the instantaneous surface charge magnitude is likely to be far below the saturation limit. This hypothesis will be revisited later in more detail.

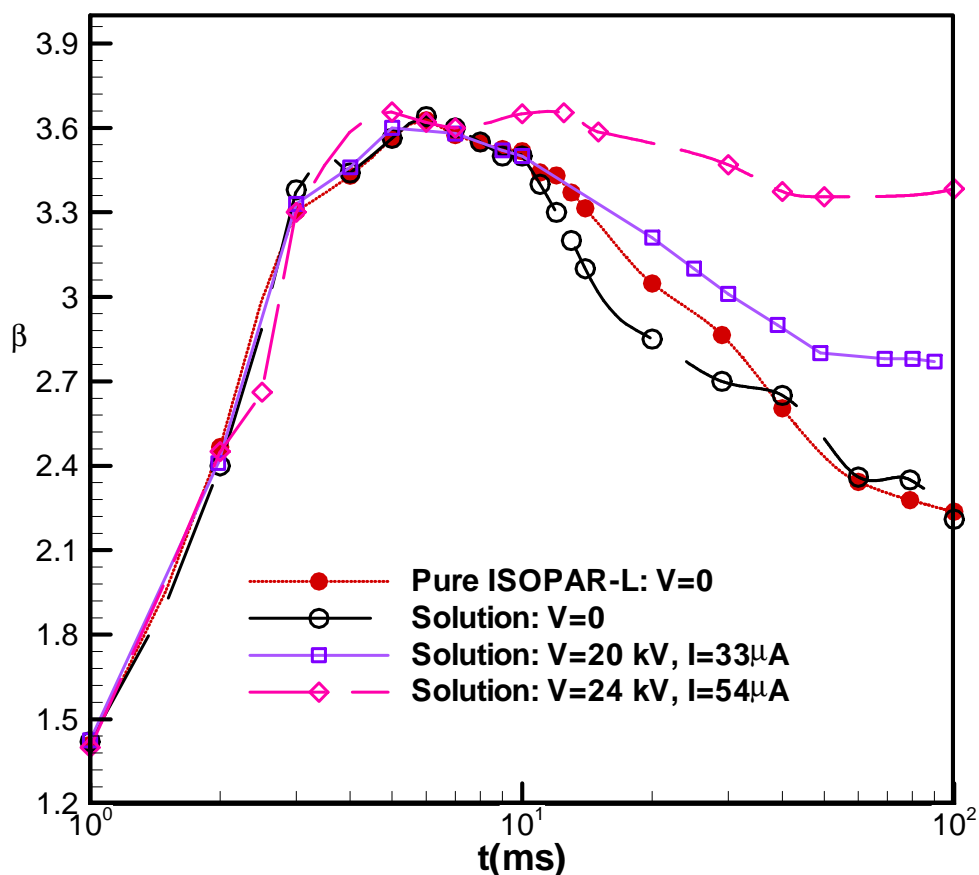


**Fig. 6 Dynamic spreading ratio of ISOPAR-L droplet with  $3.3 \times 10^{-3}$  M AOT additive in the presence and absence of corona discharge.**

In order to further examine the theoretical postulations, the electrical conductivity of ISOPAR-L was elevated by dissolving low concentrations of di-2-ethylhexyl sodium sulfosuccinate (AOT) in ISOPAR-L. For this solution other thermophysical properties remain approximately unchanged [10]. Fig. 6 compares the dynamic evolution of pure ISOPAR-L and the solution of ISOPAR-L with  $3.3 \times 10^{-3}$  M AOT in the absence and presence of corona discharge. Comparison of the evolution characteristics confirms that

the thermophysical properties of the liquid do not show any significant changes. For pure ISOPAR-L the retraction can be eliminated at 20 kV (Fig. 5). For the doped material, the droplet retraction is somewhat suppressed at 20 kV, but it is still significant. By further increasing the applied voltage up to 24 kV ( $I=54\ \mu\text{A}$ ), the retraction is remarkably suppressed although some slight retraction can still be observed. As it can be inferred from both the experiments and the theoretical postulation presented in Eq.(1), the elevated conductivity of the ISOPAR-L solution results in scaling down the accumulated surface charges, interfacial electric pressure, and consequently the resistance against the droplet retraction. The observations for conductive liquid droplets exposed to the corona discharge showed that the dynamics of evolution is not influenced by the ionic discharge. For this extreme case, since the electrical pressure is inversely proportional to electrical conductivity the surface charge may not be developed over the interface and the electrical pressure is not appreciable to suppress retraction for an impacted aqueous droplet evolution.

Fig. 7 shows the contact line speed at onset of the droplet retraction (slope of the spreading characteristics curves) as a function of applied voltage for all experimental cases. At voltages below the onset of corona discharge, where the discharge current is zero, there is no influence of the electric field. At the corona discharge threshold  $V\sim 6$  kV, the corona current was  $I=1\ \mu\text{A}$  and the retraction process shows no measurable changes. By increasing the applied voltage to 8 kV ( $I=2\ \mu\text{A}$ ), the rate of interfacial charging is almost doubled and the interfacial electric force becomes strong enough to slightly suppress the retraction. By increasing the applied voltage to 16 kV ( $I=17\ \mu\text{A}$ ), corona discharge completely eliminates the retraction stage for silicone oil and suppresses the retraction rate for the ISOPAR-L droplet more than 500%. For the solution with elevated electrical conductivity, the retraction rate is suppressed less than 200%. These results show that for liquids with higher electrical conductivity, one must apply stronger ion injection (corona voltage and corona current) to compensate for the interfacial charge reduction due to the conduction phenomenon. This observation is consistent with previous explanations and confirms the pivotal role of electrical conductivity in determining the electrical pressure magnitude and the retraction rate at a given corona voltage.



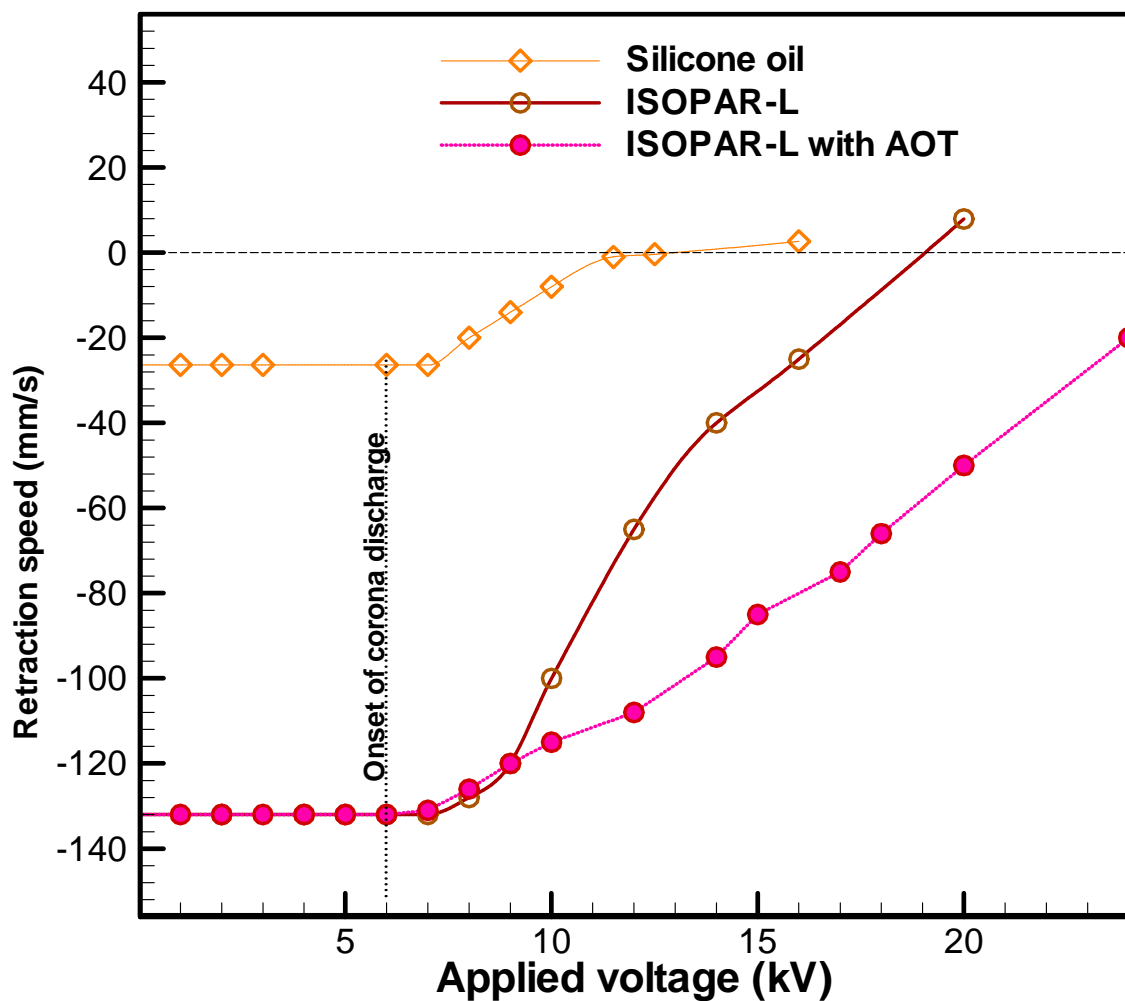


Figure 7: Retraction speed versus applied voltage.

## 8.4 Discussion

When the corona discharge is absent, the dynamics of an impacted droplet during early stages of the impact and the expansion is governed by two dimensionless numbers, Reynolds (ratio of inertia to viscous force),  $Re_{im} = \frac{\rho V_o D}{\mu}$ , and Weber (ratio of inertia to surface tension force),  $We_{im} = \frac{\rho V_o^2 D}{\sigma}$ . Whereas for the retraction stage, the inertia force is less important and the process is primarily governed by Capillary number  $Ca_{ret} = \frac{V_{ret} \mu}{\sigma}$ , which relates the competition between the viscous forces and surface tension. In the retraction phase, the capillary forces accelerate the retraction, while the viscous forces create resistance against it and decelerate the process [5].

In order to understand the effect of corona discharge on the droplet deposition process in both the expansion and retraction phases, an order of magnitude analysis based on relevant dimensionless numbers can be informative. Since the droplet spreading of an impacted droplet during the expansion phase is governed by Reynolds,  $Re_{sp}$ , and Weber numbers,  $We_{sp}$ , both numbers are defined based on the initial droplet diameter and the impact velocity. For the retraction stage, these two dimensionless numbers and the Capillary number are defined based on retraction speed and film diameter at the onset of retraction. Introducing a new dimensionless number based on electrical pressure can be beneficial to compare the electric force with the other forces during these two phases. In order to compare the contribution of the electric pressure generated by the corona discharge, the ratio of dimensionless numbers in the presence and absence of corona discharge should be compared. For the expansion stage, in the absence of corona discharge, the ratios of the Reynolds and Weber numbers are:  $Re_{sp}/Re_{ret} \approx \frac{100}{0.5}$ ,  $We_{sp}/We_{ret} \approx \frac{800}{0.01}$ . Comparing these ratios, it can be concluded that the inertia effect in the spreading stage significantly dominates over both viscous and capillary forces. Since the inertia forces have only a small effect on the retraction process, we consider the Capillary number. For our experiments in the absence of discharge, the retraction Capillary number is very small  $Ca_{ret} = \frac{V_{ret} \mu}{\sigma} \approx \frac{0.0004}{0.02} \ll 1$ . This suggests that the capillary forces are dominant. The Electro-capillary number for the expanded film exposed to the corona discharge can be defined as:

$$Ca_E = \frac{\xi \left(\frac{V^4}{S^6}\right)^D}{\sigma} \text{ where } \xi \text{ is } \left(\frac{9\alpha K_a \epsilon_a^2}{8 \epsilon_f \sigma_f}\right)^2 \quad (1)$$

Substituting experimental values of the imposed corona discharge parameters ( $V=12.5$  kV,  $S=38$  mm) for silicone oil, it can be concluded that the electric force is comparable with the capillary forces  $Ca_E \approx \frac{0.03}{0.02} = 1.5$ . Since the Capillary number is very small, it is clear that the electric force is significantly larger than the viscous forces. This can be examined by comparing the Capillary number for retraction and electrically inhibited retraction Capillary number:  $\frac{Ca_{E,ret}}{Ca_{ret}} = \frac{\xi \left(\frac{V^4}{S^6}\right)^D}{V_{ret}\mu} \approx \frac{0.03}{0.00035} \gg 1$ . Therefore, the retraction of silicone droplet is expected to be suppressed at this specific applied voltage and electrode separation. For silicone oil at  $V=16$  kV, the electro-Capillary number,  $Ca_E \approx \frac{0.21}{0.02} \sim 10$ , shows one order of magnitude increase. At this applied voltage, electric force is dominant and the retraction is inhibited (see Fig.4).

Comparison of the inertia force with the interfacial electric force during the expansion stage is also informative. During the expansion phase, we showed that the inertia force is  $10^4$  times larger than the capillary forces, while the electric force is only 10 times larger than the capillary force. This infers that the inertia force is  $10^3$  times larger than the electric force during the expansion stage and the inertia is dominant force even assuming the maximum charge accumulation over the droplet interface at saturation limit. These results further support the previous experimental evidence that the corona discharge has no visible influence during the expansion phase.

It should be noted that, in this analysis, any net charging of the droplet during its flight time and charge leakage during the collision are neglected. This assumption may be particularly valid for liquids with lower electrical conductivity [9], higher droplet velocities and shorter electrode gap spacings. Therefore, including these realistic conditions in a simplified model may add unnecessary complexity to the problem. However, in order to practically minimize the error due to these effects, the electrode separation and droplet flight path in this analysis were set to be identical for all experiments.

## 8.5 Conclusions

We have demonstrated that for low conductivity droplets the retraction can be suppressed even at moderate levels of corona discharges. It has been shown that for an impacted dielectric droplet at strong enough corona discharge, not only is the sequential droplet retraction eliminated, but also the initial expansion stage can be followed by a monotonic film expansion. For higher electrical conductivities, more intense corona discharge is required to decelerate the retraction stage. It can be concluded that the unipolar ion injection has no effect at the early stage of the droplet impact since the inertia is the dominant force in the expansion stage. The proposed technique is only applicable for dielectric liquids and is not effective for conductive impacted droplets.

## References

- [1] Frohn, A., Roth, R., 2000, *Dynamics of Droplets* Springer, Berlin.

- [2] Bernardin, J.D., Stebbins, C. J., Mudawar, I., 1997, Mapping of impact and heat transfer regimes of water drops impinging on a polished surface, *Int. J of Heat and Mass Trans.* **40(2)**, 247-267.
- [3] Bussmann, M., Chandra, S., Mostaghimi, J., 2000, Modeling the splash of a droplet impacting a solid surface, *Phys. Fluids* **12**, 3121-3132.
- [4] Mehdizadeh, N.Z., Chandra, S., Mostaghimi J., 2004, Formation of fingers around the edges of a drop hitting a metal plate with high velocity, *J. Fluid Mech.* **510**, 353-373.
- [5] Carré, A., Gastel, J., Shanahan, M., 1996, Viscoelastic effects in the spreading of liquids, *Nature* **379**, 432-434.
- [6] Bergeron, V., Bonn, D., Yves Martin, J., Vovelle, L., 2000, Controlling droplet deposition with polymer additives, *Nature* **405**, 772-774.
- [7] Vega, F., Pérez, A.T., 2002, Instability in a non-ohmic/ohmic fluid interface under a perpendicular electric field and unipolar injection, *Phys. Fluids* **14**, 2738-2751.
- [8] Mott, N.F., Gurney, R.W., 1964, *Electronic Processes in Ionic Crystals* Dover, New York.
- [9] Adamiak, K., 2002, Rate of charging of spherical particles by monopolar ions in electric fields, *IEEE Trans. Ind. Appl.* **38(4)**, 1001-1008.
- [10] Vega, F., García, F., 2006, Pattern imaging of primary and secondary electrohydrodynamic instabilities, *J. Fluid Mech.* **549**, 61-69.
- [11] Bartolo, D., Boudaoud, A., Narcy, G., Bonn, D., 2007, Dynamics of non-Newtonian droplets, *Phys. Rev. Lett.* **99**, 174502.
- [12] Smith, M.I, Bertola, V., 2010, Effect of polymer additives on the wetting of impacting droplets, *Phys. Rev. Lett.* **104**, 154502.
- [13] Mahmoudi, S.R., Adamiak, K., Castle, G.S.P., Spreading of a dielectric droplet through an interfacial electric pressure, *Proc. R. Soc. A. in press.*

- [14] Bartolo, D., Josserand, C., Bonn, D., 2005, Retraction dynamics of aqueous drops upon impact on non-wetting surfaces, *J. Fluid Mech.* **545**, 329-338.
- [15] Worthington, A., 1876, On the form assumed by drops of liquids falling vertically on a horizontal plate, *Proc. R. Soc. A.* **25**, 261–271.
- [16] Clanet, C., B´eguin, C., Richard, Qu´er´e, D., 2004, Maximal deformation of an impacting drop, *J. Fluid Mech.* **517**, 199–208.
- [17] Chandra, S., Avedisian, C. T., 1991, On the collision of a droplet with a solid surface, *Proc. R. Soc. A* **432**, 13-41.
- [18] Ukiwe, C., Kwok, D. Y., 2004, On the maximum spreading diameter of impacting droplets on well-prepared solid surfaces, *Langmuir* **21**, 666–673.

## Chapter 9

### Summary of the thesis

#### 9.1 Summary

The effect of electrostatic forces on various heat transfer and mass transport problems in gaseous and dielectric liquid media were investigated and a new corona-discharge assisted technique for controlling of the spread of liquid films was proposed. As described in Chapter 1, EHD effects may enhance the transport phenomena in both micro-scale and macro-scale by contributing to the momentum balance. The investigations conducted in this study were presented in seven chapters. In the first four chapters, electric field and EHD effects were used in the bulk of the gas and dielectric fluid to enhance heat transfer or mass transport. In the last three chapters, we put forth a new concept of net flow motion through interfacial electric pressure over the dielectric liquid/vapor interface. It was demonstrated that corona discharge bombardment of the droplet/film interface may induce net electrostatic interfacial pressure, which can be effectively used to control droplet spreading dynamics or the retraction phase of impacting droplets. It was also demonstrated that ultra thin films of dielectric liquids, whose thickness is in nanometer scale, can be deposited over a metallic substrate by the same technique. The main contributions of the current study presented in each chapter are summarized below.

##### 9.1.1 Effect of corona discharge on natural convection heat transfer

Natural convection heat transfer enhancement through corona wind has been the subject of extensive studies for more than 50 years. The previous authors used the energy balance method to predict average EHD heat transfer enhancements for various shapes of external objects. However, there has been little knowledge about the local heat transfer

enhancements. In Chapter 1, an interferometric study of corona discharge heat transfer enhancement from a horizontal isothermal cylinder was performed. The corona emitter electrode was a sharp blade electrode while the collector electrode was the grounded heated cylinder. An optically-large plate Mach-Zehnder interferometer was used to visualize the thermal boundary layer around the cylinder and further quantify the heat transfer measurements. For the first time, the local heat transfer was extracted from the interferograms and compared with numerical simulation results. By applying 17 kV voltage to a blade corona electrode, a maximum 100% local heat transfer enhancement at the lower stagnation point of the heated cylinder was obtained at relatively low Rayleigh numbers. Also, for voltages above 15.5 kV and currents above 6  $\mu\text{A}$ , the numerical results showed that the electric body force becomes strong enough to produce high velocity gradients near the blade. This strong velocity gradient results in a recirculation zone established below the cylinder. The recirculation zone causes an insufficient entrainment of the cool fresh air into the thermal boundary layer at  $0^\circ < \theta < 80^\circ$  and results a decrease in local Nusselt number at the same location. Stronger recirculation is produced by higher corona currents. It was also found that the corona wind is more effective at low Rayleigh numbers, where the buoyancy-driven flow is weaker.

### 9.1.2 Mono-dispersed droplet cooling

In Chapter 2, two-phase cooling of free-falling mono-dispersed water droplets impacting on a smooth upward-facing horizontal heated disk at pre-CHF regimes was revisited. The main reasons of this reinvestigation were: (i) the existing droplet cooling correlations are not applicable for Weber numbers less than 50 (ii) several complications were found in the experimental setups of the previous studies, which made their results and their proposed correlations unreliable (iii) it was intended to explore the potential application of the imposed electric field on boiling enhancement of the droplet cooling technique. Extensive sets of experiments with a corrected experimental setup were performed to find the effect of droplet size and impacting frequency on boiling curves and CHF in the absence of electric field. Two different regimes, low Weber number ( $We < 50$ ) and very low Weber number ( $We < 20$ ) were identified. Two different correlations were proposed to predict the experimental CHF at these different regimes. The experiments in the presence



of electric field were not as successful because the imposed electric field significantly changed the path of the falling droplets. Moreover, the sporadic jetting and random Taylor cone formation re-directed the main volume of the coolant off the heated surface. These results show that for this particular situation there is no advantage to using electric fields to enhance the droplet cooling effect.

### 9.1.3 Jet impingement boiling heat transfer

Direct jet impingement boiling heat transfer operating at low flow rates is of great interest for controlling localized moderate heat fluxes in equipment having delicate mechanical structures, where aggressive techniques, such as high-speed jets, are not suitable. Boiling heat transfer from an upward facing disk targeted by a falling jet was studied experimentally at different volumetric flow rates and various jet lengths. The working fluid was chosen to be the dielectric liquid HFE7100 and the heated spot was an 8-mm diameter disk. Using previous CHF correlations in their original form, valid at very low volumetric flow rates, result in large disagreements since it was found that variation in the jet length changes the boiling characteristics. It was demonstrated that although the circular hydraulic jump formation within the heater diameter may suppress the heat transfer under certain conditions, moving the jet closer to the target may significantly improve the boiling curves at the critical heat flux (CHF) regime.

At low flow rates, the CHF increases as the jet length decreases, while for moderate and high flow rates the boiling curves show approximately a universal behavior for different jet lengths. For such low flow rates, the effect of jet length on boiling curves was shown to be related to the variation of the cross section of the falling jet and the formation of the hydraulic jump at radial distances smaller than the heater diameter. The current CHF experimental data for different jet lengths are correlated by including the effect of jet length in the previous correlation proposed by Sharan and Lienhard.

In the absence of electric field, a simple way to increase the momentum of the liquid sheet around the rim is increasing the flow rate. An alternative way to enhance the momentum of the liquid sheet around the edge is to introduce EHD forces. It was

demonstrated that imposing voltages about 11 kV with jet separations about 4 mm at the lowest flow rate of 6 cc/min causes CHF enhancements of more than 100%. Unlike the droplet cooling case the presence of an imposed electric field, the imposed electric field to falling jets is promising.

#### 9.1.4 Conduction micropumping

Shrinking the dimensions of EHD pumps has been a subject of great interest, since it may reduce the range of operating voltage and the size of the power supply. Although one may find several micro-scale designs for ion injection and induction pumps, very limited work has been conducted to scale-down the conduction pumps. This may be due to the fact that conduction pumping has only been proposed very recently. Since conduction pumping eliminates the direct ion injection from the solid/ liquid interface, it preserves the thermophysical and electrical properties of the liquid. This interesting feature of the conduction pumps makes them interesting for long-term and sensitive applications, where a reliable operation of the EHD pump is needed. Moreover, study of the conduction pumping in thin dielectric liquid layers confined between electrodes provides intuitive understanding about the charge transport mechanism and pressure generation across the dielectric films.

In Chapter 4, a single-stage axisymmetric conduction micropump in the vertical configuration has been proposed. This micropump consists of four components: high voltage ring electrode, grounded disk-shaped electrode, insulator spacer and inlet/outlet ports. The high voltage electrode and grounded electrode of the device were etched on two separate commercial Liquid Crystal Polymer substrates with 30 $\mu$ m copper cladding using standard lithographic techniques. The final spacing between the two electrodes and the overall size of the device were measured to be 286  $\mu$ m and 50 mm $\times$ 70 mm $\times$  5mm, respectively. The static pressure generation of the micropump was measured at different applied voltage using three different dielectric liquids, 10-GBN Nynas and Shell Diala AX transformer oils, and N-hexane. The range of applied voltages was reduced one order of magnitude with respect to a similar macro-scale design. The range of operating voltage fell between 300 to 1500 VDC and a maximum pressure generation up to 100Pa was

achieved at 1500 VDC applied voltage. In order to further verify the experimental results, a numerical simulation was also performed. The pressure head generation was predicted numerically and compared with experimental results at different applied voltages. Several considerations for reducing the electrode separation in micro-scale design of the conduction pump were highlighted.

### 9.1.5 Concept of droplet spreading

A corona discharge-assisted technique for spreading of a gently deposited dielectric droplet into a uniform thin film over a dry isothermal conductive substrate is proposed here for the first time. It was shown that the droplet expansion process can be controlled through variation of the corona discharge parameters and/or discharge exposure time. The proposed explanation of the corona discharge-assisted spreading was confirmed by several qualitative and quantitative experiments. It was confirmed that the interaction of the surface charge density and intense electric field generates an interfacial electrical pressure and leads to a uniform axisymmetric spreading of the droplet in the radial direction. It was also demonstrated that the proposed technique can be analogous to the classical Stefan's squeezing liquid flow between two separated parallel disks. Through several simplifications, a mathematical model based on this analogy was developed. The dynamics of the film spreading due to the corona discharge can be predicted through a simplified analytical model based on this analogy. It was found that the dynamics of the liquid film formation for intermediate corona discharge exposure time obeys  $D(t) \sim t^{1/6}$  law, where  $D(t)$  is the diameter of the film and  $t$  is the corona discharge exposure time.

### 9.1.6 Different regimes of spreading

The studies in Chapter 5 were extended and are the subject of Chapter 6, which answers the following questions: What will happen if the droplet is exposed to corona discharge for long time? Is it possible to obtain ultra-thin film of a liquid through the proposed technique?

In this chapter, it has been demonstrated that the corona discharge spreading technique can be effectively used to produce uniform ultra thin films. Four different regimes of film

spreading have been identified and characterized. Since the charge transport mechanism across the film determines the dynamics of spreading, different regimes of charge carrier transport have been postulated and implemented to predict the rate of spreading. These mechanisms were confirmed both experimentally and theoretically. For each regime, a theoretical hydrodynamic model along with a description of the charge carrier transport mechanism has been proposed to predict the observed dynamics of spreading.

At the very beginning of the corona exposure (Regime I), the dielectric film expansion is governed by the transient surface charge accumulation and obeys the law  $D(t) \sim t^{1/2}$ . After the interfacial charging of the dielectric layer reaches a quasi-steady state, the spreading enters into Regime II, which was discussed in detail in Chapter 5. In this regime, the film expands monotonically with  $D(t) \sim t^{1/6}$  and the thickness of the film decreases. When the thickness of the film reaches some specific value in the order of hetero-charge layer thickness, a transition to Regime III is observed and the spreading is accelerated. The acceleration is found to be related to the electrostatic component of the disjoining pressure due to the hetero-charge layer attractive force. The transition to Regime IV, the most interesting regime, appears when the corona discharge exposure time is extended further and the thickness of the liquid film reaches sub-micrometer levels. In this regime, a new type of precursor film with thicknesses in the order of hundreds of Angstrom appears around the apparent contact line to the main film. The behavior of the precursor film is diffusive and rapidly expands ahead of the main film over the substrate due to the electrostatic component of the disjoining pressure. The observed accelerated precursor film is reminiscent of the conventional molecular precursor films, but its rate of expansion is significantly more rapid. A mathematical model is proposed to understand this electrostatically accelerated precursor film.

### 9.1.7 Droplet retraction inhibition

High-speed droplets colliding with a non-wetting substrate expand and subsequently retract. Suppressing the retraction phase is one of the most challenging problems in liquid film coating and impacting droplets over a non-wetting surface since it is encountered in several important applications. For the first time, a new active technique, based on the

corona discharge-assisted spreading concept, is proposed to control the deposition process of an impacted dielectric droplet over a non-wetting grounded substrate. An electric pressure resulting from the electric surface charge produced by the corona discharge squeezes the droplet interface towards the grounded substrate and generates a resistance against the droplet retraction. It is demonstrated that the electrical pressure effectively suppresses the droplet retraction at voltages above the corona discharge threshold. Applying stronger corona discharge voltages, it was demonstrated that not only is the droplet retraction prevented, but also further spreading can be achieved.

## 9.2 Proposal for future works

The presented work may suggest several applications as described below.

### 9.2.1 Ionic discharge heat exchangers

The natural convection heat transfer enhancement technique can be used for commercialized ionic heat exchangers. Particularly for microgravity conditions, where the energy management is of great concern, the corona discharge enhanced heat exchangers may find great interest since the energy consumption is small in the order of few miliwatts per meter of the heat exchanger tube. The electric field can replace the gravitational field to simulate natural convection in microgravity condition. Therefore, a detailed study of corona wind effect of an array of tubes rather than a single tube might be of great interest in outer space applications.

### 9.2.2 Conduction pumping: a candidate for heat removal element

Although the static pressure generation of a single-stage conduction pump is not significant, stacking micropumps to create large static pressure generation seems to be feasible. The multi-stage conduction micropump may find applications as a pumping element in heat management circuits.

### 9.2.3 Thin film evaporator

Thin film evaporation is an efficient technique for heat transfer and mass transport in several important applications including oil refinery and drying technologies. The corona discharge spreading technique can be used to create thin films for heat/mass transport enhancement purposes particularly the evaporation rate of the volatile liquids. This may find several applications in which wettability of the solid surface is of the great concern.

### 9.2.4 Metal Coating: monolayer deposition

The conventional coating techniques exploit high pressure atomization techniques for deposition of dielectric liquids on metallic substrates. The traditional techniques introduce significant amounts of pollution in the form of toxic mist-particles and micro-satellite droplets due to the high velocity impacting droplets over the substrate. Dielectric coating of conductive substrates through corona discharge may significantly suppress or even eliminate the unwanted particles or micro-droplets. The thickness of the dielectric coating generated by corona discharge assisted technique can be controlled from millimeters to nanometers. As main advantages of the technique, the corona discharge-assisted technique may reduce the energy consumption to 1000 times lower values and minimize the coating material wastage. Both features of the new technique, low energy consumption and optimization of coating material wastage, may help minimizing the greenhouse gas emissions directly and/or indirectly.

## Curriculum Vitae

**Name:** Seyed Reza Mahmoudi

**Post-secondary  
Education and  
Degrees:** University of Tehran  
Tehran, Tehran, Iran  
1999-2003 B.Sc.

University of Tehran  
Tehran, Tehran, Iran  
2003-2006 M.Sc.

The University of Western Ontario  
London, Ontario, Canada  
2009-2012 Ph.D.

**Related Work  
Experience** Teaching Assistant  
The University of Western Ontario  
2009-2012

### **Publications:**

S. R. Mahmoudi, K. Adamiak, G. S.P. Castle , M. Ashjaee "The Effect of Corona Discharge on Free Convection Heat Transfer from a Horizontal Cylinder" Experimental Thermal and Fluid Science, July 2010, Volume. 34, Issue.5 pp.528-537.

S.R. Mahmoudi, K. Adamiak, G.S. P. Castle "Two-Phase Cooling Characteristics of Mono-Dispersed Droplets Impacted on a Heated Surface" ASME/JSME Thermal Engineering Joint Conference, March 2011, Honolulu, HI, USA

S. R. Mahmoudi, K. Adamiak, G. S.P. Castle "Study of Electrohydrodynamic Micropumping Through Conduction Phenomenon" IEEE Transactions on Industry Applications, September 2011, Volume. 47, Issue.5, pp. 2224-2234.

S. R. Mahmoudi, K. Adamiak, G. S.P. Castle " Spreading of a Dielectric Droplet through an Interfacial Electric Pressure" Proceedings of the Royal Society, London Series A, November 2011, Volume. 467, pp. 3257- 3271.

S.R. Mahmoudi, G.S.P. Castle, K. Adamiak "Retraction Control of an Impacted Dielectric Droplet through Electrical Pressure" Soft Matter, January 2012, Volume. 8, Issue.3, pp. 808-813.